Institut Laue-Langevin

University of Reading

Department of Chemistry

PhD in Chemistry

PhD Thesis

Neutron Reflectometry and Ellipsometry applied to Atmospheric Night-time Oxidation

Supervisor:
Dr Christian Pfrang

Author:
Federica Sebastiani

ILL Supervisor:
Dr Richard Campbell

UNIVERSITY OF READING

Neutron Reflectometry and Ellipsometry applied to Atmospheric Night-time Oxidation

PhD in Chemistry

Department of Chemistry

School of Chemistry, Food and Pharmacy

Federica Sebastiani

I confirm that this is my own work and the use of all material from other sources has been properly and fully acknowledged.

Abstract

The fate of atmospheric aerosol is currently attracting increased attention from the scientific community because its impact on the Earth's radiative balance and on cloud formation is still largely unknown. To understand the ageing process of aerosol it is helpful to investigate heterogeneous reactions occurring between organic surface films and gas-phase oxidants. While most studies have focused on the abundant daytime oxidants O_3 and OH, during the night-time the OH concentration is very low and the concentration of the more potent NO_3 becomes significant.

In this thesis insoluble organic monolayers at a planar air-water interface were used as proxies for films on atmospheric aerosol, and the surface excess kinetics were monitored in situ using a combination of neutron reflectometry (NR) and ellipsometry. A range of compounds were chosen to allow a study of the effects on the reaction kinetics and product formation of the chain length, type of headgroup and degree of unsaturation on the organic molecule as well as the type of oxidant. To allow the work to be performed several key developments were carried out: a refined method for NR data analysis, the commissioning of a dedicated new miniature sample chamber, rigorous calibration of the oxidant concentrations and development of a kinetic model. The limitations of ellipsometry as a substitute for NR for the study of pure systems were explored, yet its potential to provide complementary information about product formation was demonstrated. Six reactions of pure organic monolayers revealed that the degree of unsaturation of the chain was by far the biggest factor for the reaction rate, although other differences were also systematically examined. Two binary mixtures were investigated showing that the reaction rate is consistently lower in mixed films, which may help to explain discrepancies in the literature between laboratory studies

To my family

Acknowledgements

First of all, I want to thank my supervisors: Christian Pfrang and Richard Campbell. They always offered support, encouragement and productive discussion. Their advice and comments were always fruitful and educational.

Special thanks to Alessio Laloni, besides being an invaluable friend, he helped me in designing the MIMIK chamber and making it work.

I want to thank Giovanna Fragneto for her support and wise advice since I started working with her as stagiaire in 2010. The ellipsometry measurements would not have been possible without the Partnership for Soft Condensed Matter, which gave me the access to the ellipsometer.

I want to thank Oleg Konovalov for hosting me in his laboratory at the ESRF to record isotherms and BAM images.

I want to thank the Walker Institute for funding my stay at the University of Reading, where I performed part of the spectroscopy studies. The conclusion of these studies was possible thanks to Mark Newton, who hosted me in his laboratory at the ESRF.

I want to thank Chrsitian Pfrang for introducing me into the collaboration with the groups of Ulrich Pöschl and Manabu Shiraiwa at the Max Planck Institute for Chemistry (Mainz, Germany). I want to thank Ulrich and Manabu for giving me such a great opportunity to work in a very exciting environment, where I learnt about modelling and I developed the model for describing my experimental data.

I want to thank the group of people (mostly Italians...) with whom I shared the lunch breaks and many other food-related experiences outside the ILL! I want to thank Giuliana, John, Andrea and Simona for the lovely time spent together. Special thanks to my office mate and friend Giacomo who made even the longest day in the office pleasant and funny. I want to thank my office neighbour and friend Yuri for having shared coffee breaks while discussing about neutron reflectometry, Matlab codes and Latex bugs. Thanks to all the friends I left in Italy for being present and interested to

Contents

Introduction

Over the last decades, aerosols have attracted more and more attention from the scientific community because the impact on the Earth's radiative balance and on cloud formation is still largely unknown [1, 2, 3]. Atmospheric aerosols derive from natural process (e.g. volcano, blown dust, sea-spray) and from human activities (e.g. combustion, cooking). Anthropogenic emissions have heavily increased during the last century, and the role of aerosol particles is seen as becoming more and more important especially in the chemistry of the troposphere.

A key feature for the aerosol behaviour is the presence of organic material both in the bulk and at the surface [4]. The composition and lifetime of aerosol particles in the atmosphere is determined by the ageing process due to exposure to trace gases, such as O_3, OH, NO_3, or other oxidants (e.g. Cl and Br). To study the aerosol ageing process it is crucial to investigate the heterogeneous reaction occurring between the particles and gas-phase oxidants. While homogeneous chemistry is well described at the molecular level, the study of heterogeneous reactions remains a major challenge. Field measurements suggest that heterogeneous reactions may change the chemical composition of particles and in particular of their surface films [5]. The reactions may alter important properties of the particles like aerosol hydrophilicity, toxicity and optical properties.

Most of the studies to date have investigated the heterogeneous reaction of organic aerosols by O_3 and OH, which are the main oxidants during daytime. During night-time the OH concentration is very low and then the concentration of the NO_3 may become significant. Therefore while OH radicals control the chemistry of the daytime atmosphere, NO_3 radicals have a similar role during the night-time [6, 7].

molecules allows the investigation of the effects of chain length, headgroup and degree of unsaturation on the reaction kinetics and products formed.

In order to monitor the surface excess of the organic molecule during the oxidation reaction, a combination of neutron reflectometry (NR) and ellipsometry is used. NR requires the use of deuterated forms of the molecules and the access to neutron beam time is limited, but is extremely powerful for partial and selective deuteration. Ellipsometry is proposed as lab-based substitute for NR for the studies of pure systems, and its capabilities are investigated through the comparison of the results of both techniques on single-component monolayers exposed to O_3 and NO_3.

The study of heterogeneous reactions at the air–water interface is made possible thanks to four key advances: refinement of the background treatment in the analysis of the NR data, improvements in the sample environment by design and commissioning of a new chamber, rigorous measurements of the oxidant concentrations and development of a kinetic model to interpret the data.

The high flux and the stability of FIGARO at the Institut Laue-Langevin (Grenoble, France) is exploited through the acquisition of data at the air–water interface that is far faster than was previously possible. Also, surface excesses down to minimal coverage need to be determined precisely, and for this a refined method of background treatment is implemented.

To allow a reliable comparison between NR and ellipsometry, a dedicated miniaturised reaction chamber is required. The MIMIK (Multi-Instruments Miniaturised Kinetics) chamber is a next generation sample chamber which is suitable for both NR and ellipsometry. The chamber has a gas delivery system optimised for homogeneous diffusion.

A quantitative study of the kinetics of the heterogeneous reactions requires knowledge of the oxidant concentrations used. The concentration of O_3 is determined by UV-Vis spectroscopy, while $[NO_3]$ measurements are more involved. In this case, NO_3 is produced in situ by reacting O_3 with NO_2; the dependence of $[NO_3]$ on the initial $[NO_2]$ and $[O_3]$ is modelled. To determine the concentration of NO_3, the steady state concentrations of NO_2 and N_2O_5 are measured by FTIR spectroscopy as a function of the initial $[NO_2]$.

of the single component systems using NR and ellipsometry determine the possibility to use ellipsometry as a substitute for NR in isotropic and single component monolayers. The kinetic analysis of the measured surface excess decays for six systems provides information on the rate of the heterogeneous reaction and indirect information on the formation of surface-active products. The results obtained for different molecules will be discussed in relation of their chemical structures. Furthermore, the comparison between O_3 and NO_3 oxidation for the MO systems only indicates to what extent night-time oxidation is relevant to aerosol ageing.

Through the exploitation of isotopic contrast variation in NR, the relative rate coefficients of organic compound in binary mixtures is determined for two systems. The estimation of the oxidant uptake coefficient allows the comparison with literature data on similar organic molecules that are generally studied in the condensed-phase (i.e. droplets or thick films). Field studies have been shown to determine uptake coefficients lower than those found for pure model systems used for laboratory studies. The comparison of results from field studies with the results on binary mixtures indicates if the mixing of different organic compounds in the surface film can help to explain the discrepancy.

Chapter 1

Atmospheric chemistry: an overview

Atmospheric science is an applied discipline, which is concerned with the structure and the evolution of the planetary atmosphere and with the wide range of phenomena occurring within it. An increasingly important theme is atmospheric chemistry [11]. Gases react in the atmosphere, and the transformation of these gases in distinct regions of the atmosphere are governed by their chemical behaviour. The main aim of the study of atmospheric chemistry is to understand all the factors which control the concentrations of the species in the atmosphere [12].

1.1 Atmosphere: chemical composition

Oxygen (O_2) and nitrogen (N_2) account for 99% of the molecules in the atmosphere; Figure 1.1 and Table 1.1 provide the composition of the atmosphere. The inert gas Argon (Ar) represents almost all of the 1% left. The remaining portion consists of trace gases, which attract the attention of scientists because they determine the main features of the atmosphere, where life is possible.

1.1.1 Trace gases

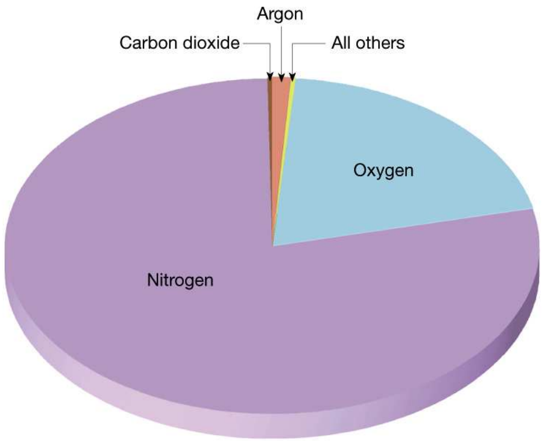

Figure 1.1: Graphical representation of the atmosphere composition. Figure adapted from Ref.[13].

Gas	Fractional concentration by volume
Nitrogen - N_2	78.08 %
Oxygen - O_2	20.95 %
Argon - Ar	0.93 %
Water vapour - H_2O	0-4 %
Carbon dioxide - CO_2	380 ppmv
Neon - Ne	18 ppmv
Helium - He	5 ppmv
Methane - CH_4	1.75 ppmv
Krypton - Kr	1 ppmv
Hydrogen - H_2	0.56 ppmv
Nitrous oxide - N_2O	0.3 ppmv
Ozone - O_3	10-100 ppbv
Nitrogen species - NO_y	10 pptv- 1 ppmv

Table 1.1: Dry tropospheric air composition at a pressure of 1 atm [11]. Concentrations of trace gases are given in ppmv, which is parts per million by volume. 1 ppmv = 10^3 ppbv = 10^6 pptv

Ozone

or by the photolysis of nitrogen dioxide, NO_2. In urban areas ozone production is increased by the presence of organic gases. The great variability of the $[O_3]$ values, as reported in Table 1.1, is due to the different production efficiencies in different locations in the atmosphere. In particular, urban areas present a typical concentration of 10 ppbv, in the troposphere it is around 4 ppbv and in the stratosphere 100 ppbv (ozone layer) [14, 11, 12]. The high concentration in the stratosphere contributes to the reduction of UV radiation, hence any decrease of $[O_3]$ in this region is harmful for the life on Earth. Parallel to this, an increase in the region up to 10 km height can have detrimental effects for human health and nature as it is highly reactive and toxic. [14].

Nitrogen oxides

Nitrogen monoxide, NO, is a radical. Radical molecules are strongly reactive because they have an unpaired electron in their shells, unlike molecules such as H_2 and N_2, which have only paired electrons. NO is emitted by soil, plants, combustion processes, lightning and in chemical reactions. NO production by lightning or combustion is due to the high temperatures available. Molecular oxygen, O_2, if heated at temperature of the order of ~ 2000 K, dissociates thermally and produces NO following the reactions chain below:

$$O_2 \longleftrightarrow O + O \tag{R 1.2}$$

$$O + N_2 \longleftrightarrow NO + N \tag{R 1.3}$$

$$N + O_2 \longleftrightarrow NO + O \tag{R 1.4}$$

For instance, the passage of aircraft is a known source of the production of NO molecules at high altitude. The typical concentration of NO in remote zones of the troposphere ranges from 5 pptv at sea level to 20-60 pptv in the high troposphere. In urban areas [NO] can reach 0.1 ppmv in the early morning.

Nitrogen dioxide (NO_2) is mainly produced by the oxidation of NO, and other sources are chemical reactions and combustion processes. The typical concentration into the species $NO_X = NO + NO_2$. The main sink for NO_X during daytime is the reaction which produces nitric acid, HNO_3, i.e. $OH + NO_2 + M \longrightarrow HNO_3 + M$. In the troposphere, HNO_3 is easily solubilised by precipitation.

During night-time the NO_X is made up of NO_2 only, because only the reaction R 1.5 still occurs. Furthermore, because of the absence of light the photolabile nitrate radical, NO_3, and the dinitrogen pentoxide, N_2O_5, can accumulate:

$$NO_2 + O_3 \longrightarrow NO_3 + O_2 \qquad \text{(R 1.7)}$$

$$NO_2 + NO_3 + M \longleftrightarrow N_2O_5 + M \qquad \text{(R 1.8)}$$

N_2O_5 reacts with water molecules rapidly following the heterogeneous reaction:

$$N_2O_5 + H_2O(s) \longrightarrow 2HNO_3 \qquad \text{(R 1.9)}$$

NO_3 and N_2O_5 have great relevance in the night-time oxidation of organic compounds, and together with NO_X they are called NO_Y.

Once daylight appears, N_2O_5 and NO_3 photolyse:

$$N_2O_5 + h\nu \longrightarrow NO_2 + NO_3 \qquad \text{(R 1.10)}$$

$$NO_3 + h\nu\,(\lambda < 580\,\text{nm}) \longrightarrow NO_2 + O \qquad \text{(R 1.11)}$$

$$NO_3 + h\nu\,(\lambda < 700\,\text{nm}) \longrightarrow NO + O_2 \qquad \text{(R 1.12)}$$

N_2O_5 is consumed in a few hours, while NO_3 in only a few seconds. As a result the life time of NO_X is ca. one day. The NO_X are transported on a long spatial and temporal scale thanks to peroxyacetyl nitrate (PAN), which acts as a long term reservoir because of its low solubility in water [14].

1.1.2 Particulate matter

Together with molecules in gaseous state, particulate matter (aerosols) are also found sulfate, sodium, ammonium, trace metals, chloride, nitrate, crustal elements, water and carbon containing compounds [14]. The carbonaceous fraction is made up by both elemental (e.g. graphite, carbon soot) and organic carbon [16]. Figure 1.2 displays typical relative compositions of aerosol in two different environments, urban and rural settings.

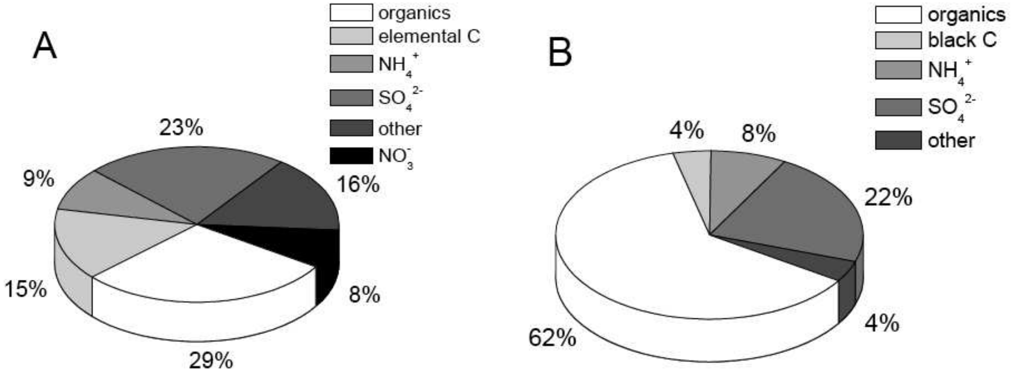

Figure 1.2: Composition of aerosol particles in (A) an urban air mass (Los Angeles) [17] and (B) a rural setting in Hungary [18]. Adapted from Ref. [19].

Anthropogenic emissions have heavily increased during the last century. Particulate matter directly impacts on human health, atmosphere and climate.

Aerosol particles directly affect the Earth's radiation balance, either absorbing or reflecting the incoming solar radiation and the outgoing terrestrial radiation. Since aerosols absorb and scatter sunlight, less solar radiation reaches the surface of the Earth. This phenomenon is believed to have a cooling effect on the Earth-atmosphere system [14].

Particulate matter provides cloud condensation nuclei (CCN) leading to formation of fog or cloud droplets, when it is in a super saturated water vapour environment. The chemical composition of the aerosol particles determines their effectiveness as CCN, hence influencing indirectly the radiation budget [14]. When considering the effect of aerosol particle on public health, particulate matter with a diameter $< 2.5\,\mu m$ (called $PM_{2.5}$) is generally investigated, because it can be inhaled and transported deep into aerosols can be found as pure organic particles, or alternatively mixed with inorganic material. These mixtures may exist as homogeneous or phase-separated mixtures. Field studies have observed aerosol particles that seem to consist of more than one phase or contain an immiscible surface film [20, 21]. The abundance of water vapour in most air masses results in a ubiquitous distribution of aqueous droplets in the troposphere. As shown in Figure 1.3, long chain aliphatic acids are a dominant class of organics in the troposphere. These acids are surface active due to their hydrophilic headgroup (COOH) and their hydrophobic tail (aliphatic chain). Therefore, in mixed inorganic/organic particles the organic material can form stable films on the surface of the aqueous droplet [20, 21]. Aqueous ocean spray droplets covered by water insoluble organics (e.g. fatty acids) from marine organisms are an example of these coated aerosols [21, 22].

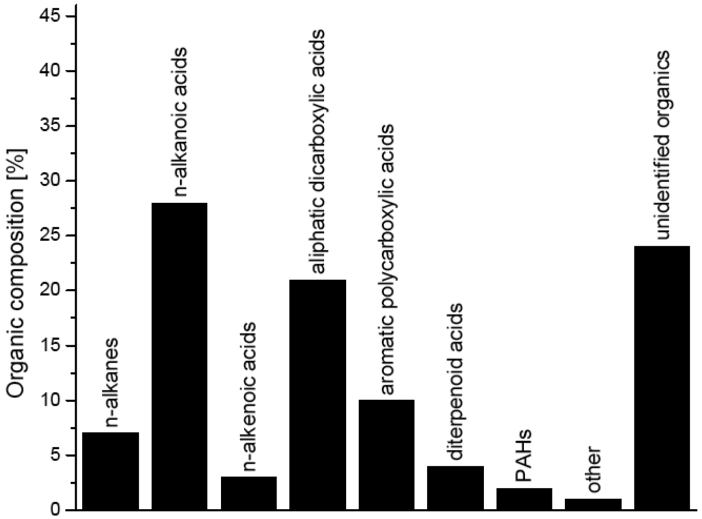

Figure 1.3: Composition of the resolvable elutable organics in aerosol particles in Los Angeles [17]. Adapted from Ref. [19].

This thesis focuses on reactions of organic monolayers at the air–water interface with atmospheric oxidants. A range of organics was selected for this work in order to investigate the effect of headgroup, chain length and saturation degree on the heterogeneous

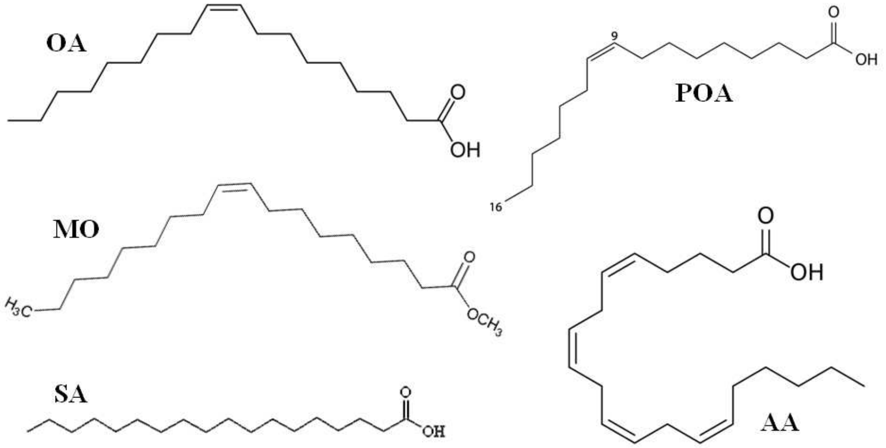

Figure 1.4: Molecular structures of the five different organic compounds investigated in this thesis. OA is oleic acid, MO is methyl oleate, SA is stearic acid, POA is palmitoleic acid and AA is arachidonic acid.

saturated surfactants and an important tracer for meat cooking emissions [29]. Despite being detected at comparable atmospheric concentrations to the popular model surfactant OA, POA and its oxidative ageing has not been examined in any detail. AA is the most common unsaturated fatty acid in cellular membranes and thus impacts on the membrane's physical properties thereby affecting protein function and trafficking [30]. AA will partition to the surface of aqueous droplets because of its surfactant properties, and thus be exposed to gas-phase oxidants present in the atmosphere. It contains four double bonds that will react rapidly with all initiators of atmospheric oxidation including ozone and nitrogen oxides. AA may decompose into hygroscopic products with particular relevance for the growth of atmospheric droplets, cloud formation and thus climate [10, 2]. Unlike the previous organic compounds, SA is a saturated surfactant, which provides provides reactive sites for H/D-abstraction by the key night-time oxidant NO_3. The H/D-abstraction from saturated fatty acids is expected to be significantly slower [7, 31] than the reaction with double bonds of unsaturated surfactants like OA or MO. This expectation is based on analogy with gas-phase studies, but no previous study has shown this directly at the air-water interface.

1.2 Reactions in atmospheric chemistry

In this section a brief introduction on how to model a chemical reactions is given. The basic principles necessary to describe the chemical kinetics are provided. Chemical kinetics is used for the calculation of the rate coefficients of chemical reactions. The relative variation of concentration per unit time of a given reactant in a reaction is called rate.
In the following paragraphs, two basic examples of gas-phase reactions and an example of heterogeneous reaction are described [14, 32].

Unimolecular reaction

A reaction of the first-order is written as:

$$A \longrightarrow B + C \tag{R 1.13}$$

and the variation of the concentration for the species A is expressed by:

$$-\frac{d}{dt}[A] = k_1[A] \tag{1.1}$$

where k_1 is the rate coefficient for a first order reaction and its unit is s^{-1}.
Few reactions are of the first order. The two classical examples are radioactive decay and photolysis. A typical radioactive decay is ${}^{238}_{92}U \rightarrow {}^{234}_{90}Th + \alpha -$ particle. More relevant to the atmosphere is the photodissociation, or photolysis, as an example of a first order reaction. The chemical change is due to the absorption of the photon energy ($h\nu$) by a molecule:

$$A + h\nu \longrightarrow B + C \tag{R 1.14}$$

In this case the rate coefficient is called j_A. Another unimolecular reaction, occurring in the atmosphere, is the thermal decomposition of a molecule; even if the energy needed for the decomposition is given by the collision with another molecule M. Usually, M represents O_2 and/or N_2 (as seen in reaction R 1.1) and the reaction is written as:

According to Eq. 1.2 [A] decreases by 1/e of its initial value in a time $\tau = 1/k_1$. τ is usually called mean lifetime of A in the reaction R 1.13.

Bimolecular reaction

A bimolecular reaction, known as second order reaction, involves two molecules A and B, not necessarily of different species, which collide giving rise to two products C and D:

$$A + B \longrightarrow C + D \qquad \text{(R 1.16)}$$

The rate for reaction R 1.16 is:

$$-\frac{d}{dt}[A] = -\frac{d}{dt}[B] = \frac{d}{dt}[C] = \frac{d}{dt}[D] = k_2[A][B], \qquad (1.3)$$

where k_2 is the rate coefficient of the reaction and usually it is expressed in cm^3 $molecule^{-1}$ s^{-1}.

To generalise, the rate for a reaction like $aA + bB \longrightarrow eE + fF$ is:

$$\pm\frac{d}{dt}[X] = k_r[A]^a[B]^b \qquad (1.4)$$

where the units of k_r is $(cm^3\, molecule^{-1})^{a+b-1}\, s^{-1}$ and [X] is the concentration of one of the reactant (sign −) or one of the product (sign +).

A termolecular reaction similar to reaction R 1.15 but without decomposition is given by $A + B + M \rightarrow AB + M$, and it can be thought of as a second order or a third order reaction, depending on conditions. The collision of three molecules at the same moment is unlikely to occur. Usually a first collision between A and B produces an intermediate state $AB^\dagger$ (dagger indicates the excitation of a vibrational state), $A + B \rightarrow AB^\dagger$. Therefore, to release the energy excess of $AB^\dagger$ a collision with a generic molecule M occurs: $AB^\dagger + M \rightarrow AB + M$. In the specific case of atmosphere, M, is again likely to be N_2 or O_2 and the variation of [AB] over time is (see Ref. [14] for more detail):

$$\frac{d}{}[AB] = \frac{k_a k_s [A][B][M]}{} \qquad (1.5)$$

Reaction 1.6 is a third order reaction and reaction 1.7 is a second order reaction.
An atmospherically-relevant example, which can be a second or third order reaction depending on the thermodynamic conditions, is the production of O_3 via the reaction R 1.1.

Gas-Surface Reactions

In this thesis, gaseous reactions are used to produce NO_3 and N_2O_5 (see Section 5.3), however the reaction under study is the one occurring between the gas-phase oxidant and the organic monolayers at the air–water interface. In fact, the aim of this study is to investigate surface reactions relevant to aqueous aerosol coated with organic films.
A is a molecule in the gas phase and it has a Brownian motion in three dimensions. The number of molecules A colliding in a unit area per unit time (flux, Φ_A) is:

$$\Phi_A = \frac{1}{4} n_A \bar{v}_A \tag{1.8}$$

where n_A is the number concentration of A and $\bar{v}_A$ is the mean speed of the molecules A. $\bar{v}_A$ is derived from the velocity distribution of Maxwell:

$$\bar{v}_A = \left(\frac{8k_B T}{\pi m_A}\right)^{\frac{1}{2}} \tag{1.9}$$

where k_B is the Boltzmann constant, T is the absolute temperature in K and m_A is the molecular mass of A. Assuming an aerosol particle to be spherical with radius R_p, the number of collisions per second is $\left(\frac{1}{4} n_A \bar{v}_A\right)\left(4\pi R_p^2\right)$. In the case of a flat interface, with a well known surface area per unit air volume (A_p, cm^2cm^{-3}), the rate of collisions with the surface is $\left(\frac{1}{4} n_A \bar{v}_A\right) A_p$. Not all collisions lead to a reaction. Therefore an uptake coefficient γ is defined and it represents the probability of the reaction occurrence. γ is experimentally determined as the ratio of the number of occurred reactions over the total number of collisions. Generally, γ depends on the type of particle and on the temperature.

In a heterogeneous reaction (reactants in different states) the variation of concentration,

1.3 Study of gas-liquid heterogeneous reactions: experimental techniques

The study of the kinetics of a chemical reaction focuses generally in achieving one or both of two main goals: (i) characterisation of the reaction mechanism, hence analysis of the sequence of elementary steps giving rise to the overall reaction; (ii) determination of the absolute rate of the reaction and/or its individual elementary steps [34].

The measurement of the reaction rate is performed by monitoring the concentration of one of the reactants or products as a function of time. Several experimental procedures allow the study of chemical reactions; however any kinetic experiment essentially consists of mixing the reactants and initiating the reaction on a timescale that is negligible compared to that of the reaction, and then monitoring the concentration(s) of one or more reactants and/or products as a function of time.

Chemical kinetics of gas-phase and liquid-phase species have been studied in their separated states for over a century [35, 36]. A validated theoretical framework for homogeneous reactions has been developed, and extensive databases of kinetic parameters are available [37, 38]. However, the study of the gas-liquid heterogeneous reaction is relatively recent and not nearly as well developed. These heterogeneous reactions have a higher complexity both experimentally and theoretically. In the 1950s, Danckwerts presented analytical expressions describing the uptake of gas-phase species by liquids in terms of measurable parameters [39]. The introduced expressions were based on equations of heat conduction and included the effect of the Henry's law solubility on gas uptake, liquid-phase reactions of the solvated molecules, and the mass accommodation coefficient, α (defined as the probability that a molecule colliding on the liquid surface enters the liquid). Experimental studies of gas–liquid interaction have not advanced as fast as the mathematical formulations. However, in the last 30 years a range of experimental laboratory techniques was developed to allow measurements of kinetic parameters, such as accommodation and uptake coefficients.

The principle of the measurement of the rates of gas–liquid reactions is simple [35, 36]. A known surface area of the liquid is exposed to gas-phase molecules, and after a conto study the kinetics of the reaction at gas–liquid interface [35, 36].

Droplet train flow reactor

In a droplet train flow reactor, gas–liquid interactions are studied by monitoring the gas-phase concentration of a trace species in contact with a stream of droplets with ca. 100 µm diameter entrained in a vertical flow tube [36, 40]. A monodisperse, spatially collimated train of droplets is produced by forcing a liquid through a vibrating orifice, driven by an electrically pulsed piezoelectric ceramic. The droplet train passes through a vertical low pressure (5–20 Torr) flow tube which contains the trace gas species mixed with an inert carrier gas (helium) and vapour of the liquid being studied. The trace gas is introduced through one of three loop injectors located along the flow tube. By selecting the gas inlet port and the droplet velocity, the gas–droplet interaction time can be varied between 2–20 ms, allowing solubility effects to be investigated. The lower limit of the uptake coefficient that can be measured by this technique is 1×10^{-3}. Changes in the droplets may be monitored with optical spectroscopic techniques.

Bubble train reactor

In the bubble train reactor, the trace gas is contained in bubbles that pass trough a column of liquid [36, 41]. The bubble train reactor allows the study of longer gas–liquid interaction times in the $1 - 100$ s range. The measurable uptake coefficients range from 1×10^{-3} to 1×10^{-7}. Gas bubbles containing the trace species and an inert carrier gas are injected into the flowing column of liquid with a movable injector so that the gas–liquid interaction time may be varied. After the bubbles burst, a mass spectrometer measures the remaining amount of trace gas. The analysis needs complex modelling, which takes into account the change in shape of the bubbles travelling along the liquid column and the convective mixing occurring in the liquid layer next to the bubbles.

Wetted wall flow reactor

In a wetted wall flow reactor, uptake is measured on a layer of liquid coating the inside

Aerosol flow reactors and aerosol chambers

In an aerosol flow reactor, aerosol particles are introduced into a laminar flow tube similar to the ones used for the wetted wall flow reactor experiments [36, 43]. Particle concentrations and size distributions are measured with an optical particle counter or with a differential mobility analyser/ condensation particle counter combination in order to determine the condensed-phase surface area exposed to the trace gas species. The chemical composition of the aerosol particles before and after exposure can be measured with an aerosol mass spectrometer to yield information about condensed-phase reaction products. The trace gas species is introduced through a movable injector so that the exposure time can be varied. The density of the trace gas can be monitored with mass or optical spectrometric techniques. Typical exposure times are 10 to 100 s, resulting in a lower limit of measurable uptake coefficient of 10^{-4}.

If the aerosol particles are introduced into a static chamber, an aerosol chamber experiment can be performed. The residence time can be up to many hours, enabling the study of slow gas–liquid reactions. The trace gas species can be introduced into the chamber or generated in situ. Fourier transform infrared spectroscopy is used to monitor the trace gas concentration.

These two techniques allow the study of small aerosol droplets, which simulate more closely real atmospheric aerosols.

Single-droplet techniques

Several techniques have been developed to measure the gas–liquid interactions on a single droplet. The basic principle of these techniques is to trap a single droplet and then expose it to the trace gas. The change in droplet size and/ or chemical composition is monitored respectively with optical and spectroscopic techniques. The dimension of the aerosol droplet is determined by the method of trapping, for example acoustic levitation can trap droplets of diameter ranging from 40 µm to 2 mm [44]. For smaller droplets (diameter $5-12$ µm) optical tweezers have been used [45, 9, 46].

determination of a tentative reaction mechanism both for saturated and unsaturated surfactants. The SAM on the solid substrate mimics the organic coating on solid inorganic aerosol particles, while to study the organic coating on aqueous aerosol particles the water should be used as substrate.

Studies on organic monolayers at the air–water interface have been performed in a modified flow cell introduced by Knopf et al. [42]. Several types of organics have been investigated and the N_2O_5 uptake coefficients were determined [48, 49]. Wadia et al. [50] studied the kinetics and gas-phase products of the reaction of O_3 with an unsaturated phospholipid at the air–water interface. Thompson et al. [51] studied the surface excess and surface pressure of the phospholipid monolayer, instead of monitoring the gas phase species as in the work of Wadia et al. [50]. The approach of Thompson et al. was used to investigated oleic acid monolayers exposed to NO_2 [52] and to O_3 [53] by King et al..

The real-time monitoring of the surface excess of an organic monolayer at the air–water interface by neutron reflectometry (NR) measurements allows to study the kinetics and the fate of the monolayer as a function of the gas-phase oxidant concentration. NR is sensitive to changes in deuteration state of the sample. For example, the mechanism of the reaction can be investigated by changing the partial deuteration scheme of the molecule. Relative rate coefficients in binary mixture may be studied by NR, using a deuterated molecule mixed with an hydrogenated one.

The detailed treatments of NR and ellipsometry, which are the techniques used in this thesis to study the oxidation reaction, may be found in Chapter 2 and Section 3.3.1, respectively.

Chapter 2

Neutron Reflectometry

2.1 Introduction

The reflection of neutrons was demonstrated by Fermi and Zinn [54] almost seventy years ago. Neutron reflection follows the same fundamental equations as optical reflectivity but with different refractive indices. Neutrons interact with nuclei, and the neutron refractive index, n_r, depends on the mass number, A, (proton and neutron number) instead of the atomic number, Z, (i.e. electron number) as for X-ray. Different isotopes have a different strength on the scattering of neutrons. This ability of the nucleus to scatter neutrons is quantified and defined as scattering length, b. The refractive index of any material is a function of the scattering length density, ρ, of its constituent nuclei and the neutron wavelength, λ:

$$n_r^2 = 1 - \frac{\lambda^2}{\pi}\rho. \tag{2.1}$$

For almost the following forty years, neutrons were used principally to determine the scattering lengths of nuclei. In the last twenty years, neutron reflectometry, NR, has emerged as a powerful technique for the investigation of the structure of the interface itself, composition features and magnetisation [55]. As with light, total reflection may occur when neutrons pass from a medium of higher refractive index to one of lower study of interfaces, with respect to other techniques, make it an important technique. For example, a resolution of a fraction of a nanometre can be achieved because of the short wavelengths available. The sample is not destroyed by the neutron beam, and buried interface can be investigated, because of the high penetration of neutrons into certain materials. Furthermore, the technique of isotopic substitution allows one to achieve large contrasts in scattering length density. A detailed description of theoretical principles of neutron scattering in general can be found in references [55, 56, 57]. In the following sections a brief overview of the theory strictly related to NR is presented.

2.2 Neutron reflection

In order to perform a neutron reflection experiment the following components are necessary: a radiation source, a wavelength selector or chopper, a system of collimation, the sample and a detector system. The neutrons are produced either by a nuclear reactor (continuous neutron beam), or a spallation source (pulsed neutron beam). A specular neutron reflection experiment is performed to measure the reflectivity as a function of the wave vector perpendicular to the reflecting surface, q, usually called the momentum transfer, see Figure 2.1. Given $q = 4\pi \sin(\theta)/\lambda$, the q-range can be probed either by changing incident angle while the neutron wavelength is fixed (monochromatic mode) or by varying the wavelength while the incident angle is fixed. The second approach is called time-of-flight (TOF), as the wavelength determines the time taken for the neutron, with a given energy, to go from the source to the detector (pulsed beam) or from chopper to detector (continous beam). For TOF measurements, the resolution in q is related to the resolution in θ and in time:

$$\left(\frac{\delta q}{q}\right)^2 = \left(\frac{\delta \theta}{\theta}\right)^2 + \left(\frac{\delta t}{t}\right)^2 , \qquad (2.2)$$

where δt is the pulse time width and t is the time-of-flight of the pulse. In principle the resolution of the time binning at the detector is also a factor but in practice this is chosen to be much smaller than δt. Even if the TOF method is less efficient than is of the order of 10^{-7} when water in present in the sample environment.

Modelling of the data

To conclude this section, an introduction to neutron reflectivity data analysis is provided, and a detailed description may be found in Section 4.2. Usually, in order to analyse the specular reflection data a model of the interface is constructed, for instance a series of parallel layers of homogeneous material. Each layer is described by three parameters: scattering length density ρ, thickness d and surface roughness σ. These features can be used to calculate a model reflectivity profile by means of the optical matrix method [58]. A boundary may be smooth but with one material diffused into the other therefore real interfaces between materials may be rough over a large range of length scales. It turns out that in both the rough and diffuse cases the specular reflectivity is reduced by a factor $e^{-q^2\sigma^2}$, where σ is a characteristic length scale of the layer imperfection, i.e. the surface roughness. It is in effect similar to the Debye-Waller factor, which describes the attenuation of x-ray scattering or coherent neutron scattering caused by thermal motion [59, 60]. The Abeles method [61] allows the inclusion of the surface roughness in the model R(q). The two external layers of the series of interfaces are considered seminfinite with fixed scattering length density. The calculated profile is compared to the measured profile and the quality of the fit is given by using a χ^2 in the least-squares method. Since one profile may not be described by a unique model, the use of different isotopic contrasts together with physical and chemical constraints of the system can lead to the achievement of a more unambiguous model of the interface.

Isotopic contrast variation is based on the fact that different nuclei scatter neutrons with different amplitudes, and sometimes, as in the case of protons and deuterons, with opposite signed scattering lengths ($\rho_{H_2O} = -0.56 \times 10^{-6}$Å^{-2}; $\rho_{D_2O} = 6.35 \times 10^{-6}$Å^{-2}). By combining hydrogenated and deuterated materials, the reflectivity profile of a system can be substantially changed while keeping the same chemical structure at the interface. Furthermore, by adjusting the H/D ratio, solvents that are contrast matched to the medium through which neutrons pass before reaching the interface, can be pre-

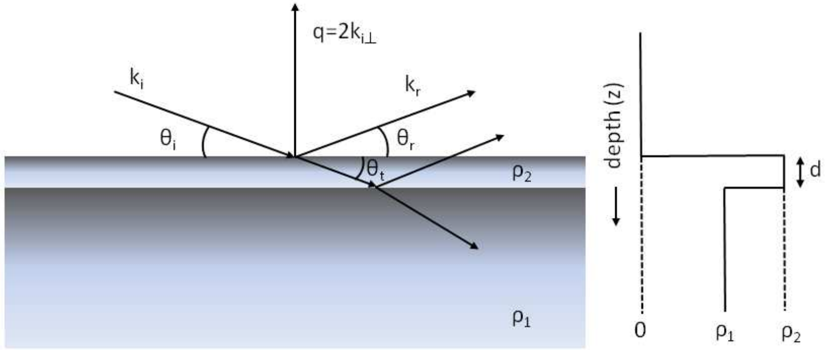

Figure 2.1: Reflection of an incident beam from two ideal flat interfaces. k_i and k_r are the incident and the reflected wave vectors, with angles $\theta_i = \theta_r$ in the incident plane; q is the momentum transfer; ρ_1 is the scattering length density of the seminfinite substrate and ρ_2 is the one for the thin layer. The scattering length density profile as function of depth is shown on the right.

Specular neutron reflectivity is a tool to study the structure normal to the interface. In particular, it is an accurate, precise, sensitive and direct method to determine the surface excess as long as the surfactant is available in deuterated form. In this specific case, the model used to describe the system is made up by a uniform layer with a refractive index different to that of the subphase. The refractive index depends on the scattering length density and the neutron wavelength (see Eq. 2.1), and ρ is given by $\sum_i b_i n_i$, where b_i is the scattering length and n_i the number density for the i-th species. Usually $n_r < 1$ ($n_{r;air} = 1$) hence $\rho > 0$, given that the neutron beam can be totally reflected if $\theta_i < \theta_{cr}$, where $\theta_{cr} = \arccos n_r / n_{r;air}$, called critical angle; the angle of incidence, θ_i, is the one formed by the incoming beam at the surface (see Fig. 2.1). As an example, if we consider an air–D_2O interface, which has a total reflection below a critical q value, an absolute value of reflectivity can be determined.

Our interest is addressed to a specific case: deuterated surfactant at the air–liquid interface, where the liquid is a mixture of H_2O/D_2O with $\rho = 0\,\text{Å}^{-2}$, known as air contrast matched water (ACMW). For this situation the intensity of the reflection is strictly related to the presence of deuterated material at the interface:

surface excess, Γ, is given by:

$$\Gamma = \frac{1}{N_{Av}\, A_{hg}} = \frac{\rho\, d}{N_{Av}\, b} \tag{2.4}$$

where A_{hg} is the area per molecule and N_{Av} is the Avogadro's number. By comparing Eqs 2.3 and 2.4, it is found that at low q the reflectivity is proportional to the square of the surface excess, $R \propto \Gamma^2$. A fundamental feature of Γ is that its value is insensitive to the model chosen, even if the values of ρ and d are model-dependent; in fact, at low q they vary in an inverse way giving the same product.

At first sight, the technique is very powerful, but it is necessary to be careful and consider all possible sources of errors in the calculation of Γ based on neutron reflectivity data. The accuracy of Γ is related to the accuracy of the instrument calibration, to the background determination and to the statistical quality of the data. The calibration of neutron intensities, in theory, should give rise to negligible errors, because below the critical angle (feature of any air–liquid interface) the reflection is total (i.e. $R = 1$) and this allows one to scale all the data. In fact, the system used for the calibration is air–D_2O. Once the normalisation factor is determined, it is applied to all the data based on the assumption that the neutron flux from the reactor is constant throughout the experiment. The reflectivity of clean D_2O is easily reproducible and the instrument set up as well (errors on the order of $< 2\%$ are expected). Therefore the error on the calibration is expected to be small, especially because in experiment where ACMW is present the background value is roughly 10^{-5} and its subtraction or determination tends to be the main factor when taking into account the treatment of reflectivity data for low surface excesses.

2.4 Neutron Reflectometer

All the NR data presented in this manuscript have been collected on FIGARO. In this section a brief description of the instrument is given.

strike the interface from above or below in a wide q-range. With an incoming beam of wavelengths comprised between 2 and 30 Å, it is possible to attain a q-range from 0.0045 to 0.42 Å^{-1} by using two incoming angles of 0.62 and 3.8°.

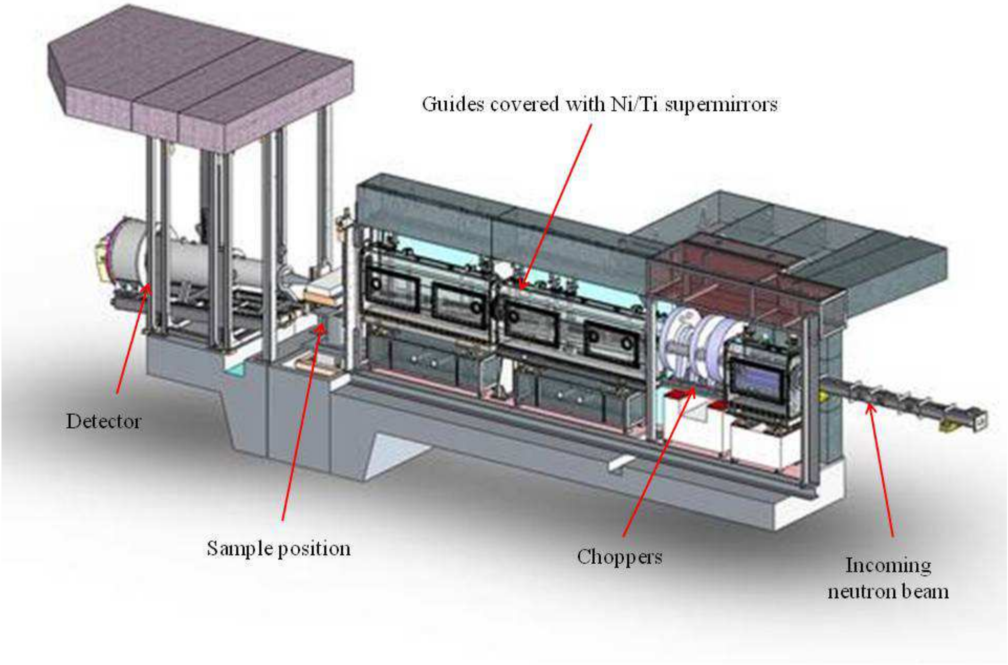

Figure 2.2: Side view of FIGARO, adapted from Ref. [64].

One useful feature of FIGARO is the ability to relax the resolution to increase and have maximum of flux at a very low incident angle where the reflectivities of a monolayer is high. Hence the instrument is extremely well suited to the study of kinetic processes with time slices possible on the order of 1 s. The first component of the instrument is a choice of two frame–overlap mirrors to remove neutrons with wavelengths above 20 or 30 Å. Four choppers follow, with carbon fiber discs of 800 mm diameter and 45° aperture, independently rotating at a speed of up to 2000 rpm. There are different distances between different pairs of discs such that 6 different wavelength resolutions active and passive anti-vibration systems and x-y-z translation axis. A two-dimensional multitube detector is positioned at a distance of 3 m from the sample. It can move up and down to detect the reflected and direct beams at all angles. It consists of an aluminium plate with 64 square holes of $7-$ mm internal size and $2-$ mm resolution along the $250-$ mm height.

2.4.2 FIGARO settings for kinetic experiments

The concentration change of a deuterated monolayer of surfactant at the air–ACMW interface due to oxidation was followed by NR. The settings of the instrument were adjusted to record R(q) profiles in few seconds, typically 5 s. The q-range was restricted to $0.007 - 0.07 \text{Å}^{-1}$ by choosing an incident angle of 0.62° and a wavelength interval of $2 - 20$ Å. The resolution of λ was fixed to 7 %, in order to maximise the neutron flux at the sample, which allowed the quantification of surface excess down to a few percent of a monolayer (see Section 4.2). All the kinetic data reported in Chapters 7 and 8 were collected with these settings. A slightly different setup was used for the structural characterisation of the deuterated monolayer at the air–ACMW interface (Section 6.2). To determine the thickness of the monolayer, a wider q-range was needed, and the R(q) profile was also acquired at an incident angle of 3.8°. The acquisition time for these static measurements was set to 10 minutes for the first angle (0.62°) and 30 minutes for the second one (3.8°).

A dedicated reaction chamber was designed to perform the kinetic experiments on FIGARO, which is described in detail in Chapter 5. To record the NR data, the chamber was fixed on the FIGARO sample stage and then aligned (Fig. 2.3).

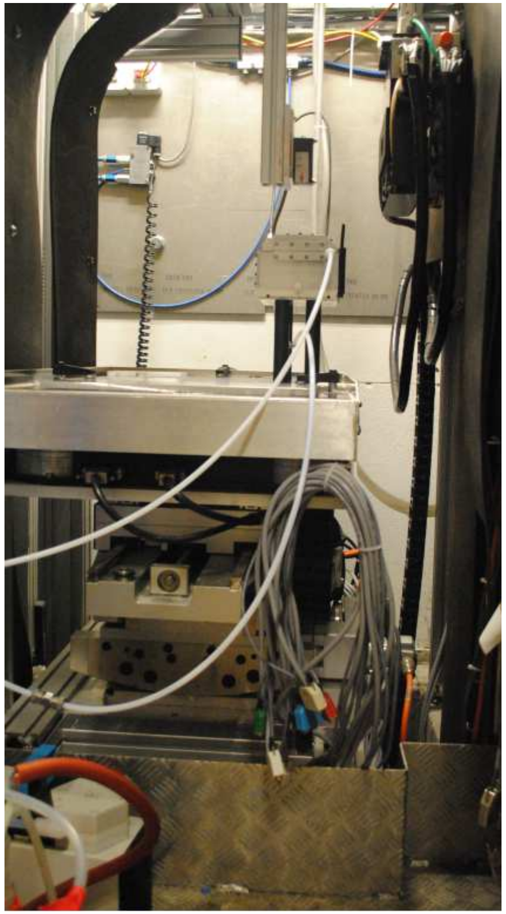

Figure 2.3: FIGARO sample position with MIMIK reaction chamber mounted on the

Chapter 3

Other techniques

3.1 Introduction

This chapter introduces the various techniques used to characterise the chemical systems and to gain complementary information to NR. The organic coated aerosol surface has been modelled as an organic monolayer at the air–water interface. The thermodynamic properties of this film have been investigated by measuring the pressure isotherm as a function of the surface area with a Langmuir trough. The optical properties of the organic film were investigated using Brewster Angle Microscopy (BAM) and ellipsometry. The oxidation of the organic monolayer was driven by exposure to NO_3 and O_3, which were produced in situ. The concentrations of the oxidants were determined from spectroscopic measurement, such as UV-Vis and FTIR spectroscopy.

3.2 Air–water interface

In order to mimic the aerosol surface and to focus on the reaction happening at the surface, floating monolayers were chosen as the model system.

Amphiphilic molecules of atmospheric interest are, for instance, oleic acid, stearic acid, palmitoleic acid and arachidonic acid [45, 65, 66, 10]. Their common features are the polar head (a carboxylic group) and the hydrophobic tail, which can be either saturated

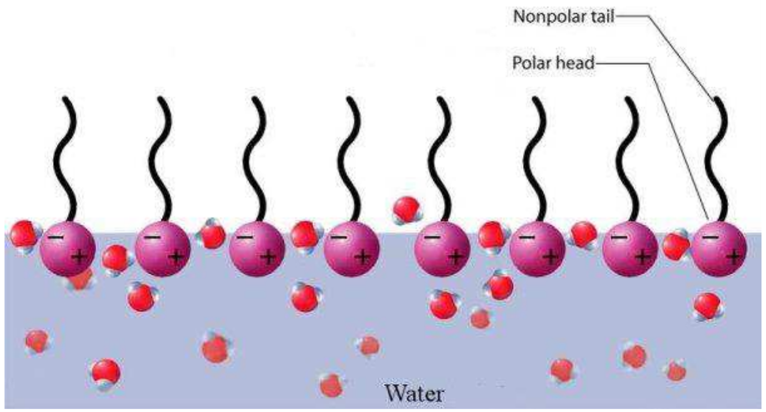

Figure 3.1: Surfactant molecules arranged at an air–water interface. Some molecules of water are displayed as well.

surfactants film formed at the air–water interface is called monolayer when it is a one-molecule thick layer. Depending on the solubility of the surfactants, the monolayers formed may be divided into two categories: 'Gibbs monolayers' (soluble) and 'Langmuir monolayers' (insoluble) [67]. The amphiphiles used in this work form Langmuir monolayers. The formation of insoluble monolayer is commonly done by previously dissolving the amphiphile in a volatile solvent such as chloroform and then spreading some drops of solution on the surface [67]. Once the solvent evaporated, the monolayer is left at the air–water interface.

3.2.1 Langmuir trough

In order to study the thermodynamic behaviour of the monolayer, a surface film balance called a Langmuir trough is used [67]. It consists of a shallow hydrophobic trough with hydrophobic barriers that are usually constructed of poly-(tetrafluoroethylene), PTFE, and is equipped with an electronic device for measuring the surface tension (details in Ref. [67]). In order to record a pressure–area isotherm, the trough is slightly overfilled with water and the barriers, lying across the trough, divide the available surface and are used to restrict the area of a monolayer spread on the water surface. The monolayer is

The decrease in surface tension, γ, is usually reported as surface pressure, Π:

$$\Pi = \gamma_w - \gamma_m \tag{3.2}$$

where γ_w is the surface tension for pure water and γ_m is the surface tension of the water with the monolayer. As stated previously the Langmuir trough allows to record isotherms, which may be used to reveal phases and phase transitions of the monolayer. The principal film phases are: gaseous phase, liquid-expanded phase, liquid-condensed phase and solid phase. Often monolayer may not exhibit all the phases described, because of narrow ranges of thermodynamic quantities available in practice.

3.3 Interaction of light with an interface

Light travels at speed c in vacuum, where the refractive index, n, is defined to be 1. The refractive index of any other medium is higher than 1, hence the speed of light results smaller by a factor of $1/n_m$, where n_m is the refractive index of the medium. A plane wave, travelling at the speed c/n_1 and impinging at an interface between two media of different refractive index, may be transmitted through the media changing the speed to c/n_2 or reflected back into the incoming media. On the assumption the two media are isotropic and the interfaces are sharp, we can use the Fresnel's model [58] to describe the variation in electric field of the plane wave.

The electric field of a plane wave is divided in two components, E_s perpendicular to the incidence plane and E_p parallel to it. The incidence angle θ_i and the transmission angle θ_t are related through Snell's law [58]. The variations of E_s and E_p due to reflection are given by the Fresnel's coefficients [58]:

$$\begin{aligned} r_p &= \frac{E_p^r}{E_p^i} = \frac{n_2 \cos\theta_i - n_1 \cos\theta_t}{n_1 \cos\theta_t + n_2 \cos\theta_i} \\ r_s &= \frac{E_s^r}{E_s^i} = \frac{n_1 \cos\theta_i - n_2 \cos\theta_t}{n_1 \cos\theta_i + n_2 \cos\theta_t} \end{aligned} \tag{3.3}$$

In summary, given a generic incident wave, it can be decomposed into p- and s-polarised parts. The polarisation state of the reflected wave can be deduced through the application of the previous formula, and the optical properties of the interface are then revealed.

3.3.1 Ellipsometry at the air–water interface

As shown in Section 3.3 a light beam reflected at an interface will change its polarisation state, i.e. the light polarised perpendicular to the reflection plane (s-polarised) reflects differently from the light polarised parallel to the plane (p-polarised). The relative amplitude and the phase of the p and s components vary by different amounts. The attenuation, called Ψ, and the phase shift, known as Δ, depend on the optical properties of the surface and the angle of incidence, θ_i. These values are related to the Fresnel reflectivity coefficients, r_p and r_s, parallel and perpendicular components respectively [68],

$$\frac{r_p}{r_s} = \tan(\Psi)\exp(i\Delta) = \mathrm{Re}(r) + i\mathrm{Im}(r) \tag{3.6}$$

Ellipsometry is widely used to study adsorption at solid–liquid and solid–vapour interfaces, because of the large contrast due to different refractive index of the two components. For a transparent air-liquid interface a key limitation is that Ψ is very insensitive to the optical properties of the layer in the thin film limit ($d \ll \lambda$). Therefore measurements of Δ only are usually related to the properties of the layer [68].

Manning-Benson et al. [69] have exploited the sensitivity of ellipsometry to study the dynamic adsorption at an expanding air–water interface where they carefully examined the relation between ellipticity, ϵ, and surface excess, Γ. Without going into many details, their approach is described in the following text.

For the reflection of light at a transparent dielectric material, r_p is minimised at the Brewster's angle, ($\theta_B = \arctan\frac{n_2}{n_1}$, see further details in Section 3.3.4). Furthermore, $\mathrm{Re}(r_p/r_s) = 0$ and the ellipticity coefficient ϵ is given by $\mathrm{Im}(r_p/r_s)$. For a monolayer at the air–water interface ϵ is related to the relative permettivity ε, [62]:

where γ is the surface tension. Because $\varepsilon_{H_2O} = 1.78$ at $\lambda = 632.8\,\mathrm{nm}$ [71], η_R is negative and the contribution to ϵ is positive. By assuming an optically isotropic material the value η_S is given by:

$$\eta_S = \int \frac{[\varepsilon(z) - 1][\varepsilon(z) - \varepsilon_{H_2O}]}{\varepsilon(z)} dz \tag{3.9}$$

where $\varepsilon(z)$ is the profile of relative permettivity along the normal to the surface. Given that the value of ε for liquid hydrocarbon is 2.05 [72], η_S is positive and the contribution to ϵ negative.

In the specific case where a uniform isotropic layer of hydrocarbon-based surfactant is adsorbed at the air–water interface, η_R can be thought of as independent of the surface excess (i.e. weak dependence on surface tension, γ) and then η_S will vary linearly with Γ in the thin film limit. As a result, the ellipticity ϵ will be linearly proportional to Γ. In this context, a single measurement of Γ at a given concentration can be used to calibrate the ellipticity [73]. The greatest advantage of ellipsometry is its high sensitivity to an adsorption layer. The measurements can also be extremely fast ($\sim 10^{-2}\,\mathrm{s}$), although most instruments acquire data in a timescale of $\sim 5\,\mathrm{s}$, and the probed surface very small ($\sim \mathrm{mm}^2$). It is a suitable technique to follow dynamic adsorption processes.

However, when the surfactant monolayer is not optically isotropic, other contribution to the ellipticity will be added [74]. These uncertainties complicates the evaluation of $\varepsilon(z)$ and usually require additional calibration by using complementary techniques.

The ellipsometric signal can exhibit temporal fluctuation if the sample has lateral inhomogeneities, for example domains of aggregates. The quantitative analysis of these data is not obvious, however information may be obtained from the qualitative analysis, as discussed in Section 7.8.1.

3.3.2 Beaglehole Picometer Light Ellipsometer

Instead of a light standard null ellipsometer, with a rotating polarising element, Picometer Light ellipsometer in the Partenership for Soft Condensed Matter was used in this work. This instrument employs a photoelastic birefringence modulator to control

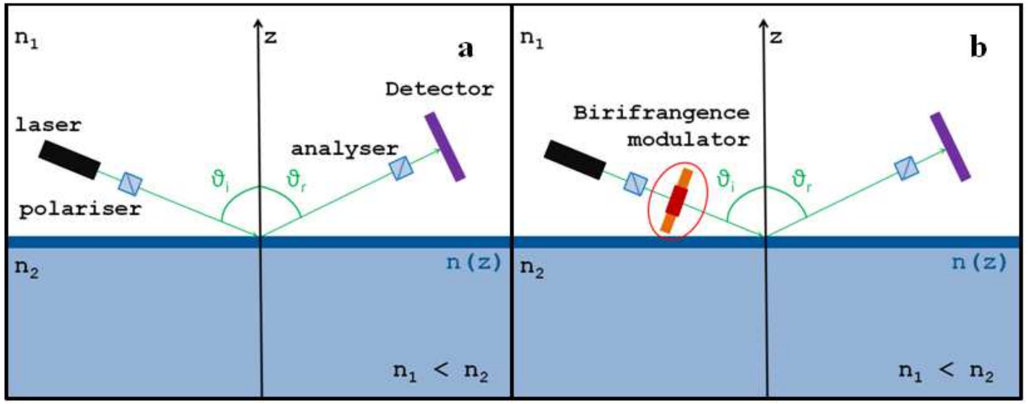

Figure 3.2: a. Scheme of a traditional nulling ellpsometer. b. Scheme of the phase–modulated ellipsometer.

operation of the instrument requires no moving parts and provides a continuous signal readout [75], however it is possible to measure with the rotating analyser in order to decrease systematic errors. This approach is somewhat different from traditional null ellipsometry.

The birefringence modulator consists of an isotropic glass slab (fused silica) of thickness d (10 mm). It is set into longitudinal oscillation at its resonance frequency ω at a wavelength of vibration of 2L, with L the length of the slab. The mechanical oscillation is driven electrically by the piezoelectric effect using a quartz crystal of the same length L that is attached to the glass slab. The periodic uniaxial strain $\delta(\omega)$ which is produced in the centre of the glass slab results in a periodic change in the refractive index for light polarised parallel to the oscillation direction. This is called the photoelastic effect. It leads to a periodic variation $\Delta n(\omega)$ in the refractive index difference for light polarised parallel and perpendicular to the oscillation direction given by

$$\Delta n(\delta, \omega) = \alpha\delta(\omega) \tag{3.10}$$

with α the piezo-optic constant. This strain-induced birefringence gives a phase shift between the light polarised in the two directions of

The signal from a phase–modulated ellipsometer is more closely related to Re(r) and Im(r), but these parameters are still not measured directly. The parameters x and y have been introduced to describe the phase–modulated ellipsometry signal [75]:

$$\begin{aligned} x &= \mathrm{Re}(r)\frac{2}{1+\mathrm{Re}(r)^2+\mathrm{Im}(r)^2} \\ y &= \mathrm{Im}(r)\frac{2}{1+\mathrm{Re}(r)^2+\mathrm{Im}(r)^2} \end{aligned} \tag{3.12}$$

The Picometer Light ellipsometer measures x and y directly, and for this reason they are used as the standard representation parameters for this instrument. Data measured with a phase–modulated ellipsometer can also be converted to the traditional parameters Ψ and Δ. While the conversion from Ψ, Δ to Re(r), Im(r) is straightforward (see Eq. 3.6), the reverse conversion has ambiguities:

$$\begin{aligned} \tan\Psi &= \sqrt{\mathrm{Re}(r)^2+\mathrm{Im}(r)^2} \\ \tan\Delta &= \mathrm{Im}(r)/\mathrm{Re}(r) \end{aligned} \tag{3.13}$$

The choice of the quadrant of the angles Ψ and Δ is a convention (see Ref.[75] for details). At the Brewster angle for a bare substrate, $\mathrm{Re}(r) = 0$, and $\Delta = 90^\circ$.

Since at the air–water interface the ellipsometer is not sensitive to Ψ, we just consider variations in Δ. The presence of a thin film at the air–water interface changes the value of Δ with respect to the clean interface. From this variation and on the assumption of a fixed refractive index for the layer, we can calculate the thickness using a model. In particular, I have used the software package Film Wizard^{TM}. Figure 3.3 shows the results of the thickness calculations based on the measured value of $\Delta - \Delta_{H_2O}$ and the refractive indices of the surfactants used in this work. From calculation of the thickness of the layer, the surface excess, Γ, is found through equation [77]:

$$\Gamma = \frac{d\,(n_{\mathrm{molecule}} - n_{H_2O})}{M_w\,\frac{dn}{dc}} \tag{3.14}$$

where dn/dc is in the refractive index increment in cm^3 g^{-1} and the units of d are in

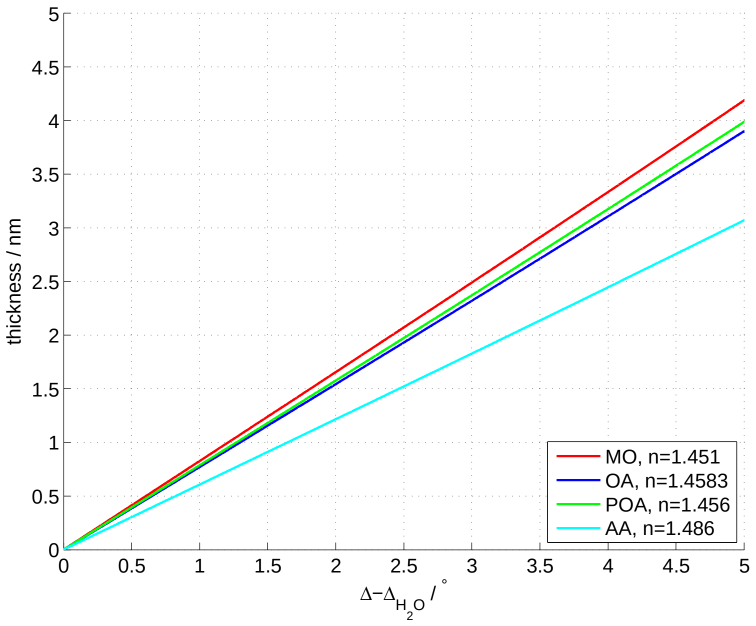

Figure 3.3: Calculations to demonstrate that the measured value of $\Delta - \Delta_{H_2O}$ depends on the thickness of the monolayer at the air–water interface and on the refractive index of the amphiphile molecules. Even a small variation in n, e.g. $n_{OA} - n_{POA} = 0.0023$, results in a measurable change in $\Delta - \Delta_{H_2O}$.

Parallel to this approach, which needs to assume a refractive index for the organic film, we can calibrate the ellipsometric data against the surface excess obtained from NR measurements. The data shown in Chapters 7 and 8 were analysed independently from the NR data. Nevertheless, good agreement with the NR data was found.

3.3.4 Brewster Angle Microscopy, BAM

The total reflection of light, occurring at the Brewster's angle when the p-polarised electromagnetic wave comes from low refractive index, n_1, medium to one with $n_2 > n_1$, may be used to obtain information on the structure and morphology of a monolayer at the air–water interface. Hénon and Meunier [79] developed at the beginning of the nineties a microscope sensitive to the surface density and to the anisotropy due to is at the air–water interface, the reflection can arise from three different sources: the monolayer thickness, interfacial roughness and the monolayer anisotropy. Firstly, if the two media are separated by a layer with a thickness, d, with a refractive index n(z), the intensity of the reflected wave can be approximated as Drude did [81]:

$$r_p(\theta_{Br}) = \imath r_s(\theta_{Br})\epsilon, \tag{3.17}$$

where $r_s(\theta_{Br})$ is the reflection intensity of a Fresnel interface for an s-polarised wave (the phase shift of $\pi/2$ between p and s polarisations is indicated by the imaginary unit $\imath$). The ellipticity, ϵ, can be calculated as:

$$\epsilon = \frac{\pi}{\lambda}\frac{\sqrt{n_1^2 + n_2^2}}{n_1^2 - n_2^2}\int_{-\infty}^{+\infty}\frac{[n(z)^2 - n_1^2][n(z)^2 - n_2^2]}{n(z)^2}dz. \tag{3.18}$$

This equation is correspondent to Eq. 3.7 because μ_r can be assumed to be unity and then $n^2 = \varepsilon_r$. Eq. 3.18 shows that a variation in thickness can be detected because the layer thickness affects the value of n(z).

The contribution of the interfacial roughness for a monolayer at the air–liquid interface is due only to thermal fluctuations [70]. Because the surface tension for a monolayer spread on a free water surface is large, fluctuations give a negligible contribution at the first order approximation. This approximation introduces an error on the monolayer thickness calculation around ~ 3Å.

As it is well known, the coexistence of several phases in a monolayer gives rise to anisotropy. This phenomenon can strongly increase the intensity of the reflected light and this increase can be calculated by the 4 × 4 matrix method [82]. For an optically anisotropic monolayer without a vertical axis of symmetry, the intensity of the reflected wave is a function of the orientation of the molecules in the monolayer plane (Fig. 3.4.d).

Nanofilm EP3 Brewster angle microscope

The Nanofilm EP3 Brewster angle microscope is made up by two arms, one where the

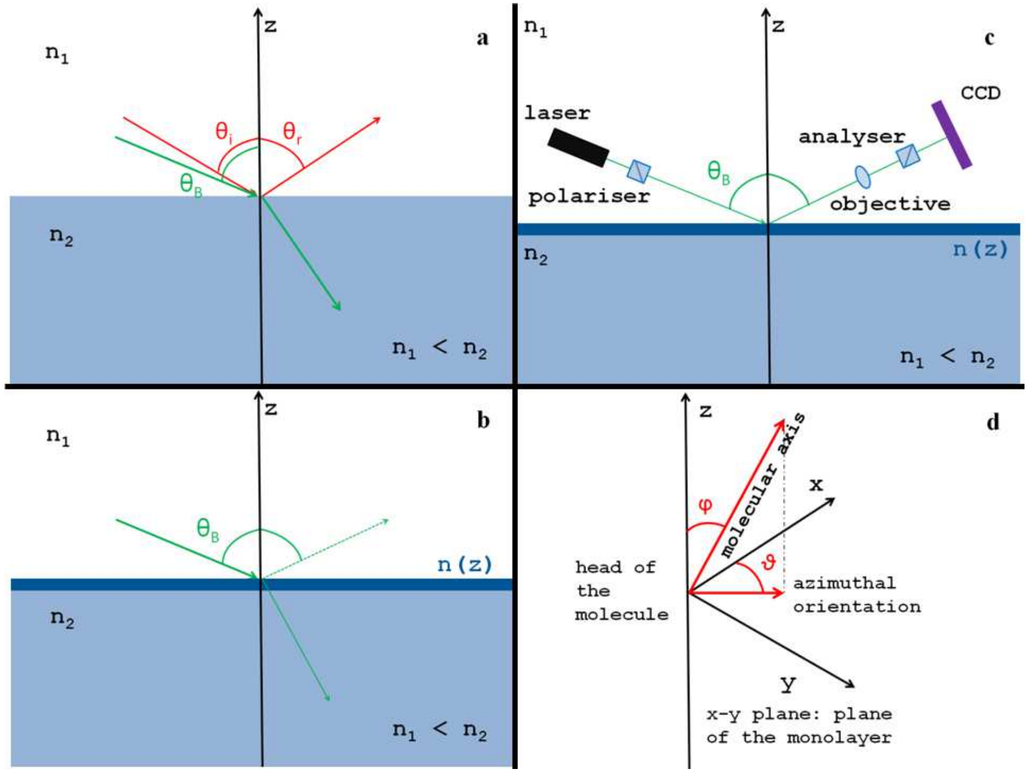

Figure 3.4: A series of sketches are shown. a.: the Brewster angle, θ_B, for the free air–water interface is drawn and the green arrows show the behaviour of a p-polarised light incident at θ_B. b.: a film at the air–water interface of refractive index n(z) produces a reflected light (dashed line). c.: schematic representation of the components of the BAM instrument. d. the two angles describing the position of a molecule at the interface are shown, where φ is the polar tilt angle and θ is the azimuthal orientation angle. The head of the molecule is assumed to be in the point $(0, 0, 0)$ of the coordinate system drawn.

The monolayer is inclined with respect to the objective axis, then the focused image will be just a narrow stripe. In order to obtain a complete image, several stripes are focused successively and then the software reconstructs the image. By an accurate calibration of the intensity scale, for a dense and thick monolayer, differences of the order of $5-10\%$ in the thickness or in the surface density can be distinguished. Known this, the reflected intensity allows to distinguish domains with different thicknesses the great advantage of this technique is the absence of fluorescent probes, such as those used in fluorescence microscopy. The development of a monolayer and its domains can be followed thanks to their different reflection properties. Furthermore, if an analyser in the reflection arm of the BAM instrument is provided, it allows one to vary the contrast between different domains and to investigate if and how molecules (thought as rod-shaped) are tilted with respect to the normal at the plane. An appropriate calibration can allow one to relate the intensity of the signal to the tilt angle [83, 84], however this capability was not used in the work presented.

The BAM imaging was useful to understand if the organic films were isotropic or not, in order to interpret correctly the ellipsometric data using a linear $\Gamma(\Delta)$ assumption. Furthermore, the miscibility property of the binary mixture have been determined. The results of those measurement are shown and discussed in Section 6.2.

3.4 Absorption Spectroscopy

This section introduces briefly the two techniques used to determine the oxidant concentrations: UV-Visible (UV-Vis) and Fourier Transform InfraRed (FTIR) spectroscopy. Both techniques are based on the absorption of electromagnetic radiation by atoms and molecules.

Absorption spectroscopy is employed as an analytical chemistry tool to determine the presence of a particular molecule in a sample and, in many cases, to quantify its amount [85]. The most common arrangement is to direct a beam of radiation of given intensity, I_0, at a sample and detect the intensity of the radiation that passes through it, I (Fig. 3.5). The transmitted intensity, I, can be used to calculate the absorbance, A, which is defined as $\log(I_0/I)$. According to the Beer–Lambert law, A is proportional to the absorber concentration, c and the path length, l, as

$$A = \log\left(\frac{I_0}{I}\right) = \varepsilon(\tilde{\nu})\, c\, l \tag{3.19}$$

where ε, which is the molar absorption coefficient or extinction coefficient is a func-

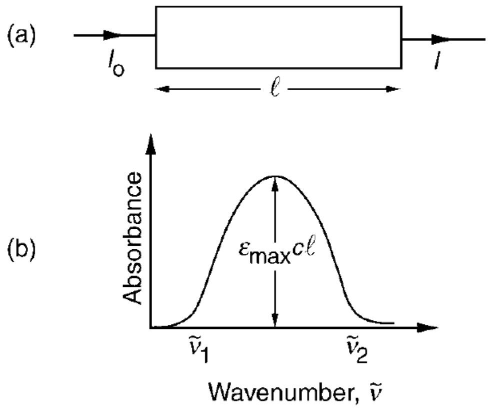

Figure 3.5: a. An absorption experiment: I_0 is the initial intensity of the radiation, I is the transmitted radiation and l is the sample path length. b. An absorption band with absorption coefficient ε_{max}, where c is the concentration of the absorbing material in a liquid or gaseous phase (schematics adapted from Ref. [85]).

of inner shell electrons in atoms are investigated by X-ray absorption. These changes can also be combined (e.g. rotation-vibration transitions), leading to new absorption lines at the combined energy of the two transitions. The energy associated with the quantum mechanical change determines the frequency of the absorption line, but several types of interactions can result in a shift of the line. Frequency shifts can be caused by external electric and magnetic fields and by interactions of the absorbing molecules with neighbouring molecules. For instance, absorption lines of a gas phase molecule can shift significantly when that molecule is in a liquid or solid phase, since the interaction with neighbouring molecules is stronger.

Absorption lines of an experimental spectrum always have a width and shape, which are determined by the instrument used for the observation, the material absorbing the radiation and the physical environment of that material. In general, lines are found to have the shape of a Gaussian or Lorentzian distribution. It is also common to characterise solely the intensity and width of the line instead of the entire shape. The spectrometer used to record the absorption lines may determine their width. In fact, the spectrometer has an inherent limit on how narrow a line can be resolved and so thanks to the specificity of the absorption spectra. A wide variety of applications rely on the use of absorption spectroscopy [86]. For instance, infrared gas analyzers can be used to identify the presence of pollutants in air, distinguishing the pollutant from nitrogen, oxygen, water and other natural air constituents [87, 88]. The identification of unknown samples is possible by comparing a measured spectrum with a library of reference spectra. In many cases, it is possible to determine qualitative information about a sample even if it is not in a library. An absorption spectrum can be quantitatively related to the amount of material present using the Beer–Lambert law (Eq. 3.19). Determining the absolute concentration of a compound requires knowledge of the compound's absorption coefficient. The absorption coefficient for some compounds is available from reference sources, and it can also be determined by measuring the spectrum of a calibration standard with a known concentration of the absorber.

Principle of operation

The most straightforward approach to absorption spectroscopy is to generate radiation with a source, measure a reference spectrum of that radiation with a detector and then re-measure the sample spectrum after placing the material of interest in between the source and detector. The two measured spectra can then be compared to determine the material's absorption spectrum. The sample spectrum alone is not sufficient to determine the absorption spectrum because it will be affected by the experimental conditions, such as the spectrum of the source, the absorption spectra of other materials in between the source and detector and the wavelength-dependent characteristics of the detector. The reference spectrum will be affected in the same way by these experimental conditions and therefore the comparison of the two spectra yields the absorption spectrum of the sample.

3.4.1 UV-Visible spectroscopy

The visible region of the spectrum comprises photon energies of 1.8 eV to 3 eV ($\lambda = 400 - 700\,\mathrm{nm}$), and the near ultraviolet region, out to 200 nm, extends this energy as a graph of absorbance, A, versus wavelength, λ. As described previously, the absorbance of a sample will be proportional to the number of absorbing molecules (e.g. their molar concentration in the sample tube). It is also necessary to correct the absorbance value for operational factors if the spectra of different compounds are to be compared in a meaningful way. The absorption coefficient is particularly useful when comparing the spectra of different compounds and determining the relative strength of light absorbing functions (chromophores). From the Beer–Lambert law, ε, is defined as:

$$\varepsilon = \frac{A}{c\,l} \tag{3.20}$$

where A is the absorbance , c is the sample concentration and l is the light path length trough the sample.

UV-Vis spectroscopy was used to determine the concentration of O_3 produced by exposure of O_2 to a UV lamp (Section 6.3.1).

3.4.2 IR spectroscopy

The infrared region of the electromagnetic spectrum comprises photon wavenumbers of $13300\,\mathrm{cm}^{-1}$ to $10\,\mathrm{cm}^{-1}$ (corresponding energy between 1.6 eV and 1.2 meV and λ between 750 nm to 1 mm). Vibrational motions of most molecules fall into this region. Absorption of IR radiation increases the vibrational state of the molecule, and can also change its rotational state, but it does not affect the electronic state [85]. The IR region is further divided into three sections: the near IR ($13300 - 4000\,\mathrm{cm}^{-1}$), the mid-IR ($4000 - 400\,\mathrm{cm}^{-1}$) and the far-IR ($400 - 10\,\mathrm{cm}^{-1}$). Composition, arrangement and binding type affect the types of vibrations possible for each molecule. The absorption will appear as a series of characteristic peaks, since the vibrational states are quantised. A molecule with n atoms can show $3n - 5$ (linear) or $3n - 6$ (non linear) vibrations. Not every vibrations leads to absorption. In order to have IR absorption the vibration must change the dipole moment of the molecule. In Figure 3.6 the CO_2 possible vibrational modes are shown, out of the 4 available modes, just 3 are IR active.

to the radiation. IR spectroscopy was generally considered to be able to provide only qualitative and semiquantitative analyses of common samples, especially when the data were acquired using the conventional dispersive instruments [85]. However, the development of reliable FTIR instrumentation and strong computerized data–processing capabilities have greatly improved the performance of quantitative IR work [90]. Thus, modern infrared spectroscopy has gained acceptance as a reliable tool for quantitative analysis. Deviations from Beer–Lambert law occur more often in infrared spectroscopy than in UV–Visible spectroscopy. Both instrumental and sample effects cause these deviations. Instrumental effects include insufficient resolution and stray radiation. In dispersive IR instruments [90], the resolution is closely related to the slit width, while for FTIR spectrometers it is associated to the optical path difference between two beams in the interferometer. Stray light levels in FT instruments are usually negligible. Sample effects include chemical reactions and molecular interactions such as hydrogen bonding. The Beer–Lambert law deviations result in a nonlinear relationship for plots of absorbance against concentration. It is therefore a good practice to obtain calibration curves that are determined empirically from known standards.
A brief overview of the FTIR spectrometer is given in the next section.

FTIR spectrometer

Compared to the classical IR dispersion spectrometer [90], the FTIR spectrometer has many advantages. The principle of operation is based on the interference between two beams of IR radiation, one reflecting on a fixed mirror and one on a movable mirror. The sum of the two beams creates a sequence of constructive and destructive interferences, which passes through the sample producing an interferogram (Figure 3.7). The Fourier transform converts the interferogram into a spectrum, changing

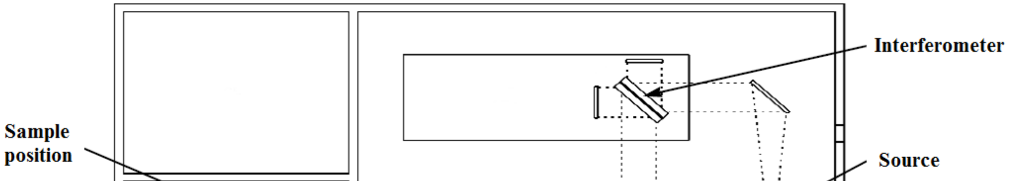

in all the frequency range. The resolution can reach values below 0.001 cm^{-1}, allowing efficient discrimination of the absorption lines. The signal-to-noise ratio can be highly improved by summing electronically many scans of the spectrum.

The FTIR spectroscopy measurements were performed to quantify the concentration of NO_3, which was produced in situ. Direct measurement of $[NO_3]$ is not possible in the IR region. However, modelling the chemical reactions used to produce NO_3 (Section 6.3.2) provided the relation among the compounds. The measurements of $[NO_2]$ and $[N_2O_5]$ permitted to calculate $[NO_3]$ (see Section 6.3.2).

Chapter 4

Data analysis

4.1 Introduction

This chapter describes the two main data analysis procedures used and optimised over the course of this PhD project. In Section 4.2 the treatment of experimental data recorded with NR is presented. Special attention was paid to the background treatment (Section 4.2.3) in order to allow a careful quantification of the surface active material left after reaction. In Section 4.3, the model developed to describe the heterogeneous reaction is illustrated. In particular, it is shown how the surface excess profiles recorded by both NR and ellipsometry can be interpreted to gain kinetic information about the surface reaction.

4.2 NR data

The NR data acquisition provides a two-dimensional time–of–flight (TOF) detector image. Figure 4.1 shows an example of raw data recorded for a monolayer of deuterated oleic acid at the air–ACMW interface. On the x-axis the wavelength is reported, which is calculated from the TOF. The y-axis represents the vertical axis of the detector, hence it provides the position and the width of the specular peak. The horizontal position of

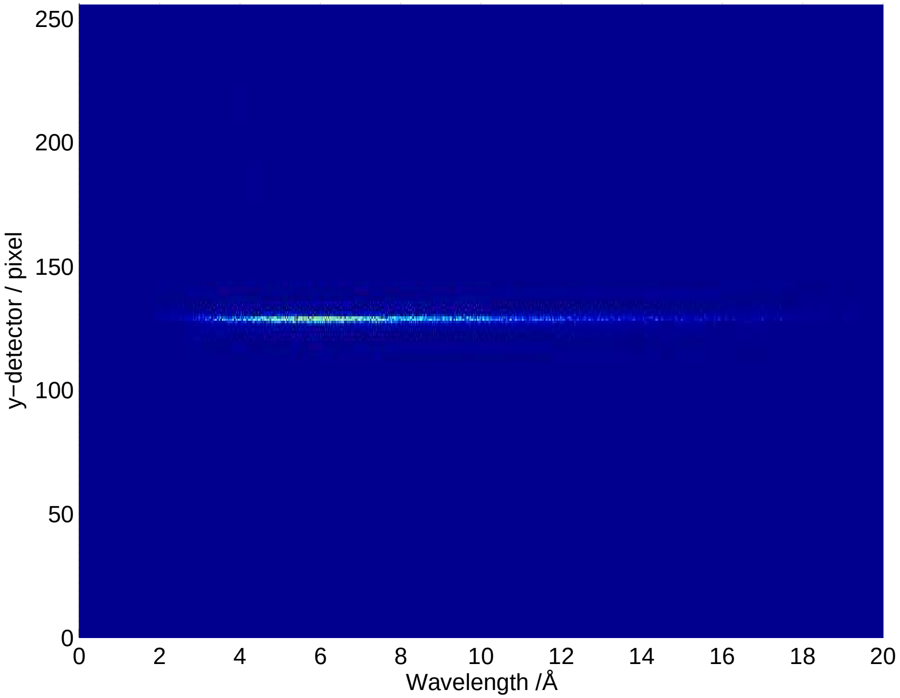

Figure 4.1: 2D TOF detector image shows the specular reflectivity peak due to a monolayer of deuterated oleic acid at the air–ACMW interface. The x-axis reports the neutron wavelength, the y-axis reports the detector pixel and the color (from blue to red) corresponds to the neutron counts.

the reflectivity. Another important ancillary measurement, it is the reflectivity of D_2O, which shows a total reflection, i.e. $N_r/N_i = 1$, below a critical q value as it is needed to correct the overall normalisation. Most of the data presented in this thesis have been recorded at an angle of 0.62° which leads to a q-range between 0.007 to 0.07 Å^{-1}. This low angle ensures a strong signal, allowing a very high time resolution necessary to reveal the kinetic features of the heterogeneous reaction under investigation, e.g. data shown in Fig. 4.1 were recorded in 5 s.

The q-range can be extended to higher value changing the incident angle, for example recording data at 3.78° the maximum q is 0.25 Å^{-1}. A change in the incident angle implies corresponding changes of other settings, such as the slit widths. It is necessary function of q, taking into account the calibration to the incident wavelength distribution and the detector efficiency. COSMOS can correct the specular peak subtracting the background and then calculates the reflectivity.

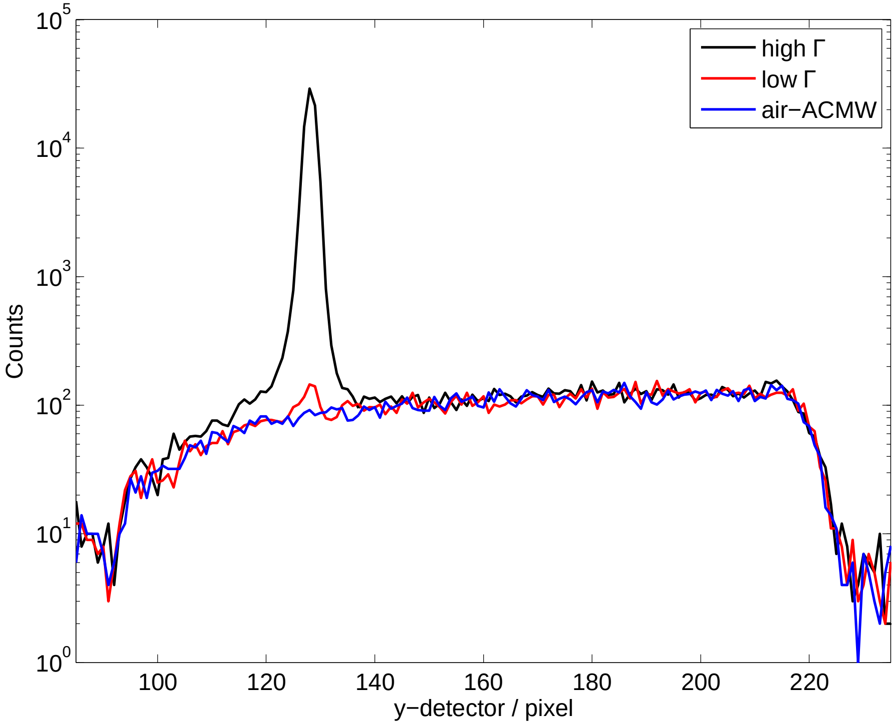

Figure 4.2: The neutron counts are displayed as a function of the detector y-position. The black line refers to a complete d-methyl oleate monolayer, the red line refers to a few percent of d-methyl oleate monolayer and the blue line refers to the clean air–ACMW interface (i.e. with no monolayer present).

Figure 4.2 shows the projection of the 2D TOF image, where the specular peak is clearly visible and it is centred around pixel 128. The detector area exposed to neutrons is restricted to 85 − 226 pixels, which results in the clear drop of neutron counting outside this interval. Figure 4.2 reports the comparison of signals recorded with (i) a d-methyl oleate monolayer, (ii) a few percent of a d-methyl oleate monolayer and (iii) a clean air–ACMW interface (i.e. with no monolayer present). Focusing on the re-

4.2.2 Obtaining surface excess from R(q)

Once the reflectivity profiles are obtained from the raw data, a fitting procedure is necessary to obtain physical information about the sample, such as the monolayer thickness, the surface excess and - in the case of multicomponent systems - the surface composition. Several programs are available to analyse R(q). Motofit [93] (program running on Igor Pro, Wavemetrics, Oregon) was chosen because of its high versatility. The fitting procedure can be divided into two steps: the theoretical calculation of R(q) based on the Abeles formulation [61] and the least squares fitting of the experimental data. The parameters for the reflectivity calculation are optimised in order to get the best fit to the experimental data, and errors on parameters are obtained. In order to calculate the theoretical R(q) using the Abeles matrix method [61], the sample has to be modelled as a stratified medium. Figure 4.3 shows the model used to analyse the experimental data: a monolayer characterised by thickness, d, scattering length density, ρ and roughness, σ. Both air and ACMW have $\rho = 0$. During the reaction the layer can change both ρ and d, since we do not have reliable information on d because of the low q range ($0.007 - 0.07\,\text{Å}^{-1}$), this parameter is kept fixed. This choice is acceptable

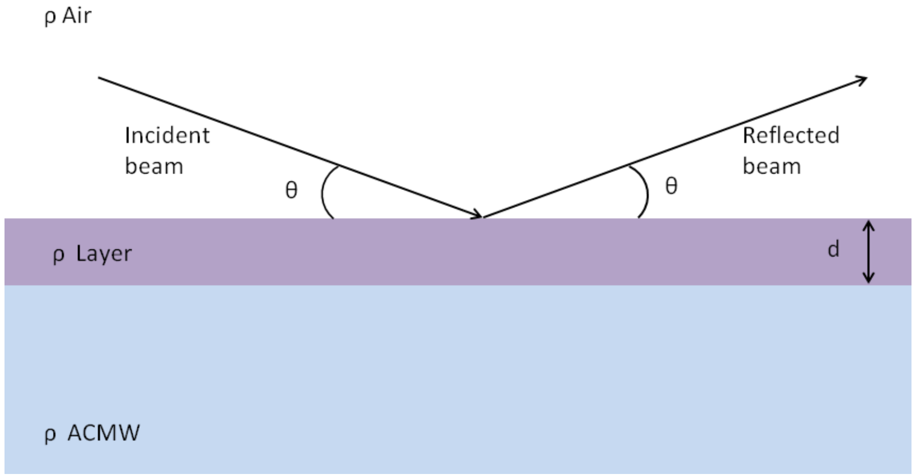

Figure 4.3: Model used for reflectivity fitting.

and ρ was the free parameter (see blue squares in Fig. 4.4). The value for d = 4Å was chosen assuming the shape of the organic surfactant to be a cylinder, which may lie down at low coverage, hence the layer has a minimum thickness corresponding to the diameter of the cylinder. The resulting surface excess values were in agreement within errors, hence we decided to use the first approach, since it was less time consuming.

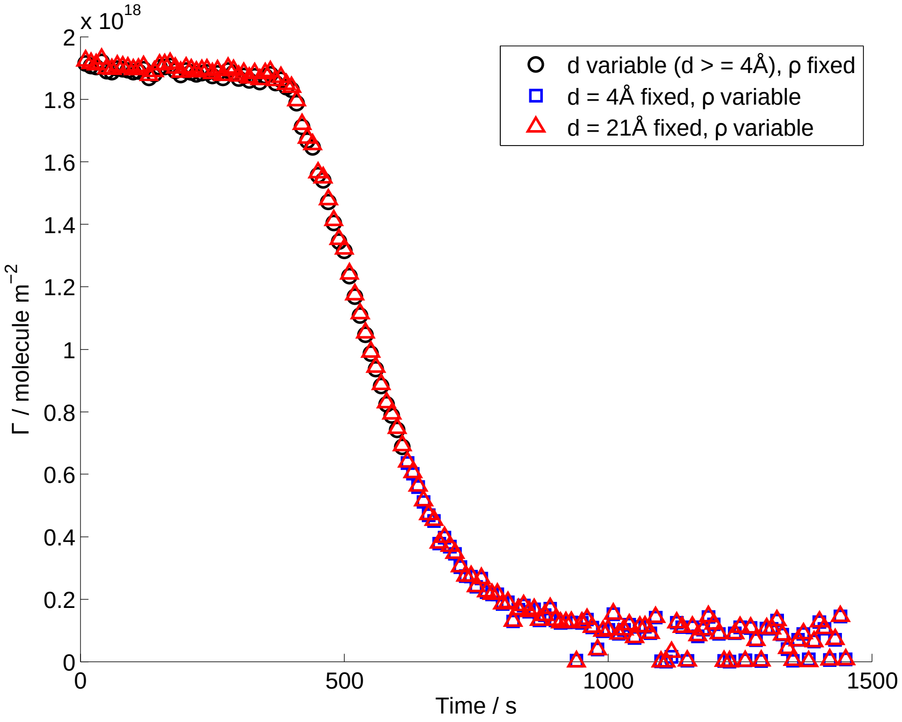

Figure 4.4: The surface excess decay as a function of time is calculated using the two different fitting approaches described in the text and in the legend. Both approaches lead to the same results. Error bars were within the symbol dimensions and are omitted for clarity.

4.2.3 Background treatment for low signal

A typical reaction experiment has initially a well characterised layer of fatty acids with deuterated tails, and oxidation of the film is expected to result in loss of intensity product yield estimation. To address this issue, I developed a new approach in order to avoid the introduction of systematic errors due to over- or under-estimation of the background level.

In Fig. 4.4 an example of a surface excess decay is shown. A higher scatter in the data when approaching low Γ ($< 2 \times 10^{17}$ molecule m^{-2}) can be noticed. This effect was due to the low counting rate and the introduction of artefacts by background subtraction. Furthermore, the analysis of NR data, recorded with a clean air–ACMW interface, lead to a surface excess of 3.6×10^{16} molecule m^{-2}, which corresponds to $1 - 2$ % of an initial monolayer ($\sim 2 \times 10^{18}$ molecule m^{-2}) (see red circles in Figure 4.5). The new approach provided a surface excess of about 10^{14} molecule m^{-2}, corresponding to ~ 0.01 % of Γ of a full monolayer (see blue squares in Figure 4.5), which is low enough to allow the careful quantification of surface active products. COSMOS processing for background

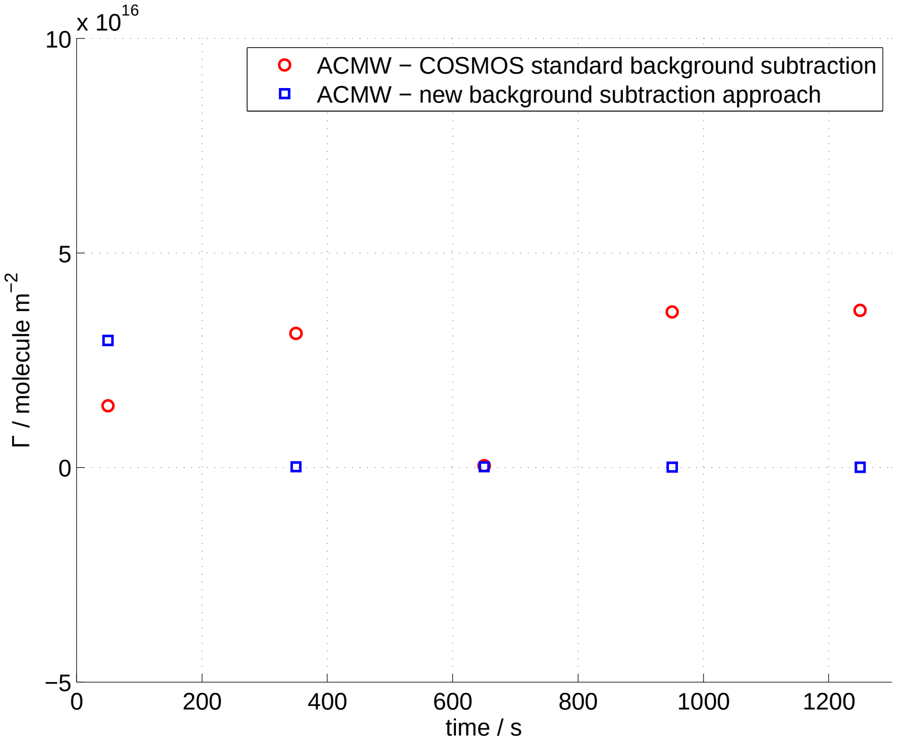

Figure 4.5: Surface excess values obtained from the NR data on clean air–ACMW

raw data including the subtraction step in COSMOS. The intervals used for calculating the background value were optimised in order to result in a derived surface excesses for ACMW-only measurements as low as possible. Once the reduced data were obtained, the reflectivity as function of the momentum transfer (q) was fitted in Motofit [93]. Because of the noise in the low coverage data (see Fig. 4.2 red line), the background subtraction process resulted in some cases in negative reflectivity values, which are physically unrealistic and therefore cannot be modelled appropriately using any fitting program. In fact, any fitting packages, when loading a reflectivity profile with negative points, do not take those points into account leading to incorrect results. Systematic errors are propagated into the surface excess calculation, which are negligible at high coverage but they start to became important at low coverage.

In my approach, in order to avoid negative reflectivity values, the reduction step was performed without any subtraction of the background. Physically meaningful reflectivity profiles were obtained, which are suitable for any fitting program. Out of the programs available, Motofit was chosen, because of the possibility to perform the χ^2 minimisation, weighted by the errors in the reflectivity data points. At this stage a non-zero value for the background was used in the fitting procedure. The background

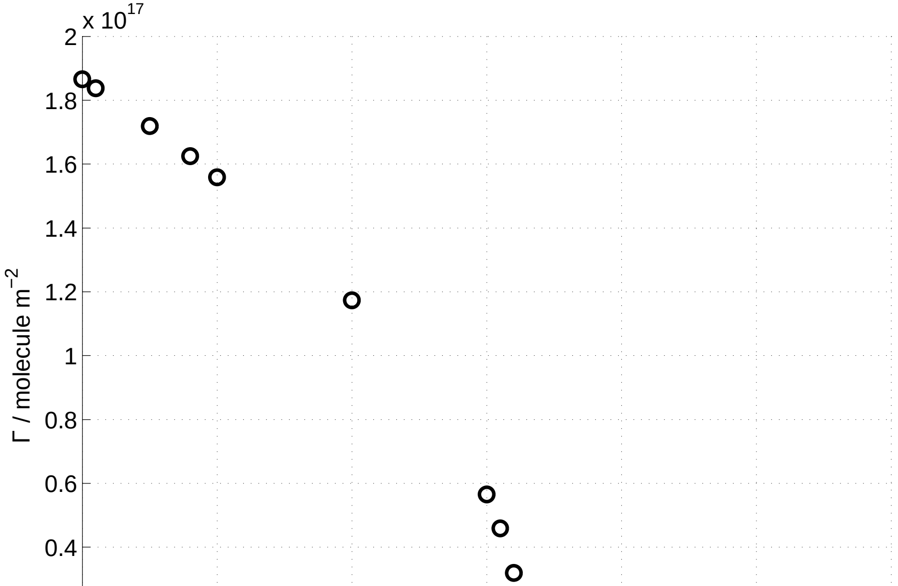

for each value the surface excess, Γ, was calculated. Figure 4.6 shows the results of this systematic analysis of the clean air–ACMW data. A suitable value for the background of 3.4×10^{-5} was refined and used for the fitting of all the reflectivity profiles recorded in the same beam time. This second approach resulted in lower surface excess values ($\sim 0.01\,\%$ of the Γ of a full monolayer) and in less scattered data compared to the standard procedure (see Figure 4.5). For each beam time, ACMW data were recorded and treated as described above to obtain the background value, which can slightly change due to the instrument settings and the neutron beam status.

The background treatment described above is necessary when dealing with very low reflectivity, i.e. close to the background level. This may occur when dealing with fully deuterated surfactants at low surface excess or with partially deuterated surfactants. So far, NR was used to investigate the surface excess of deuterated monolayer at the air–ACMW interface and the interfacial composition of mixtures, with an expected precision of $5 - 10\,\%$ [94, 62, 95]. In this work, the precision requested was much lower, and the demand was met thanks to the background method introduced and the capability of the FIGARO reflectometer. The instrument settings of FIGARO allowed to record R(q) for the q-range $0.007 - 0.07\,\text{Å}^{-1}$, which ensures a good signal even at low surface excess (see Section 2.4).

It is important to remember that in these extreme conditions (i.e. quantifying precisely a negligible surface excess at the air–ACMW interface) the R(q) data are very scattered with at least 10% statistical error. Furthermore the absolute values of the reflectivity are very low ($\sim 10^{-5}$) compared with the initial signal given by a deuterated fatty acid monolayer ($\sim 10^{-2}$).

This process of refining the background treatment together with the low-q strength of FIGARO may allow the use of a partially deuterated samples or even hydrogenated ones, where the contrast is much weaker than in fully deuterated monolayers. Furthermore, it may also be feasible to investigate if the oxidants are incorporated into monolayers at the air–water interface. Moreover, this systematic study has already proved to be useful to other FIGARO users to perform a more accurate analysis of the kinetic behaviour.

The techniques used to follow the surface reactions (see Chapter 2 and Section 3.3) provide the surface excess of the organic surfactant as a function of time, $\Gamma(t)$. In the following sections I describe the approaches to analyse those profiles and their validity.

4.3.1 Surfactant exposed to O_3

The first system studied during my PhD was methyl oleate, MO, exposed to O_3 [33]. Even if it is not the main topic of my project, it is closely related to it, and I have been centrally involved in all of the experiments, the data analysis and the kinetic fitting.

In order to fit the surface excess decay, we need to describe the reaction mechanism. We assume that each O_3 molecule can attack just one methyl oleate molecule:

$$\mathrm{MO} + \mathrm{O_3} \longrightarrow \text{products} \tag{R 4.1}$$

In terms of concentrations, we can write the following differential equation:

$$-\frac{d[\mathrm{MO}]}{dt} = k_{\mathrm{surf;MO;O_3}}[\mathrm{MO}][\mathrm{O_3}]_s \tag{4.1}$$

[MO] is the surface excess of MO (generally called Γ, in molecule cm^{-2}) and $k_{\mathrm{surf;MO;O_3}}$ is the rate coefficient (in cm^2 $\mathrm{molecule}^{-1}$ s^{-1}). $[\mathrm{O_3}]_s$ (in molecule cm^{-2}) is the coverage of ozone that dissolves into an organic layer at the air–water interface corresponding to $[\mathrm{O_3}]_v^{\mathrm{chamber}}$ (in molecule cm^{-3}) in the gas phase. $[\mathrm{O_3}]_s$ is calculated assuming that the surface concentration is constant in time and is equal to Henry's Law solubility (see Eq. 6.2). The gas phase concentration of ozone during the reaction was not constant owing to the gas volume above the trough and the mixing of the added ozone. Assuming that the chamber acted as a well stirred reactor with constant and matching input and output flows the concentration of ozone in the chamber, $[\mathrm{O_3}]_v^{\mathrm{chamber}}$, may be calculated as:

$$[\mathrm{O_3}]_v^{\mathrm{chamber}} = [\mathrm{O_3}]_v \left[1 - \exp\left(-\frac{f}{v}t\right)\right] \tag{4.2}$$

The fitting function has been implemented in the Curve Fitting routine of Igor Pro and each decay has been analysed individually. A weighted least square fitting was chosen in order to take into account the error bars on the surface excess values. For each $[O_3]_s$ used, a k_1 was obtained and a $k_1([O_3]_s)$ profile has been plotted and fitted with an orthogonal distance regression line to obtain the second order rate coefficient $k_{surf;MO;O_3}$.

4.3.2 Surfactant exposed to NO_3

Organic oxidation driven by NO_3 shows several reaction channels, which are not well described by the approach used for $MO + O_3$ system. Different mechanisms need to be taken into account in order to fit the experimental data. A specific model has been developed for the heterogeneous reaction at the air–water interface. This model builds on the formalism and terminology of the PRA framework [96]. It is a combination of KM-SUB and K2-SURF, and it has been adapted to the planar geometry.

KM-SUB and K2-SURF were introduced by Shiraiwa et al. [97, 98] and in the last years they have been applied to describe several experimental data and conditions, e.g. Refs [99, 100]. Both models describe the evolution of the kinetic parameters of an organic droplet exposed to oxidant. I adapted the model to a monomolecular organic layer at the air–water interface. The oxidant loss due to the reaction and transport to the bulk water has been taken into account. The organic reactants used in the experiments show a very low solubility and slow diffusion in water, hence the loss due to transport to the bulk could be neglected. Since the product branching ratio of the heterogeneous reaction is not known, and the techniques used cannot identify individual products, I divided the products into three categories: volatile, soluble and surface active species. The distinction between soluble and volatile species is made on the basis of the product yields known for bulk reaction and considering their vapour pressures and solubilities. Because of the method used to produce NO_3 (see Section 5.3.2) the ratio $[NO_2]/[NO_3]$ increases from 10^5 to 10^7 as $[NO_3]$ decreases from 10^9 to 10^8 molecule cm^{-3}. Since the NO_2 can adsorb and desorb from the organic layer (compare King et al. [53]), occupying reactive sites, the organic loss due to reaction

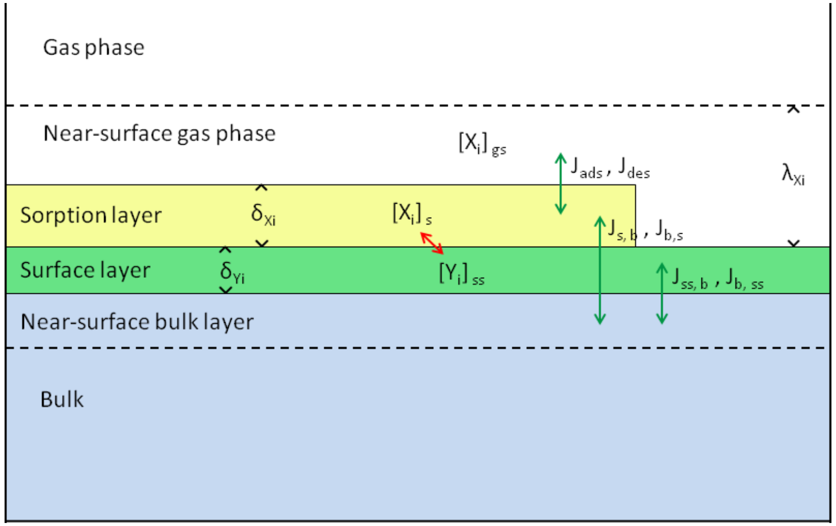

Figure 4.7: Kinetic model for an organic layer at the air–water interface. δ_{X_i} and δ_{Y_i} are the thicknesses of sorption and surface layer. λ_{X_i} is the mean free path of X_i in the gas phase. The red arrow shows chemical reactions. The green arrows show the transport fluxes.

evaporation into the gas phase.

The evolution of the gas species surface concentration, $[X_i]_s$, can be described by taking into account the following processes: adsorption, desorption, transport and reaction. From the kinetic theory, the flux of colliding X_i molecules with the surface can be expressed as

$$J_{\text{coll};\,X_i} = \frac{\omega_{X_i}}{4}\,[X_i]_{gs} \tag{4.4}$$

where $[X_i]_{gs}$ is the near-surface gas concentration that is assumed to be the same as the gas phase concentration. As a result of the finite time required to fill the chamber, as detailed in Section 4.3.1, the gas-phase concentration in the chamber is described as $[X_i]_{gs} = [X_i]_v\left(1 - \exp^{-(f=v)\,t}\right)$, where f is the flow rate, v is the volume of the chamber and $[X_i]_v$ is the oxidant concentration measured by IR spectroscopy (see Section 6.3.2 for details). ω_{NO_3} is the mean thermal velocity given by $\omega_{X_i} = \sqrt{8RT/\pi M_{X_i}}$, where M_{X_i} is the molar mass of X_i, R is the gas constant and T is the absolute temperature. The flux of gas molecules adsorbed on the organic layer is expressed by

The surface coverage is defined as the ratio between the actual and the maximum surface concentration value of the gas species, X_i: $\theta_{s;X_i} = [X_i]_s / [X_i]_{s;max} = \sigma_{X_i} [X_i]_s$. The adsorbed molecule can thermally desorb back to the gas phase. Desorption can be described by a first–order rate coefficient, $k_{d;X_i}$. which is assumed to be independent of $\theta_{s;X_i}$. The flux of desorption of gas-phase molecules can be expressed as

$$J_{des;X_i} = k_{d;X_i}[X_i]_s = \tau^{-1}_{d\,X_i}[X_i]_s \tag{4.7}$$

The desorption lifetime $\tau_{d;X_i}$ is the mean residence time on the surface in the absence of surface reaction and surface bulk transport. For NO_3 we assume to have two desorption lifetimes, $\tau_{d;NO_3;1}$ and $\tau_{d;NO_3;2}$, which are combined to give an effective desorption time $\tau_{d;NO_3;eff}$ weighted by the organic surface coverage, $\theta_{ss} = [Y]_{ss}/[Y]_{ss;0}$ as

$$\tau^{-1}_{d;NO_3;eff} = \theta_{ss}\,\tau^{-1}_{d;NO_3;1} + (1 - \theta_{ss})\,\tau^{-1}_{d;NO_3;2}. \tag{4.8}$$

This change in desorption time is related to the change of orientation of the organic molecules at the interface, i.e. for a highly packed monolayer the reactive site is assumed to be less accessible, and the oxidant has less affinity for other parts of the molecules hence the desorption is faster. When the organic surface coverage decreases the reactive sites become more accessible and the desorption is slowed down. For NO_2 we considered a single desorption lifetime, $\tau_{d;NO_2}$. Once adsorbed to the surface, the gas-phase molecules can be transported to the bulk water and vice versa. The corresponding fluxes can be expressed as

$$J_{sb;X_i} = k_{sb;X_i}[X_i]_s \tag{4.9}$$

$$J_{bs;X_i} = k_{bs;X_i}[X_i]_b \tag{4.10}$$

where $k_{bs;X_i}$ in $cm\,s^{-1}$ is a transport coefficient and can be regarded as effective transport velocity. The bulk diffusion coefficient, $D_{b;X_i}$, can be used to estimate this transport velocity, $k_{bs;X_i} \approx 4D_{b;X_i}/\pi\lambda_{X_i}$, where λ_{X_i} is the average travel distance from the near-surface bulk into the sorption layer. To estimate $k_{sb;X_i}$ the rate coefficients for

$k_{surf;Y;NO_3}$:

$$L_{surf;Y;NO_3} = k_{surf;Y;NO_3}\,[Y]_{ss}\,[NO_3]_s \tag{4.12}$$

The evolution of the NO_3 and NO_2 surface and bulk concentrations can be described as follows:

$$\frac{d[NO_3]_s}{dt} = J_{ads;NO_3} - J_{des;NO_3} - L_{surf;Y;NO_3} + J_{bs;NO_3} - J_{sb;NO_3} \tag{4.13}$$

$$\frac{d[NO_3]_b}{dt} = (J_{sb;NO_3} - J_{bs;NO_3})\frac{A}{V} \tag{4.14}$$

$$\frac{d[NO_2]_s}{dt} = J_{ads;NO_2} - J_{des;NO_2} + J_{bs;NO_2} - J_{sb;NO_2} \tag{4.15}$$

$$\frac{d[NO_2]_b}{dt} = (J_{sb;NO_2} - J_{bs;NO_2})\frac{A}{V} \tag{4.16}$$

where A is the water surface area and V is the total water volume.

The reactant, Y, can be lost just through reaction with NO_3 at the surface, hence it is described as:

$$\frac{d[Y]_{ss}}{dt} = -k_{surf;Y;NO_3}[NO_3]_s\,[Y]_{ss} \tag{4.17}$$

The products of the heterogeneous reaction can not be identified individually by the experimental techniques used, hence we divided them in three main categories: surface active (Z_S), volatile (Z_G) and soluble (Z_B) species. The surface active products will remain at the air–water interface, and the surface–bulk transport is neglected:

$$\frac{d[Z_S]_{ss}}{dt} = c_S\,k_{surf;Y;NO_3}\,[NO_3]_s\,[Y]_{ss} \tag{4.18}$$

where c_S is the branching ratio relative to the surface active products. The volatile products will leave the surface depending on their vapour pressures, but with a lack of information on the chemical composition, we decided to use a first-order loss rate coefficient, $k_{loss;G}$, to describe the overall effect, hence the differential equation for Z_G is:

$$\frac{d[Z_G]_{ss}}{dt} = c_G\,k_{surf;Y;NO_3}\,[NO_3]_s\,[Y]_{ss} - k_{loss;G}\,[Z_G]_{ss} \tag{4.19}$$

product concentration is expressed as:

$$\frac{d[Z_B]_{ss}}{dt} = c_B\, k_{surf;\,Y;\,NO_3}\, [NO_3]_s\, [Y]_{ss} + k_{bss;Z_B}\, [Z_B]_b - k_{ssb;\,Z_B}\, [Z_B]_{ss} \tag{4.20}$$

$$\frac{d[Z_B]_b}{dt} = (k_{ssb;\,Z_B}\, [Z_B]_{ss} - k_{bss;Z_B}\, [Z_B]_b)\, \frac{A}{V} \tag{4.21}$$

where c_B is the branching ratio relative to the surface active products.

The differential equations 4.13-4.21 describe the evolution of the various species. This system of equations cannot be solved analytically, hence the ODE solver of MATLAB® [101] has been used for numeric solving. In order to fit the $\Gamma(t)$, provided by NR and ellipsometry, a minimisation of the value of χ^2 has been performed with the use of the fminuit package [102].

Chapter 5

Multi-Instruments Miniaturised Kinetics (MIMIK) chamber

5.1 Introduction

Organic monolayer at the air–water interface have been widely studied in the last decades. Considerable efforts have been made to understand the interactions and physical properties of such systems in a static state (constant surface area). Recently, the study in non-equilibrium conditions has also attracted the attention of many scientists, and interesting features have been pointed out [103, 104, 105, 106].

Our interest is focused on the atmospherically relevant chemical reaction happening at the aerosol surface, which involves an insoluble organic monolayer and gas-phase oxidants. In the literature we found several studies of reactions of organic droplets exposed to oxidants [45, 10, 107, 108], but no satisfying de-convolution of the surface reaction from the bulk reaction has been achieved [99, 109].

A very powerful technique to study interfaces is neutron reflectometry (NR). Neutrons are non-destructive for biological and soft-organic materials, and by selective deuteration of monolayer components they give access to additional information, being sensitive to the scattering length densities. Using a wide beam footprint, NR experiments provide quantitative measurements of the surface excess of a monolayer at the

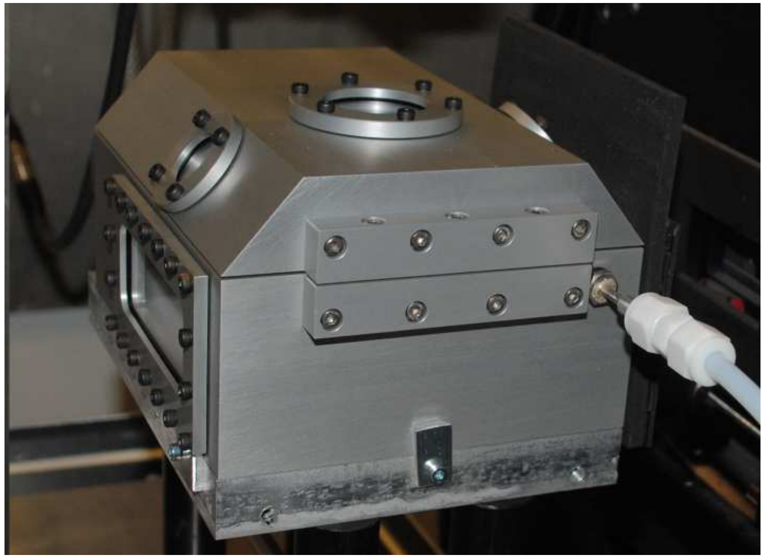

Figure 5.1: Photograph of the MIMIK chamber installed on the FIGARO sample stage where a neutron window (side), laser alignment window (top), ellipsometry windows (sloped) and gas inlet (front) are visible.

compared to 25 dm^3 of a previous chamber containing a commercial Langmuir trough) ensures much faster build up of the concentration of the gas-phase oxidant, which is crucial for kinetic studies. NR and ellipsometry allow to determine the surface excess of the surfactant as a function of time. For accurate kinetic analysis, it is very important to minimise the time between switching on the oxidant flow and reaching the steady state concentration; this mixing time can be taken into account in the analysis [33], but it limits accuracy and time resolution of the measurement. Another source of error for kinetic studies is a non-homogeneous gas diffusion. To minimise this we paid particular attention on designing the internal geometry of the chamber and the gas delivery system, taking advantage of fluid dynamics simulations [110, Priv. Comm.]. The experience gained with our previous reaction chamber, suitable for neutron reflectometry only, was crucial to develop the MIMIK chamber. This MIMIK chamber is compact enough to be easily handled, flexible and light to fit on most sample stages. Improved gas isolation also ensures a precise control of gas concentration and flow, out two single block of aluminum in order to minimise the possibility of gas leakage. A custom-made trough is fixed at the bottom of the chamber by nylon screws. The neutron windows are rectangular ($90 \times 40 \times 3\,\text{mm}^3$) and made of sapphire, while the ellipsometry windows are circular (25 mm diameter) and made of silica glass, which has good transmission of polarised light.

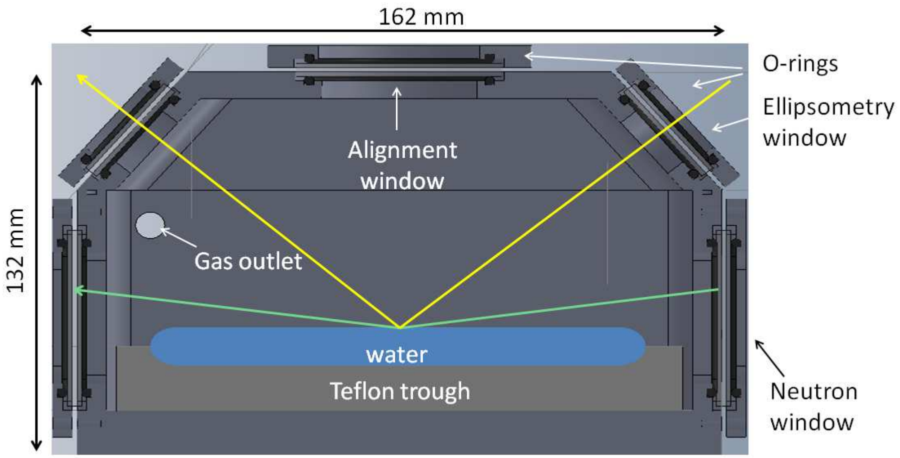

Figure 5.2: Schematic cross section of the MIMIK chamber. The green arrows indicate the path of the neutron beam and the yellow ones the path of the laser beam. The incident angle for neutron has been exaggerated for clarity. The chamber is constructed out of aluminium, and the trough made of Teflon.

Two o-rings for each window, one on each side, ensure gas-tight sealing, as a result of clamping by window frames fixed by stainless steel screws. The inlet and outlet ports for the gas flow are placed diametrically opposite on the short walls of the bottom part; the relative position of inlet and outlet has been chosen to optimise the homogeneity of the gas diffusion. The custom-made stainless steel gas connectors (see on the right hand side in Fig. 5.1) consist of a thin–walled stainless steel tube (1/8 inch outer diameter), which is inserted in and welded to a drilled hexagonal stainless steel screw. On the outer wall a 1/4 inch tube is welded to the small tube, and on the inner part it is connected to a custom–made Teflon injector; see detailed description in Section 5.2.1. The features of the injector can be tuned to allow different ranges of flow rates (see the error introduced by evaporation was found to be negligible and automatic height adjustment was thus not required.

5.2.1 Maximising the homogeneity of gas diffusion

Once the main design for the MIMIK chamber was completed, the position of the inlet and the outlet for the gas was carefully chosen. In particular for the gas inlet, a specific injector had to be designed and constructed. The injector is a piece of Teflon tube (O.D. 1/4 inch, I.D. 1/8 inch) with 11 holes of diameter 1 mm in a straight line parallel to the main axis of the tube; the distance between holes is 1 cm. The end of the tube is closed with a Teflon cap. This injector can be rotated around its axis in order to change the flow direction with respect to the chamber wall. The orientation angle has been fixed to 45° after several tests performed with a fluid dynamics simulation package available on SolidWorks [111].

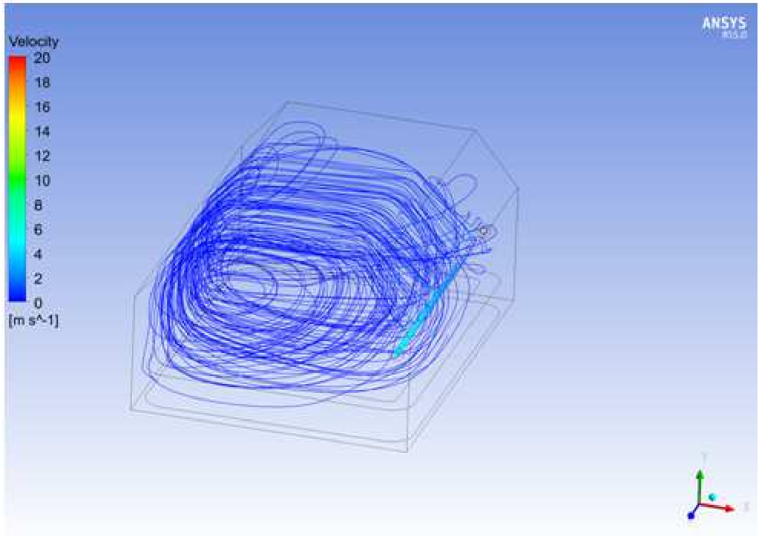

Figure 5.3: Velocity field in the MIMIK chamber represented by a streamline plot. The holes are oriented at 45° with respect to the horizontal plane and the air forms whirls reaching the water surface with only a low velocity. Adapted from Ref. [110, Priv. Comm.].

pressure gradient of only 2×10^{-3} mbar, hence the water surface is minimally affected by the gas flow (see Figs 5.3 and 5.4).

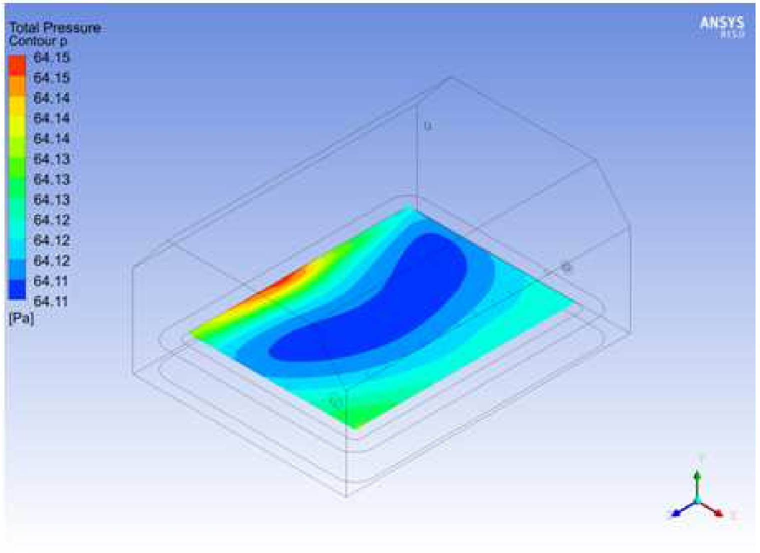

Figure 5.4: Pressure contour plot for the plane just above the water surface showing a very weak change in pressure, 2×10^{-3} mbar, suggesting that the water surface is minimally affected by the gas flow.

5.2.2 Suitability for NR and Ellipsometry

The ability to use the same sample environment for NR and ellipsometry measurements is extremely important for our kinetic experiments. In order to make the chamber suitable for both techniques, apart from dimension constraints, the main issue to be resolved was to allow geometrically the incidence of neutrons and the laser beam to the interface. The neutron beam impinges on the interface at very low angle (0.62°). Sapphire windows were chosen because of their high neutron transmission and placed on the wall without any particular tilting angle. The polarised light for the ellipsometry measurements arrives at the surface with an angle of 50° to the surface normal (Fig. 5.5). In order to avoid any loss of polarisation, the light has to pass through the

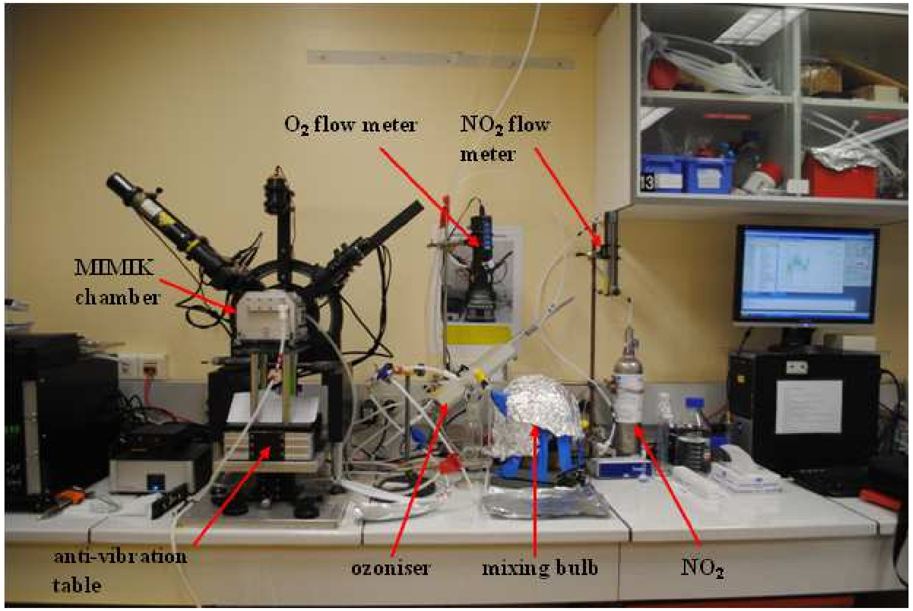

Figure 5.5: Photograph of the MIMIK chamber and the experimental setup for kinetic experiment performed with the ellipsometer. The alignment stage for the MIMIK chamber was placed on an active anti-vibration table.

5.3 Material and Methods

In this section the experimental set-up and procedure to prepare the sample will be described.

5.3.1 Surfactant solutions

NR and ellipsometry were used to study the oxidation of organic monolayers at the air–water interface. To prepare the insoluble monolayer at the air–water interface, it is common to use a Langmuir trough [67], which allows careful control of the surface pressure thanks to the precise movement of the barriers. This approach was used in the previous reaction chamber, but for the new set-up we decided to remove the barriers, together with the motors and the pressure sensor to reduce the gas volume of the chamber, as explained in Section 5.2. Without the barriers, the starting film was

Molecule	Chemical composition	Molecular weight (g/mol)	Scattering length (fm)
d33-methyl oleate*	$C_{19}O_2H_3D_{33}$	329.69	346.80
methyl oleate	$C_{19}O_2H_{36}$	296.49	3.22
d34-oleic acid	$C_{18}O_2D_{34}$	316.67	358.05
oleic acid	$C_{18}O_2H_{34}$	282.46	4.05
d14-palmitoleic acid*	$C_{16}O_2H_{16}D_{14}$	268.49	151.49
palmitoleic acid	$C_{16}O_2H_{30}$	254.41	5.72
d35-stearic acid	$C_{18}O_2D_{35}H$	319.69	360.98
stearic acid	$C_{18}O_2H_{36}$	284.48	-3.43
arachidonic acid	$C_{20}O_2H_{32}$	304.47	24.83

Table 5.1: List of the organic surfactants used for all the experimental work. $\star$ indicates the custom-deuterated molecules provided by the Oxford Deuteration Facility.

6.2.3). Prior to the spreading, the molecules need to be dissolved in an organic solvent, which needs to be sufficiently volatile to leave the water surface after deposition, but not too volatile to change the solution concentration while extracting the solution from the flask. Chloroform ($>$ 99.8 %, Sigma-Aldrich) is the organic solvent used to dissolve all the molecules under investigation, as it is a good solvent for all of them and the volatility meets the stated requirements. In Table 5.1 the full list of the surfactants used for the experimental work is displayed. Some of the molecules used were fully or partially deuterated; details for those are shown as well. The solutions were prepared shortly before the experiments, in order to reduce errors in the concentration due to solvent evaporation. Some milligrams of surfactant were dissolved in chloroform in a volumetric flask of 5 or 10 ml, achieving a final concentration of typically ca. $1\,\mathrm{mg\,ml^{-1}}$. From the concentration (c in $\mathrm{molecule\,cm^{-3}}$), the available area of the water surface (S in cm^2) and the volume of solution spread (V in µl) the initial surface excess, Γ, can be calculated:

$$\Gamma(\mathrm{molecule\,cm^{-2}}) = 10^{-3}\,\frac{c\,V}{S} = \frac{10^{16}}{A_{hg}} \tag{5.1}$$

where the factor 10^{-3} takes into account the conversion from µl to cm^3, $\mu\mathrm{l} = 10^{-3}\mathrm{cm}^3$. A_{hg} is the area per molecule, or per head group, and is given in $\mathrm{Å}^2$, the factor 10^{16}

had evaporated, and subsequently is was exposed to the gas-phase oxidants.

5.3.2 Gas flow system

The gas phase oxidants, O_3 and NO_3, used in this work to study the heterogeneous reaction with organic monolayer were not provided in a gas cylinder – as was the case for molecular oxygen – but had to be produced in situ since they are not sufficiently stable for long-term storage.

Ozone was produced by the exposure of molecular oxygen to UV light; further details on the ozone generator, its features and calibration can be found in Section 6.3.1. The nitrate radicals, NO_3, were produced from the reaction between O_3 and NO_2. NO_2 was supplied in small gas cylinders (112 dm^3) by Scientific and Technical Gases Ltd (Newcastle-under-Lyme, UK). NO_2 was provided as a mixture with synthetic air at a concentration of 1000 ppm with an analytical tolerance of ± 2%.

A sketch of the gas flow system is shown in Figure 5.6 and photographs of the real setup are shown in Figures 5.5 and 5.7. In order to produce ozone, the NO_2 cylinder

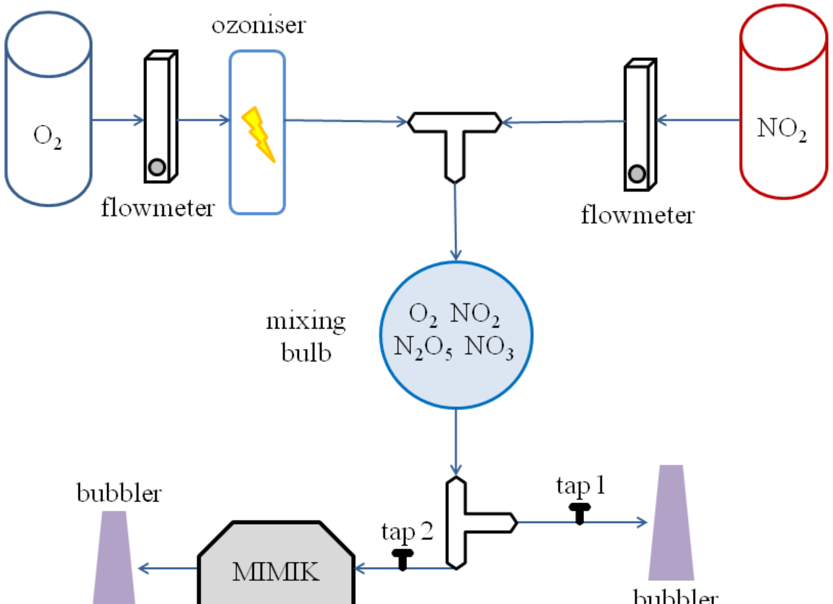

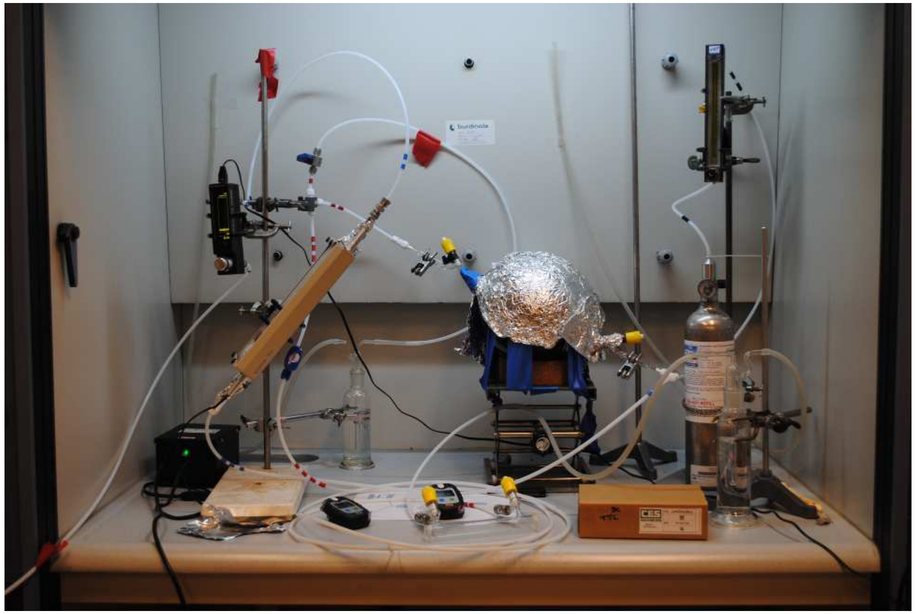

Figure 5.7: Photograph of the gas flow system as mounted for the FTIR measurements. The oxygen cylinder is not visible. All the tubing is made of Teflon, and all the connectors are made either of Teflon or stainless steel.

is 1.2 dm^3 min^{-1} and the flow rate of NO_2 is in the range 0.06 − 0.36 dm^3 min^{-1}. The mixing bulb has a volume of 5 dm^3, and the inlet part is made of a glass cylinder with 21 small holes on the surface, which enhances the mixing of the components. The residence time in the mixing bulb ranges from 2 to 4 minutes, which is long enough to establish equilibrium within the products (see Section 6.3.2). The concentration of NO_3 is tuned by changing the NO_2 flow rate and hence its concentration. A full description of the chemical reactions and the spectroscopic measurements needed to quantify $[NO_3]$ can be found in Section 6.3.2. The tubing is made from Chemfluor^{r} (PTFE), with an outer diameter of 1/4 inch and an inner diameter of 1/8 inch; this material has been chosen for its high chemical resistance. A digital flow meter (Model MV-302, MASS–VIEW, Bronkhorst) has been used for the control of the O_2 flow. For the NO_2 a ball flow meter resistant to NO_2 corrosion has been used. All the connectors used were made of Teflon or stainless steel to ensure chemical resistance.

closed and measurement of the surface excess starts with a time resolution of 5 s. In the meantime the gas-phase oxidant production is started and the oxidant is initially sent directly to the exhaust (see Fig. 5.6). After 10 minutes, tap 2 leading to the MIMIK chamber is opened while tap 1 (to exhaust) is closed, so that the gas mixture starts to flow into the reaction chamber. At this moment the reaction is started. The measurement is stopped when the signal from the monolayer reaches a plateau, which could mean absence of surface active material left (signal down to background level) or formation of a non-reactive monolayer (signal distinguishable from background level). For very low oxidant concentrations, measurements were stopped when the experiment had reached a total acquisition time of 4-5 hours even if a plateau in the measured surface excess values had not been achieved.

5.4 Performance tests

The performance of the MIMIK chamber has been tested carefully, from the gas tightness to the stability of the organic film with and without gas flow. Special care was taken to detect any wave formation at the water surface, which could destabilise the organic film and at the same time affect the NR signal.

5.4.1 Flow-induced vibrations on the water surface

In order to prove the minimisation of the vibrations at the water surface due to the gas flow, the trough was mounted on FIGARO and filled with 80 ml of D_2O, which shows a strong specular peak in NR measurements. Once the chamber was closed a measurement without flow was recorded as a standard, then the flow of oxygen was increased from $1.2\,\mathrm{dm^3\,min^{-1}}$ to $2.6\,\mathrm{dm^3\,min^{-1}}$, and for each setting NR data were acquired for one minute. If vibrations are present the width of the peak increases. In Figure 5.8 the neutron counts are reported as a function of pixel position on the y-axis of the 2D detector. The peak width is expected to be 6 pixels (~ 12 mm), and we did not measure a significant deviation from this value; just a small change for

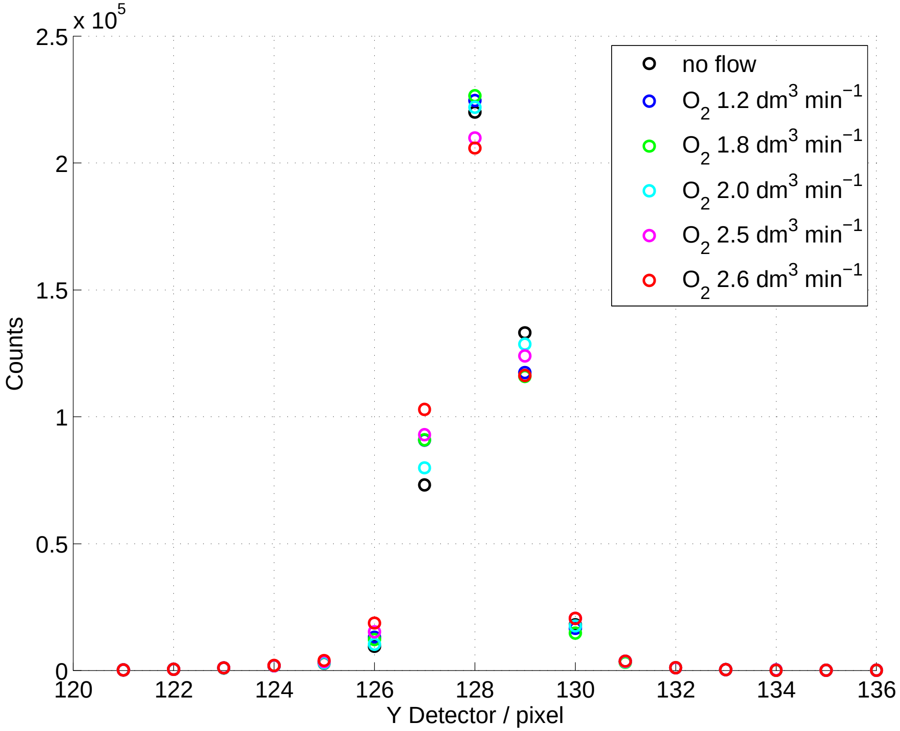

Figure 5.8: The projection of the 2D TOF detector image shows the intensity of the specular peak as a function of detector pixel position. The error bars were all within the symbol dimensions and hence are omitted for clarity. The peak height is slightly lower for flow rate 2.5 and 2.6 dm^3 min^{-1}, however the peak width is acceptable. In the legend the O$_2$ flow rates are reported.

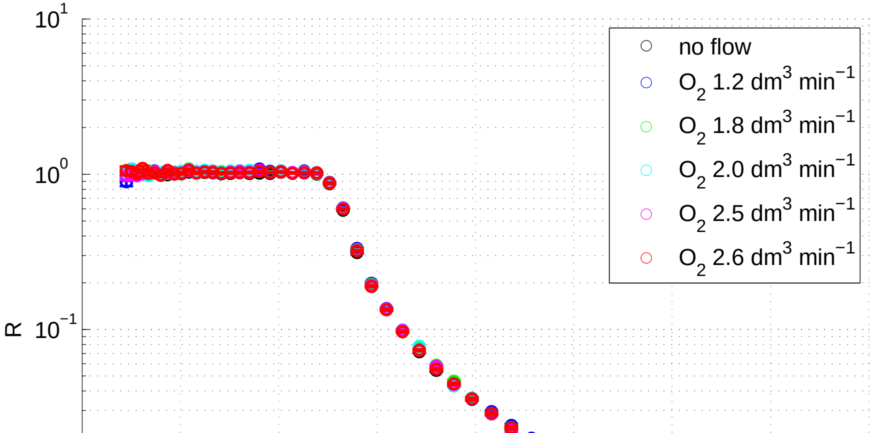

the consistency of the kinetic results, i.e. the rate coefficient measured for single-component systems using the two techniques. Furthermore, we wanted to compare those results with the ones from the reaction experiment performed with the previous chamber. The reaction studied was between a monolayer of methyl oleate and gas phase ozone.

Leaving the discussion on the rate coefficient to Section 7.2, I want to highlight the point that the value found with NR using the previous chamber is consistent with the one found with the MIMIK chamber using ellipsometry and NR. The previous chamber had a free volume of $25\,\mathrm{dm}^3$ and the flow rate was $15\,\mathrm{dm}^3\,\mathrm{min}^{-1}$, the sealing was poor and the gas diffusion was hardly reproducible as it lacked a well fixed gas inlet. Nevertheless, even though it was far from perfect, the quantitative analysis of surface reactions was reliable, probably due to the use of high concentrations of $O_3 \sim 10^{13}\,\mathrm{molecule\,cm}^{-3}$ and its long half–life [113].

Thanks to the use of NR and ellipsometry a comparison of the oxidative decay of hydrogenated methyl oleate and the deuterated form can be performed. From NR

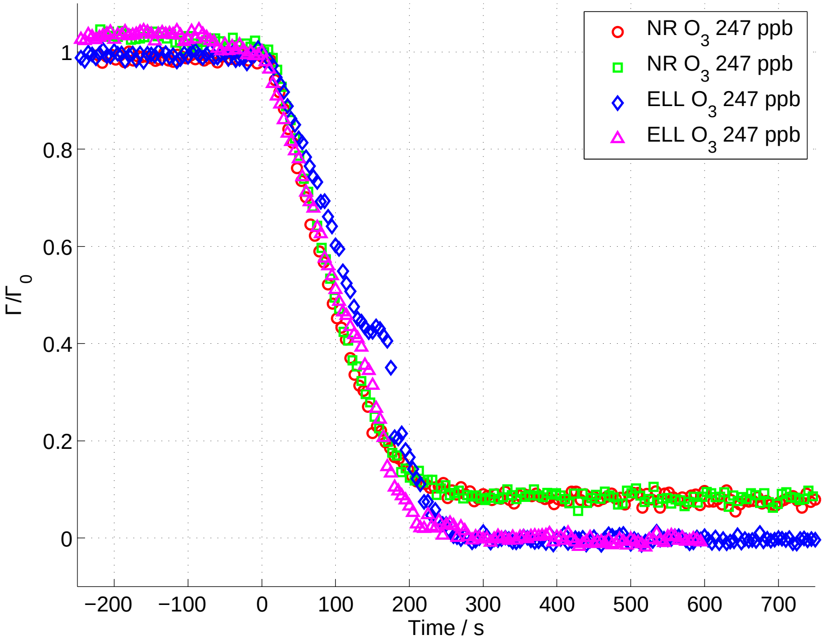

surface excess decay was identical. The kinetic fitting of those $\Gamma(t)$ lead to the same rate coefficient, as it is shown in Section 7.2.

Chapter 6

Preparatory study of the chemical compounds

6.1 Introduction

In order to study the heterogeneous oxidation occurring at the organic coated aerosol surface, a proxy for this coating is needed together with the production of a gas oxidant at measurable and reproducible concentrations.

The organic coated aerosol has been modelled as an organic monolayer at the planar air–water interface. Several molecules were used as proxies, e.g. oleic acid, either as a single component film or in a binary mixture. A preliminary characterisation of those films is reported in Section 6.2.

The gas oxidant used in this study were O_3 and NO_3. Both needed to be produced in situ. The gas flow system has been described in Section 5.3.2, while measurements are shown in Sections 6.3.1 and 6.3.2. Since NO_3 was not directly measurable, relevant reactions have been modelled in order to determine the relation between the concentrations of the various gas species involved and thus to allow the calculation of $[NO_3]$ (see Section 6.3.2).

Molecule	Chemical composition	Δ^x	C : D
methyl oleate	$C_{19}O_2H_{36}$	cis $-\ \Delta^9$	18:1
oleic acid	$C_{18}O_2H_{34}$	cis $-\ \Delta^9$	18:1
palmitoleic acid	$C_{16}O_2H_{30}$	cis $-\ \Delta^9$	16:1
stearic acid	$C_{18}O_2H_{36}$		18:0
arachidonic acid	$C_{20}O_2H_{32}$	cis, cis, cis, cis $-\ \Delta^5, \Delta^8, \Delta^{11}, \Delta^{14}$,	20:4

Table 6.1: List of the organic surfactants used for the preliminary characterisation of the organic monolayer, the position of the double bond (Δ^x), and the unsaturation degree (C:D = number of carbon atom to number of double bonds in the chain) are reported. All the molecules were used as received from Sigma-Aldrich. Purity was $\geq$ 98.5 %.

binary mixture, this characterisation was fundamental to determine the miscibility of the components [114]. NR data were acquired to determine the thickness of the full monolayer in the case of single components. These measurements were possible for the organic compounds available in perdeuterated forms. The hydrogenated form of the organic molecules studied are listed in Table 6.1, and details on the deuterated forms may be found in Table 5.1.

Isotherms and BAM images allowed to determine the phase behaviour of the organic molecules used in this work. For example, the maximum compression before collapse of the films was obtained and this information was fundamental to determine the amount of molecule to be spread for the NR and ellipsometry measurements. Furthermore, the assessment of the absence of anisotropy in the monolayers was crucial to investigate the surface reaction with ellipsometry as complementary lab-based technique of NR. The NR measurement of deuterated monolayers allowed to determine the thickness of the full monolayers and to assess the reliability of the estimated scattering length densities (see estimation method in Section 6.2.2). For the binary mixture, the combination of isotherms and BAM imaging provided information on the miscibility of the components and the collapsing behaviour. Again, these information were crucial to determine the suitable initial amount of molecules to be spread at the air–water interface for NR experiments. Furthermore, the understanding of the miscibility of the components in point of the BAM (Nanofilm_ep3bam, Accurion GmbH, Germany). The BAM instrument and Langmuir trough were placed on a passive anti-vibration table and enclosed in a box to avoid contamination of the monolayer and instability due to air-turbulence. The temperature of the subphase was kept at 25 °C using a water circulating bath. Millipore water (resistivity of 18.2 MΩ cm at 25 °C) was used as the subphase. The surfactants were dissolved in chloroform ($>$ 99.8 %, Sigma-Aldrich) and then spread at the clean air–water interface, which was pre-cleaned by aspiration using a pump. Once the solvent had evaporated, the compression started.

While acquiring the values of surface pressure during the compression, the BAM images were recorded. The incident and reflection arms of the BAM instrument were set to 53.1° with respect to the surface normal. The analyser was set to 10° and the polariser to 2°; the laser source had a wavelength of 532 nm. The objective was a 10× with a field of view of 400 µm and lateral resolution of about 2 µm (on a stationary sample). To record the image, the focus line was selected, and then the acquisition was carried out in ‘grab’ mode or in ‘quality’ mode (or in between). ‘Grab’ mode allows fast acquisition, with a lack of quality, because just a slice of the image is on focus; this mode is very useful when the objects at the surface move quickly as a result of, e.g., lateral Marangoni flows in the surface layer [115]. The ‘quality’ mode allows one to acquire all the field of view in focus. The image quality can be tuned, and it is proportional to the acquisition time, hence it is appropriate to use the second mode for stationary samples. Most of the images shown in the following sections were acquired using a medium quality mode.

For the experimental procedure relevant to the thickness measurement with NR, details can be found in Section 2.4. The film was prepared through the procedure described in Section 5.3.1, and the MIMIK chamber was used as the sample environment. Two neutron incident angles were used to acquire the reflectivity profile in a broad range of q (up to 0.25 Å^{-1}) and the data were analysed as described in Section 4.2.

6.2.2 Methyl oleate, MO

Figure 6.1 shows the pressure–area isotherm for hMO; the compression was carried out a hMO monolayer upon compression is 16 mN m^{-1}, and the BAM image (Fig. 6.2.b) suggests the formation of bulk liquid droplets on the surface (white spots).

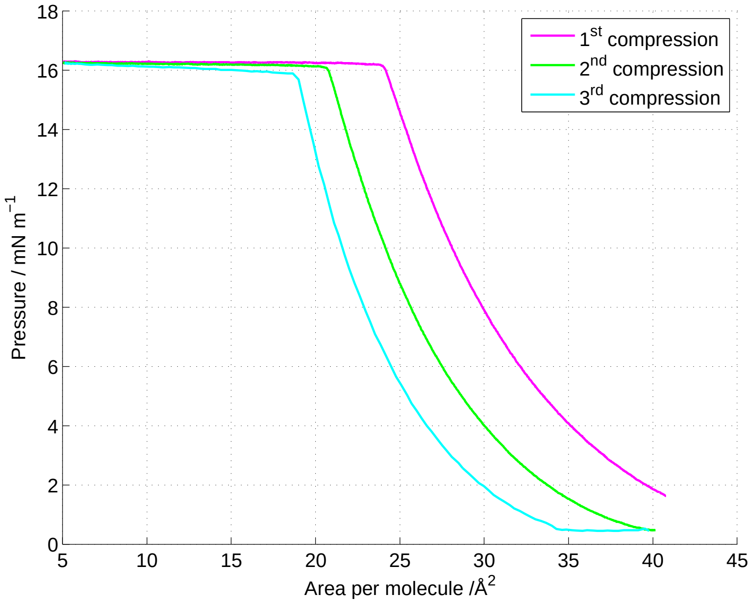

Figure 6.1: Surface pressure isotherm of hMO at 25 °C on a pure water subphase. Two further compressions of the same monolayer are also displayed.

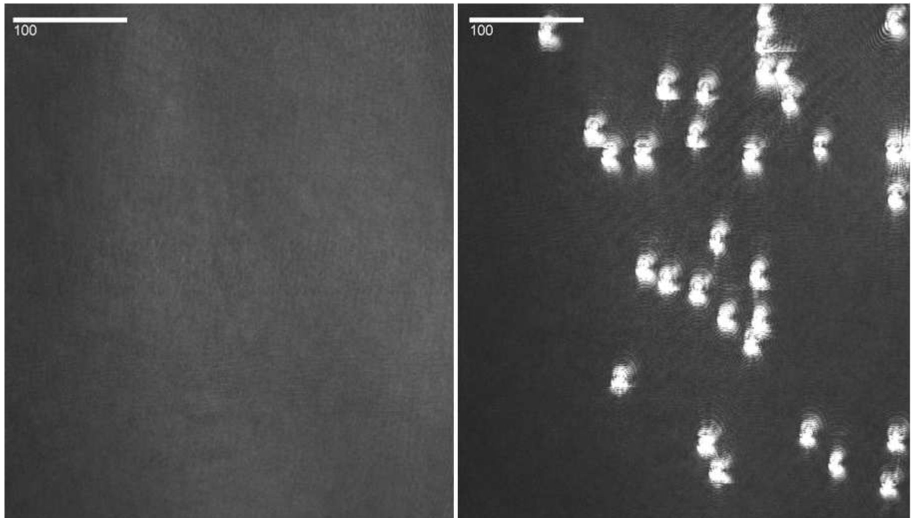

the molecules studied. These values were constrained in the fit. A fit of the R(q) profile reveals a layer thickness of 16.1 ± 0.1 Å and the solvent penetration, SP, of 1.3 ± 0.1%. The value found for SP suggests that the calculated scattering length density is reliable, in fact no mixing of chain with air or water is expected.

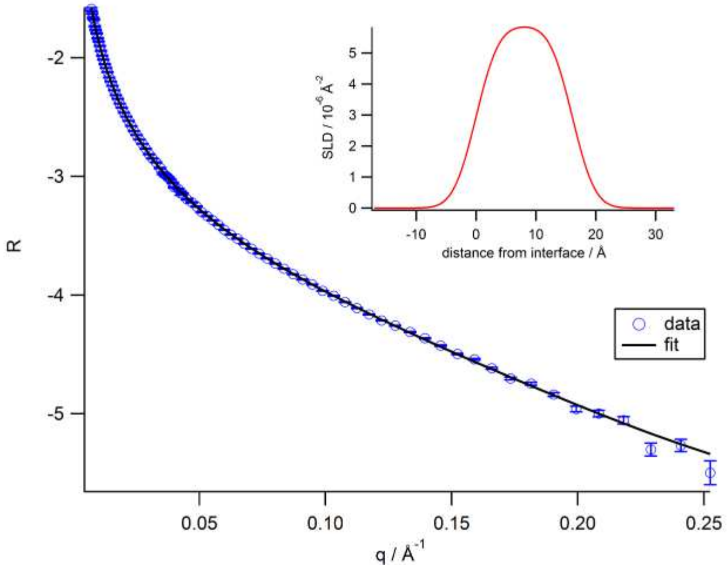

Figure 6.3: Reflectivity profile of a dMO monolayer recorded over a wide q-range. The fitting of this R(q) profile provides the layer thickness and the solvent penetration (SP).

6.2.3 Oleic acid, OA

Figure 6.4 shows the pressure–area isotherm for hOA; the compression was carried out three times. Again, the shift of the second and third isotherms on the x-axis respect to the first one indicates a loss of material during the compression; however the loss is smaller than for hMO (Fig. 6.1). The maximum pressure reached is 32 mN m^{-1}. The shape of the isotherm below that pressure is again typical of a liquid expanded phase, L_e, which suggests disordered chains. Compared to hMO, the chains can pack tighter, and probably this is due to the smaller headgroup; hOA has a COOH head and the hMO presents a COOCH. Figure 6.5 a reports the in-plane structure of the hOA film

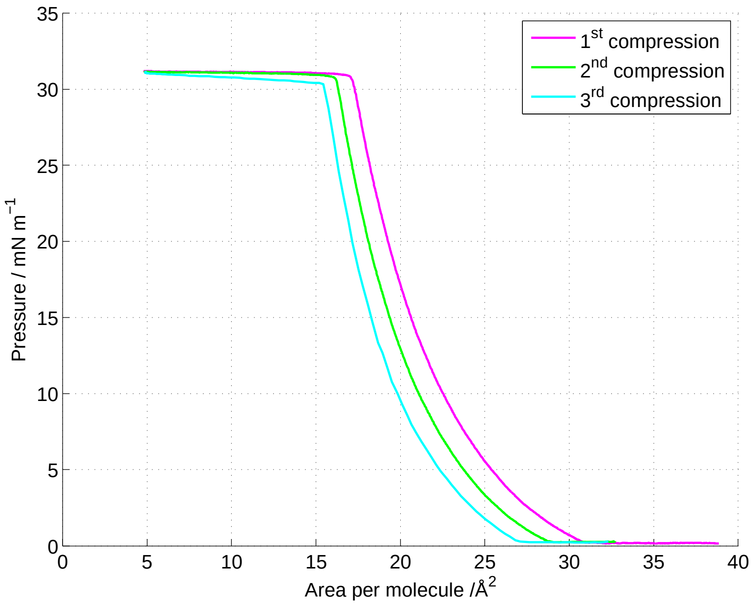

Figure 6.4: Surface pressure isotherm of hOA at 25 °C on a pure water subphase. Two further compressions of the same monolayer are also displayed.

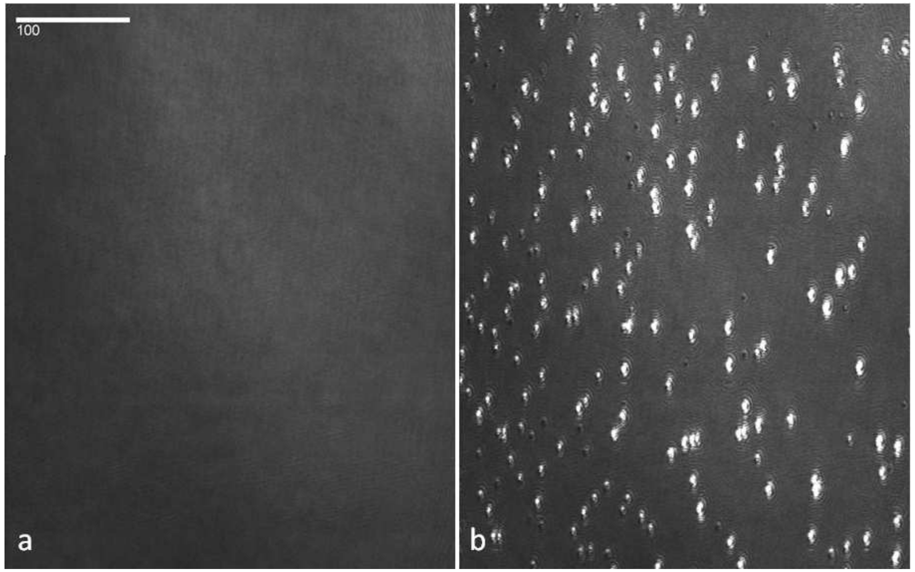

Figure 6.5: BAM images of the hOA monolayer at 25 °C on a pure water subphase recorded at two pressures: a. 3 mN m^{-1}, the layer is isotropic; b. 32 mN m^{-1}, the layer

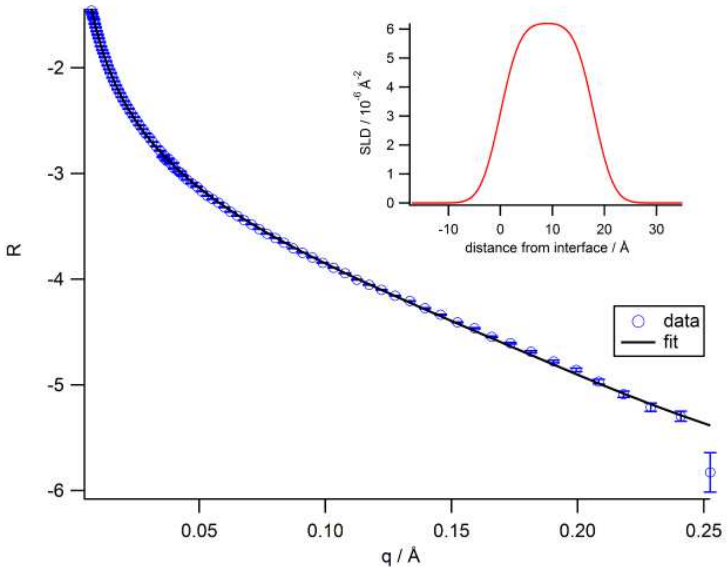

Figure 6.6: Reflectivity profile of a dOA monolayer recorded over a wide q-range. The fitting of this R(q) profile provides the layer thickness and the solvent penetration (SP).

6.2.4 Stearic acid, SA

Stearic acid is different to OA and MO, because the aliphatic chain is saturated. Figure 6.7 shows the pressure–area isotherm for hSA, the compression was carried out two times. The second isotherm overlays the first one indicating no loss of material during the compression, which was observed for hMO and hOA.

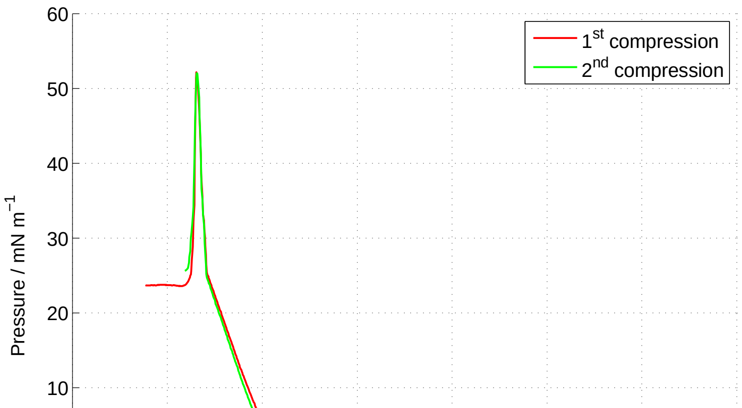

above 52 mN m^{-1} further compression leads to the collapse of the monolayer and the pressure drops dramatically to ~ 24 mN m^{-1}. Stearic acid has the same headgroup as oleic acid, but it has no carbon-carbon double bond in the chain, hence the chain can pack very tightly. Figure 6.8.a displays the in-plane structure of the hSA film at 0 mN m^{-1}, where domains with different reflection property can be distinguished. This suggests presence of various chain arrangements, hence the coexistence of gas phase and liquid condensed phase for zero pressure. At a pressure of 45 mN m^{-1} before collapse, the second BAM image (Fig. 6.8.b) suggests the formation of organised structures in the solid phase.

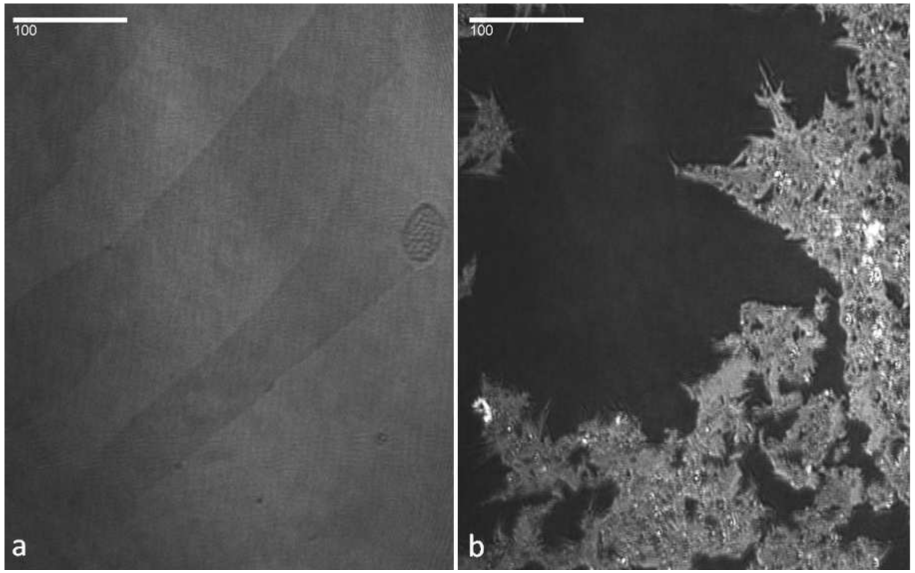

Figure 6.8: BAM images of the hSA monolayer at 25 °C on a pure water subphase recorded at two pressures: a. 0 mN m^{-1}, domains can be distinguished; b. 45 mN m^{-1}, organised structure are formed. The white bar corresponds to 100 µm.

The dSA film thickness has been measured by NR and the R(q) profile is shown in Figure 6.9. The solvent penetration was fixed to 0 %. A fit of the R(q) profile reveals a layer thickness of 21.6 ± 0.1 Å and the scattering length density of $8.1 \pm 0.1 \times 10^{-6}$ Å^{-2}. The scattering length density was not calculated following the procedure described in Section 6.2.2, because the calculation following Ref. [116] lead to an overestimation of

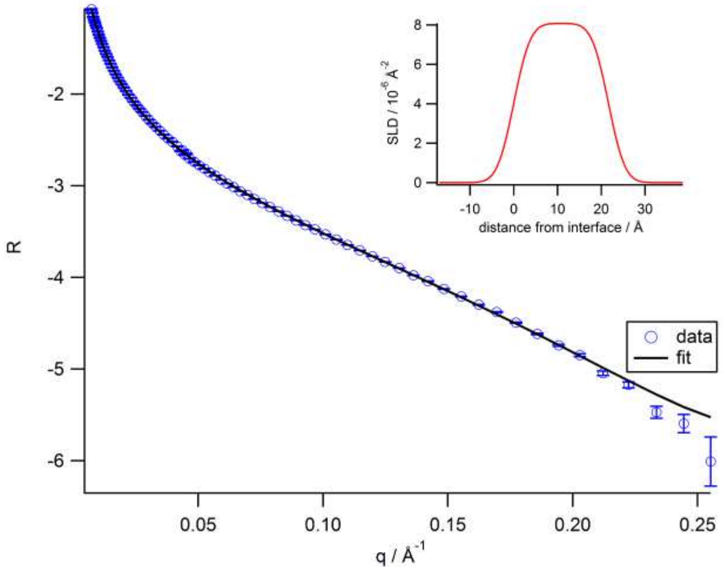

Figure 6.9: Reflectivity profile of a dSA monolayer recorded over a wide q-range. The fitting of this R(q) profile provides the layer thickness and the solvent penetration (SP).

6.2.5 Palmitoleic acid, POA

Figure 6.10 shows the pressure–area isotherm for hPOA; the compression was carried out three times. Like with the other unsaturated monolayers studied above, the shift of the second and third isotherms on the x-axis with respect to the first one indicates a loss of material during the compression.

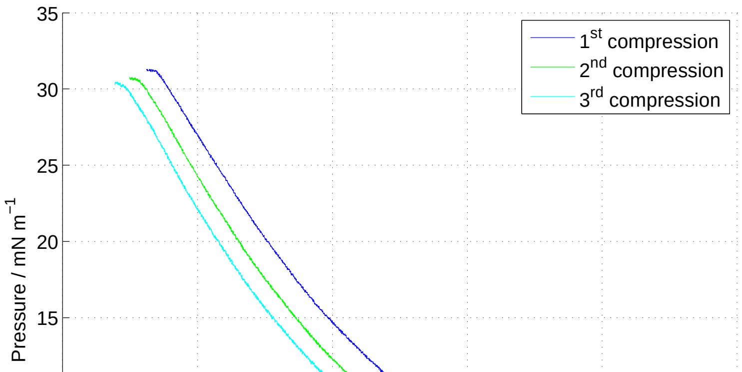

expanded phase, L_e, which suggests disordered chains. Compared to hOA, hPOA has the same structure from the headgroup to the carbon double bond, and then it is shorter by two CH_2 groups (Table 6.1). The minimum area per headgroup is larger than the one for hOA (~ 23 Å^2 vs 17 Å^2), and the pressure starts to increase before the compression required for hOA (~ 45 Å^2 vs 32 Å^2). The increase in pressure is more gradual than those observed for the previous molecules studied. Figure 6.11.a displays the in-plane structure of the hPOA film at low pressure where the layer is again totally featureless and isotropic. Unfortunately, BAM images were not taken for high pressure. It is reasonable to imagine a similar collapse behaviour as seen for hOA and hMO, since the surface pressure isotherm is smooth and no phase transitions were found as for the other unsaturated molecules.

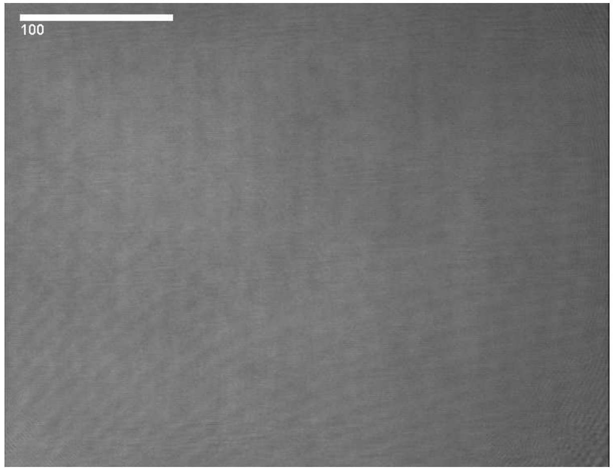

Figure 6.11: BAM images of the hPOA monolayer at 25 °C on a pure water subphase recorded at low pressure. The layer is isotropic.

The dPOA film thickness has been measured by NR and the R(q) profile is shown in Figure 6.6. The scattering length density was calculated as explained in the previous section 6.2.2 and fixed to 3.2×10^{-6} Å^{-2} (note that the lower value in this case is explained by the fact that the molecule was only partially deuterated, see Table 6.1). A fit to the R(q) profile reveals a layer thickness of 19.1 ± 0.1 Å and a solvent penetration of 21.2 ± 0.1%. The aliphatic tail of dPOA is shorter than that for dOA and dMO.

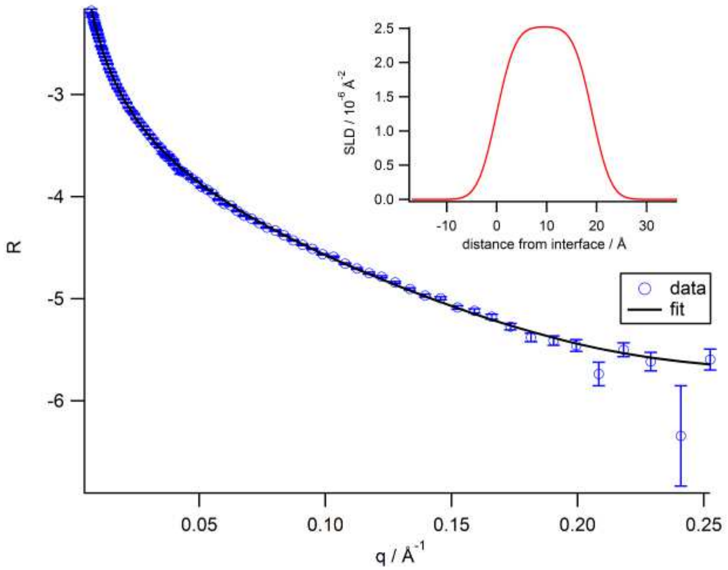

Figure 6.12: Reflectivity profile of dPOA monolayer recorded over a wide q-range. The fitting of this R(q) profile provides the layer thickness and the solvent penetration (SP).

6.2.6 Arachidonic acid, AA

Figure 6.13 shows the pressure–area isotherm for hAA; the compression was carried out three times. Again, the shift of the second and third isotherms on the x-axis with respect to the first one indicates a loss of material during the compression. The loss of material is on the same order of the loss of the other unsaturated molecules. The maximum pressure reached is 27 mN m^{-1}. Again, the shape of the isotherm below that pressure is typical of a liquid expanded phase, L_e, which suggests disordered chains. Compared to hOA, hSA and hPOA, hAA has the same headgroup but it has a longer aliphatic chain and four unsaturated C=C bonds (see Table 6.1). The minimum area per headgroup is the largest among the previous molecules (~ 27 Å^2), and the pressure starts to increase at a compression well before that in the other isotherms (~ 55 Å^2). The increase in pressure is slower than the previous molecules studied. Figure 6.14.a reports the in-plane structure of the hAA film at low pressure, the layer is isotropic and

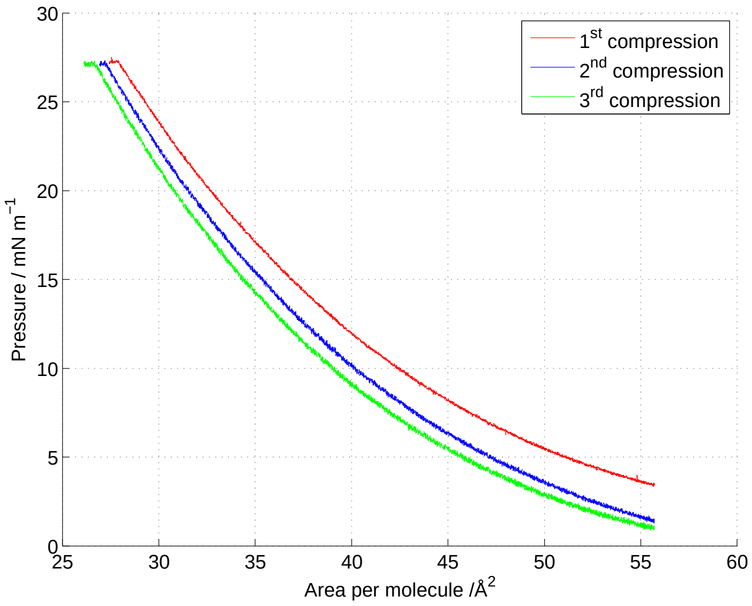

Figure 6.13: Surface pressure isotherm of hAA at 25 °C on a pure water subphase. Two further compressions of the same monolayer are also displayed.

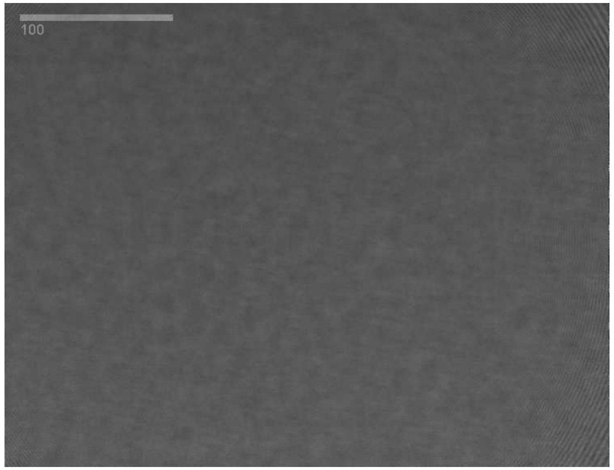

Figure 6.14: BAM images of the hAA monolayer at 25 °C on a pure water subphase recorded at low surface pressure. The layer is isotropic.

6.2.7 Binary mixtures

the miscibility of the two components at surface pressures below 22.5 mN m^{-1}. A collapsed phase (Fig. 6.16.b) results in a similar BAM image to those recorded for the single components hMO and hOA.

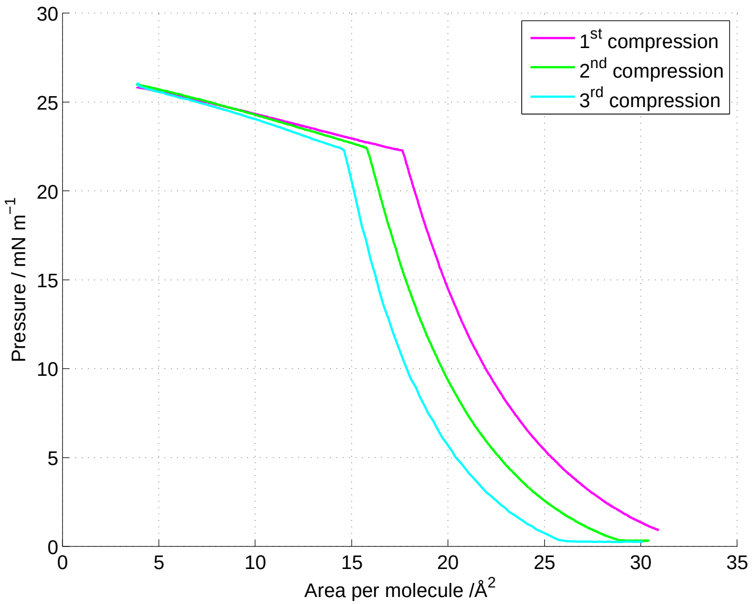

Figure 6.15: Surface pressure isotherm of the mixture (1:1 mol) of hMO and hOA at 25 °C on a pure water subphase. Two further compressions of the same monolayer are displayed.

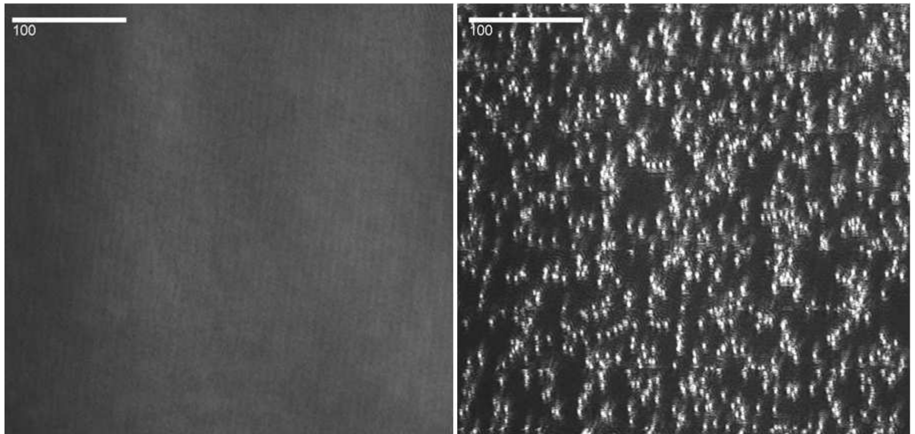

Methyl oleate and stearic acid

Figure 6.17 shows the pressure–area isotherm of the mixture hMO–hSA (1:1 mol). As for hMO, a shift on the second and third compression suggests a loss of molecules, but it is not clear why the loss is larger than what was previously observed. The overall shape of the isotherm is similar to that from a monocomponent hMO film, but the maximum pressure is slightly higher, 18 mN m^{-1}. The effect of hSA is not visible in the isotherms, probably because it would have been necessary to compress further. However, BAM images clearly show the non-miscibility of the two components at low and high surface pressure values. Figure 6.18.a, recorded at 4 mN m^{-1}, show the presence of separated domains. At the maximum compression, rod-like domains are distinguishable from a uniform background (Fig. 6.18.b), and the collapsed structure is very different to the one recorded for the single components.

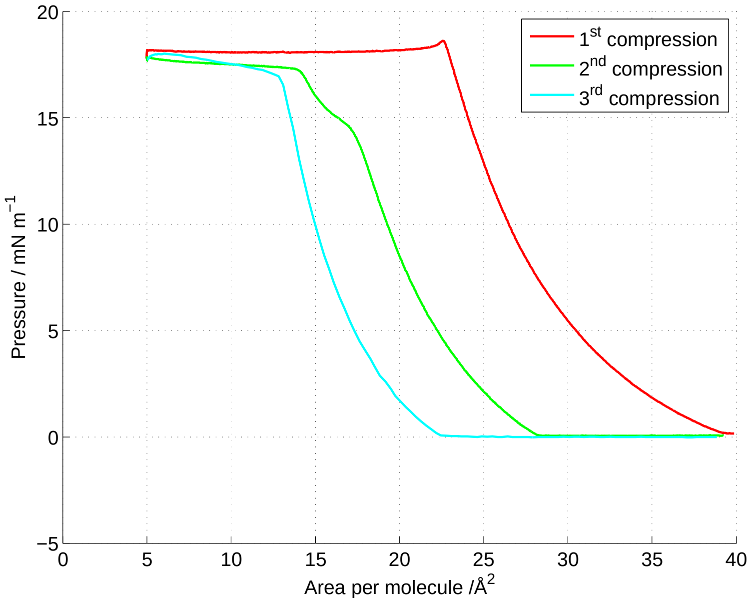

Figure 6.17: Surface pressure isotherm of the mixture (1:1 mol) of hMO and hSA at 25 °C on a pure water subphase. Two further compressions of the same monolayer are displayed.

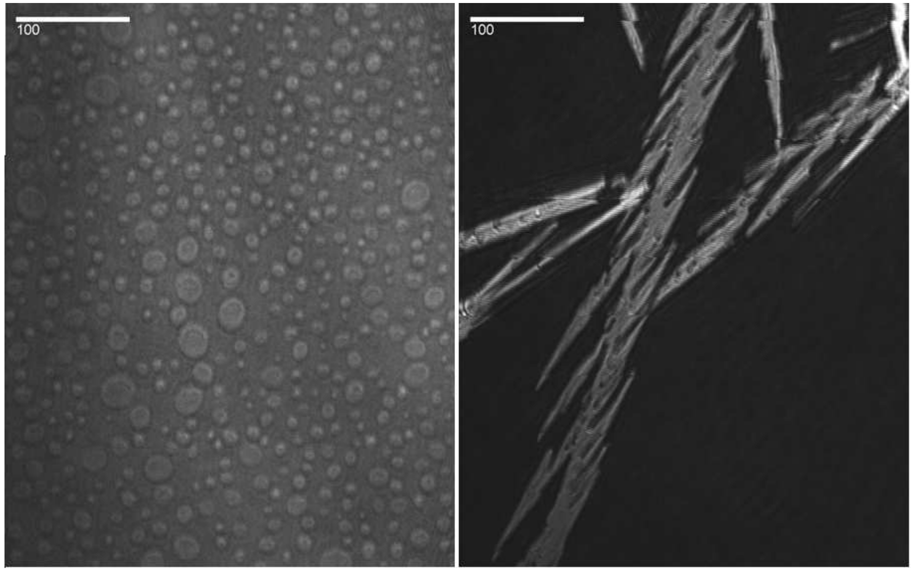

Figure 6.18: BAM images of the hMO–hSA monolayer at 25 °C on a pure water subphase recorded at two pressures: a. $4\,\mathrm{mN\,m^{-1}}$, the layer shows circular domains; b. $17\,\mathrm{mN\,m^{-1}}$, the layer collapsed and domains became rod-like (max compression). The white bar corresponds to 100 µm.

Oleic acid and stearic acid

Figure 6.19 shows the pressure–area isotherm of the mixture hOA–hSA (1:1 mol). As for the hOA, a shift on the second compression suggests loss of molecules. The shape of the first isotherm up to $32\,\mathrm{mN\,m^{-1}}$ is similar to the hOA film, and then a first small drop of the pressure is recorded before the pressure stays constant until $7\,\mathrm{\AA^2}$. Upon further compression, a steep increase and then a drop is recorded, this is a feature related to hSA. The second compression shows different features, which could be due to the presence of collapsed structures, which do not re-equilibrate during expansion. The BAM images clearly show the non-miscibility of the two components recorded at three different surface pressure values. Figure 6.20.a, recorded at $0\,\mathrm{mN\,m^{-1}}$, show the presence of separated domains. Just before the pressure plateau ($32\,\mathrm{mN\,m^{-1}}$), condensation nuclei appear while the circular domains are still visible (Fig. 6.20.b). At the maximum pressure, $40\,\mathrm{mN\,m^{-1}}$, rod-like domains are distinguishable from a

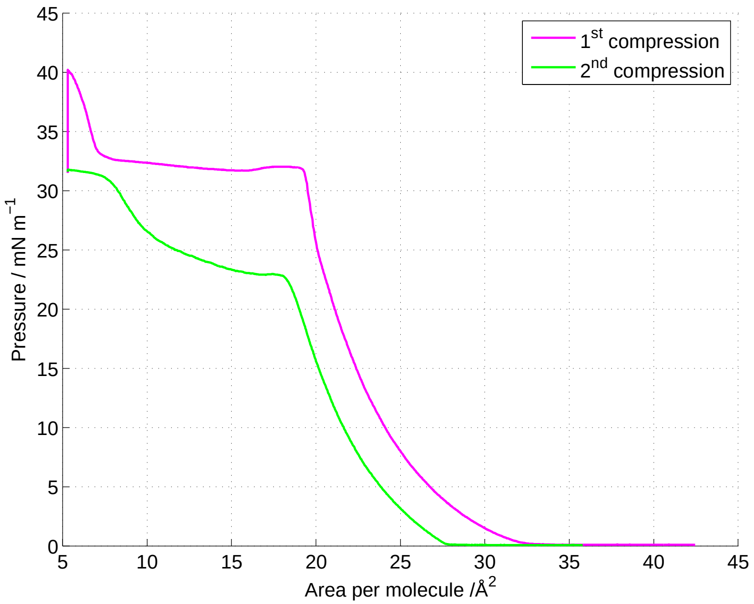

Figure 6.19: Surface pressure isotherm of the mixture (1:1 mol) of hOA and hSA at 25 °C on a pure water subphase. A further compressions of the same monolayer is displayed.

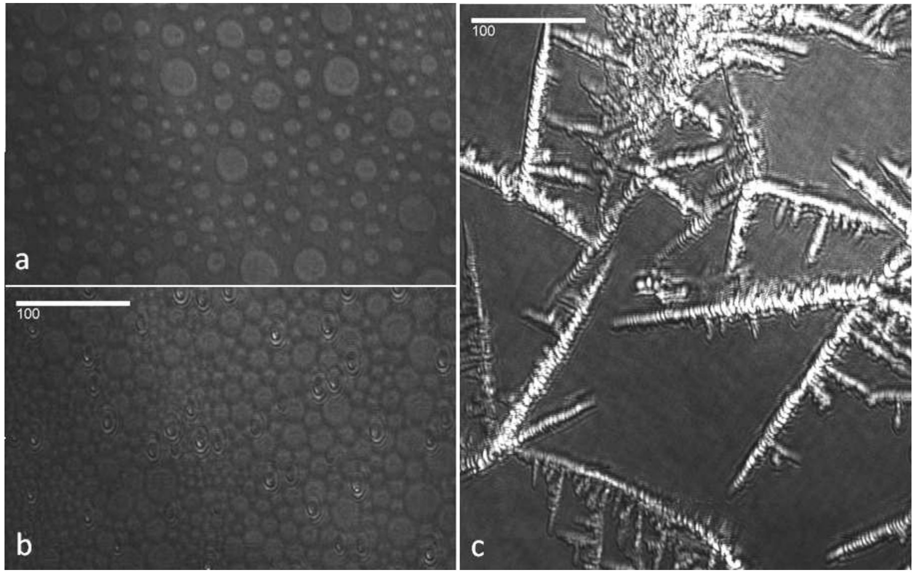

Figure 6.20: BAM images of the hOA–hSA monolayer at 25 °C on a pure water sub-

6.3 In situ production of gas oxidant

I studied the surface reaction of organic monolayer at the air–water interface initiated by O_3 and NO_3; these gas-phase oxidants were produced in situ both for the NR and ellipsometry experiments. Since the measurements of the gas concentrations was not feasible online, the gas setup was reproduced and for each reaction condition spectroscopic data were collected, which were analysed to obtain qualitative and quantitative information. The gas flow system is described in detail in Section 5.3.2.

In this chapter the spectroscopic data recorded and their analysis are described. This allowed to quantify the concentrations of ozone (O_3), nitrogen dioxide (NO_2) and nitrogen pentoxide (N_2O_5). O_3 has a strong peak in the UV-Vis region, N_2O_5 has a strong absorbance in the IR region, NO_2 absorbs in both regions. To calculate $[NO_3]$, a mathematical description of the reactions has been developed and relations between the steady-state concentrations of NO_2, N_2O_5 and NO_3 were derived.

6.3.1 O_3

The ozone is produced with a pen-ray ozoniser (UVP Ltd Pen-Ray continuous flow generator, UK). The ozone generator is a box containing two parallel tubes, one made of quartz, where the oxygen molecules can flow through and the other contains the UV lamp, which can be covered with an aluminium tube (a schematic view is shown in Figure 6.21). The quartz tube is drawn as a red rectangle, the UV-lamp as a light blue rectangle and the aluminium tube is represented as a dark blue rectangle.

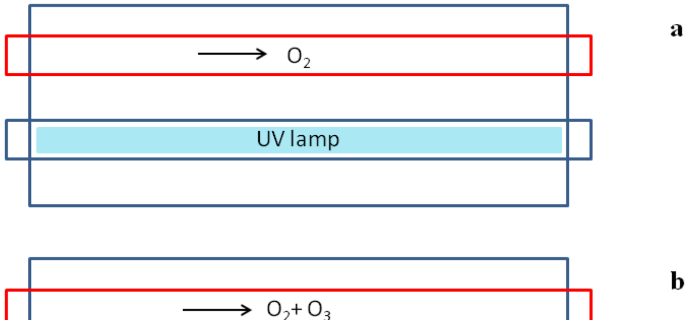

the ozone concentration for each setting of the ozoniser, the corresponding UV-Vis spectra were measured.

This paragraph gives a brief description of the experimental procedure and the resulting ozoniser calibration. The gas flow system is described in Section 5.3.2. For the measurements of the ozone concentrations, the oxygen cylinder is connected via a suitable regulator to the flowmeter, which is linked to the quartz tube of the ozoniser. A glass chamber with calcium fluoride windows is connected by Teflon tubing to the exit of the quartz tube. The gas chamber is then filled by the mixture oxygen with ozone produced by exposure of molecular oxygen to UV light. Then, the chamber is disconnected from the gas flow system and placed on the sample area of the UV-Vis spectrometer (Lambda 900, UV-Vis-NIR Spectrometer, Perkin Elmer). For each ozoniser setting, min. three UV-Vis spectra are measured , in order to obtain a mean value and error of the absorbance spectrum. The background spectrum was recorded with the gas chamber filled with pure molecular oxygen. After removing the background, the absorbance intensity at 253.8 nm was taken, and assuming an absorption cross section of $\varepsilon = 1.137 \times 10^{-17}$ cm^2 molecule^{-1} [118], the ozone concentration could be calculated using the Beer–Lambert Law:

$$[O_3] = \frac{A}{\varepsilon l} \tag{6.1}$$

where A is the absorbance, l is the path length ($l = 18$ cm) and $[O_3]$ is in molecule cm^{-3}. The measurements were recorded for two different flow rates: 0.6 dm^3 min^{-1} and 1.2 dm^3 min^{-1}. The calibration curve for those flows are shown in Figure 6.22. For both flow rates the value at 10 intervals lies below the linear trend which is due to the fact that the UV lamp is fully exposed already in between the 9th and 10th interval of the aluminium tube. For the linear fit the last point was excluded. In Table 6.2 the fitting results are reported.

Flow rate (dm^3 min^{-1})	Slope (10^{13} molecule cm^3)
0.6	2.22 ± 0.03
1.2	1.20 ± 0.02

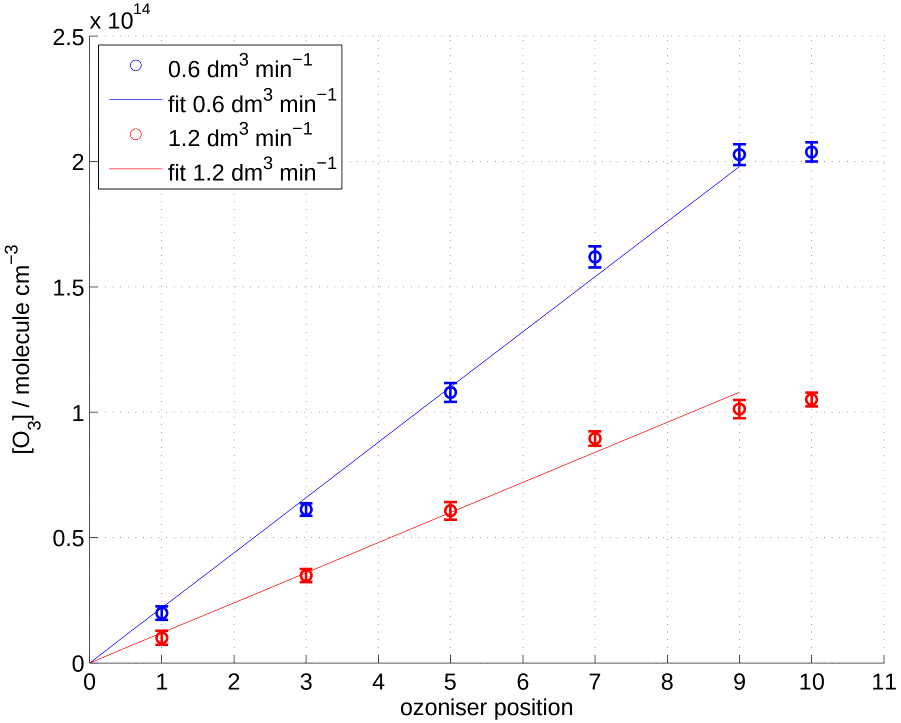

Figure 6.22: Calibration curves for the ozoniser with two different O_2 flow rates. Solid lines show the linear fit to the experimental data points. Data corresponding to x= 10 are not taken into account for the linear least squares fitting.

that the surface concentration is constant in time and is proportional to Henry's Law solubility constant,7, k_H^{cc} [119, 120]:

$$\begin{aligned} [O_3]_s &= k_H^{cc}\,[O_3]_v\,\delta && (6.2)\\ k_H^{cc} &= \frac{k_H}{0.0409}\,\text{dimensiolessr} && (6.3)\\ k_H\,(T = 298.15\,K) &= 0.48\,M\,atm^{-1} = 480\,mole\,m^{-3}\,atm^{-1} && (6.4) \end{aligned}$$

$\delta = 2\,nm$ is the surface layer thickness. The basic assumption is that O_3 from the gas phase replenishes the surface faster than the rate at which it reacts with the organic film.

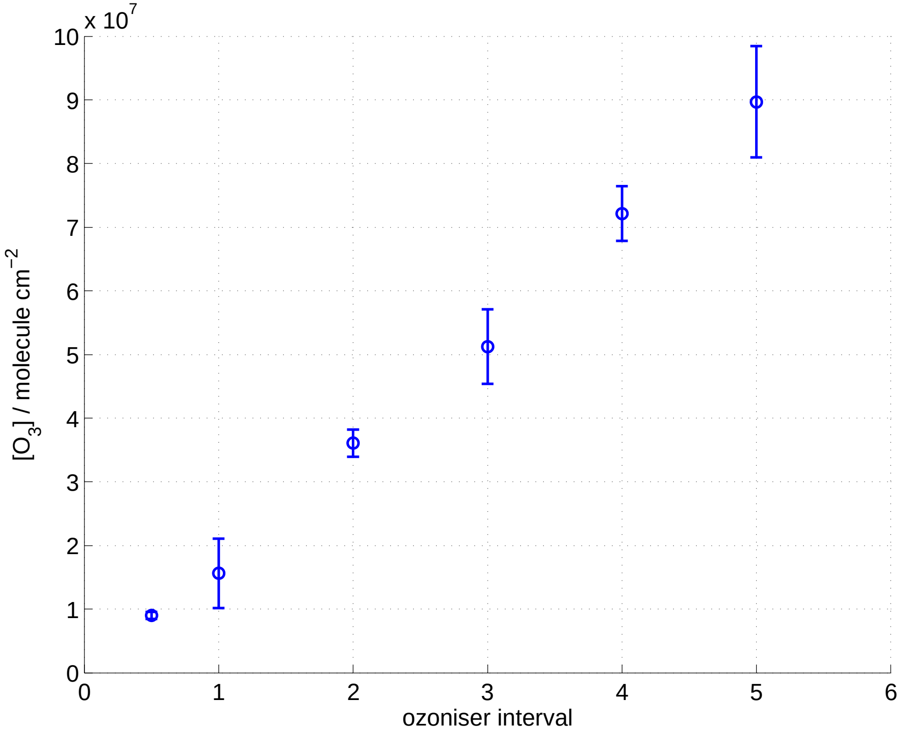

Figure 6.23: Estimated ozone surface concentration for oxygen flowing at 1.8 $dm^3\,min^{-1}$. The calibration has been extrapolated from measurements at O_2 flows of 0.6 and 1.2 $dm^3\,min^{-1}$ for low UV exposure ($x \leq 5$). Error bars were calculated by uncertainty propagation of the calibration slopes and of the flow rates.

6.3.2 NO_3

We produced NO_3 by reacting varying concentrations of NO_2 with a given ozone concentration. $[NO_2]$ is always in large excess of $[O_3]$ to ensure that all the ozone is consumed before the gas flow reaches the organic film. $[NO_3]$ could not be measured directly, but we calculated $[NO_3]$ from spectroscopic measurements of $[NO_2]$ and $[N_2O_5]$.

Reaction model

The reactions considered for description of the in situ production of NO_3 are shown below (R 6.1-R 6.3).

conditions, i.e. temperature and pressure are appropriately taken into account; the conditions chosen for the calculation are 298.15 K (25 °C) and atmospheric pressure, 1 atm). For further details on the equations 6.5-6.11 see Ref. [14]. The first reaction is a bimolecular reaction and the rate coefficient is described as:

$$k_1(T) = A \exp\left(-\frac{E}{RT}\right) \tag{6.5}$$

where $A = 1.2 \times 10^{-13}\,\mathrm{cm^3\,molecule^{-1}\,s^{-1}}$ and $E/R = 2450\,\mathrm{K}$ [37], those values are valid for temperature ranging from 230 to 360 K .

Reaction R 6.2 is a termolecular reaction and the rate coefficient, $k_2(T,[M])$, is estimated using the expression described by Troe [121]. The concentration of the third body, [M], is related directly to the pressure, in the atmosphere M is the sum of N_2 and O_2 and approximating to ideal gas we can use $[M] = N_{Av}/V_{mole} = 2.46 \times 10^{19}\,\mathrm{molecule\,cm^{-3}}$.

$$k_2(T,[M]) = \frac{k_{0;2}(T)\,[M]}{1 + (k_{0;2}(T)\,[M]/k_{\infty;2}(T))}\,0.6^{\left[1+(\log(k_{0;2}(T)[M]/k_{\infty;2}(T)))^2\right]^{-1}} \tag{6.6}$$

where $k_{0;2}(T)$ is the low-pressure limiting value for $k_2(T,[M])$ and the dependance on temperature is expressed as [14, 121]:

$$k_{0;2}(T) = k_{0;2}^{300}\left(\frac{T}{300}\right)^{-n} \tag{6.7}$$

where $k_{0;2}^{300} = 2 \times 10^{-30}\,\mathrm{cm^6\,molecule^{-2}\,s^{-1}}$ is the value at 300 K and $n = 4.4$ (valid for T in the range $200 - 300\,\mathrm{K}$), both values were taken from Ref. [37]. The $k_{\infty;2}(T)$ is the high-pressure limit value for $k_2(T,[M])$ and the dependance on temperature is expressed as [14, 121]:

$$k_{\infty;2}(T) = k_{\infty;2}^{300}\left(\frac{T}{300}\right)^{-m} \tag{6.8}$$

where $k_{\infty;2}^{300} = 1.4 \times 10^{-12}\,\mathrm{cm^3\,molecule^{-1}\,s^{-1}}$ is the value at 300 K and $m = 0.7$ (valid for temperature in the range $200 - 400\,\mathrm{K}$), both values were taken from Ref. [37].

Rate	Value
$k_1(298.15\,\mathrm{K})$	$3.2\times 10^{-17}\,\mathrm{cm}^3\,\mathrm{molecule}^{-1}\,\mathrm{s}^{-1}$
$k_2(298.15\,\mathrm{K})$	$1.18\times 10^{-12}\,\mathrm{cm}^3\,\mathrm{molecule}^{-1}\,\mathrm{s}^{-1}$
$k_3(298.15\,\mathrm{K})$	$0.06\,\mathrm{s}^{-1}$

Table 6.3: Estimation of the rate constants for the reactions R 6.1-R 6.3 in the conditions: T = 25 °C and pressure 1 atm.

where $k_{0;3}^{300} = 1.3\times 10^{-3}\,\mathrm{cm}^3\,\mathrm{molecule}^{-1}\,\mathrm{s}^{-1}$ is the value at 300 K, L = 11000 K and p = 3.5 (valid for temperature ranging from 200 to 400 K), all values stated were taken from Ref.[37]. The high-pressure limit for $k_3(T,[M])$ is expressed as:

$$k_{\infty;3}(T) = k_{\infty;3}^{300}\left(\frac{T}{300}\right)^{q}\exp(-N/T) \tag{6.11}$$

where $k_{\infty;3}^{300} = 9.7\times 10^{14}\,\mathrm{cm}^3\,\mathrm{molecule}^{-1}\,\mathrm{s}^{-1}$ is the value at 300 K, N = 11080 K and q = 0.1 (valid for temperature in the range 200 − 400 K). All the values are taken from Ref. [37].

Once all the rate coefficients are obtained for the correct conditions (Table 6.3), the differential equations describing the reactions R 6.1-R 6.3 (Eqs 6.12 - 6.15) can be solved numerically in order to obtain the concentrations as a function of time for the various chemical compound.

$$\begin{aligned}
\frac{d[O_3]}{dt} &= -k_1[O_3][NO_2] && (6.12)\\
\frac{d[NO_2]}{dt} &= -k_1[O_3][NO_2] - k_2[NO_2][NO_3] + k_3[N_2O_5] && (6.13)\\
\frac{d[N_2O_5]}{dt} &= k_2[NO_3][NO_2] - k_3[N_2O_5] && (6.14)\\
\frac{d[NO_3]}{dt} &= k_1[NO_2][O_3] - k_2[NO_3][NO_2] + k_3[N_2O_5] && (6.15)
\end{aligned}$$

I implemented the system of equations in Matlab® [101]. The solutions have been computed for several initial $[NO_2]$ values, corresponding to the gas conditions chosen for the NR, ellipsometry and IR experiments. The initial concentration of ozone was

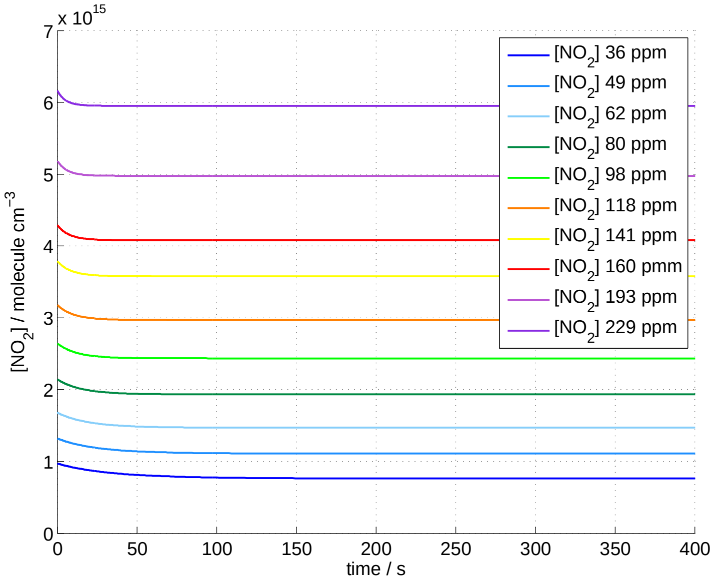

Figure 6.24: Time evolution of $[NO_2]$ calculated from the Eqs 6.12-6.15 for several initial values of $[NO_2]$. The initial $[NO_2]$ values are reported in the legend.

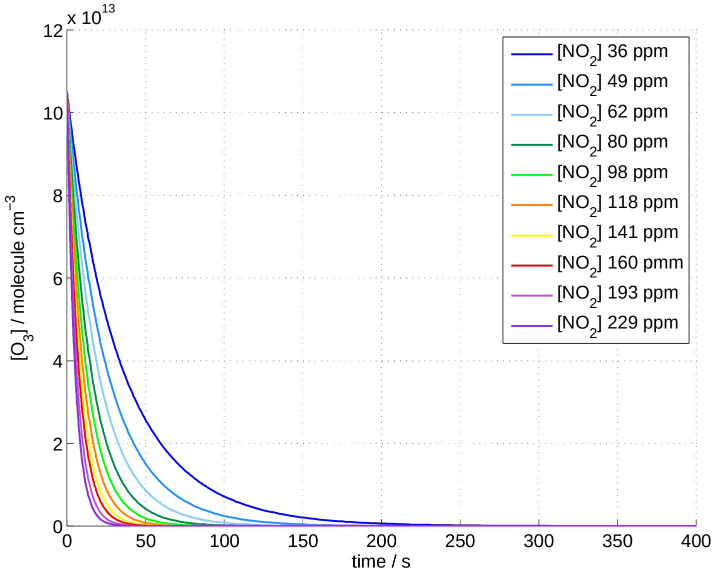

Figure 6.25: The consumption of O_3 as a function of t, calculated from Eqs 6.12-6.15 as a function of the different initial $[NO_2]$ values is displayed.

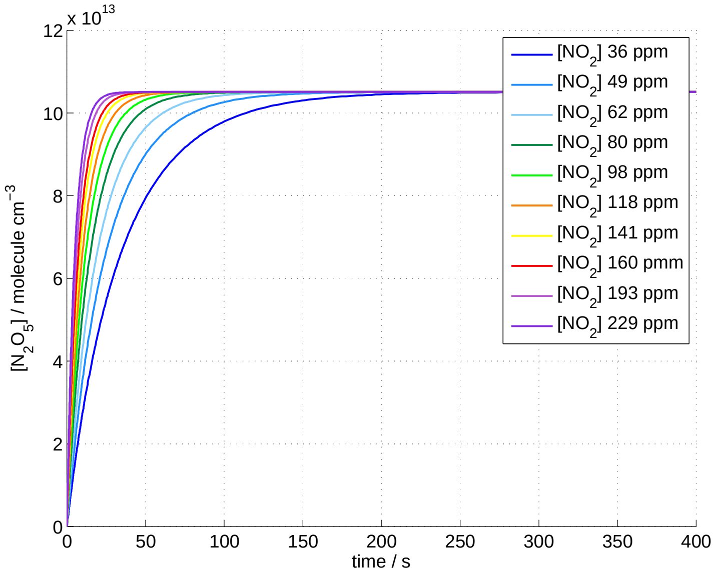

Figure 6.26: The formation of N_2O_5 as a function of t, calculated from the Eqs 6.12-6.15, is shown for several initial values of $[NO_2]$.

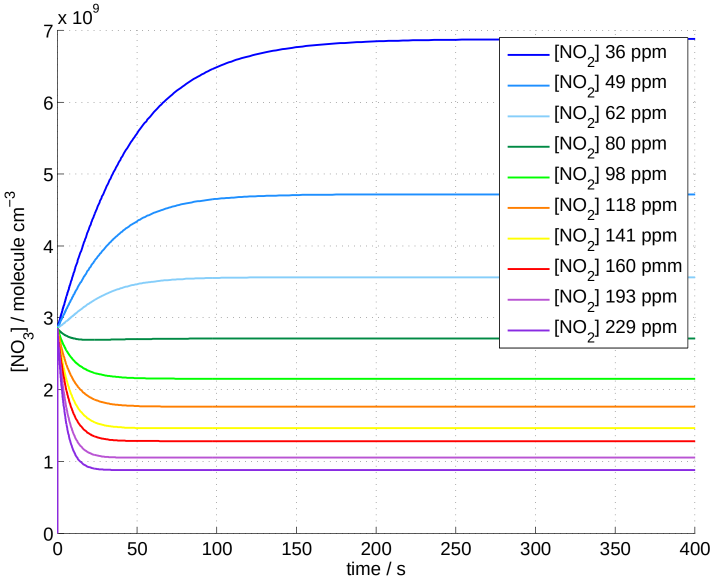

Figure 6.27: The formation of NO_3 as a function of t, calculated from the Eqs 6.12-6.15, for several initial $[NO_2]$ is shown.

the experimental data recorded with NR. In fact, during the NR experiments, the gas setup was placed outside the sample room, where the reaction chamber was placed. In extreme weather conditions in Grenoble, the temperature recorded at the gas setup was sometimes up to 5 °C higher or lower compared to the sample room temperature, which was kept fairly constant to (25 ± 2) °C.

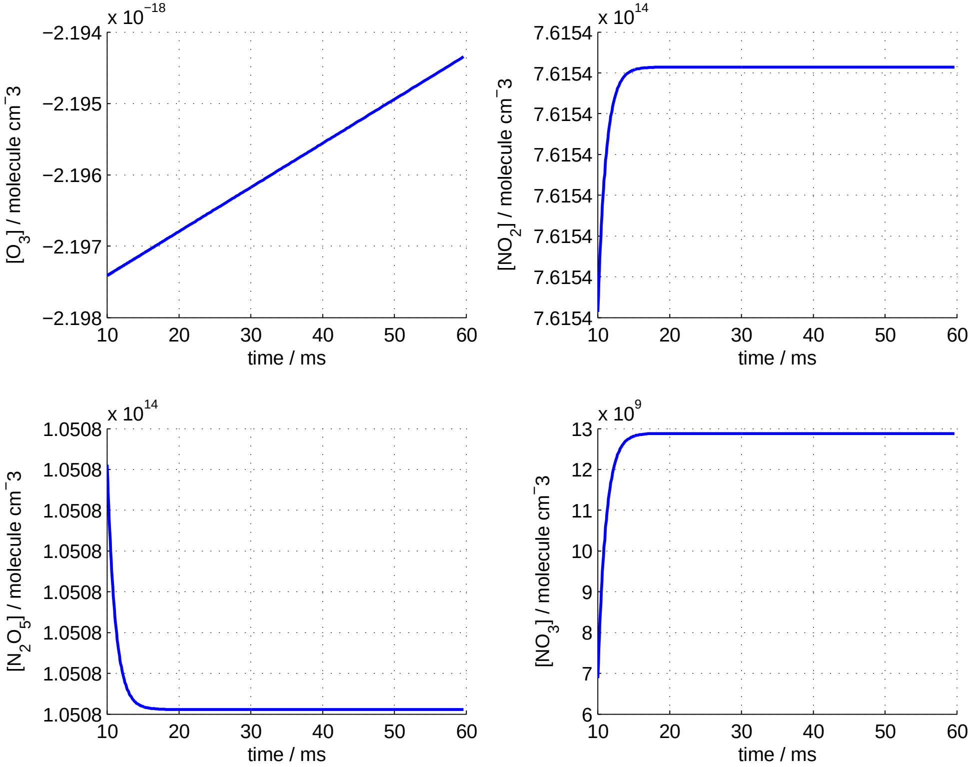

Figure 6.28: The evolution of the concentrations of O_3, NO_2, N_2O_5 and NO_3 due to temperature increase from 298 K to 303 K (initial concentration of NO_2 = 36 ppm). The equilibrium is reached in tens of milliseconds.

The development of this model provides the means to calculate the NO_3 concentration from the concentrations of NO_2 and N_2O_5. Those concentrations may be measured by IR spectroscopy. Once the reactions R 6.1-R 6.3 achieve the steady states the measured values for [NO_2] and [N_2O_5] allow calculation of the [NO_3] using the following equation:

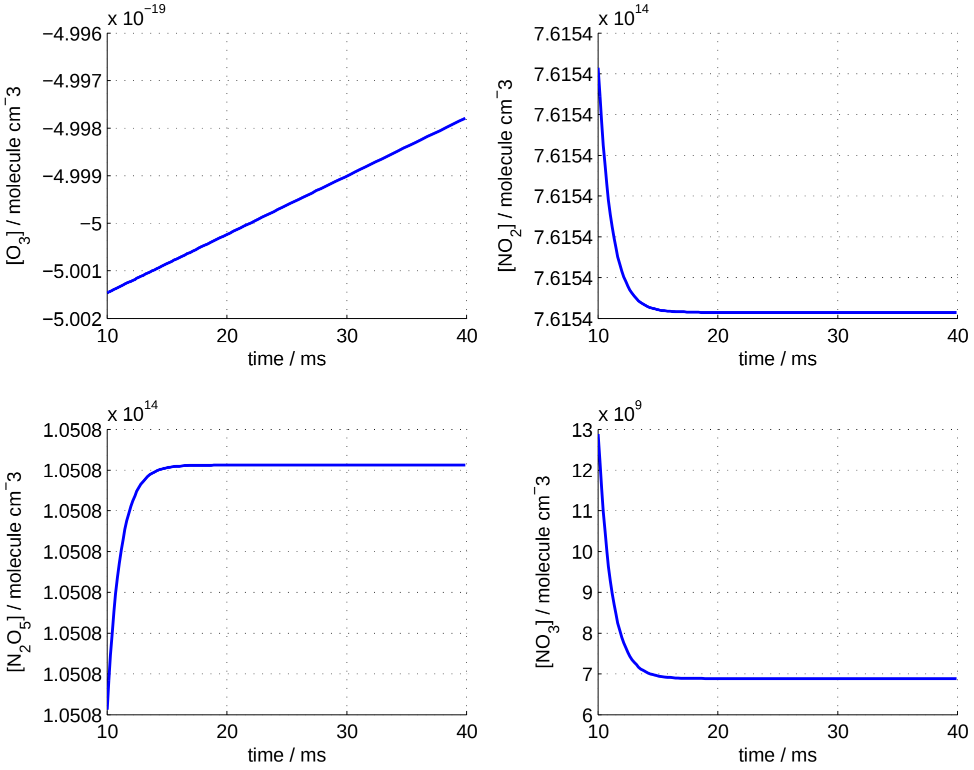

Figure 6.29: The evolution of the concentrations of O_3, NO_2, N_2O_5 and NO_3 due to the temperature decrease from 303 K to 298 K (initial concentration of NO_2 = 36 ppm). The equilibrium is reached in tens of milliseconds.

IR measurements

The measurements of the concentrations have been performed with an FTIR spectrometer (IFS/ 66 S, Bruker). For the very low concentrations to be detected, the most sensitive detector of the FTIR spectrometer was chosen which was a photoconductive detector (MCT D315). The acquired spectrum was averaged over 100 scans and the resolution was fixed to 1 cm^{-1}. The gas setup is described in detail in Section 5.3.2 and a photograph is shown in Figure 5.7. A systematic study of the gas mixture composition as a function of $[NO_2]$ was performed. $[NO_2]$ in the cylinder was 1000 ppm in air, to obtain various concentrations the flow rate of NO_2 was varied from 45 $cm^3\,min^{-1}$ to

NO_2 flow rate ($cm^3\,min^{-1}$)	[NO_2] (ppm)
45	36
62	49
80	62
104	80
130	98
161	118
197	141
228	160
290	193
360	229

Table 6.4: The flow rates of NO_2 are reported in the first column. The resulting concentrations due to mixing with O_2 flowing at $1.2\,dm^3\,min^{-1}$ are reported in the second column.

dures, e.g. flow meter settings. The gas sampling chamber used for this measurements was the same as the one for the UV-Vis study: a glass cylinder with a path length of 18 cm, and two circular CaF_2 windows of a diameter of 2.5 cm. The chamber inlet was connected to the exit of the $5\,dm^3$ mixing bulb (see Figure 5.6 and 5.7). The outlet was connected to a bubbler. For the connections Teflon tubing and either Teflon or stainless steel gas connectors were used. The flow was admitted to the chamber for 10 min, then the chamber taps were closed and the chamber was disconnected from the gas flow system. Immediately after, the chamber was placed in the sample area of the spectrometer and the measurements were recorded. Once the $NO_2 - O_2$ mixture was measured, the glass chamber was connected again to the gas flow system and the O_2 was exposed to UV light, after 10 min, the glass chamber filled with the mixture $NO_2 - O_2 - N_2O_5$ was again put into the IR measurement area and the data were acquired. Background measurements were recorded with the chamber filled with pure oxygen. The spectral contribution of the atmospheric gases, H_2O and CO_2, was eliminated with the atmospheric compensation routine of the FTIR instrument software. The treatment of the data has been performed with the software provided with the instrument (OPUS 5.5, Bruker). In order to obtain the absorbance due to the inves-

[124, 125]. Initially, I did not expect to measure HNO_3, since the gas flow system was considered to be in dry conditions. The spectra show clearly the presence of HNO_3 which can be attributed to the reaction between N_2O_5 and water. For this reason, the peak at $1700\,cm^{-1}$ has not been used to quantify N_2O_5, because it overlapped with the peak due to nitric acid. The absorbance intensity at $1250\,cm^{-1}$ was used to obtain $[N_2O_5]$ with an absorption cross section of $1.81 \times 10^{-18}\,cm^2\,molecule^{-1}$ [123]. As

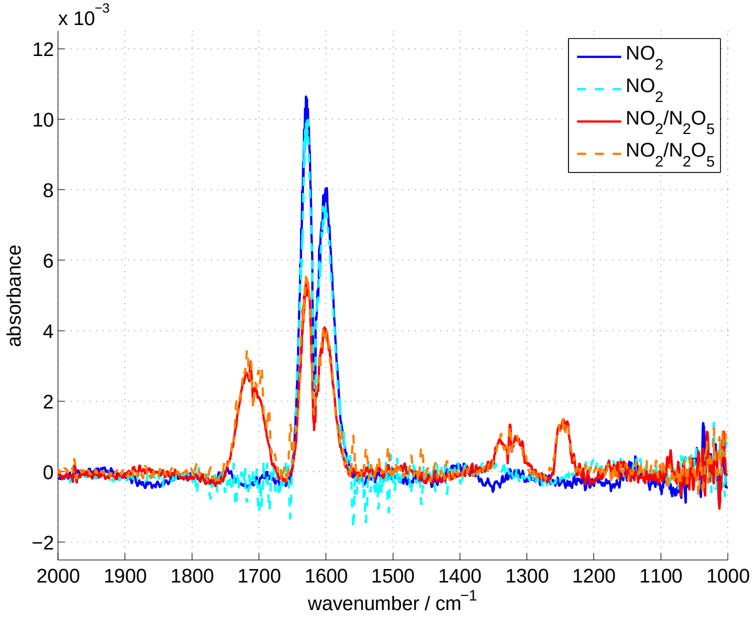

Figure 6.30: Absorbance spectra recorded with FTIR spectroscopy. The concentration of NO_2 was 36 ppm. The blue solid line and the light blue dashed line represents the spectra recorded for NO_2 carried by O_2. The red solid line and the orange dashed line refer to the spectra recorded for the mixture of $NO_2 - N_2O_5$ produced by the reactions R 6.1-R 6.3 and carried by O_2. The background and baseline subtractions have been performed using the OPUS software.

found with the theoretical calculation, the concentration of N_2O_5 is not varying as a function of the NO_2 initial concentration (see Fig. 6.33). The value obtained is about half of what the model predicted (see Fig. 6.26). Since the ozone production is fairly stable and reproducible, we suggest that this reduced N_2O_5 can be explained by the

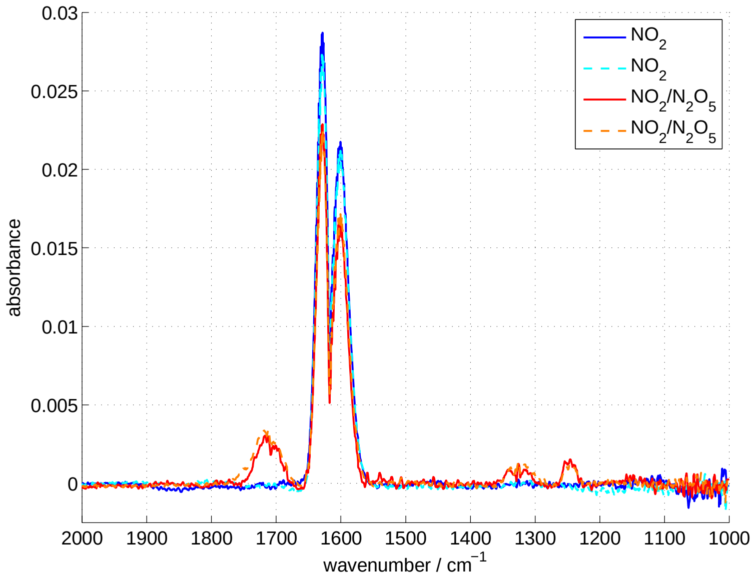

Figure 6.31: Absorbance spectra recorded with FTIR spectroscopy. The concentration of NO_2 was 98 ppm. The blue solid line and the light blue dashed line represent the spectra recorded for NO_2 carried by O_2. The red solid line and the orange dashed line refer to the spectra recorded for the mixture of $NO_2 - N_2O_5$ produced by the reactions R 6.1-R 6.3 and carried by O_2. The background and baseline subtractions have been performed using the OPUS software.

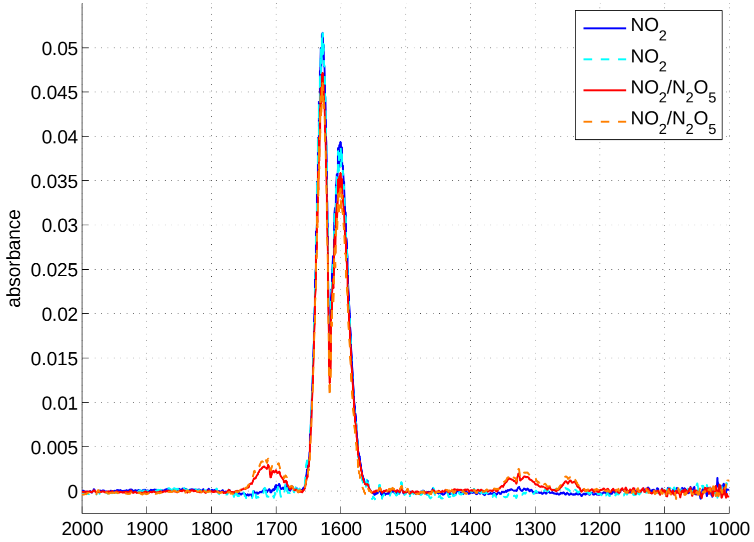

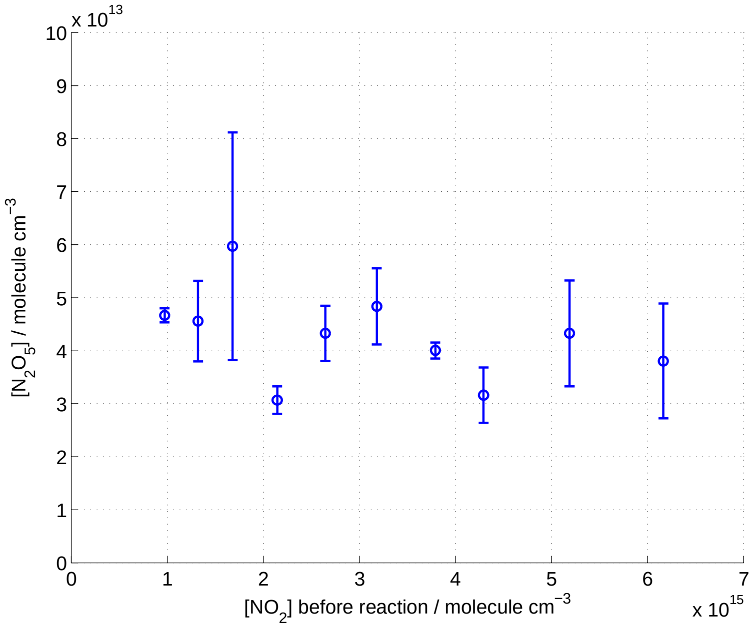

Figure 6.33: The concentration of N_2O_5 produced in reactions R 6.2-R 6.3 is shown as a function of the initial concentration of NO_2. The concentration has been calculated from the intensity of absorbance peak centered at 1250 cm^{-1}. The production is almost constant since it is due to the $[O_3]$, which is kept constant.

peak near 1600 cm^{-1} and $\varepsilon_{NO_2}(1628\,cm^{-1}) = (5.57 \pm 0.05) \times 10^{-19}\,cm^2\,molecule^{-1}$ for the peak near 1628 cm^{-1}.

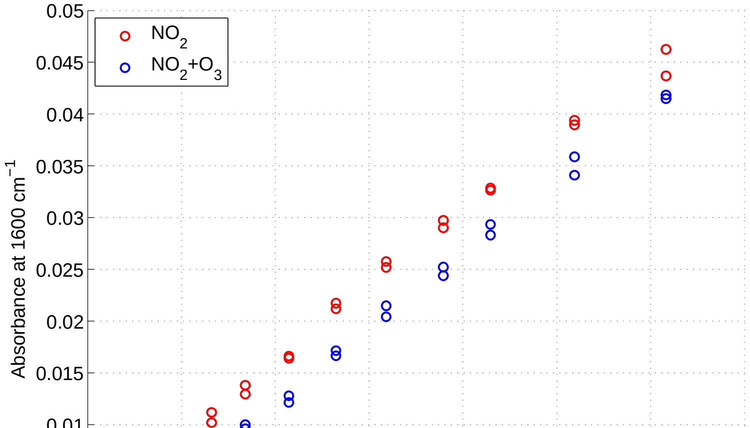

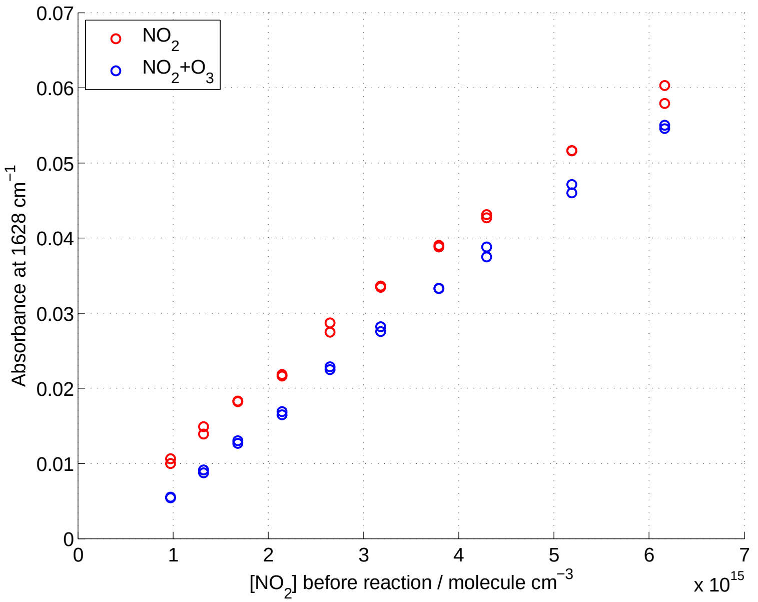

Figure 6.35: Intensity of the absorbance peak around 1628 cm^{-1} as a function of the initial [NO_2]. Blue circles represent NO_2 mixed with O_3, red circles represent the NO_2 not exposed to O_3.

is almost constant as a function of the initial concentration (Figures 6.36 and 6.37). The NO_2 loss measured is about four times the initial O_3 concentration, hence it is double of the value expected from the model ($\sim 2.1 \times 10^{14}$ molecule cm^3). In the model the equilibrium between NO_2 and N_2O_4 was not considered, and hence this may account for the extra loss of NO_2 recorded. Furthermore, other minor reactions were not taken into account in the model, such as the NO_2 photolysis and the heterogeneous reaction on NO_2 with liquid water [126].

Even if other reactions were found to affect the final concentrations of NO_2 and N_2O_5, the amount of NO_3 produced is determined by the reactions R 6.2-R 6.3, which control the equilibrium within the $NO_2 - N_2O_5 - NO_3$ system, hence [NO_3] can be calculated using Equation 6.17. The concentration of NO_3 is shown in Figure 6.38 as a function of the initial [NO_2]. [NO_3] ranges from 13 ppt to 160 ppt, which is representative for atmospheric conditions [127]. Any loss of NO_3 due to reactions different from the

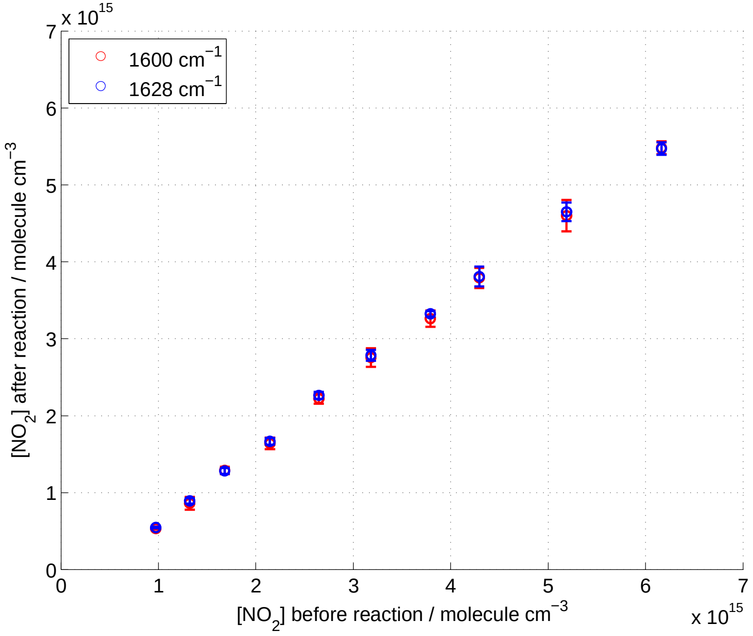

Figure 6.36: The concentration of NO_2 after the reaction with O_3 is shown as a function of the initial concentration of NO_2. The concentration has been calculated separately for each absorbance peak (red for $1600\,cm^{-1}$, blue for $1628\,cm^{-1}$).

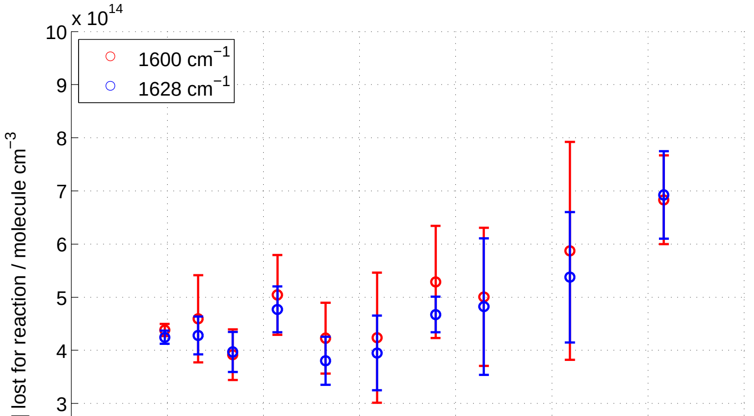

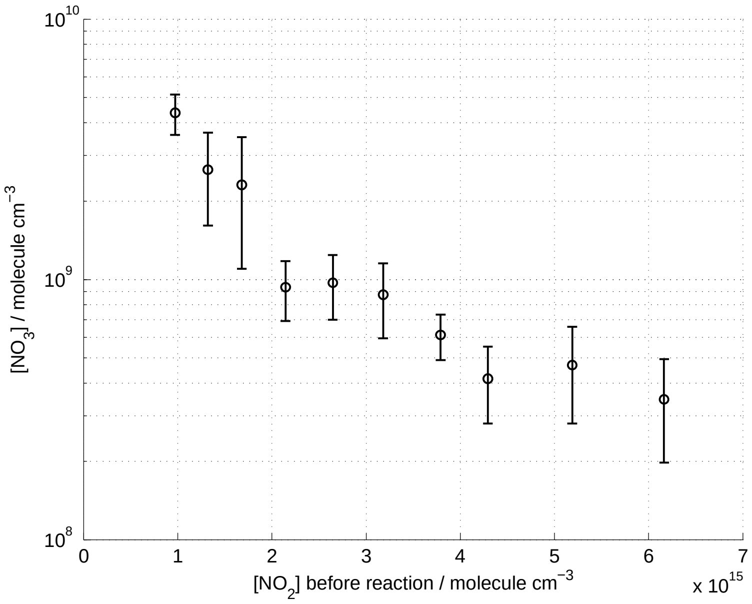

Figure 6.38: The concentration of NO_3 produced in reactions R 6.1-R 6.3 and calculated from Eq. 6.17 is shown as a function of the initial concentration of NO_2. As expected, the NO_3 production decreases as $[NO_2]$ increases.

Chapter 7

Kinetic experiments of pure organic monolayers

7.1 Introduction

In this chapter the kinetic experiments performed with the single component monolayers are presented. The results of the kinetic analysis are discussed. The surface excess as a function of time is obtained both from NR and ellipsometry measurements. The results obtained by the two technique are compared.

Each section describes the surface oxidation kinetics of the single component film. The MO oxidation is presented both for O_3 and for NO_3. All the other molecules (OA, SA, POA and AA) were exposed just to NO_3.

The main objectives of these studies are summarised here.

- To obtain the kinetic parameters specific to the heterogeneous reaction driven by gas phase oxidants O_3 and NO_3.
- To examine whether the lab-based ellipsometry technique is a reliable substitute to NR in the investigation of surface reactions.
- To investigate the effect of chain length, degree of chain unsaturation and head-

7.2 Methyl oleate exposed to O_3

The present section concerns the oxidation kinetics and fate of MO monolayers at the air–water interface that are exposed to O_3. The aims are to determine the second-order rate coefficient for the loss of organic material from the interface, to rationalise the importance of bulk oxidation of methyl esters, to examine whether any organic material remains at the air–water interface, and to assess the atmospheric impact of these processes.

The investigation by NR of this system was performed with the original, large reaction chamber. This chamber had a gas volume of ~ $25\,\mathrm{dm^3}$ and it contained a commercial Langmuir trough equipped with a pressure sensor (Mini PS4, Nima, UK). The total flow rate used was $15\,\mathrm{dm^3\,min^{-1}}$. A carrier O_2 flow of $10\,\mathrm{dm^3\,min^{-1}}$ was mixed with a O_2 flow of $5\,\mathrm{dm^3\,min^{-1}}$ passed trough the ozoniser. The ozoniser calibration for this flow rate was provided by Christian Pfrang, and further details may be found in Ref. [33]. The dMO was provided by the Oxford Deuteration Facility and was dissolved in chloroform, as described in Section 5.3.1; however the monolayer was formed by compression of the barriers until a pressure of $7\,\mathrm{mN\,m^{-1}}$ was reached.

The other experimental data presented in this section and in the following ones were acquired using the MIMIK chamber and its custom-made trough without barriers (Chapter 5). The sample preparation has been described in detail in Section 5.3, where information about the gas-phase oxidant production may also be found.

7.2.1 NR

Figure 7.1 shows surface excess decays of dMO monolayers at the air–ACMW interface as a function of time with respect to ozone gas-phase concentration, $[O_3]_v$. Independent of the value of $[O_3]_v$ used, the reactions remove more than 90 % of the organic layer from the air–ACMW interface. The chemical purity of dMO in terms of surface-active deuterium-containing molecules is estimated to be not less than 95 %. In light of the dMO purity, the reaction is ~ 95 % efficient in removing the organic layer. Data recorded with a different batch of dMO showed a removal of the organic monolayer

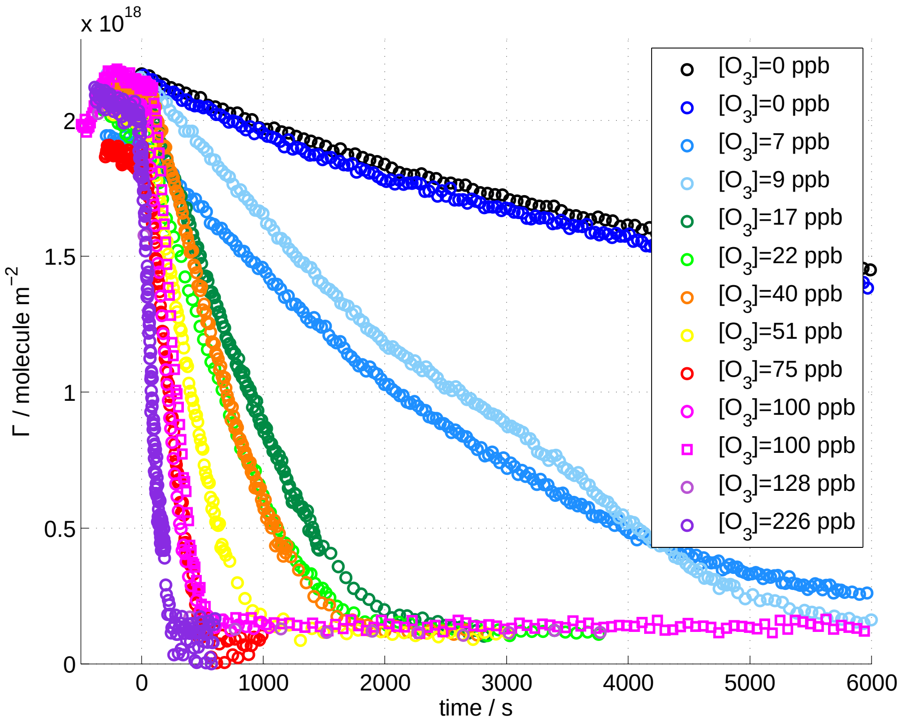

Figure 7.1: Surface excess decays of dMO monolayers exposed to different $[O_3]_v$; mean concentration values are displayed in the legend (subscript 'v' is omitted). 1 ppb = 2.7×10^{10} molecule cm^{-3} and following Smith et al. [120] we assumed it corresponds to $[O_3]_s$ of 6.35×10^4 molecule cm^{-2}. Surface excess values were obtained from NR data. Time t = 0 s represents the start of the O_3 exposure. Data are shown without error bars for clarity. The relative errors are on the order of 1 %.

molecules reorient and lie down at the interface. This process may alter the accessibility of the reaction site (the C = C bond) and introduce errors into the fits. The cutoff value of the surface excess 7×10^{17} molecule m^{-2} for the organic film was calculated considering the measured area per molecules, its molecular volume [116], and the assumption that the shape of the molecules can be approximated to a cylinder.

Figure 7.2 shows the values of k_1 obtained experimentally as a function of the O_3 surface concentration, $[O_3]_s$, demonstrating a clear linear relation. An orthogonal distance regression fitting procedure weighted by the uncertainties both of k_1 and

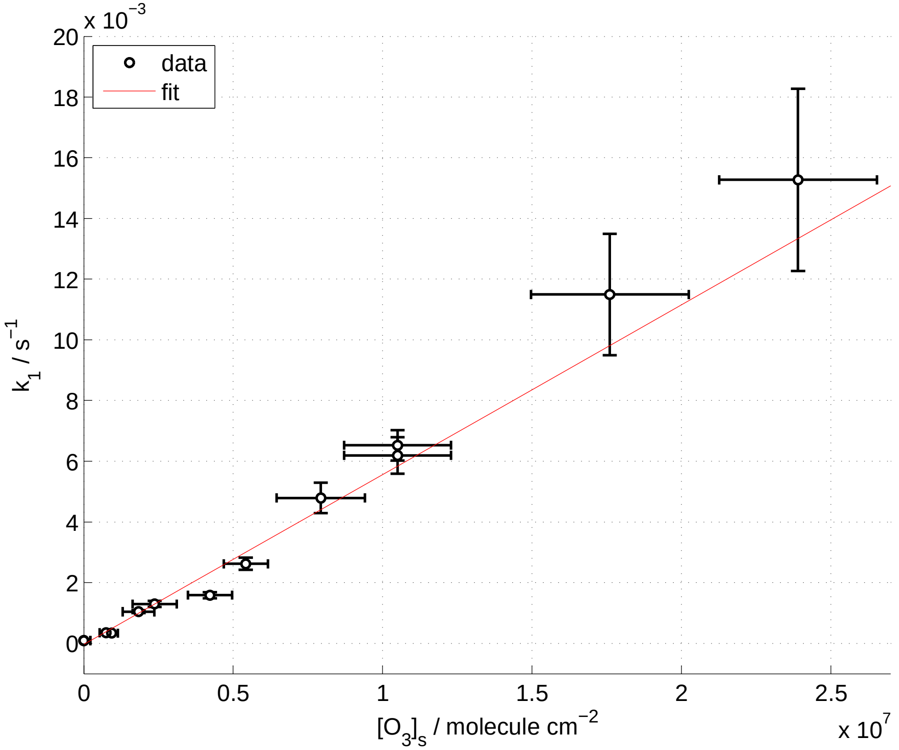

Figure 7.2: Pseudo-first order rate coefficients for dMO at the air–ACMW interface, k_1, as a function of the ozone surface concentration, $[O_3]_s$. The data points and error bars represent experimental data and associated uncertainties at one standard deviation. The solid line corresponds to an orthogonal distance regression fit weighted by the uncertainties both in k_1 and $[O_3]_s$.

7.2.2 Ellipsometry

The oxidation of hMO exposed to O_3 has been investigated with ellipsometry using the MIMIK chamber as the reaction chamber and following the experimental procedures described in Section 5.3. The ellipsometric data were analysed according to the approach defined in Section 3.3.3. This data analysis approach is based on the assumption that the organic layer has a unique refractive index and a uniform thickness. While the reaction is occurring, products may form. Even if they are not stable at the air–water interface, they may not be lost instantaneously (by volatilisation or solubili-

signal [73], this is why the minimum surface excess value is higher for ellipsometry.
Figure 7.3 shows the hMO surface excess for several O_3 conditions as a function of time. The two slowest decays, $[O_3] =$ 247 ppb and $[O_3] =$ 143 ppb, show a monotonic decrease of the surface excess until 1×10^{18} molecule m^{-2}. Below this value, the overall slope changes slightly and some fluctuations, i.e. spikes in surface excess, appear. Those spikes are well above the experimental errors, hence they may be related to product formation at the air–water interface. The spikes are not reproducible in time; see comparison of the repeats in Fig. 7.3. These fluctuations may be related to lateral inhomogeneities moving in and out of the laser beam in time. Furthermore, they could be due to formation of domains of products in a different phase, and hence a different refractive index. This suggests that the organic layer below the surface excess of 1×10^{18} molecule m^{-2} is not optically uniform anymore.

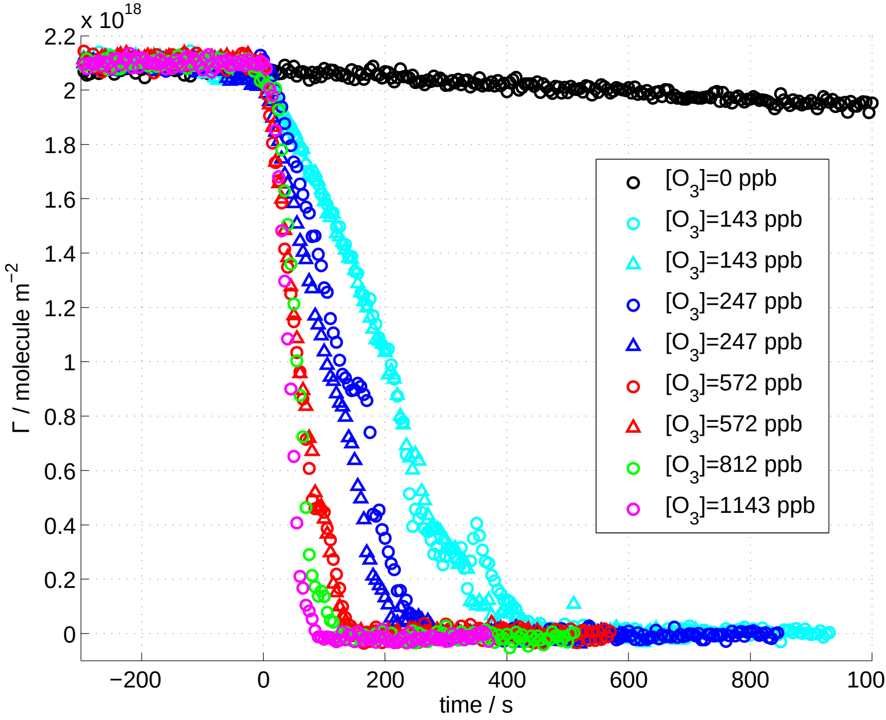

Figure 7.3: Surface excess for hMO monolayers measured by ellipsometry. The oxygen flow rate was fixed to 1.8 $dm^3\,min^{-1}$ and the setting of the ozoniser was vari-

reaction chamber.

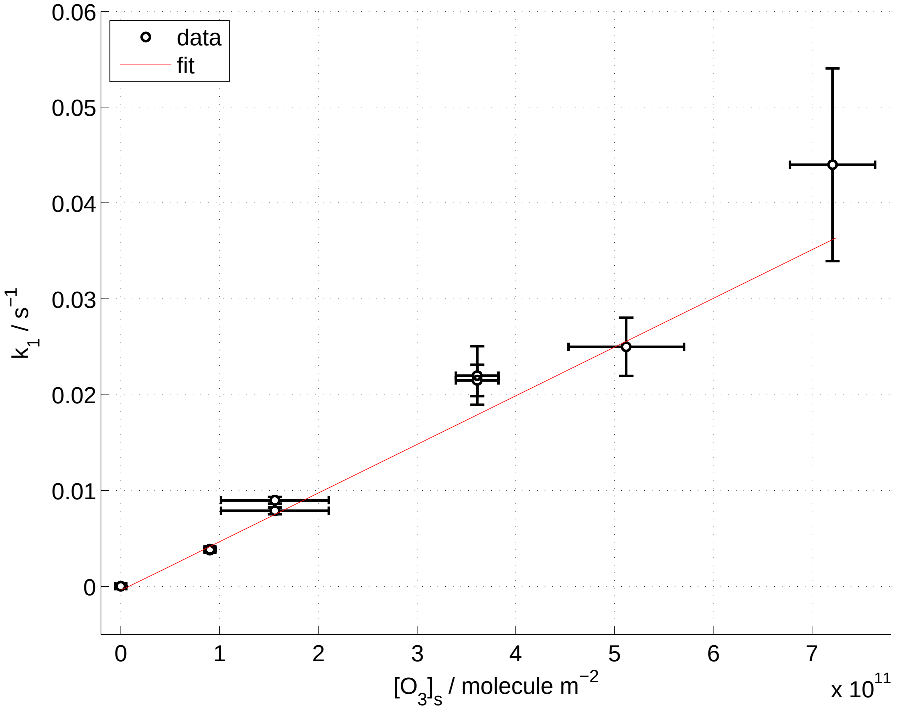

Figure 7.4: Pseudo-first order rate coefficients for hMO at the air–water interface, k_1, as a function of the ozone surface concentration, $[O_3]_s$. The data points and error bars represent experimental data and associated uncertainties at one standard deviation. The solid line corresponds to an orthogonal distance regression fit weighted by the uncertainties both in k_1 and $[O_3]_s$.

7.3 Oleic acid exposed to NO_3

The present section concerns the oxidation kinetics and fate of OA monolayers at the air–water interface that are exposed to NO_3. The organic film was prepared as described in Section 5.3.1 and the gas conditions were changed according to the procedure explained in Section 5.3.2. Experimental data were recorded using the MIMIK chamber either on FIGARO with a dOA (see Table 5.1), or on the ellipsometer with the hOA. The two sets of surface excess data were analysed independently in order to gain information on the kinetic parameters.

The kinetic model applied to both data sets was based on the same assumptions, while the product yields were estimated from the plateau values of Γ measured with NR. The differential equations describing the reaction kinetics were solved numerically and the resulting function was used to fit the experimental data (a detailed description of the model may be found in Section 4.3.2). The fitting has been performed in two ways. $\Gamma(t)$ recorded for different $[NO_3]$ were fitted simultaneously, hence the kinetic parameters (e.g. rate constant, desorption lifetime, etc.) were forced to be the same for all gas conditions; the superscript ‘multi’ in the tables indicates the simultaneous fit. The other approach was to fit each single $\Gamma(t)$ individually (indicated by superscript ‘sing’ in the tables), which led to a set of kinetic parameters for each oxidant condition. A comparison of the two fitting approaches is presented, and the kinetic parameters obtained from NR and ellipsometry data are also compared.

7.3.1 NR

Figure 7.5 shows the surface excess decays of dOA monolayers at the air–ACMW interface as a function of time with respect to $[NO_3]$. The reaction lead to a non-zero surface excess value, $\sim 5 \times 10^{17}$ molecule m^{-2}, at the end of the reaction. This plateau value is reached after an initial decay, which lasts between $\sim$ 5 minutes and over 2 hours depending on the oxidant conditions. $[NO_3]$ ranges from (15 ± 5) ppt to (86 ± 45) ppt. For some of the gas conditions, the monolayer oxidation was carried out two or three times with the same gas concentration, presenting a reasonable reproducibility for high

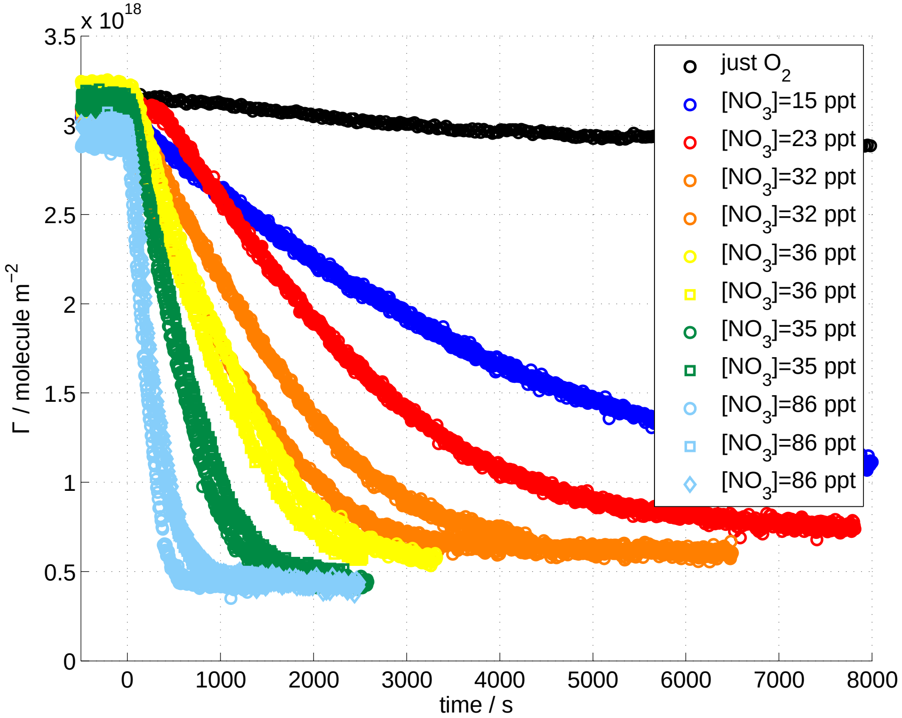

Figure 7.5: Surface excess decays of dOA exposed to different [NO_3]; mean values are displayed in the legend (1 ppt = 2.7×10^7 molecule cm^{-3}). Data were recorded with NR. Time t = 0 s represents the start of the exposure. Data are shown without error bars for clarity. The relative errors are on the order of 1 %.

line) for high [NO_3], while for low [NO_3] the resulting fits are both acceptable. This difference will be found for all the data presented hereafter, and it is due to the χ^2 calculation and minimisation in the simultaneous fit. In fact, the χ^2 is calculated for each data point and the sum of all the χ^2 values is minimised. The fast decays present fewer data points than the slow decays, hence the main contribution to the value of χ^2 will be from the slow decays, and those will influence more than the fast ones. To account for this effect, the individual fit of each run was performed as well.

The experimental data are reported without error bars for visual clarity; however the experimental errors were used in the fitting procedure to calculate the value of χ^2. Together with the fitting function (light blue line for simultaneous fit and red line for

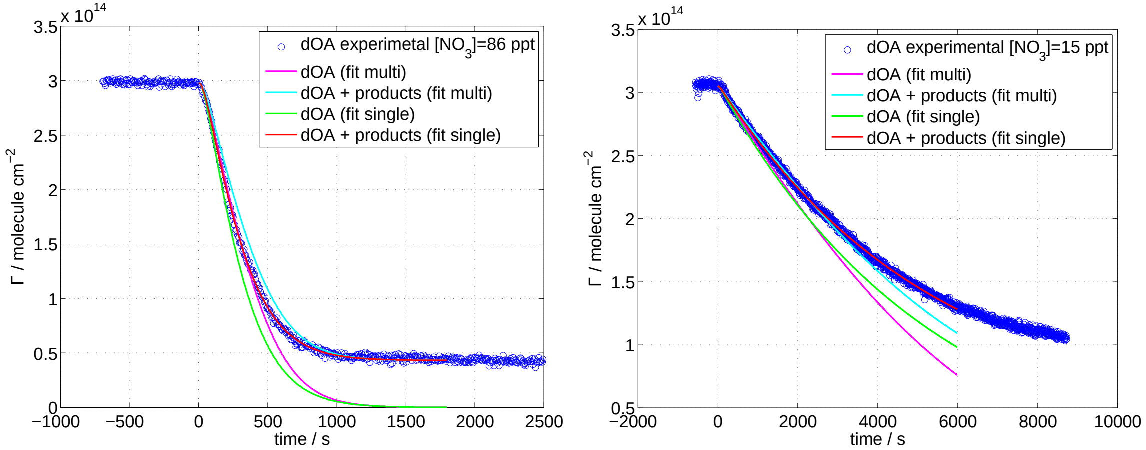

Figure 7.6: Examples of the experimental surface excess of dOA exposed to NO_3 fitted with the kinetic model. Comparison of the two fitting approaches (single and multi) is displayed. The calculated decays of dOA are shown as comparison with the calculated decays of dOA and products. (left) $[NO_3] = 86\,ppt$. (right) $[NO_3] = 15\,ppt$.

dOA molecule is expected to break into two parts, which maintain almost the same ratio between scattering length and molecular volume. In a first approximation, the scattering length of the product results to be half of the scattering length of dOA and the product film thickness can be thought to be half of the dOA film thickness. Given that and considering Eq. 2.4, the resulting surface excess of the products corresponds to the value calculated with ρ and d of dOA without requiring any conversion factor. The kinetic model depends on several parameters, and some of them are strictly correlated. For example, for a given gas species time evolution, which may be described by certain accommodation coefficients ($\alpha_{s;0;X_i}$ where X_i is NO_3 or NO_2) and certain desorption lifetimes ($\tau_{d;X_i}$), a good fit may be obtained as well with a lower $\alpha_{s;0;X_i}$ and an higher $\tau_{d;X_i}$. The accommodation coefficient represents the probability of the gas-phase molecule to absorb at the organic layer, hence the lower $\alpha_{s;0;NO_3}$ is, the smaller is the probability of the reaction with the organic molecule. The desorption lifetime represents the mean residence time of the molecule absorbed at the surface, hence the longer the time is, the higher is the probability for the gas molecule to react (valid for NO_3). NO_2 does not react with the organic layer [52], but these parameters still the range of variability was optimised through a preliminary sensitivity study performed manually, changing in the Matlab code the value of k_{surf}. The suitable range of values found was $(1 - 5) \times 10^{-8}$ cm^2 molecule^{-1} s^{-1}, which is significantly higher than the best fit value provided by Shiraiwa et al. [128] for abietic acid exposed to NO_3 (1.5×10^{-9} cm^2 molecule^{-1} s^{-1}).

The optimisation of the kinetic parameters was performed systematically by the χ^2 minimisation routine fminuit [102].

The fitting approach described above has been applied to all the molecules studied hereafter, accounting for different products description and kinetic parameter ranges.

A preliminary analysis of the $\Gamma(t)$ profiles was needed to choose the kinetic parameters related to the products, which have been used as fixed input parameters. The product yields were optimised to $c_S = 0.145$ for the surface active products, $c_G = 0.45$ for the volatile products and $c_B = 0.35$ for the soluble products. A systematic study was performed to determine the effect of the loss of volatile and soluble products on the resulting surface excess profiles. For the volatile products, it was found that a first-order loss rate coefficient, $k_{loss;G}$, above 1×10^{-1} s^{-1} does not change the $\Gamma(t)$ profile, hence a value of 5×10^{-1} s^{-1} was chosen. For the soluble products, the loss will occur upon diffusion in the subphase, hence the relevant parameter is the diffusion coefficient into the bulk water, $D_{b;Z_B}$. The calculated $\Gamma(t)$ was affected by the presence of soluble products only for values of $D_{b;Z_B}$ below 10^{-14} cm^2 s^{-1}, since no evidence of such an effect was found in the experimental data the value of $D_{b;Z_B}$ was fixed to 10^{-7} cm^2 s^{-1}.

The best fit values for the kinetic parameters related to the heterogeneous reaction between a dOA films and gas-phase NO_3 are summarised in Table 7.1. The simultaneous fit of the 6 different gas conditions results in the value $k_{surf} = (2.2 \pm 1.8) \times 10^{-8}$ cm^2 molecule^{-1} s^{-1}, which is in agreement with the range of values found fitting individually the various runs: k_{surf} ranges from 1.13×10^{-8} to 2.18×10^{-8} cm^2 molecule^{-1} s^{-1}. The best fit values for the $[NO_3]$, $[NO_3]^{multi}$ and $[NO_3]^{sing}$, are systematically below the mean value suggested by the spectroscopic measurements apart from the

	86 ppt	35 ppt	36 ppt
$[NO_3]$ / 10^8 molecule cm^{-3}	23 ± 12	9.3 ± 2.4	9.7 ± 2.7
$[NO_3]^{multi}$ / 10^8 molecule cm^{-3}	26.0 ± 0.1	11.5 ± 0.01	8.2 ± 1.6
$[NO_3]^{sing}$ / 10^8 molecule cm^{-3}	24.0 ± 0.1	9.10 ± 0.01	6.00 ± 0.01
$[NO_2]$ / 10^{15} molecule cm^{-3}	1.3 ± 0.1	1.6 ± 0.1	2.2 ± 0.1
$[NO_2]^{multi}$ / 10^{15} molecule cm^{-3}	1.00 ± 0.01	1.4 ± 0.2	1.9 ± 0.1
$[NO_2]^{sing}$ / 10^{15} molecule cm^{-3}	1.00 ± 0.01	1.87 ± 0.01	1.92 ± 0.01
$(k_{surf})^{multi}$ / 10^{-8} cm^2 molecule^{-1} s^{-1}	2.2 ± 1.8		
$(k_{surf})^{sing}$ / 10^{-8} cm^2 molecule^{-1} s^{-1}	1.80 ± 0.01	1.97 ± 0.01	2.18 ± 0.01
$(\tau_{d;NO_3;1})^{multi}$ / 10^{-9} s	5.2 ± 2.4		
$(\tau_{d;NO_3;1})^{sing}$ / 10^{-9} s	9.00 ± 0.01	8.60 ± 0.01	7.77 ± 0.01
$(\tau_{d;NO_3;2})^{multi}$ / 10^{-9} s	13 ± 9		
$(\tau_{d;NO_3;2})^{sing}$ / 10^{-9} s	15.00 ± 0.01	24.2 ± 0.7	11.6 ± 0.01
$(\tau_{d;NO_2})^{multi}$ / 10^{-8} s	6.00 ± 0.01		
$(\tau_{d;NO_2})^{sing}$ / 10^{-8} s	3.80 ± 0.01	3.50 ± 0.01	4.30 ± 0.01

	32 ppt	23 ppt	15 ppt
$[NO_3]$ / 10^8 molecule cm^{-3}	8.7 ± 2.8	6.1 ± 1.2	4.2 ± 1.4
$[NO_3]^{multi}$ / 10^8 molecule cm^{-3}	7.4 ± 1.4	4.2 ± 1.8	2.40 ± 0.04
$[NO_3]^{sing}$ / 10^8 molecule cm^{-3}	4.81 ± 0.01	4.74 ± 0.01	2.52 ± 0.01
$[NO_2]$ / 10^{15} molecule cm^{-3}	2.7 ± 0.2	3.3 ± 0.2	3.8 ± 0.3
$[NO_2]^{multi}$ / 10^{15} molecule cm^{-3}	2.7 ± 0.3	3.5 ± 0.2	4.10 ± 0.04
$[NO_2]^{sing}$ / 10^{15} molecule cm^{-3}	3.00 ± 0.01	3.56 ± 0.01	3.81 ± 0.01
$(k_{surf})^{multi}$ / 10^{-8} cm^2 molecule^{-1} s^{-1}	2.2 ± 1.8		
$(k_{surf})^{sing}$ / 10^{-8} cm^2 molecule^{-1} s^{-1}	2.15 ± 0.01	1.74 ± 0.01	1.13 ± 0.01
$(\tau_{d;NO_3;1})^{multi}$ / 10^{-9} s	5.2 ± 2.4		
$(\tau_{d;NO_3;1})^{sing}$ / 10^{-9} s	10.00 ± 0.01	6.00 ± 0.01	10.00 ± 0.01
$(\tau_{d;NO_3;2})^{multi}$ / 10^{-9} s	13 ± 9		
$(\tau_{d;NO_3;2})^{sing}$ / 10^{-9} s	10 ± 0.01	10.60 ± 0.01	10.00 ± 0.01
$(\tau_{d;NO_2})^{multi}$ / 10^{-8} s	6.00 ± 0.01		
$(\tau_{d;NO_2})^{sing}$ / 10^{-8} s	5.21 ± 0.01	5.04 ± 0.01	3.88 ± 0.01

molecule cm^{-3}. This suggests a correlation between those two parameters, hence both sets of parameters are valid and may be used to describe the system.

7.3.2 Ellipsometry

The oxidation of hOA due to NO_3 exposure was studied with the ellipsometer using the MIMIK chamber. The experiments were performed in the laboratory and the external temperature was found to vary between 23 °C and 26 °C, which is similar to the temperature variability typical of the FIGARO sample area. The experimental procedures may be found in the previous section.

Figure 7.7 shows the surface excess decays of hOA monolayers at the air–water interface as a function of time with respect to $[NO_3]$. $[NO_3]$ ranges from (35 ± 9) ppt to (160 ± 30) ppt.

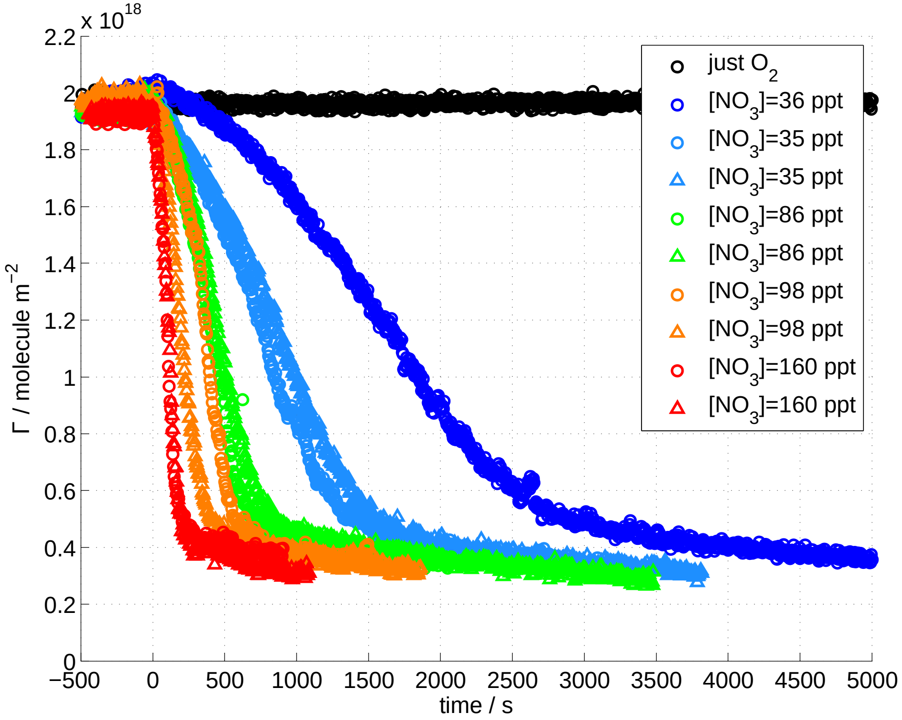

Figure 7.7: Surface excess decays of hOA exposed to different values of $[NO_3]$; mean values are displayed in the legend. Data were recorded with ellipsometry. Time $t = 0$ s represents the start of the exposure. Data are shown without error bars for clarity. The relative errors are on the order of 1 %.

the MO oxidation did not show any similar effect (either O_3 - Section 7.2 - and NO_3 - Section 7.6), and these reactions do not produce any surface-active products. None of the previous considerations leads to a clear explanation of the phenomenon observed, and hence the choice on whether to consider or not the beginning of the surface excess decay is arbitrary. The kinetic analysis was performed considering the data from the beginning of the decay.

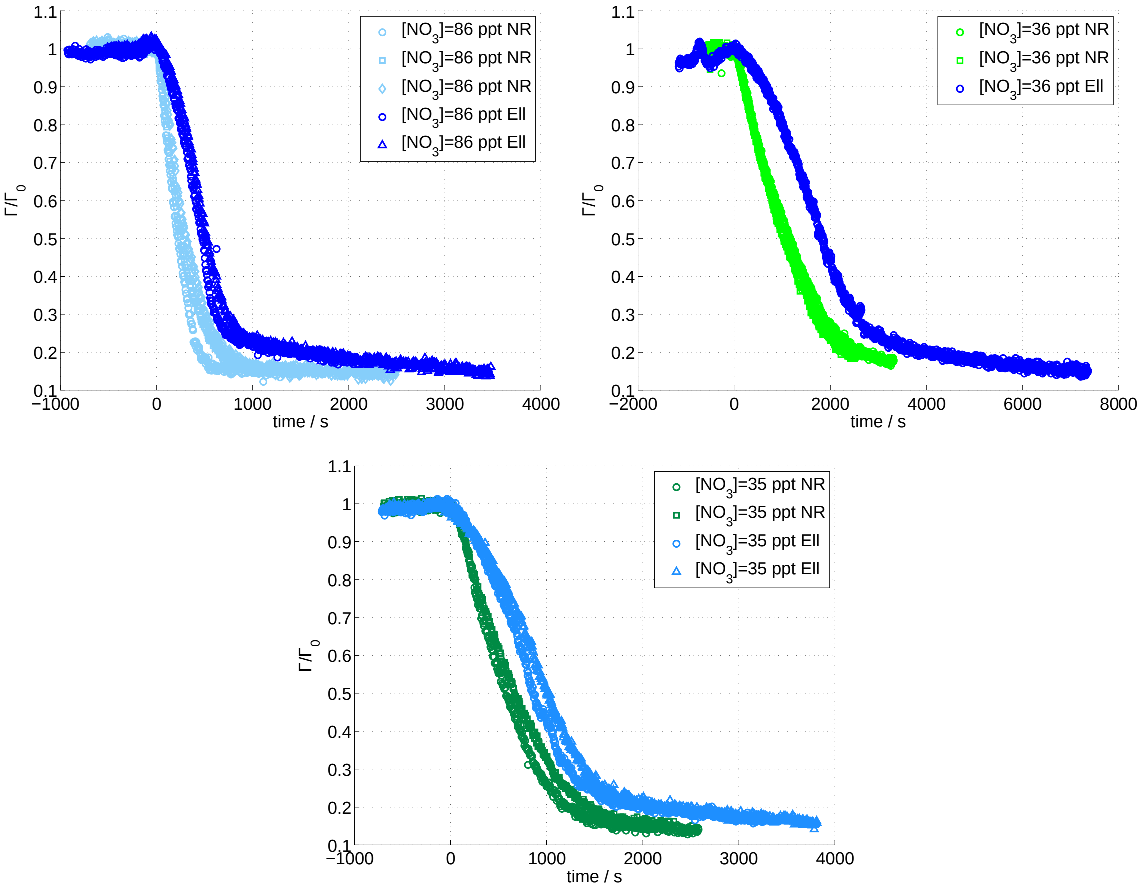

Figure 7.8: Comparison of the surface excess decays recorded with NR-dOA (NR) and ellipsometry-hOA (Ell) for OA exposed to $[NO_3] = 86$ ppt (top left), $[NO_3] = 36$ ppt (top right) and $[NO_3] = 35$ ppt (bottom). The surface excess decays have been normalised to their initial values.

for greater amounts of molecules spread. These observations suggest that there are surface-active products, the quantity of which is related to the amount of starting material. The presence of impurity on the starting material could be another explanation, however the test performed with hMO confirmed the relation between amount of molecule spread and time length of the plateau without leaving any surface-active material. Due to the restricted access to NR beam time, these tests have not been repeated with NR to validate the results obtained with ellipsometry. However, this effect can be explained with the presence of hOA droplets lying on top of the hOA monolayer [112], which is evident from the BAM images in Section 6.2.3. The monolayer is consumed upon oxidation but molecules from the droplets may spread and maintain a high surface excess until the droplets disappear. To account for this, the initial value for the theoretical Γ(t) was adjusted to a higher value than the initial plateau value and the experimental data were considered for fitting after the initial plateau ended. For an easier comparison, the data shown in Fig. 7.8 were shifted to meet the start of the decay of the NR data. For NR this effect was less pronounced, it may be due to different measurement strategy and sensitivity of the technique. Furthermore, the amount of material spread could have been slightly lower for NR, resulting in less number of droplets.

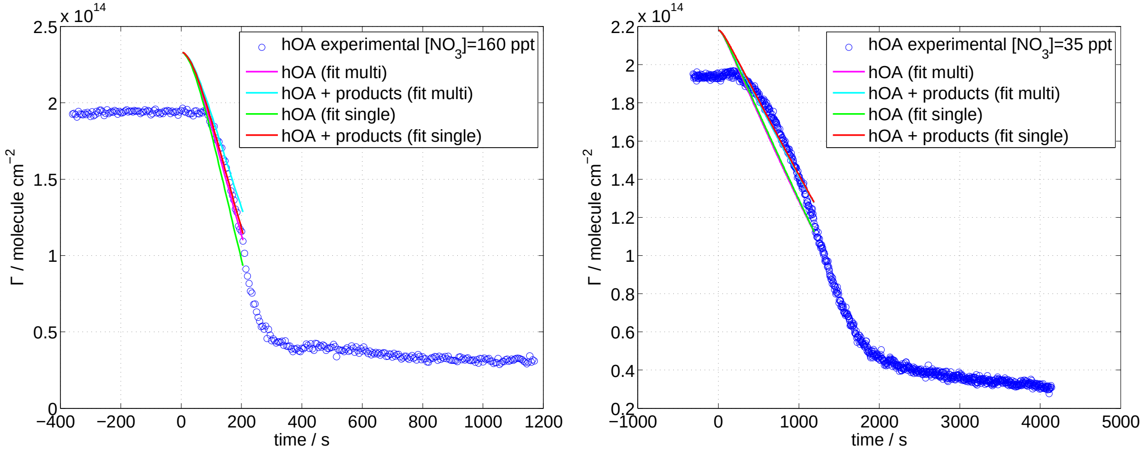

Figure 7.9: Experimental surface excess of hOA exposed to NO_3 fitted with the kinetic

strict correlation between two parameters provides different descriptions of the system resulting in the same fit quality. The difference between $(\tau_{d;\,NO_3;\,2})^{multi}$ and $(\tau_{d;\,NO_{;}\,2})^{sing}$ may be due to the same reason.

The kinetic parameters provided by the two experimental techniques present some accordance and some discrepancy. The rate coefficients result to be in good agreement, and for both NR and ellipsometry, the data recorded at lower $[NO_3]$ provide k_{surf} values lower than the average. This effect may be due to an overestimation of the values of $[NO_3]$, which affects more the low concentrations than the higher ones. The desorption lifetimes, $\tau_{d;\,NO_3;\,1}$, provided by both fitting approaches of the ellipsometric data are in good agreement with the range of values determined by NR. This agreement is found for the NO_2 desorption lifetime as well. The main difference between the two techniques arises in the desorption lifetime, $\tau_{d;\,NO_3;\,2}$, which is for ellipsometry between two and three times the values obtained for NR. This parameter is generally determined by the second half of the $\Gamma(t)$ profile (compare Eq. 4.8), hence the increased loss in the second part of $\Gamma(t)$ measured with ellipsometry may affect that value, which could compensate a slight underestimation of k_{surf}.

	160 ppt	98 ppt	86 ppt
$[\mathrm{NO_3}]$ / 10^8 molecule cm^{-3}	44 ± 7	26 ± 10	23 ± 12
$[\mathrm{NO_3}]^{multi}$ / 10^8 molecule cm^{-3}	55.0 ± 0.1	24.0 ± 0.1	15.0 ± 0.1
$[\mathrm{NO_3}]^{sing}$ / 10^8 molecule cm^{-3}	51.5 ± 0.1	24.0 ± 0.1	11.2 ± 0.1
$[\mathrm{NO_2}]$ / 10^{15} molecule cm^{-3}	0.53 ± 0.01	0.86 ± 0.08	1.30 ± 0.05
$[\mathrm{NO_2}]^{multi}$ / 10^{15} molecule cm^{-3}	0.6 ± 0.1	0.6 ± 0.1	1.0 ± 0.1
$[\mathrm{NO_2}]^{sing}$ / 10^{15} molecule cm^{-3}	0.5 ± 0.1	0.6 ± 0.1	1.5 ± 0.1
$(k_{surf})^{multi}$ / 10^{-8} cm^2 molecule^{-1} s^{-1}	1.26 ± 0.01		
$(k_{surf})^{sing}$ / 10^{-8} cm^2 molecule^{-1} s^{-1}	3.3 ± 0.1	3.8 ± 0.1	3.9 ± 0.1
$(\tau_{d;\mathrm{NO_3};1})^{multi}$ / 10^{-9} s	7.00 ± 0.01		
$(\tau_{d;\mathrm{NO_3};1})^{sing}$ / 10^{-9} s	3.0 ± 0.1	3.0 ± 0.1	3.0 ± 0.1
$(\tau_{d;\mathrm{NO_3};2})^{multi}$ / 10^{-9} s	35.4 ± 0.1		
$(\tau_{d;\mathrm{NO_3};2})^{sing}$ / 10^{-9} s	40.0 ± 0.1	40.0 ± 0.1	40 ± 0.1
$(\tau_{d;\mathrm{NO_2}})^{multi}$ / 10^{-8} s	5.6 ± 0.1		
$(\tau_{d;\mathrm{NO_2}})^{sing}$ / 10^{-8} s	3.0 ± 0.1	3.0 ± 0.1	0.47 ± 0.01

	35 ppt	36 ppt
$[\mathrm{NO_3}]$ / 10^8 molecule cm^{-3}	9.3 ± 2.4	9.7 ± 2.7
$[\mathrm{NO_3}]^{multi}$ / 10^8 molecule cm^{-3}	7.2 ± 0.1	5.0 ± 0.1
$[\mathrm{NO_3}]^{sing}$ / 10^8 molecule cm^{-3}	6.7 ± 0.1	7.3 ± 0.1
$[\mathrm{NO_2}]$ / 10^{15} molecule cm^{-3}	1.6 ± 0.1	2.2 ± 0.1
$[\mathrm{NO_2}]^{multi}$ / 10^{15} molecule cm^{-3}	1.3 ± 0.1	2.5 ± 0.1
$[\mathrm{NO_2}]^{sing}$ / 10^{15} molecule cm^{-3}	1.4 ± 0.1	1.9 ± 0.1
$(k_{surf})^{multi}$ / 10^{-8} cm^2 molecule^{-1} s^{-1}	1.26 ± 0.01	
$(k_{surf})^{sing}$ / 10^{-8} cm^2 molecule^{-1} s^{-1}	2.9 ± 0.1	1.74 ± 0.01
$(\tau_{d;\mathrm{NO_3};1})^{multi}$ / 10^{-9} s	7.00 ± 0.01	
$(\tau_{d;\mathrm{NO_3};1})^{sing}$ / 10^{-9} s	3.0 ± 0.1	3.0 ± 0.1
$(\tau_{d;\mathrm{NO_3};2})^{multi}$ / 10^{-9} s	35.4 ± 0.1	
$(\tau_{d;\mathrm{NO_3};2})^{sing}$ / 10^{-9} s	40.0 ± 0.1	40.0 ± 0.1
$(\tau_{d;\mathrm{NO_2}})^{multi}$ / 10^{-8} s	5.6 ± 0.1	
$(\tau_{d;\mathrm{NO_2}})^{sing}$ / 10^{-8} s	3.5 ± 0.1	4.7 ± 0.1

7.4 Stearic acid exposed to NO_3

All the organic molecules considered in this thesis so far contain at least one unsaturation in the aliphatic tail, except stearic acid. The C=C bond is expected to be the key reactive site for both O_3 and NO_3. However, NO_3 may abstract hydrogen atoms from the aliphatic tail [7, 31], in addition of breaking the double bond. In order to investigate the contribution of the hydrogen abstraction, a saturated surfactant, i.e. stearic acid, was exposed to NO_3 and the surface excess was monitored with NR. Ellipsometry data were not acquired because the stearic acid presents optical anisotropy even at low surface excess (see Section 6.2.6).

7.4.1 NR

Figure 7.10 shows the comparison between the surface excess of a dSA monolayer exposed to O_2 and exposed to NO_3 at (86 ± 45) ppt. The data were recorded for more than 8 hours for each gas condition. The surface excess of the monolayer exposed to the nitrate radical is comparable to the data recorded for O_2 exposure, both profiles show a slow increase in surface excess in the first 40 minutes. The interpretation of this increase in surface excess is unclear: it may be due to a slow increase in packing of the aliphatic chains or/and to absorption of gas-phase species to the interface. Apart the initial increase in $\Gamma(t)$ values, no measurable change in the surface excess has been recorded, and hence the film is assumed to be stable on the probed time scale. However, it is important to highlight that the NR is sensitive just to change in scattering length density, ρ, and thickness, d, of the deuterated monolayer. If the monolayer chemical composition is changed upon reaction with NO_3 (i.e. formation of organonitrates [47]) but the ρ and d remains unchanged the resulting $\Gamma(t)$ will be constant. This result is in accordance with the findings of Knopf et al. [129], where the exposure to 100 ppt of NO_3 for one week resulted in a maximum of 10 % of the organic monolayer volatilised (the monolayer was supported on a solid substrate). However, when stearic acid is mixed with oleic acid in the monolayer (see Section 8.3), the formation of organonitrates upon reaction with NO_3 could affect the overall rate coefficient of oleic acid.

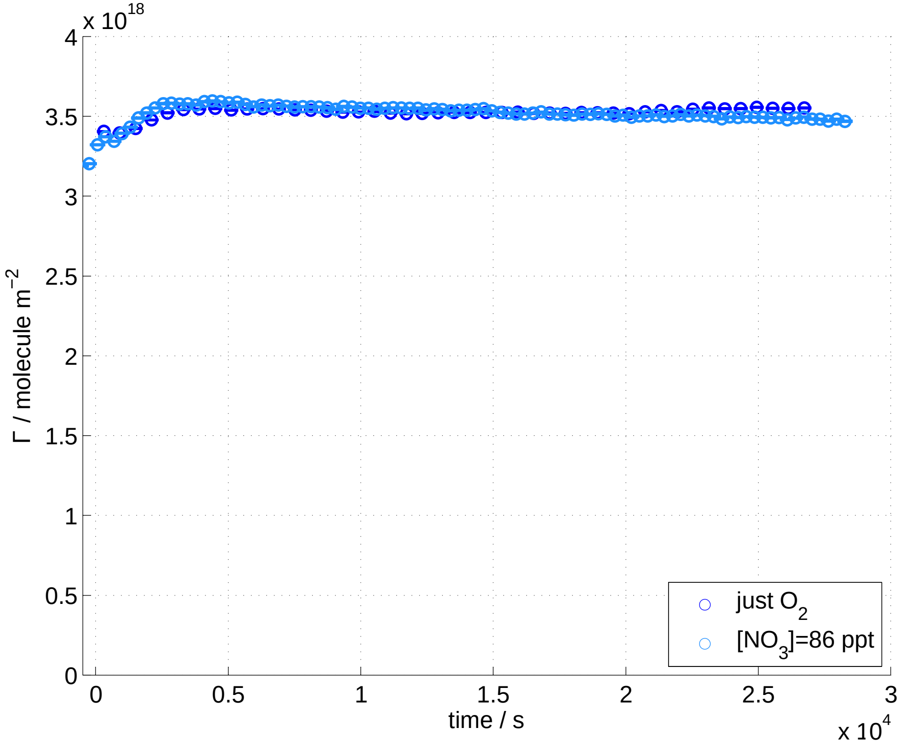

Figure 7.10: Surface excess of dSA exposed to O_2 and to $[NO_3] =$ 86 ppt. Data recorded with NR. Time t = 0 s represent the start of the exposure. No evident change in surface excess is produced by exposure to NO_3. Both surface excess decays have a slow increase over the first 40 minutes.

7.5 Palmitoleic acid exposed to NO_3

In this section, the oxidation kinetics and fate of POA monolayers at the air–water interface that are exposed to NO_3 are investigated. The experiments were performed as describe previously for OA and in Section 5.3. The surface excess profiles were obtained both by NR and ellipsometry. For both instruments the MIMIK chamber was used as the reaction chamber. The POA for NR measurements was a custom-made deuterated form provided by the Oxford Deuteration Facility. 14 deuterium atoms were present between the carbon double bond and the terminal methyl group. POA has a chemical structure similar to OA. In fact the portion from the carboxylic

($[NO_3] < 32$ ppt), the plateau value was not reached because the reaction was stopped prematurely due to the constraints of limited beam time. Compared to dOA, the decays appear to be faster for the same oxidant condition. One reason could be the easier access to the reactive site because of the shorter chain, and another could be related to the half deuteration. In fact, even if part of the dPOA molecule remains at the interface, it may effectively be invisible if it may be hydrogenated. On the assumption that the double bond is the reactive site and breaks during the oxidation process, the half deuteration may help in determining which part of the molecule remains at the interface, through the comparison of the NR results with the ellipsometry results.

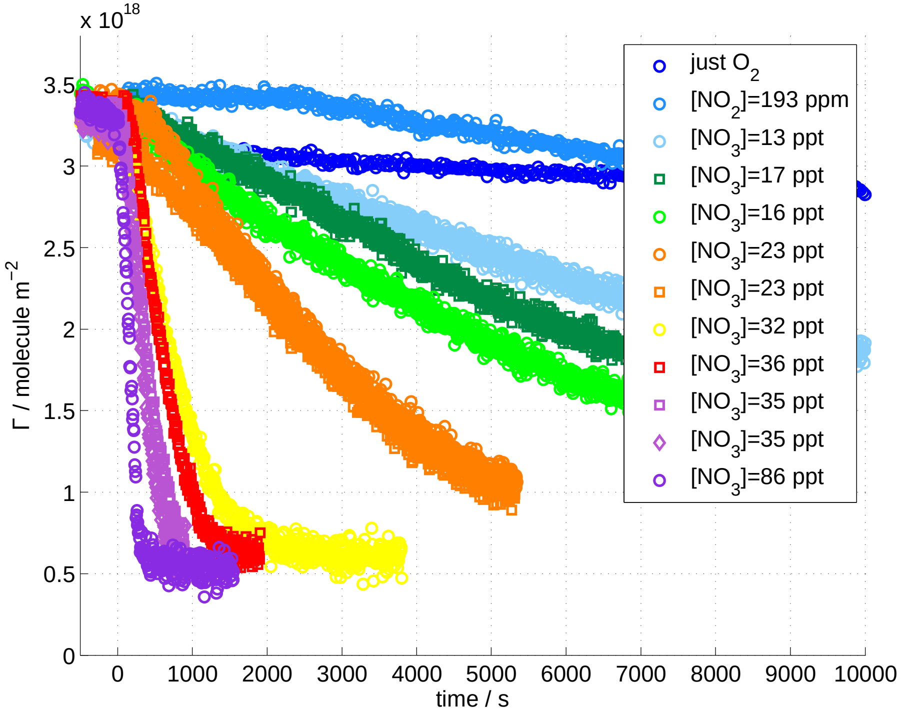

Figure 7.11: Surface excess decays of dPOA exposed to different $[NO_3]$; mean values are displayed in the legend. Data were recorded with NR. Time t = 0 s represents the start of the exposure. Data are shown without error bars for clarity. The relative errors are on the order of 1 %. The experimental data are more scattered than those for the previous molecules studied, because the dPOA was just half-deuterated (i.e. 14 D, see Table 5.1), hence the contrast was weaker.

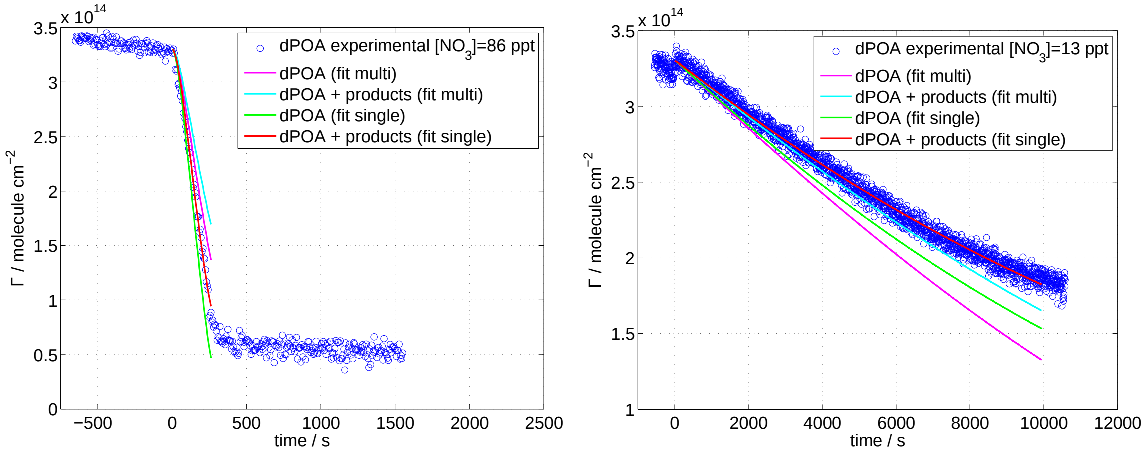

Figure 7.12: Experimental surface excess of dPOA monolayers exposed to NO_3 fitted with the kinetic model. Comparison of the two fitting approaches (single and multi) is displayed. The calculated decays of dPOA are shown as comparison with the calculated decays of dPOA and products. (left) $[NO_3] = 86$ ppt. (right) $[NO_3] = 13$ ppt.

molecule^{-1} s^{-1}, which is included in the range of values found from fitting individually the various runs, k_{surf} bewteen $(0.7 - 3.8) \times 10^{-8}$ cm^2 molecule^{-1} s^{-1}. Considering the individual fits, it may be noted that the fast runs ($[NO_3] > 35$ ppt) are better described by a higher rate coefficient than the slow runs. This effect may be related to either an underestimation of the $[NO_3]$ when $[NO_3] > 35$ ppt or an overestimation when $[NO_3] < 35$ ppt. However, considering the corresponding desorption lifetimes of NO_3, $\tau_{d;NO_3;1}$, a correlation between desorption lifetime and rate coefficient may be found. A smaller value of $\tau_{d;NO_3;1}$ may compensate for a higher value of k_{surf} with respect to the results of the simultaneous fit (for example consider condition $[NO_3] = 36$ ppt in Table 7.3). The other desorption lifetimes of NO_3, $\tau_{d;NO_3;2}$, seems not to be correlated with the rate coefficient, and the values suggested by the individual fits are spread around the result obtained by the simultaneous fit. This lack of correlation may be due to the fact that this parameter is mostly related to the second part of the decay (see Eq. 4.8 in Section 4.3.2), which is not considered in the fitting. The last kinetic parameter of interest is the desorption lifetime of NO_2, $\tau_{d;NO_2}$, which is $(5.9 \pm 0.1) \times 10^{-8}$ s for the

	86 ppt	35 ppt	36 ppt
$[NO_3]$ / 10^8 molecule cm^{-3}	23 ± 12	9.3 ± 2.4	9.7 ± 2.7
$[NO_3]^{multi}$ / 10^8 molecule cm^{-3}	32.0 ± 0.1	9.0 ± 0.1	8.9 ± 0.1
$[NO_3]^{sing}$ / 10^8 molecule cm^{-3}	31.5 ± 0.1	7.0 ± 0.1	6.6 ± 0.1
$[NO_2]$ / 10^{15} molecule cm^{-3}	1.3 ± 0.1	1.6 ± 0.1	2.2 ± 0.1
$[NO_2]^{multi}$ / 10^{15} molecule cm^{-3}	1.6 ± 0.1	1.3 ± 0.1	1.9 ± 0.1
$[NO_2]^{sing}$ / 10^{15} molecule cm^{-3}	1.6 ± 0.1	1.8 ± 0.1	1.9 ± 0.1
$(k_{surf})^{multi}$ / 10^{-8} cm^2 molecule^{-1} s^{-1}	1.6 ± 0.1		
$(k_{surf})^{sing}$ / 10^{-8} cm^2 molecule^{-1} s^{-1}	3.0 ± 0.1	3.1 ± 0.1	3.8 ± 0.1
$(\tau_{d;NO_3;1})^{multi}$ / 10^{-9} s	8.3 ± 0.1		
$(\tau_{d;NO_3;1})^{sing}$ / 10^{-9} s	7.3 ± 0.1	9.5 ± 0.1	6.5 ± 0.1
$(\tau_{d;NO_3;2})^{multi}$ / 10^{-9} s	26.4 ± 0.1		
$(\tau_{d;NO_3;2})^{sing}$ / 10^{-9} s	47.5 ± 0.1	32.0 ± 0.1	36.7 ± 0.1
$(\tau_{d;NO_2})^{multi}$ / 10^{-8} s	5.9 ± 0.1		
$(\tau_{d;NO_2})^{sing}$ / 10^{-8} s	5.6 ± 0.1	3.9 ± 0.1	1.8 ± 0.1

	32 ppt	23 ppt	15 ppt
$[NO_3]$ / 10^8 molecule cm^{-3}	8.7 ± 2.8	6.1 ± 1.2	4.2 ± 1.4
$[NO_3]^{multi}$ / 10^8 molecule cm^{-3}	8.0 ± 0.1	2.6 ± 0.1	1.3 ± 0.1
$[NO_3]^{sing}$ / 10^8 molecule cm^{-3}	5.7 ± 0.1	2.8 ± 0.1	0.53 ± 0.01
$[NO_2]$ / 10^{15} molecule cm^{-3}	2.7 ± 0.1	3.3 ± 0.1	3.8 ± 0.1
$[NO_2]^{multi}$ / 10^{15} molecule cm^{-3}	2.4 ± 0.1	3.3 ± 0.1	3.5 ± 0.1
$[NO_2]^{sing}$ / 10^{15} molecule cm^{-3}	2.4 ± 0.1	3.6 ± 0.1	4.0 ± 0.1
$(k_{surf})^{multi}$ / 10^{-8} cm^2 molecule^{-1} s^{-1}	1.6 ± 0.1		
$(k_{surf})^{sing}$ / 10^{-8} cm^2 molecule^{-1} s^{-1}	2.1 ± 0.1	1.0 ± 0.1	2.3 ± 0.1
$(\tau_{d;NO_3;1})^{multi}$ / 10^{-9} s	8.3 ± 0.1		
$(\tau_{d;NO_3;1})^{sing}$ / 10^{-9} s	10.2 ± 0.1	12.1 ± 0.1	19.6 ± 0.1
$(\tau_{d;NO_3;2})^{multi}$ / 10^{-9} s	26.4 ± 0.1		
$(\tau_{d;NO_3;2})^{sing}$ / 10^{-9} s	44.5 ± 0.1	36.5 ± 0.1	20.0 ± 0.1
$(\tau_{d;NO_2})^{multi}$ / 10^{-8} s	5.9 ± 0.1		
$(\tau_{d;NO_2})^{sing}$ / 10^{-8} s	2.9 ± 0.1	4.9 ± 0.1	4.4 ± 0.1

	17 ppt	13 ppt
$[NO_3]$ / 10^8 molecule cm^{-3}	5 ± 2	3.5 ± 1.5
$[NO_3]^{multi}$ / 10^8 molecule cm^{-3}	2.8 ± 0.1	0.9 ± 0.1
$[NO_3]^{sing}$ / 10^8 molecule cm^{-3}	1.4 ± 0.1	0.90 ± 0.01
$[NO_2]$ / 10^{15} molecule cm^{-3}	4.6 ± 0.2	5.5 ± 0.1
$[NO_2]^{multi}$ / 10^{15} molecule cm^{-3}	4.3 ± 0.1	5.8 ± 0.1
$[NO_2]^{sing}$ / 10^{15} molecule cm^{-3}	4.7 ± 0.1	5.2 ± 0.1
$(k_{surf})^{multi}$ / 10^{-8} cm^2 molecule^{-1} s^{-1}	1.6 ± 0.1	
$(k_{surf})^{sing}$ / 10^{-8} cm^2 molecule^{-1} s^{-1}	2.1 ± 0.1	0.7 ± 0.1
$(\tau_{d;NO_3;1})^{multi}$ / 10^{-9} s	8.3 ± 0.1	
$(\tau_{d;NO_3;1})^{sing}$ / 10^{-9} s	15.4 ± 0.1	16.0 ± 0.1
$(\tau_{d;NO_3;2})^{multi}$ / 10^{-9} s	26.4 ± 0.1	
$(\tau_{d;NO_3;2})^{sing}$ / 10^{-9} s	21.2 ± 0.1	24.8 ± 0.1
$(\tau_{d;NO_2})^{multi}$ / 10^{-8} s	5.9 ± 0.1	
$(\tau_{d;NO_2})^{sing}$ / 10^{-8} s	2.7 ± 0.1	2.9 ± 0.1

Table 7.4: Kinetic parameters, resulting from the fitting of the experimental data recorded with NR, of the system dPOA+ NO_3 are displayed. Each column represents an oxidant condition. Superscripts 'sing' and 'multi' refer to the two types of fitting performed (see text for details). Lines 1 ($[NO_3]$) and 4 ($[NO_2]$) of each table report the values measured with FTIR spectroscopy and their associated errors. All the others values and errors are obtained from the kinetic fitting.

7.5.2 Ellipsometry

The oxidation of hPOA by NO_3 was also studied with ellipsometry. Figure 7.13 displays the surface excess decays of hPOA monolayers at the air–water interface as a function of time with respect to $[NO_3]$. $[NO_3]$ ranges from (32 ± 10) ppt to (160 ± 30) ppt. Similarly to OA, the shape of the $\Gamma(t)$ profiles is different from the one recorded with NR measurements (see Figs 7.14 and 7.15). The comparison is made for each gas condition normalising the absolute scale of the $\Gamma(t)$ profile to its initial value. Two main differences may be highlighted: the decay at the beginning for the ellipsometry data is slower than in the NR data, and a plateau is reached by NR data at long reaction times, while ellipsometry data show a gradual loss towards nearly-zero surface excess. Those two differences may be related to reaction products and the possibility of the presence

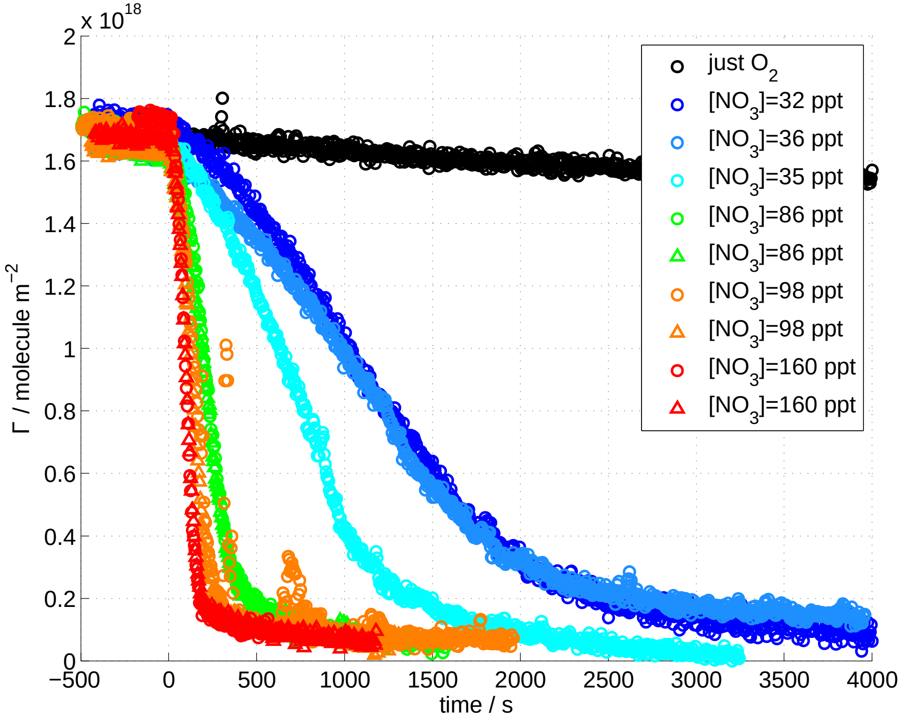

Figure 7.13: Surface excess decays of hPOA exposed to different [NO_3], mean values are displayed in the legend. Data were recorded with ellipsometry. Time t = 0 s represents the start of the exposure. Data are shown without error bars for clarity. The relative errors are on the order of 1 %.

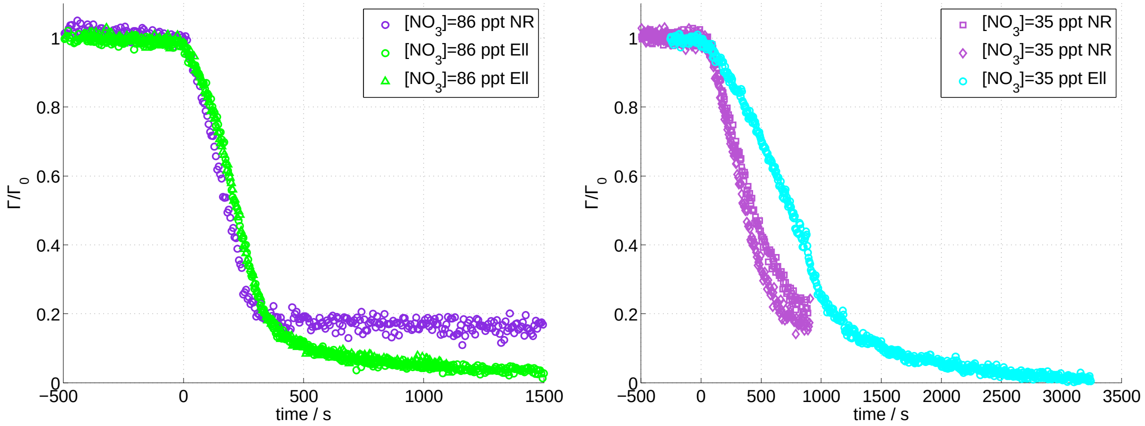

Figure 7.14: Comparison of surface excess decays recorded with NR dPOA (NR) and

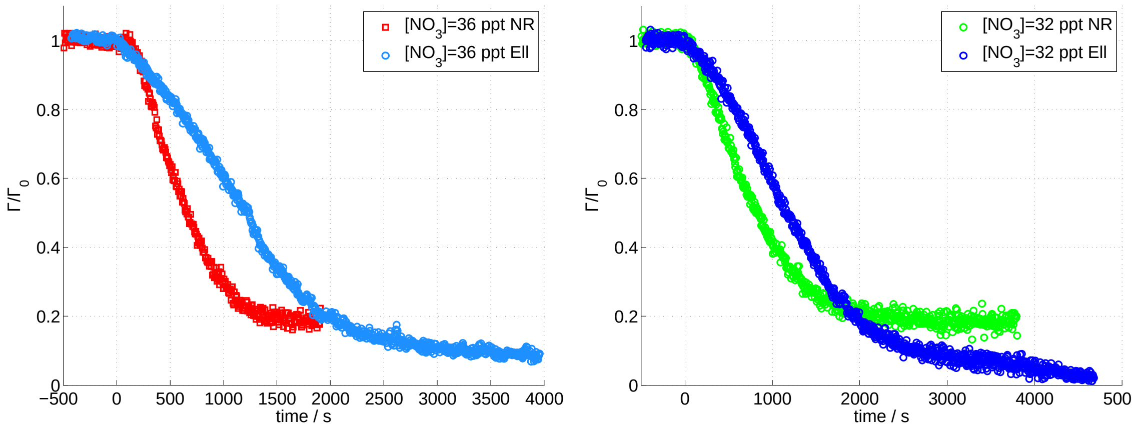

Figure 7.15: Comparison of surface excess decays recorded with NR-dPOA (NR) and ellipsometry-hPOA (Ell) for POA exposed to $[NO_3] = 36$ ppt (left) and $[NO_3] = 32$ ppt (right). The surface excess decays have been normalised to their initial values. The decays do not overlap.

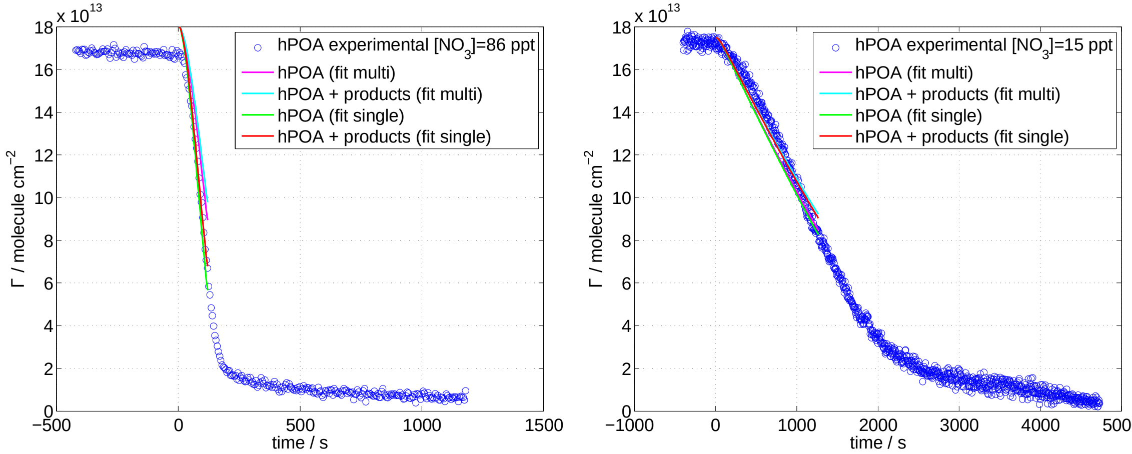

Figure 7.16: Experimental surface excess of hPOA exposed to NO_3 fitted with the kinetic model. Comparison of the two fitting approaches (single and multi) is displayed. The calculated decays of hPOA are shown as comparison with the calculated decays of hPOA and products. (left) $[NO_3] = 86$ ppt. (right) $[NO_3] = 15$ ppt.

higher value than the second, which correlates with the difference observed for the k_{surf} and $\tau_{d;NO_3;1}$. A similar trend may be found in the values found for $\tau_{d;NO_3;2}$, when

	160 ppt	98 ppt	86 ppt
$[\mathrm{NO_3}]$ / 10^{8} molecule cm^{-3}	44 ± 7	26 ± 10	23 ± 12
$[\mathrm{NO_3}]^{\mathrm{multi}}$ / 10^{8} molecule cm^{-3}	60 ± 1	50 ± 1	24 ± 1
$[\mathrm{NO_3}]^{\mathrm{sing}}$ / 10^{8} molecule cm^{-3}	46 ± 1	29 ± 1	22 ± 1
$[\mathrm{NO_2}]$ / 10^{15} molecule cm^{-3}	0.53 ± 0.01	0.86 ± 0.08	1.30 ± 0.05
$[\mathrm{NO_2}]^{\mathrm{multi}}$ / 10^{15} molecule cm^{-3}	0.10 ± 0.01	0.96 ± 0.01	1.4 ± 0.1
$[\mathrm{NO_2}]^{\mathrm{sing}}$ / 10^{15} molecule cm^{-3}	0.70 ± 0.01	0.80 ± 0.01	1.5 ± 0.1
$(k_{\mathrm{surf}})^{\mathrm{multi}}$ / 10^{-8} cm^{2} molecule^{-1} s^{-1}	1.8 ± 0.1		
$(k_{\mathrm{surf}})^{\mathrm{sing}}$ / 10^{-8} cm^{2} molecule^{-1} s^{-1}	2.8 ± 0.1	2.0 ± 0.1	2.0 ± 0.1
$(\tau_{d;\mathrm{NO_3};1})^{\mathrm{multi}}$ / 10^{-9} s	8.2 ± 0.1		
$(\tau_{d;\mathrm{NO_3};1})^{\mathrm{sing}}$ / 10^{-9} s	11.2 ± 0.1	14.8 ± 0.1	8.0 ± 0.1
$(\tau_{d;\mathrm{NO_3};2})^{\mathrm{multi}}$ / 10^{-9} s	44.7 ± 0.1		
$(\tau_{d;\mathrm{NO_3};2})^{\mathrm{sing}}$ / 10^{-9} s	37.8 ± 0.1	25.8 ± 0.1	50.0 ± 0.1
$(\tau_{d;\mathrm{NO_2}})^{\mathrm{multi}}$ / 10^{-8} s	5.7 ± 0.1		
$(\tau_{d;\mathrm{NO_2}})^{\mathrm{sing}}$ / 10^{-8} s	4.5 ± 0.1	3.3 ± 0.1	0.10 ± 0.01

	35 ppt	36 ppt	32 ppt
$[\mathrm{NO_3}]$ / 10^{8} molecule cm^{-3}	9.3 ± 2.4	9.7 ± 2.7	8.7 ± 2.8
$[\mathrm{NO_3}]^{\mathrm{multi}}$ / 10^{8} molecule cm^{-3}	6.6 ± 0.1	4.5 ± 0.1	4.5 ± 0.1
$[\mathrm{NO_3}]^{\mathrm{sing}}$ / 10^{8} molecule cm^{-3}	4.3 ± 0.1	5.6 ± 0.1	4.0 ± 0.1
$[\mathrm{NO_2}]$ / 10^{15} molecule cm^{-3}	1.6 ± 0.1	2.2 ± 0.1	2.7 ± 0.1
$[\mathrm{NO_2}]^{\mathrm{multi}}$ / 10^{15} molecule cm^{-3}	1.5 ± 0.1	2.5 ± 0.1	2.9 ± 0.1
$[\mathrm{NO_2}]^{\mathrm{sing}}$ / 10^{15} molecule cm^{-3}	1.7 ± 0.1	2.1 ± 0.1	2.4 ± 0.1
$(k_{\mathrm{surf}})^{\mathrm{multi}}$ / 10^{-8} cm^{2} molecule^{-1} s^{-1}	1.8 ± 0.1		
$(k_{\mathrm{surf}})^{\mathrm{sing}}$ / 10^{-8} cm^{2} molecule^{-1} s^{-1}	2.8 ± 0.1	1.4 ± 0.1	1.9 ± 0.1
$(\tau_{d;\mathrm{NO_3};1})^{\mathrm{multi}}$ / 10^{-9} s	8.2 ± 0.1		
$(\tau_{d;\mathrm{NO_3};1})^{\mathrm{sing}}$ / 10^{-9} s	8.0 ± 0.1	8.0 ± 0.1	8.0 ± 0.1
$(\tau_{d;\mathrm{NO_3};2})^{\mathrm{multi}}$ / 10^{-9} s	44.7 ± 0.1		
$(\tau_{d;\mathrm{NO_3};2})^{\mathrm{sing}}$ / 10^{-9} s	50 ± 1	50 ± 1	50 ± 1
$(\tau_{d;\mathrm{NO_2}})^{\mathrm{multi}}$ / 10^{-8} s	5.7 ± 0.1		
$(\tau_{d;\mathrm{NO_2}})^{\mathrm{sing}}$ / 10^{-8} s	0.40 ± 0.01	4.5 ± 0.1	0.32 ± 0.01

of surface-active products slowly volatilising, which is not the case for data measured with NR. $\Gamma(t)$ profiles measured by NR remains constant after reaching a minimum value. For future work, it may be helpful to perform an ellipsometry experiment with the deuterated form of POA to determine the presence of a non-reactive impurity and in parallel investigate the presence of deuterated impurity by NMR. The lack of knowledge about the eventual impurity in the deuterated sample affects the quantification of the surface-active product. However, the agreement between NR and ellipsometry on the kinetic parameters of the reaction suggests that the impurity does not affect the kinetic analysis.

7.6 Methyl oleate exposed to NO_3

The present section concerns the oxidation kinetics and fate of MO monolayers at the air–water interface that are exposed to NO_3. The experimental procedures are described in previous section and detailed in Section 5.3. The deuterated form of MO was provided by the Oxford Deuteration Facility (see Table 5.1). MO presents the same aliphatic chain as OA, but it has a different head group: instead of a carboxylic group it has a $COOCH_3$ group. The MO molecule occupies a larger surface area and is less stable at the air–water interface than OA because of its head group. However, the reactive site is in a similar chemical environment as OA, and any difference in reaction kinetics may be related to the chain orientation and product formation.

7.6.1 NR

Figure 7.17 displays the surface excess decays of dMO monolayers at the air-ACMW interface as a function of time with respect to $[NO_3]$. $[NO_3]$ ranges from (23 ± 4) ppt to (98 ± 40) ppt. The dMO monolayers exposed to pure O_2 or to the mixture of O_2 and NO_2 present a significant loss of surface excess with time compared to the other molecules investigated. This loss needs to be taken into account when performing the kinetic analysis of the $\Gamma(t)$ profiles.

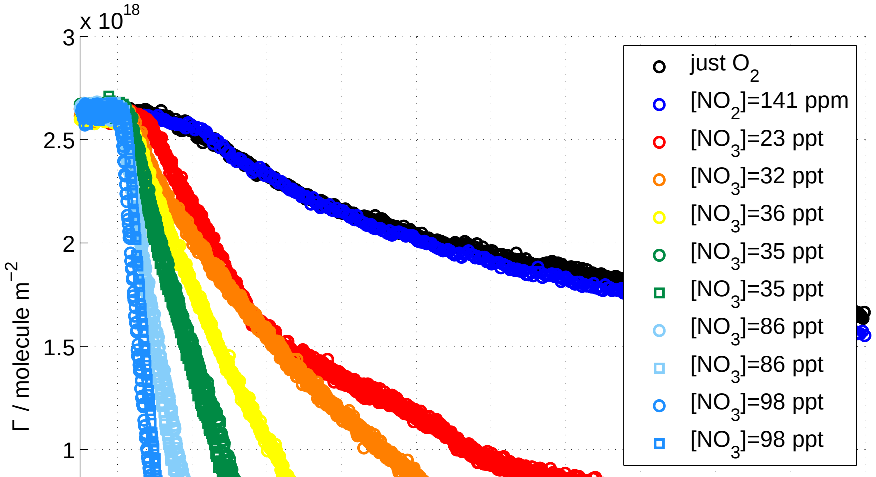

The minimum value reached by the surface excess is ~ 2×10^{17} molecule m^{-2}, which may be reduced to a negligible value by co-adding the data to increase the precision in Γ at low coverage. Therefore, no surface active products are expected to remain at the interface, as was confirmed by ellipsometry measurements. According to this criterion, the product yield was chosen as follows: $c_S = 0$, $c_G = 0.45$ and $c_B = 0.35$. Both fitting approaches, simultaneous and individual, were applied to the experimental data and two examples of the resulting $\Gamma(t)$ decays are shown in Figure 7.18; the runs exposed to the remaining oxidant conditions are shown in Figures C.1 and C.2 of Appendix C. The kinetic parameters were constrained in the following ranges: rate constant k_{surf} in the range $(0.7 - 4) \times 10^{-8}$ cm^2 molecule^{-1} s^{-1}, desorption lifetimes of NO_3 $\tau_{d;NO_3;1}$ in the range $(3 - 12) \times 10^{-9}$ s, $\tau_{d;NO_3;2}$ in the range $(10 - 30) \times 10^{-9}$ s and desorption lifetime of NO_2 $\tau_{d;NO_2}$ in the range $(0.1 - 6) \times 10^{-8}$ s.

Visually, in Figure 7.18 the individual fit (red line) describes better than the simultaneous fit (light blue line) the fast decays, which is an effect found for the previous molecules as well.

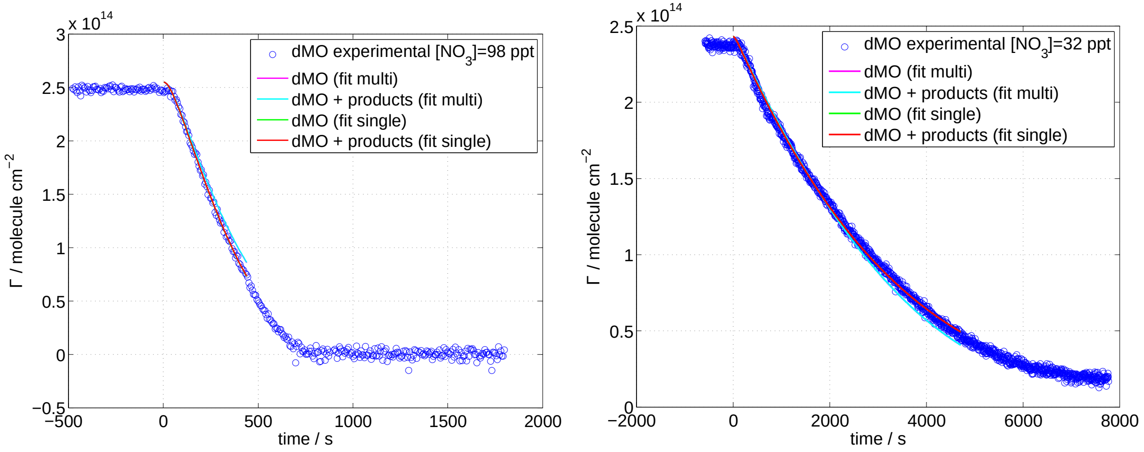

Figure 7.18: Experimental surface excess of dMO exposed to NO_3 fitted with the kinetic model. Comparison of the two fitting approaches (single and multi) is displayed. The calculated decays of dMO are shown as comparison with the calculated decays of dMO and products. (left) $[NO_3] = 98$ ppt. (right) $[NO_3] = 32$ ppt.

$(5.2 \pm 0.1) \times 10^{-8}$ s. This finding may suggest that the effect of NO_2 is overestimated in the simultaneous fit, since the variations in the other kinetic parameters do not compensate the difference in $\tau_{d;NO_2}$. Larger desorption lifetimes of NO_3 suggest a higher probability for the reaction, while the smaller value of $\tau_{d;NO_2}$ suggests faster desorption of NO_2, hence a greater number of free adsorption sites and increased probability for NO_3 to adsorb and react.

	98 ppt	86 ppt	35 ppt
$[\mathrm{NO_3}]$ / 10^{8} molecule cm^{-3}	26 ± 10	23 ± 12	9.3 ± 2.4
$[\mathrm{NO_3}]^{multi}$ / 10^{8} molecule cm^{-3}	32.0 ± 0.1	18.5 ± 0.1	8.0 ± 0.1
$[\mathrm{NO_3}]^{sing}$ / 10^{8} molecule cm^{-3}	30 ± 1	10 ± 1	7.4 ± 0.1
$[\mathrm{NO_2}]$ / 10^{15} molecule cm^{-3}	0.86 ± 0.08	1.30 ± 0.05	1.6 ± 0.1
$[\mathrm{NO_2}]^{multi}$ / 10^{15} molecule cm^{-3}	0.70 ± 0.01	1.6 ± 0.1	1.3 ± 0.1
$[\mathrm{NO_2}]^{sing}$ / 10^{15} molecule cm^{-3}	0.92 ± 0.01	1.6 ± 0.1	1.7 ± 0.1
$(k_{surf})^{multi}$ / 10^{-8} cm^{2} molecule^{-1} s^{-1}	1.7 ± 0.1		
$(k_{surf})^{sing}$ / 10^{-8} cm^{2} molecule^{-1} s^{-1}	1.7 ± 0.1	2.1 ± 0.1	1.1 ± 0.1
$(\tau_{d;NO_3;1})^{multi}$ / 10^{-9} s	5.5 ± 0.1		
$(\tau_{d;NO_3;1})^{sing}$ / 10^{-9} s	6.1 ± 0.1	6.8 ± 0.1	10.5 ± 0.1
$(\tau_{d;NO_3;2})^{multi}$ / 10^{-9} s	11.3 ± 0.1		
$(\tau_{d;NO_3;2})^{sing}$ / 10^{-9} s	17.1 ± 0.1	29.4 ± 0.1	28.2 ± 0.1
$(\tau_{d;NO_2})^{multi}$ / 10^{-8} s	5.2 ± 0.1		
$(\tau_{d;NO_2})^{sing}$ / 10^{-8} s	3.6 ± 0.1	4.0 ± 0.1	2.8 ± 0.1

	36 ppt	32 ppt	23 ppt
$[\mathrm{NO_3}]$ / 10^{8} molecule cm^{-3}	9.7 ± 2.7	8.7 ± 2.8	6.1 ± 1.2
$[\mathrm{NO_3}]^{multi}$ / 10^{8} molecule cm^{-3}	6.9 ± 0.1	4.5 ± 0.1	4.3 ± 0.1
$[\mathrm{NO_3}]^{sing}$ / 10^{8} molecule cm^{-3}	6.3 ± 0.1	4.7 ± 0.1	4.0 ± 0.1
$[\mathrm{NO_2}]$ / 10^{15} molecule cm^{-3}	2.2 ± 0.1	2.7 ± 0.1	3.3 ± 0.1
$[\mathrm{NO_2}]^{multi}$ / 10^{15} molecule cm^{-3}	2.2 ± 0.1	2.9 ± 0.1	3.2 ± 0.1
$[\mathrm{NO_2}]^{sing}$ / 10^{15} molecule cm^{-3}	1.9 ± 0.1	2.8 ± 0.1	3.3 ± 0.1
$(k_{surf})^{multi}$ / 10^{-8} cm^{2} molecule^{-1} s^{-1}	1.7 ± 0.1		
$(k_{surf})^{sing}$ / 10^{-8} cm^{2} molecule^{-1} s^{-1}	1.7 ± 0.1	0.85 ± 0.05	1.2 ± 0.1
$(\tau_{d;NO_3;1})^{multi}$ / 10^{-9} s	5.5 ± 0.1		
$(\tau_{d;NO_3;1})^{sing}$ / 10^{-9} s	5.0 ± 0.1	10.1 ± 0.1	7.7 ± 0.1
$(\tau_{d;NO_3;2})^{multi}$ / 10^{-9} s	11.3 ± 0.1		
$(\tau_{d;NO_3;2})^{sing}$ / 10^{-9} s	18.7 ± 0.1	14.2 ± 0.1	18.1 ± 0.1
$(\tau_{d;NO_2})^{multi}$ / 10^{-8} s	5.2 ± 0.1		
$(\tau_{d;NO_2})^{sing}$ / 10^{-8} s	3.0 ± 0.1	3.3 ± 0.1	3.4 ± 0.1

7.6.2 Ellipsometry

The oxidation of hMO resulting form its exposure to NO_3 is presented in this section. Surface excess decays as a function of time with respect to $[NO_3]$ are shown in Figure 7.19. $[NO_3]$ ranges from (35 ± 9) ppt to (160 ± 30) ppt. The $\Gamma(t)$ profiles may be divided in two parts: as for hMO exposed to O_3 (Section 7.2), the decrease is smooth above 1×10^{18} molecule m^{-2}, while below that surface excess the appearance of fluctuations suggest the production and subsequent loss of domains of reaction products. At long reaction times, the value of Γ is about zero, which confirms the result from the NR data (except the run at $[NO_3] = 36$ ppt, which was extremely slow compared to the others).

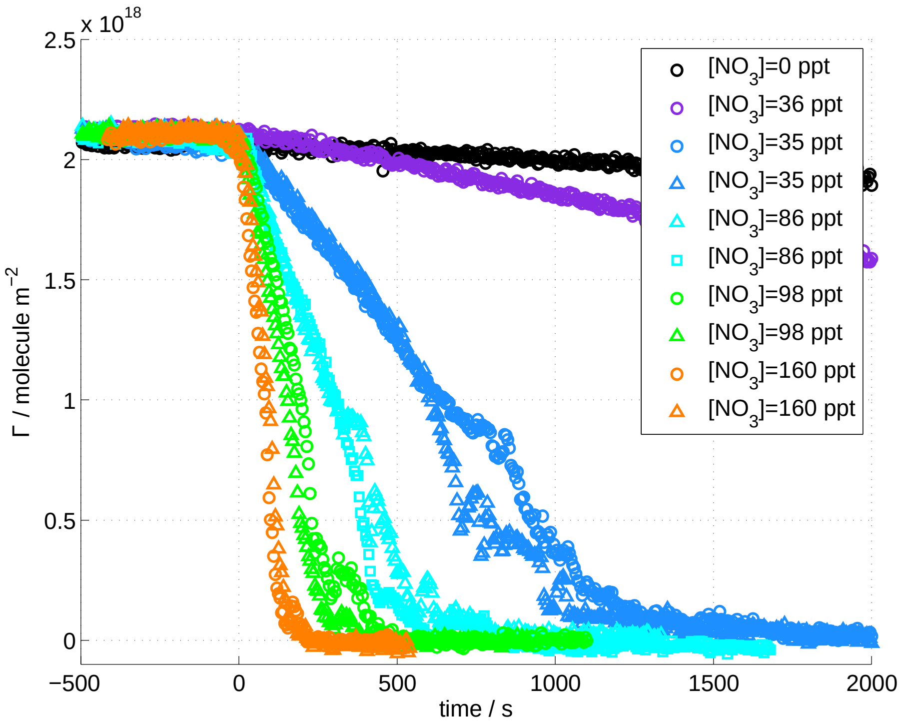

Figure 7.19: Surface excess of hMO exposed to different $[NO_3]$, mean values are displayed in the legend. Data were recorded with ellipsometry. Time $t = 0$ s represents the start of the exposure. Data are shown without error bars for clarity. The relative errors are on the order of 1 %. The reaction is comprehensive, since no material is left

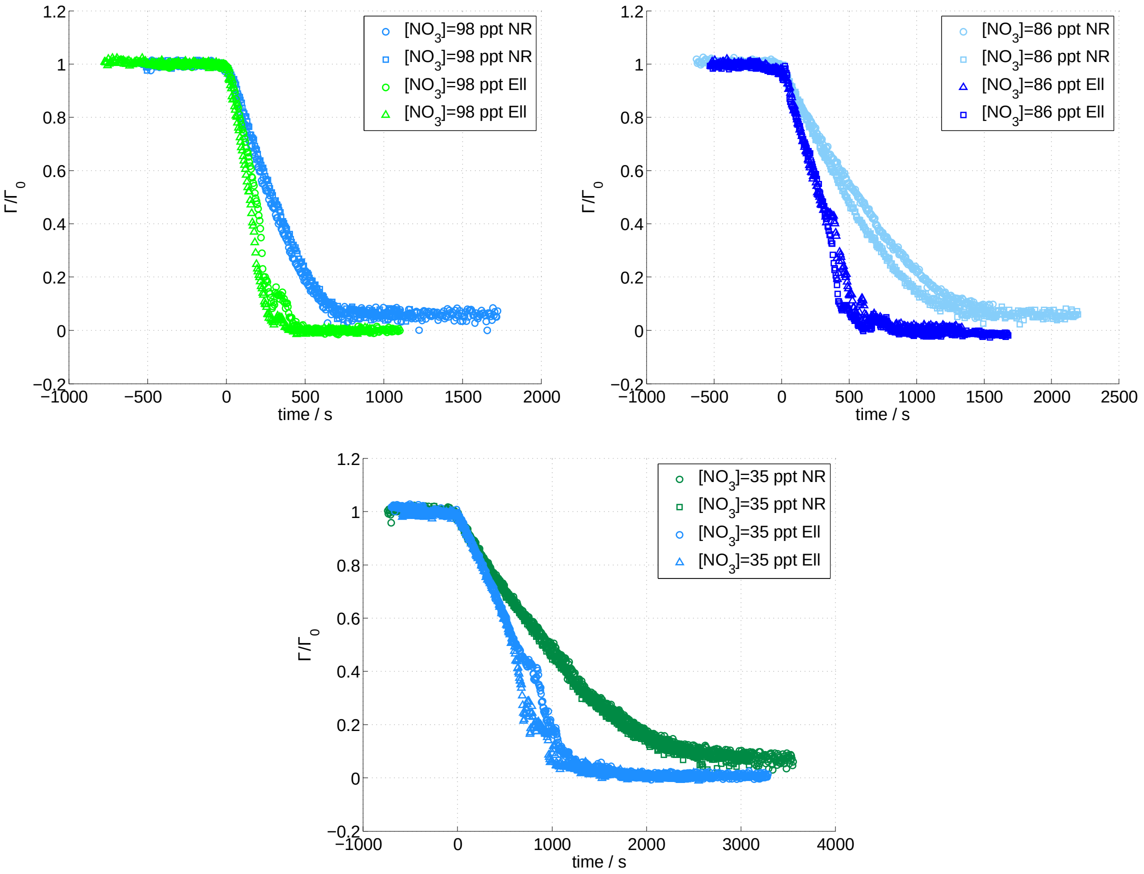

Figure 7.20: Comparison of surface excess decays recorded with NR-dMO (NR) and ellipsometry-hMO (Ell) for MO exposed to $[NO_3] = 98$ ppt (top left), $[NO_3] = 86$ ppt (top right) and $[NO_3] = 35$ ppt (bottom). The surface excess decays have been normalised to their initial values. The decays do not overlap.

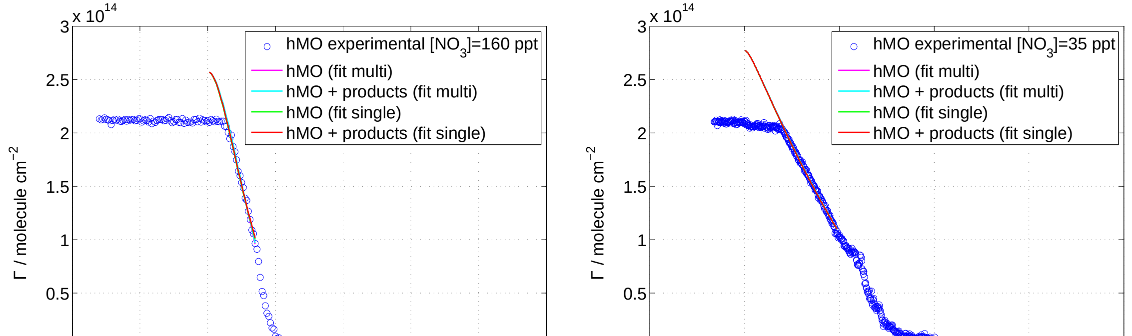

fits, k_{surf} varying in the range $(2.1 - 3.9) \times 10^{-8}$ cm^2 molecule^{-1} s^{-1}. Both desorption lifetimes of NO_3 obtained from the simultaneous fitting agree with the values found by the individual fits. The desorption lifetime of NO_2 ranges from 1.7×10^{-8} s to 4.3×10^{-8} s for the individual fits and those values are smaller than the $\tau_{d;NO_2}$ obtained by the simultaneous fit, $(4.5 \pm 0.1) \times 10^{-8}$ s.

The comparison between the kinetic parameters obtained analysing NR and ellipsometry data shows some similarities and a fundamental difference. In terms of the values obtained from the individual fits, the ranges of desorption lifetimes (both NO_3 and NO_2) overlap. Considering the simultaneous fit, the second desorption lifetime of NO_3, $\tau_{d;NO_3;2}$, obtained with the ellipsometry data is more than two times the value found for the NR data. This discrepancy is likely to be due to the different shape of the $\Gamma(t)$ recorded with the two techniques (Fig. 7.20).

The main difference between the two sets of data is found in the values of the rate coefficient, which do not agree. The extreme values of the range obtained from the individual fit of the ellipsometry data results to be twice the extreme values of the range found with the fitting of the NR data. This systematic difference is unlikely to be due to an error in the gas setup, such as production of higher $[NO_3]$. In the experimental conditions considered, the only way to produce more NO_3 would be to increase the production of O_3, but the gas production setup is already using the maximum amount of O_3 available. Otherwise, this effect could be explained with the appearance of products which may be detected by NR and contribute to the resulting $\Gamma(t)$ differently than for the ellipsometry. The characterisation of the intermediate states of the reaction would help in determining the reason of the differences found between NR and ellipsometry measurements.

	160 ppt	98 ppt	86 ppt
$[\mathrm{NO_3}] / 10^{8}$ molecule cm^{-3}	44 ± 7	26 ± 10	23 ± 12
$[\mathrm{NO_3}]^{\mathrm{multi}} / 10^{8}$ molecule cm^{-3}	54 ± 1	20 ± 1	7.4 ± 0.1
$[\mathrm{NO_3}]^{\mathrm{sing}} / 10^{8}$ molecule cm^{-3}	42 ± 1	22 ± 1	6.5 ± 0.1
$[\mathrm{NO_2}] / 10^{15}$ molecule cm^{-3}	0.53 ± 0.01	0.86 ± 0.08	1.30 ± 0.05
$[\mathrm{NO_2}]^{\mathrm{multi}} / 10^{15}$ molecule cm^{-3}	0.54 ± 0.01	1.1 ± 0.1	1.4 ± 0.1
$[\mathrm{NO_2}]^{\mathrm{sing}} / 10^{15}$ molecule cm^{-3}	0.78 ± 0.01	0.61 ± 0.01	1.6 ± 0.1
$(k_{\mathrm{surf}})^{\mathrm{multi}} / 10^{-8}$ cm^{2} molecule^{-1} s^{-1}	2.7 ± 0.1		
$(k_{\mathrm{surf}})^{\mathrm{sing}} / 10^{-8}$ cm^{2} molecule^{-1} s^{-1}	3.1 ± 0.1	3.7 ± 0.1	2.1 ± 0.1
$(\tau_{\mathrm{d;NO_3;1}})^{\mathrm{multi}} / 10^{-9}$ s	6.8 ± 0.1		
$(\tau_{\mathrm{d;NO_3;1}})^{\mathrm{sing}} / 10^{-9}$ s	8.6 ± 0.1	4.06 ± 0.03	11.8 ± 0.1
$(\tau_{\mathrm{d;NO_3;2}})^{\mathrm{multi}} / 10^{-9}$ s	26.6 ± 0.1		
$(\tau_{\mathrm{d;NO_3;2}})^{\mathrm{sing}} / 10^{-9}$ s	14.6 ± 0.1	35.6 ± 0.1	14.9 ± 0.1
$(\tau_{\mathrm{d;NO_2}})^{\mathrm{multi}} / 10^{-8}$ s	4.5 ± 0.1		
$(\tau_{\mathrm{d;NO_2}})^{\mathrm{sing}} / 10^{-8}$ s	1.7 ± 0.1	3.5 ± 0.1	3.7 ± 0.1

	35 ppt	36 ppt
$[\mathrm{NO_3}] / 10^{8}$ molecule cm^{-3}	9.3 ± 2.4	9.7 ± 2.7
$[\mathrm{NO_3}]^{\mathrm{multi}} / 10^{8}$ molecule cm^{-3}	5.5 ± 0.1	7.5 ± 0.1
$[\mathrm{NO_3}]^{\mathrm{sing}} / 10^{8}$ molecule cm^{-3}	6.1 ± 0.1	8.7 ± 0.1
$[\mathrm{NO_2}] / 10^{15}$ molecule cm^{-3}	1.6 ± 0.1	2.2 ± 0.1
$[\mathrm{NO_2}]^{\mathrm{multi}} / 10^{15}$ molecule cm^{-3}	1.4 ± 0.1	1.9 ± 0.1
$[\mathrm{NO_2}]^{\mathrm{sing}} / 10^{15}$ molecule cm^{-3}	1.6 ± 0.1	2.5 ± 0.1
$(k_{\mathrm{surf}})^{\mathrm{multi}} / 10^{-8}$ cm^{2} molecule^{-1} s^{-1}	2.7 ± 0.1	
$(k_{\mathrm{surf}})^{\mathrm{sing}} / 10^{-8}$ cm^{2} molecule^{-1} s^{-1}	2.3 ± 0.1	3.9 ± 0.1
$(\tau_{\mathrm{d;NO_3;1}})^{\mathrm{multi}} / 10^{-9}$ s	6.8 ± 0.1	
$(\tau_{\mathrm{d;NO_3;1}})^{\mathrm{sing}} / 10^{-9}$ s	7.3 ± 0.1	4.0 ± 0.1
$(\tau_{\mathrm{d;NO_3;2}})^{\mathrm{multi}} / 10^{-9}$ s	26.6 ± 0.1	
$(\tau_{\mathrm{d;NO_3;2}})^{\mathrm{sing}} / 10^{-9}$ s	26.8 ± 0.1	39.1 ± 0.1
$(\tau_{\mathrm{d;NO_2}})^{\mathrm{multi}} / 10^{-8}$ s	4.5 ± 0.1	
$(\tau_{\mathrm{d;NO_2}})^{\mathrm{sing}} / 10^{-8}$ s	3.9 ± 0.1	4.3 ± 0.1

7.7 Arachidonic acid exposed to NO_3

The results presented so far concern organic surfactants with only one double bond along the aliphatic chain, except the stearic acid which is saturated. In this section, the study of the oxidation kinetics of AA monolayers at the air–water interface exposed to NO_3 is presented; and this fatty acid contains 4 double bonds. The oxidation was investigated just with ellipsometry because the partially deuterated form of AA available commercially does not provide sufficient contrast for NR measurements. In fact, the deuterium atoms in the chain are 8 and the resulting scattering length density, calculated using the molecular volume estimated by Armen et al. [116] is 1.96×10^{-6} Å^{-2}. Missing the NR data on fully deuterated AA, a reliable determination of the product yields is not possible, however an estimation was made taking into account the results obtained for the other fatty acids, and the input parameters for the kinetic model where fixed to $c_S = 0.2$, $c_G = 0.45$ and $c_B = 0.35$. The values used for $k_{loss;G}$ and $D_{b;Z_B}$ were the same as the ones used in previous sections.

7.7.1 Ellipsometry

Figure 7.22 shows the surface excess decays of hAA monolayers at the air–water interface as a function of time with respect of $[NO_3]$.

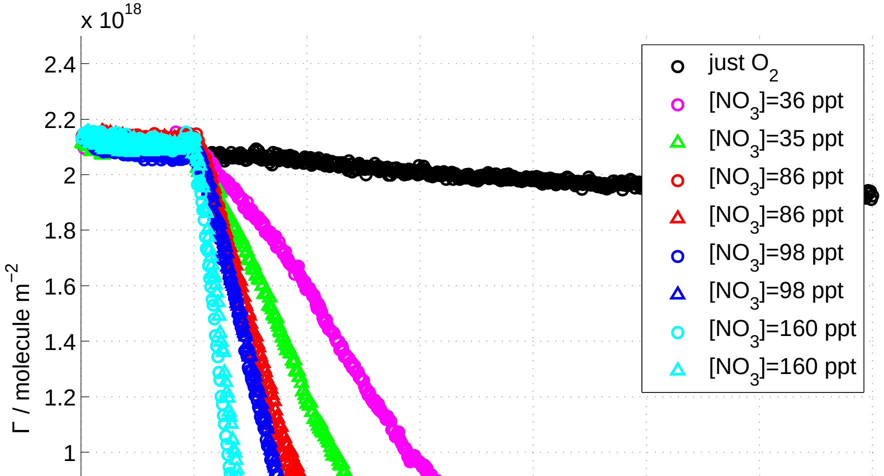

Independent of $[NO_3]$, the $\Gamma(t)$ profiles may be divided into two parts: the first part, $\Gamma > 1 \times 10^{18}$ molecule m^{-2}, shows a smooth decrease; the second part presents a slower decrease and some fluctuations. This may be due to the appearance of products, which form optically anisotropic domains.

Examples of the fit are displayed in Figure 7.23 (the complete set may be found in Appendix D). The kinetic parameters were constrained in the following ranges: k_{surf} varied in $(0.5 - 3) \times 10^{-8}$ cm^2 molecule^{-1} s^{-1}, $\tau_{d;NO_3;1}$ varied in $(5 - 18) \times 10^{-9}$ s, $\tau_{d;NO_3;2}$ varied in $(20 - 50) \times 10^{-9}$ s and $\tau_{d;NO_2}$ varied in $(0.1 - 6) \times 10^{-8}$ s. The fitting was performed following the procedures introduced in Section 7.3.

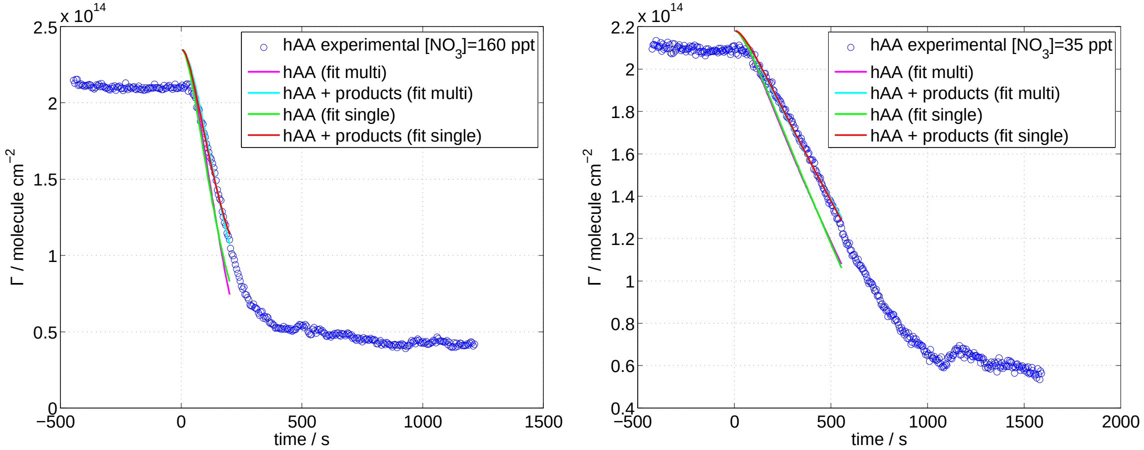

Figure 7.23: Experimental surface excess of hAA exposed to NO_3 fitted with the kinetic model. Comparison of the two fitting approaches (single and multi) is displayed. The calculated decays of hAA are shown as comparison with the calculated decays of hAA and products. (left) $[NO_3] = 160$ ppt. (right) $[NO_3] = 35$ ppt.

Table 7.8 reports a summary of the best fit values for the kinetic parameters obtained for the surface reaction between a hAA monolayer and gas-phase NO_3. The simultaneous fit of the 5 runs provides $k_{surf} = (1.5 \pm 0.1) \times 10^{-8}$ cm^2 molecule^{-1} s^{-1}, which is included in the range of values found with the individual fits k_{surf} included in $(1.02 - 2.4) \times 10^{-8}$ cm^2 molecule^{-1} s^{-1}. Both desorption lifetimes of NO_3 obtained with the simultaneous fit are in good agreement with the values determined by the

	160 ppt	98 ppt	86 ppt
$[NO_3]$ / 10^8 molecule cm^{-3}	44 ± 7	26 ± 10	23 ± 12
$[NO_3]^{multi}$ / 10^8 molecule cm^{-3}	46 ± 1	24 ± 1	18 ± 1
$[NO_3]^{sing}$ / 10^8 molecule cm^{-3}	48 ± 1	24 ± 1	21 ± 1
$[NO_2]$ / 10^{15} molecule cm^{-3}	0.53 ± 0.01	0.86 ± 0.08	1.30 ± 0.05
$[NO_2]^{multi}$ / 10^{15} molecule cm^{-3}	0.42 ± 0.01	1.2 ± 0.1	1.5 ± 0.1
$[NO_2]^{sing}$ / 10^{15} molecule cm^{-3}	0.80 ± 0.01	1.2 ± 0.1	1.3 ± 0.1
$(k_{surf})^{multi}$ / 10^{-8} cm^2 molecule^{-1} s^{-1}	1.5 ± 0.1		
$(k_{surf})^{sing}$ / 10^{-8} cm^2 molecule^{-1} s^{-1}	1.02 ± 0.01	1.02 ± 0.01	2.3 ± 0.1
$(\tau_{d;NO_3;1})^{multi}$ / 10^{-9} s	9.9 ± 0.1		
$(\tau_{d;NO_3;1})^{sing}$ / 10^{-9} s	17.0 ± 0.1	17.9 ± 0.1	5.0 ± 0.1
$(\tau_{d;NO_3;2})^{multi}$ / 10^{-9} s	37.2 ± 0.1		
$(\tau_{d;NO_3;2})^{sing}$ / 10^{-9} s	22 ± 1	20.0 ± 0.1	50.0 ± 0.1
$(\tau_{d;NO_2})^{multi}$ / 10^{-8} s	3.0 ± 0.1		
$(\tau_{d;NO_2})^{sing}$ / 10^{-8} s	6.0 ± 0.1	6.0 ± 0.1	0.11 ± 0.01

	35 ppt	36 ppt
$[NO_3]$ / 10^8 molecule cm^{-3}	9.3 ± 2.4	9.7 ± 2.7
$[NO_3]^{multi}$ / 10^8 molecule cm^{-3}	10.0 ± 0.1	6.2 ± 0.1
$[NO_3]^{sing}$ / 10^8 molecule cm^{-3}	11.5 ± 0.1	7.1 ± 0.1
$[NO_2]$ / 10^{15} molecule cm^{-3}	1.6 ± 0.1	2.2 ± 0.1
$[NO_2]^{multi}$ / 10^{15} molecule cm^{-3}	1.7 ± 0.1	2.4 ± 0.1
$[NO_2]^{sing}$ / 10^{15} molecule cm^{-3}	1.3 ± 0.1	1.9 ± 0.1
$(k_{surf})^{multi}$ / 10^{-8} cm^2 molecule^{-1} s^{-1}	1.5 ± 0.1	
$(k_{surf})^{sing}$ / 10^{-8} cm^2 molecule^{-1} s^{-1}	2.4 ± 0.1	2.3 ± 0.1
$(\tau_{d;NO_3;1})^{multi}$ / 10^{-9} s	9.9 ± 0.1	
$(\tau_{d;NO_3;1})^{sing}$ / 10^{-9} s	5.0 ± 0.1	5.0 ± 0.1
$(\tau_{d;NO_3;2})^{multi}$ / 10^{-9} s	37.2 ± 0.1	
$(\tau_{d;NO_3;2})^{sing}$ / 10^{-9} s	50 ± 1	50 ± 1
$(\tau_{d;NO_2})^{multi}$ / 10^{-8} s	3.0 ± 0.1	
$(\tau_{d;NO_2})^{sing}$ / 10^{-8} s	0.71 ± 0.01	0.45 ± 0.01

7.8 Summary and discussion

The kinetic experiments on the single component monolayers had two main goals: (i) to determine the kinetic parameters of the heterogeneous reactions and (ii) to assess the reliability of ellipsometry as a substitute for NR.

The study of heterogeneous reactions of organic monolayers at the air–water interface exposed to oxidants is crucial to understand the role of such films for the atmospheric fate of organic-coated aqueous aerosol [130]. The studies performed on these type of reactions were often carried out monitoring the gas-phase species [50, 42, 48, 49]. Gross et al. [47] investigated the oxidation of organic monolayers at an air–solid interface and apart from monitoring the gas-phase species during the reaction, they analysed the product film with several surface spectroscopic techniques. The monitoring of the organic monolayer during oxidation at the air–water interface was introduced by King and co-workers [53] for the study of oleic acid exposed to O_3. To the best of our knowledge, no-one has investigated the oxidation of organic monolayer at the air–water interface by NO_3 by in situ kinetic measurements of the surface excess.

NR is a powerful technique to determine the surface excess of a deuterated monolayer at the air–ACMW interface, and partial and selective deuteration to access reaction mechanism and individual reaction rates in mixtures holds great potential. However the access to neutron beam time is limited. This limitation is the primary motivation to investigate the capabilities of ellipsometry as lab-based technique for the studies of single-component monolayers.

7.8.1 Experimental techniques

The use of NR and ellipsometry to investigate the heterogeneous reactions occurring at the air–water interface motivated the design of a dedicated reaction chamber (see Chapter 5). The use of the same sample environment and gas production set-up for both techniques removed possible discrepancies due to different experimental conditions.

Unexpectedly, the surface excess decays recorded with NR and ellipsometry have dif-

	$(k_{surf})^{multi}$ (NR) / cm^2 $molecule^{-1}$ s^{-1}	$(k_{surf})^{multi}$ (Ell) / cm^2 $molecule^{-1}$ s^{-1}	$(\gamma)^{multi}$ (NR)	$(\gamma)^{multi}$ (Ell)
MO + O_3	$(5.7 \pm 0.9) \times 10^{-10}$	$(5.1 \pm 0.6) \times 10^{-10}$	3×10^{-5}	2.8×10^{-5}
MO + NO_3	$(1.7 \pm 0.1) \times 10^{-8}$	$(2.7 \pm 0.1) \times 10^{-8}$	1×10^{-3}	1.4×10^{-3}
OA + NO_3	$(2.2 \pm 1.8) \times 10^{-8}$	$(1.26 \pm 0.01) \times 10^{-8}$	1.6×10^{-3}	6.2×10^{-4}
POA + NO_3	$(1.6 \pm 0.1) \times 10^{-8}$	$(1.8 \pm 0.1) \times 10^{-8}$	1.3×10^{-3}	7.5×10^{-4}
AA + NO_3	/	$(1.5 \pm 0.1) \times 10^{-8}$	/	7.7×10^{-4}
SA + NO_3	$< 2 \times 10^{-12}$	/	/	/

Table 7.9: Rate coefficients, k_{surf}, and uptake coefficients, γ, for all the reactions studied in this chapter are summarised. The kinetic parameters obtained with NR and ellipsometry (Ell) are distinguished.

to an error in the amount of solution spread at the interface; however the variability due to spreading is expected to be in the order of only a few percent (e.g. compare initial values of Fig. 7.5 and Fig. 7.7). The other source of error may be the estimated refractive indices. In the thin film approximation, a lower refractive index used in the analysis results in a smaller phase shift for a given surface excess (see Fig. 3.3), hence an overestimation of the refractive indices would lead to underestimation of surface excess values. Since this effect is expected to be linear, the overall shape of the surface excess decay is not expected to be affected. The overall scaling of Γ, however, does not affect the k_{surf} values.

The difference found in the shape of the initial part of the surface excess decays measured by NR and ellipsometry represents a major issue. For OA and POA the surface excess decay measured with ellipsometry show a lower loss at the beginning of the reaction, while the MO oxidation by NO_3 has a higher rate of loss compared to NR. The lower rate of loss in the initial part of the OA and POA surface excess decays is likely to be due to product formation. Products may have different refractive indices than the reactant and they may form anisotropic domains which break the linearity between Γ and measured phase shift. In order to investigate the presence of anisotropic domains during the oxidation reaction, BAM imaging would be helpful. However, the reaction chamber used was not suitable for in situ BAM imaging, because the objective of the BAM instrument needs to be very close to the surface and this requirement could not while it provided complementary information on reactions with NO_3. In fact, the kinetic parameters provided by NR and ellipsometry agree for MO exposed to O_3, while they differ for the other systems (especially for OA and MO + NO_3). However, for the NO_3 reactions, ellipsometry provided indirect information about the appearance of products already in the first part of the surface excess decay, which were not detected by NR. The agreement between ellipsometry and NR data found for the MO+ O_3 system suggests that even though the probed areas are very different (mm^2 vs cm^2) it was measured the same surface excess decay. The deviation in the decay of the other systems reveals the presence of anisotropic domains of products which break the calibration to determine Γ from the phase shift measured using ellipsometry. To obtain quantitative information from these ellipsometry data, it would be necessary to investigate the anisotropy of the monolayer by BAM measurements. These measurements could in principle provide a calibration of the anisotropy, which could then be used to restore the relationship between Γ and the measured phase shift. With knowledge of the calibration of anisotropy, the shape of the surface excess decay may be analysed to estimate for example the lifetime of the products at the air–water interface, and studies of the phase behaviour of various mixtures of reactants and possible product may even lead to their indirect identification.

In light of the results obtained, for future work when dealing with a new system it is recommend to perform test measurements using both techniques. If the results agree, ellipsometry could substitute NR; otherwise, NR is necessary to study the kinetics of the reaction, while ellipsometry can help in extracting information about the product formation.

7.8.2 Discussion of the results and atmospheric implications

The kinetic parameters obtained by analysing the NR data allows discussions of the effect of the chemical structure, i.e. chain length, degree of unsaturation and headgroup, and the fate of MO at night, since reaction with both key night-time oxidant O_3 and NO_3 have been studied.

The different molecules studied resulted in rate coefficients on the order of 10^{-8} cm^2

bond at the interface. The present results for organic monolayers at the air–water interface are in a better agreement with the results of Moise et al., and this may suggest that the accessibility of the reactive site for these monolayers is similar to that of a thick film. The difference in reactive uptake values of NO_3 by organic monolayer adsorbed to different substrates would also be interesting to investigate.

The main findings of the present work are discussed in the following paragraphs.

Chain length and headgroup

The rate coefficients displayed in the second column of Table 7.9 for the reactions with NO_3 do not show a strong difference between the unsaturated organic compounds investigated to within the precision of the measurements. However, the direct comparison between surface excess decays allows the pointing out of a correlation between the headgroup and the presence of products at the end of the reaction. Molecules with COOH headgroup (OA and POA) left surface-active products at the air–water interface, while MO which has $COOCH_3$ as headgroup did not leave any detectable product.

In the case of ozonolysis, the MO rate coefficient is an order of magnitude higher than the value found for OA [53] with a similar experimental setup. Hearn et al. [23] compared the reactivity of pure OA and MO particles and reported different reaction mechanisms that were attributed to a larger degree of order in the OA particles. The reactive site for ozonolysis is the double bond which is in a similar chemical environment for the fatty acid and its methyl ester in a monolayer on an aqueous subphase. The reactive site is thus proposed to be more accessible to attack by ozone on geometric considerations given that at equivalent surface pressures the methyl ester head group occupies a considerably larger area than the corresponding carboxylic acid (see Sections 6.2.2 and 6.2.3).

Chain saturation

The real difference in the fate of the monolayer is made by the absence of unsaturation reactive species, located in the bulk [100], by slowing down the diffusion of the organic compound from bulk to surface and the diffusion of the oxidant from gas phase to bulk. However, the saturated fatty acids monolayer was found to prevent oxidation also of unsaturated organics at the interface, as discussed in Section 8.3 on the study of the binary mixture monolayer OA-SA.

Oxidants: O_3 vs NO_3

The study of the oxidation of MO upon exposure to O_3 and NO_3 shows - as expected - clearly a stronger oxidative power of NO_3 compared to O_3. The oxidative power may be quantified from the uptake coefficient [47] of O_3 and NO_3 as the product of uptake coefficient and gas-phase oxidant concentration. O_3 is found in the atmosphere at concentration between 10 and 100 ppb. The oxidative power calculated for the lowest concentration would be 7.5×10^6 molecule cm^{-3}. For the calculation of the oxidative power, NO_3 concentrations were chosen to be representative for a range of concentrations from high (50 ppt) to low (5 ppt) values, which could be encountered in the atmosphere owing to spatial and seasonal fluctuations [14]. The resulting oxidative powers are respectively 1.2×10^6 molecule cm^{-3} and 1.2×10^5 molecule cm^{-3}. Although the concentration of NO_3 in the atmosphere is low compared to O_3, these results suggest that night-time oxidation is likely to be dominated by NO_3. This finding suggests that further investigation of the oxidation driven by NO_3 is required to understand the fate of aerosol droplets as well as studies of the key daytime oxidant OH.

The rapid loss of the organic monolayers resulting from the experimental data of the oxidative decays does not agree with field studies, which show longer lifetime for unsaturated organics [133, 134, 135, 25]. The unsaturated organics may have longer lifetime if protected from oxidative attack by gas-phase species inside highly viscous aerosol particles [136, 137, 138] or if mixed with non-reactive species. This is the key motivation to investigate the oxidation of binary mixtures, which represent closer models to real aerosol droplets (Chapter 8).

Chapter 8

Kinetic experiments of mixed organics monolayers

8.1 Introduction

In this chapter the kinetic experiments performed with the monolayers of binary mixture exposed to NO_3 are presented. The composition of all the binary mixtures investigated is 1:1 by mole. The resulting surface excess profiles are compared qualitatively with the corresponding surface excess profiles measured with the single component monolayers. The kinetic analysis is presented and the parameters are discussed and compared with the kinetic parameters of the single component film.

Section 8.2 presents the surface oxidation kinetics of OA-MO mixtures, where both components react with NO_3. Out of the six possible pairs from dOA, hOA, dMO and hMO, two were chosen: dMO-hOA and dOA-hMO. Section 8.3 concerns the surface oxidation kinetics of the OA-SA mixture, where SA is assumed to be non-reactive, hence just the mixture dOA-hSA was investigated.

The reaction kinetics of the mixtures are discussed in comparison with the literature.

8.2 OA-MO mixture exposed to NO_3

for the deuterated form (see Table 5.1). The NR data analysis was performed in the same way as for the single component monolayers. The resulting Γ(t) profiles show the surface excess of the deuterated organic component; however to avoid confusion with the results presented for the pure monolayers, the data are always labelled with the mixture name.

The data recorded for the two mixtures are presented in separate sections, and the kinetic parameters are discussed in comparison with the parameters obtained for the corresponding pure monolayers.

dMO-hOA

Figure 8.1 displays the surface excess decays of 1:1 dMO-hOA monolayers at the air–ACMW interface as a function of time with respect to $[NO_3]$. $[NO_3]$ ranges from (23 ± 4) ppt to (98 ± 40) ppt. The minimum value reached by the surface excess is $\sim 1.5 \times 10^{17}$ molecule m^{-2}, which may be reduced to a negligible value with greater co-adding of the data Hence no surface active products are expected to remain at the interface, as it was found for the pure monolayers. According to this, the product yields were chosen as for the pure dMO monolayers: $c_S = 0$, $c_G = 0.45$ and $c_B = 0.35$. The exposure of the monolayer to pure O_2 and to $[NO_2] = (141 \pm 3)$ ppm shows a similar dMO-hOA surface excess decay, suggesting that the loss rate is determined by the gas flow together with the poor stability of the monolayer. This finding is in agreement with the data recorded on the pure monolayer (Section 7.6), hence it can be concluded that the presence of hOA does not change the stability of dMO at the air–water interface.

For each oxidant condition, the Γ(t) profile of the mixture was normalised to its initial value and compared to the normalised Γ(t) profile of the corresponding pure system. The decays were shifted in time to overlap the start of the decays. Examples of dMO-hOA surface excess decays compared to dMO decays are shown in Figure 8.2, the full set may be found in Figures E.1 and E.2 of Appendix E. The overall shape of the Γ(t) profiles is similar, however the dMO-hOA Γ(t) presents a small increase in surface excess just before the beginning of the decay, which is not found in the pure monolayer.

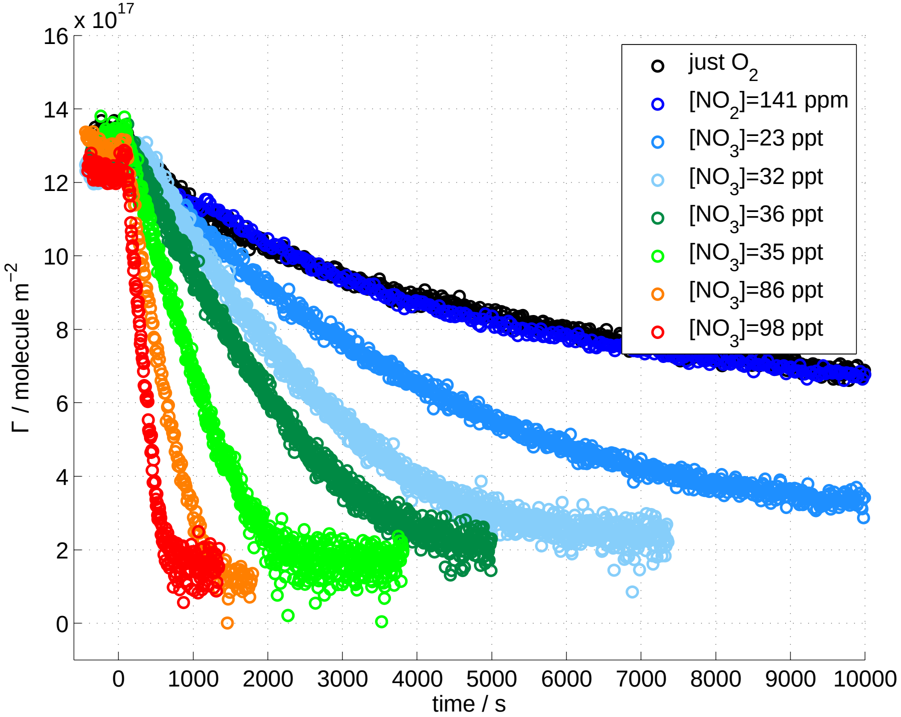

Figure 8.1: Surface excess decays of dMO-hOA exposed to different $[NO_3]$; mean values are displayed in the legend. Data were recorded with NR. Time $t = 0\,s$ represents the start of the exposure. Data are shown without error bars for clarity. The relative errors are on the order of 1 %.

and it was found that the double bond could isomerise, resulting in a change in surface pressure. No increase in the surface excess was detected, which is in agreement with the data recorded in the present work for dOA (see Section 7.3). Furthermore, they used a time resolution of 800 s, while the data presented here have a time resolution of 5 s and the increase of surface excess has a time scale between 200 s and 500 s, hence the effect would not have been detected in the work of King et al..

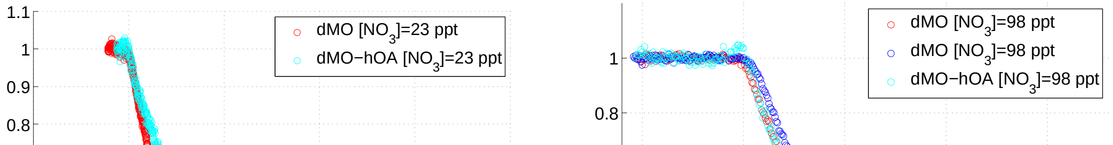

The kinetic fitting was performed applying the same model used for the pure monolayers and all the runs were fitted simultaneously ('multi' in tables). The kinetic parameters were constrained over the same ranges of values used for the pure system. This basic approach was chosen in order to have a direct comparison between oxidation of monolayers of the binary mixture and the single components. Several variations to the model may be applied to include the presence of the other organic component, e.g. the accommodation coefficient. However, the number of parameters to be determined was already large and further parameters would add greater uncertainties to the results without a real gain in information. Examples of the fits are displayed in Figure 8.3 (see Figures E.4 and E.5 of Appendix E for the complete data sets). As for the pure monolayers, the simultaneous fitting lead to an accurate description of the slow decay, while the fit of the fast one is poor. However, for the mixture it was decided to apply just the simultaneous fitting since for the pure monolayers it was found that the kinetic parameters of the simultaneous fit were in agreement with the results obtained with the individual fit of each run (see Section 7.6).

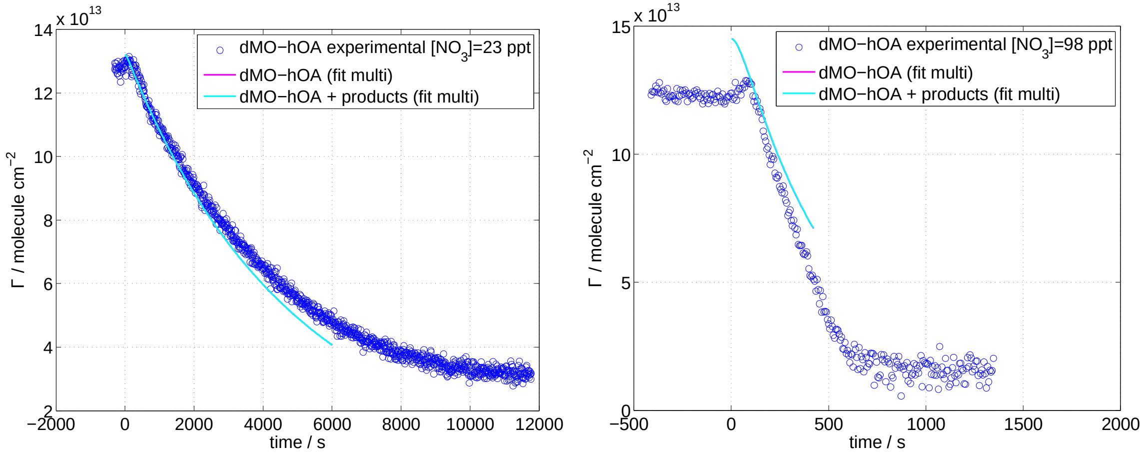

Figure 8.3: Experimental surface excess of dMO-hOA exposed to NO_3 fitted with the kinetic model. The calculated decays of dMO-hOA are shown for comparison with the calculated decays of dMO-hOA and its reaction products. (left) $[NO_3] = 23$ ppt. (right) $[NO_3] = 98$ ppt.

	98 ppt	86 ppt	35 ppt
$[NO_3]$ / 10^8 molecule cm^{-3}	26 ± 10	23 ± 12	9.3 ± 2.4
$[NO_3]^{multi}$ / 10^8 molecule cm^{-3}	32 ± 1	20 ± 1	8 ± 1
$[NO_2]$ / 10^{15} molecule cm^{-3}	0.86 ± 0.08	1.30 ± 0.05	1.6 ± 0.1
$[NO_2]^{multi}$ / 10^{15} molecule cm^{-3}	0.7 ± 0.1	1.0 ± 0.1	1.3 ± 0.1
$(k_{surf})^{multi}$ / 10^{-8} cm^2 molecule^{-1} s^{-1}	0.7 ± 0.1		
$(\tau_{d;NO_3;1})^{multi}$ / 10^{-9} s	11.7 ± 0.4		
$(\tau_{d;NO_3;2})^{multi}$ / 10^{-9} s	10.1 ± 0.4		
$(\tau_{d;NO_2})^{multi}$ / 10^{-8} s	6.0 ± 0.5		

	36 ppt	32 ppt	23 ppt
$[NO_3]$ / 10^8 molecule cm^{-3}	9.7 ± 2.7	8.7 ± 2.8	6.1 ± 1.2
$[NO_3]^{multi}$ / 10^8 molecule cm^{-3}	7.7 ± 0.5	5.9 ± 0.3	4.0 ± 0.1
$[NO_2]$ / 10^{15} molecule cm^{-3}	2.2 ± 0.1	2.7 ± 0.2	3.3 ± 0.2
$[NO_2]^{multi}$ / 10^{15} molecule cm^{-3}	2.2 ± 0.2	2.8 ± 0.2	3.6 ± 0.2
$(k_{surf})^{multi}$ / 10^{-8} cm^2 molecule^{-1} s^{-1}	0.7 ± 0.1		
$(\tau_{d;NO_3;1})^{multi}$ / 10^{-9} s	11.7 ± 0.4		
$(\tau_{d;NO_3;2})^{multi}$ / 10^{-9} s	10.1 ± 0.4		
$(\tau_{d;NO_2})^{multi}$ / 10^{-8} s	6.0 ± 0.5		

Table 8.1: Kinetic parameters, resulting from the fitting of the experimental data recorded with NR, of the system dMO-hOA+ NO_3 are displayed. Each column represents an oxidant condition. Superscripts 'multi' refers to the type of fitting performed (see text for details). Lines 1 ($[NO_3]$) and 3 ($[NO_2]$) of each table report the values measured with FTIR spectroscopy and their associated errors. All the others values and errors are obtained from the kinetic fitting.

model. However, to investigate further the effect of mixing would be beneficial to study dMO-hMO mixtures at different ratios, and then compare with the results of dMO-hOA mixtures to deconvolute the effect of the hOA, which could be physical, in the sense that the ordering in the mixed film is different from the ordering in the single component monolayer. This applies to all the mixtures studied in this work. The desorption lifetimes of NO_3 are: $\tau_{d;NO_3;1} = (11.7 \pm 0.4) \times 10^{-9}$ s and $\tau_{d;NO_3;2} = (10.1 \pm 0.4) \times 10^{-9}$ s. These two values are very close to each other, which was not the case for the pure monolayer, where the value of $\tau_{d;NO_3;1}$ was half of the value of $\tau_{d;NO_3;2}$, respectively $(5.5 \pm 0.1) \times 10^{-9}$ s and $(11.3 \pm 0.1) \times 10^{-9}$ s. This finding suggests that the availabilparameters obtained allowed a comparison between the reaction with NO_3 of dMO mixed with hOA and of pure dMO. The resulting rate coefficient for dMO-hOA exposed to NO_3 is lower than the rate coefficient found for the reaction with dMO. From these rate coefficients, the gas uptake coefficients, γ, may be estimated following the approach of Hearn et al. [23]. The rate coefficient were obtained from the rate of loss of organic material at the interface, hence the gas uptake coefficient may be thought as an effective gas uptake by the specific organic compound under investigation. The NO_3 uptake coefficient for the pure dMO monolayer is $\sim 10^{-3}$, while the NO_3 uptake coefficient for the dMO mixed with hOA is $\sim 2 \times 10^{-4}$. The interfacial mixing therefore resulted in a decrease of uptake coefficient of about 5 times. To the best of our knowledge, data on binary mixed organic monolayer at the air–water interface are not available. Experimental data recorded with a rotating flow-tube reactor by Knopf et al. [139] on biomass burning surrogates exposed to NO_3 show an uptake coefficient of $1 - 26 \times 10^{-3}$ for three organic species studied (levoglucosan, abietic acid and nitroguaiacol), and for the mixture of those 3 components in the mass ratio 60 : 2 : 1 the uptake coefficient was ranging from $(2.61 \pm 1.51) \times 10^{-3}$ to $(10.10 \pm 7.90) \times 10^{-3}$ depending on the relative humidity and experimental method used. Differently from our findings, the NO_3 uptake on the mixture was consistent with the value found for the single components; however it is important to underline that NO_3 in nitroguaiacol had an uptake coefficient one order of magnitude higher than the other two organic compounds, hence this may explain the resulting uptake coefficient for the mixture.

The lower NO_3 uptake coefficient leads to a longer lifetime of MO when mixed with another reactive molecule. This may explain the discrepancy often found between laboratory study and field measurements [133, 134, 135, 25]. Laboratory studies, which usually focus on single component model system, lead to lifetime values smaller than those measured in the atmosphere, where the aerosol is made of many organic compounds [140, 141, 142, 26, 143].

NR measurements are not chemical specific, hence the presence of intermediate products, which may behave differently depending on the surrounding environment, cannot be revealed. The investigation of these intermediate states would be interesting.

mixture as well (c_S = 0.145, c_G = 0.45 and c_B = 0.35). The loss of the soluble and volatile products was modelled as in the pure system. The exposure of the monolayer to pure O_2 (O_2 blank) produced a negligible surface excess decay overall but showed some fluctuations in the first 3000 s, which were not found for the pure system. However, the exposure to $[NO_2]$ = (141 ± 3) ppm (NO_2 blank) shows a smooth and constant surface excess profile. This discrepancy between the two blanks is hard to justify, but probably a repeat of the O_2 blank would help in understanding if the measured surface excess was physically realistic or just related to uncontrolled external causes. Unfortunately, the restricted access to NR beam time did not allow the repeat of this long run (~ 3 hours). In the kinetic analysis, the dOA-hMO film was assumed to be stable under non oxidant gas flow, as in the case of pure dOA monolayers (Figure 7.5).

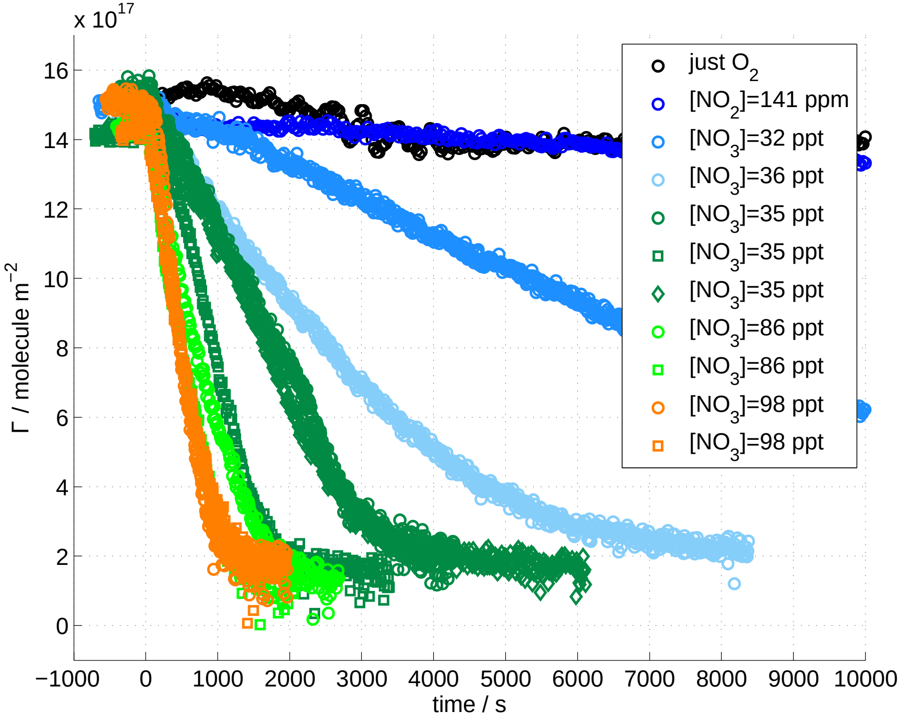

Figure 8.4: Surface excess decays of dOA-hMO exposed to different values of $[NO_3]$; mean values are displayed in the legend. Data were recorded with NR. Time t = 0 s represents the start of the exposure. Data are shown without error bars for clarity.

excess of dOA-hMO does not overlap with the dOA surface excess decay. For some of the [NO_3] values (Fig. 8.5 [NO_3] = 32 ppt) the rate of loss of dOA in the mixture is significally slower than the rate of loss of the pure dOA. However, when repeats are available (Fig. 8.5 [NO_3] = 86 ppt), the rate of loss presents a great variability both for mixture and for pure monolayer. It is important to remember that the oxidant concentrations are known only with a considerable error (at least 30 %) and this can explain the variability of the recorded rates of loss. However, the strong variation of the rate of loss of both pure system and binary mixture is not justifiable only with the uncertainty in the gas concentration, hence other factors may play a role. For example, the relative humidity, RH, can affect greatly the [NO_3] as shown by Schütze and Herrmann [144], who investigated the NO_3 uptake on aqueous surfaces and found an [NO_3] value lower than expected when the relative humidity was about 90 %. The concentration value halves with respect to the value measured at RH ~ 0 %. Since the RH is not controlled in our experimental setup, this may be the cause of the great variability observed. In particular, during the acquisition of the dOA-hMO data, the weather condition changed dramatically: from dry and hot to cold and wet. The neutron beam time was at the end of July 2013, and after the 3 days at stable temperature and RH, the weather changed to lower temperature and higher RH values. This dramatic change in conditions was not experience in the other experiments. Unfortunately, the RH could not be monitored inside the reaction chamber during the experiment and no quantitative estimation of the effect could be performed. However, to account for the reduction of [NO_3] due to RH in the kinetic fitting, the range of values was chosen appropriately.

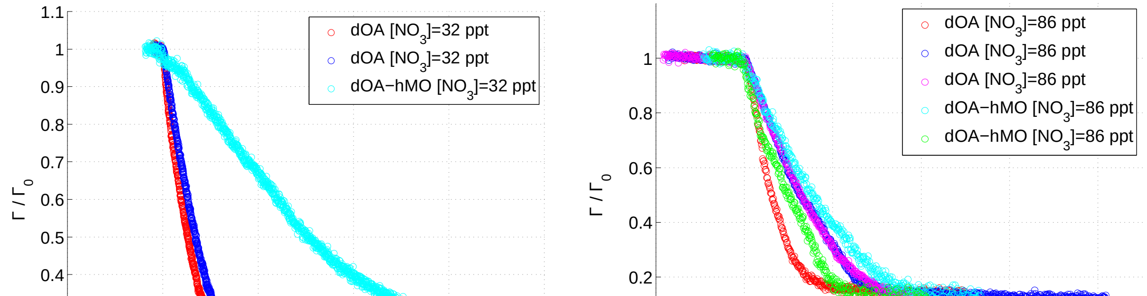

of the fits are shown in Figure 8.6 (the missing runs are displayed in Figures E.6 and E.7 of Appendix E). The quality of the fit was poor for the high [NO_3] as previously found. Similarly to the previous mixture, the fitting was performed down to a value of surface excess ~ $\Gamma_0/2$, which ensured that the films conformed to the uniform layer approximation for NR (i.e. the layer thickness is larger than the width of the aliphatic chain, absence of domains).

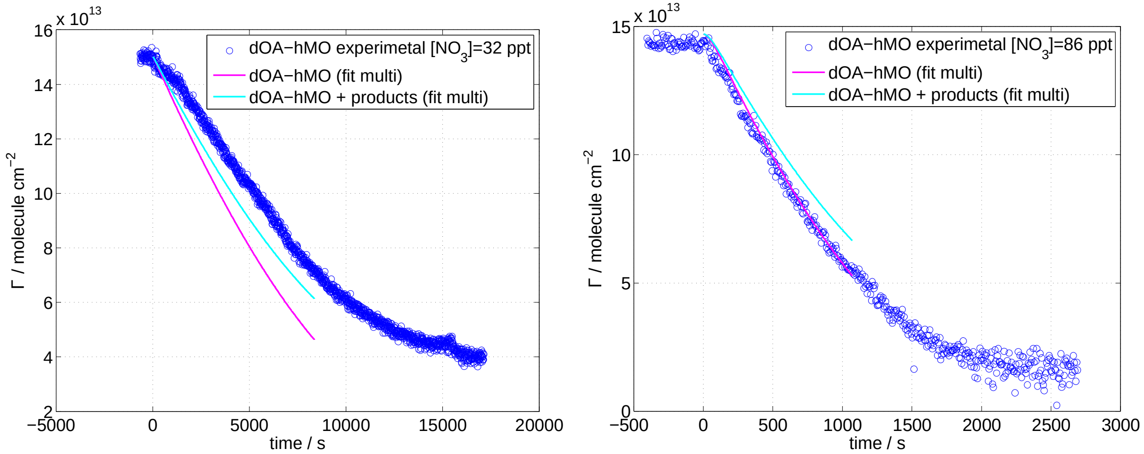

Figure 8.6: Experimental surface excess of dOA-hMO exposed to NO_3 fitted with the kinetic model. The calculated decays of dOA-hMO are shown for comparison with the calculated decays of dOA-hMO and its reaction products. (left) [NO_3] = 32 ppt. (right) [NO_3] = 86 ppt.

The best fit values for the kinetic parameters related to the surface reaction of dOA-hMO monolayers exposed to gas-phase NO_3 are summarised in Table 8.2. The fitting lead to a value of rate coefficient of $(1.00 \pm 0.05) \times 10^{-8}$ cm^2 molecule^{-1} s^{-1}, which is at the lower limit of the range chosen for the fitting. This may suggest that the range was too narrow, hence affecting the resulting parameter. However, in that case the fit would push the [NO_3] to the lower limit to compensate the rate coefficient, and this does not happen, hence the value found can be thought as the best fit. The value of k_{surf} of dOA-hMO exposed to NO_3 results as half of the value found for the pure system. This result is parallel with the dMO-hOA system, suggesting that the effect

	98 ppt	98 ppt	86 ppt
$[NO_3]$ / 10^8 molecule cm^{-3}	26 ± 10	26 ± 10	23 ± 12
$[NO_3]^{multi}$ / 10^8 molecule cm^{-3}	24 ± 1	24 ± 1	26 ± 1
$[NO_2]$ / 10^{15} molecule cm^{-3}	0.86 ± 0.08	0.86 ± 0.08	1.30 ± 0.05
$[NO_2]^{multi}$ / 10^{15} molecule cm^{-3}	1.2 ± 0.1	0.82 ± 0.02	1.03 ± 0.05
$(k_{surf})^{multi}$ / 10^{-8} cm^2 molecule^{-1} s^{-1}	1.00 ± 0.05		
$(\tau_{d;NO_3;1})^{multi}$ / 10^{-9} s	4.0 ± 0.1		
$(\tau_{d;NO_3;2})^{multi}$ / 10^{-9} s	10.0 ± 0.5		
$(\tau_{d;NO_2})^{multi}$ / 10^{-8} s	6.0 ± 0.1		

	35 ppt	36 ppt	32 ppt
$[NO_3]$ / 10^8 molecule cm^{-3}	9.3 ± 2.4	9.7 ± 2.7	8.7 ± 2.8
$[NO_3]^{multi}$ / 10^8 molecule cm^{-3}	11.5 ± 0.6	9.0 ± 0.5	4.0 ± 0.2
$[NO_2]$ / 10^{15} molecule cm^{-3}	1.6 ± 0.1	2.2 ± 0.1	2.7 ± 0.1
$[NO_2]^{multi}$ / 10^{15} molecule cm^{-3}	1.8 ± 0.2	2.4 ± 0.1	3.0 ± 0.1
$(k_{surf})^{multi}$ / 10^{-8} cm^2 molecule^{-1} s^{-1}	1.00 ± 0.05		
$(\tau_{d;NO_3;1})^{multi}$ / 10^{-9} s	4.0 ± 0.1		
$(\tau_{d;NO_3;2})^{multi}$ / 10^{-9} s	10.0 ± 0.5		
$(\tau_{d;NO_2})^{multi}$ / 10^{-8} s	6.0 ± 0.1		

Table 8.2: Kinetic parameters, resulting from the fitting of the experimental data recorded with NR, of the system dOA-hMO+ NO_3 are displayed. Each column represents an oxidant condition. Superscript ‘multi’ refers to the type of fitting performed (see text for details). Lines 1 ($[NO_3]$) and 3 ($[NO_2]$) of each table report the values measured with FTIR spectroscopy and their associated errors. All the other values and errors are obtained from the kinetic fitting.

benefit from experimental data on the binary mixtures: dOA-hOA and dMO-hMO. Those data would help in distinguishing the effect of the mixing of deuterated and hydrogenated forms of the same molecule from the effect due to mixing of different surfactants.

8.3 OA-SA mixture exposed to NO_3

The present section concerns the oxidation kinetics of monolayers made of OA and SA at the air–water interface that are exposed to NO_3. The experimental procedures were described in the previous sections. Since the dSA film exposed to NO_3 did not show change in the surface excess value, the mixture dSA-hMO was not investigated. No loss of dSA was assumed to occur on the time scale of the NR experiments (see Section 7.4), while the formation of stable reaction products cannot be excluded. The experimental data discussed in this section will concern just the mixture dOA-hSA. The hSA is virtually invisible for NR because its scattering length density is about 0.1% the value of the dOA scattering length density.

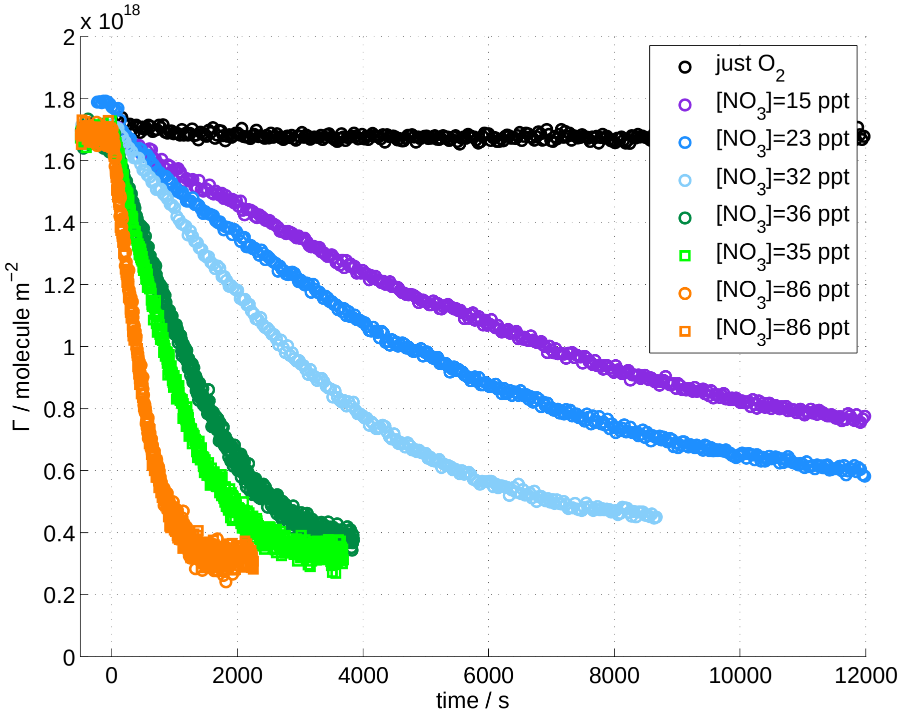

Figure 8.7: Surface excess decays of dOA-hSA exposed to different values of $[NO_3]$; mean values are displayed in the legend. Data were recorded with NR. Time t = 0 s represents the start of the exposure. Data are shown without error bars for clarity. The relative errors are on the order of 1 %.

proposed scenarios, hence the product yield for the kinetic analysis was not changed with respect to the values used for the pure system. It would be helpful to perform complementary studies by following the reaction with a chemically-specific technique, such as infrared spectroscopy or time-of-flight secondary ion mass spectroscopy [47].

The comparison between the dOA-hSA Γ/Γ_0 profile and the dOA Γ/Γ_0 profile with respect to $[NO_3]$ is shown in Figure 8.8 (the other comparisons may be found in Figures F.1 and F.2 of Appendix F). The general trend of the surface excess decays of dOA-hSA compared to dOA is a decrease in the rate of loss; however some repeats show a similar loss rate for the mixture and the pure system (e.g. see Fig. 8.8 $[NO_3] = 15$ ppt).

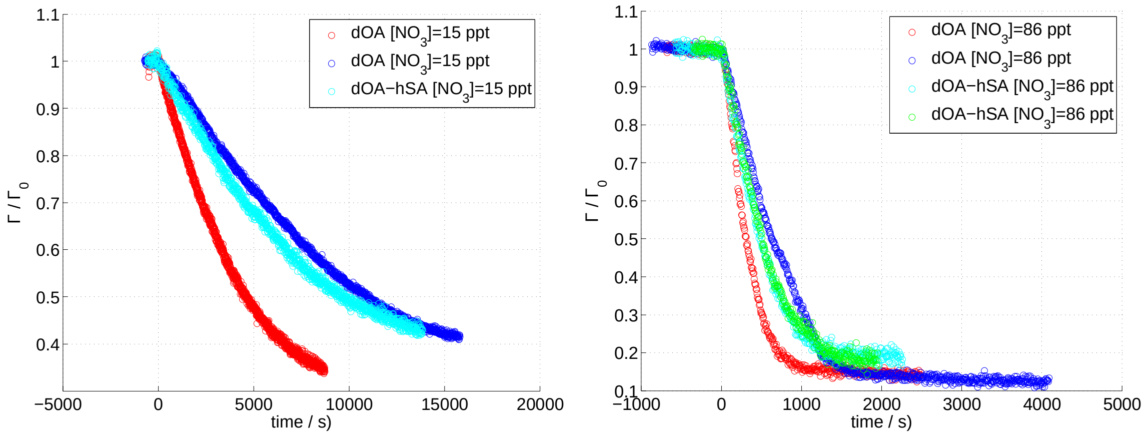

Figure 8.8: Surface excess decay of dOA-hSA compared with pure dOA. Γ was normalised to its initial value to allow a clearer comparison. (left) $[NO_3] = 15$ ppt. (right) $[NO_3] = 86$ ppt.

The kinetic analysis was performed with the model previously introduced, and the ranges of values to constrain the kinetic parameters were chosen equal to the ones used for the dOA pure system (Section 7.3).

As for the other binary mixtures, only the simultaneous fitting was applied to the experimental data and $\Gamma(t)$ profiles recorded at low $[NO_3]$ fitted better than the high concentrations. Examples of the fit are displayed in Figure 8.9 (the full data sets

	86 ppt	35 ppt	36 ppt
$[NO_3]$ / 10^8 molecule cm^{-3}	23 ± 12	9.3 ± 2.4	9.7 ± 2.7
$[NO_3]^{multi}$ / 10^8 molecule cm^{-3}	26 ± 1	11.5 ± 0.5	9.0 ± 0.6
$[NO_2]$ / 10^{15} molecule cm^{-3}	1.30 ± 0.05	1.6 ± 0.1	2.2 ± 0.1
$[NO_2]^{multi}$ / 10^{15} molecule cm^{-3}	1.4 ± 0.3	1.3 ± 0.1	1.9 ± 0.1
$(k_{surf})^{multi}$ / 10^{-8} cm^2 $molecule^{-1}$ s^{-1}	1.00 ± 0.02		
$(\tau_{d;NO_3;1})^{multi}$ / 10^{-9} s	6 ± 3		
$(\tau_{d;NO_3;2})^{multi}$ / 10^{-9} s	10 ± 1		
$(\tau_{d;NO_2})^{multi}$ / 10^{-8} s	6.0 ± 0.1		

	32 ppt	23 ppt	15 ppt
$[NO_3]$ / 10^8 molecule cm^{-3}	8.7 ± 2.8	6.1 ± 1.2	4.2 ± 1.4
$[NO_3]^{multi}$ / 10^8 molecule cm^{-3}	5 ± 2	4 ± 1	2.4 ± 0.6
$[NO_2]$ / 10^{15} molecule cm^{-3}	2.7 ± 0.2	3.3 ± 0.2	3.8 ± 0.2
$[NO_2]^{multi}$ / 10^{15} molecule cm^{-3}	2.8 ± 0.3	3.0 ± 0.1	4.1 ± 0.2
$(k_{surf})^{multi}$ / 10^{-8} cm^2 $molecule^{-1}$ s^{-1}	1.00 ± 0.02		
$(\tau_{d;NO_3;1})^{multi}$ / 10^{-9} s	6 ± 3		
$(\tau_{d;NO_3;2})^{multi}$ / 10^{-9} s	10 ± 1		
$(\tau_{d;NO_2})^{multi}$ / 10^{-8} s	6.0 ± 0.1		

Table 8.3: Kinetic parameters, resulting from the fitting of the experimental data recorded with NR, of the system dOA-hSA+ NO_3 are displayed. Each column represents an oxidant condition. Superscript ‘multi’ refers to the type of fitting performed (see text for details). Lines 1 ($[NO_3]$) and 3 ($[NO_2]$) of each table report the values measured with FTIR spectroscopy and their associated errors. All the others values and errors are obtained from the kinetic fitting.

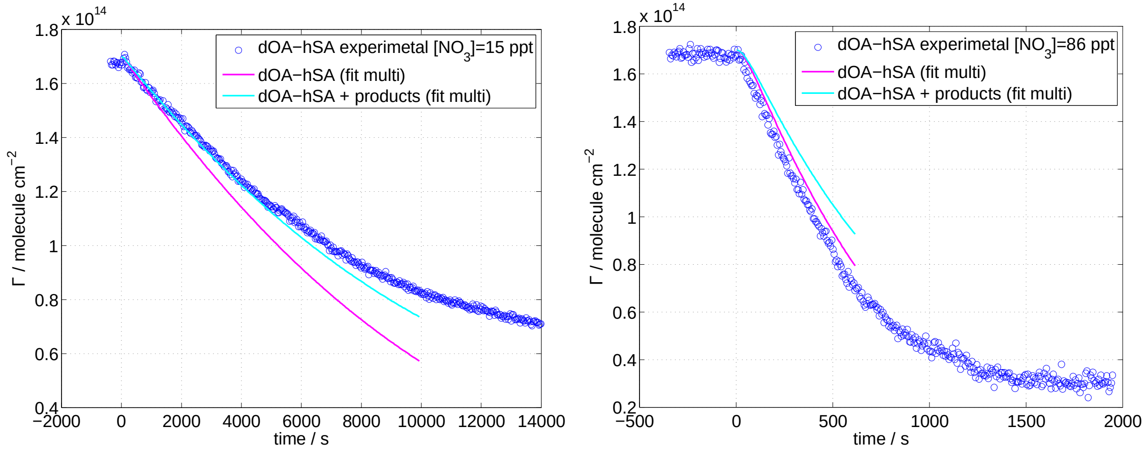

Figure 8.9: Experimental surface excess of dOA-hSA exposed to NO_3 fitted with the kinetic model. The calculated decays of dOA-hSA are shown for comparison with the calculated decays of dOA-hSA and its reaction products. (left) $[NO_3] = 15\,\mathrm{ppt}$. (right) $[NO_3] = 86\,\mathrm{ppt}$.

those found for the mixture dOA-hMO. However, considering just the direct comparison between the surface excess of the mixtures and the pure monolayers, the behaviour appears to be different. The comparison of the rate of loss of dOA-hMO with that of dOA does not provide a conclusive result, which could be due to the lack of control of RH during the experiment. The other mixture, dOA-hSA, presents always a rate of loss that is slower than that for the dOA monolayer.

The final values of $\Gamma(t)$ are slightly different: dOA mixed with hSA leaves more deuterated surface active material at the air–ACMW interface than dOA mixed with hMO. This difference suggests that the presence of hMO does not affect the reaction products of dOA exposed to NO_3, while the presence of hSA modifies the products yields. In this work, the reaction products of hSA and NO_3 and intermediate products of dOA are not considered. The different behaviour of the two mixtures may be explained by future investigations of the intermediates. Several studies, using different oxidant and organics, tried to describe these intermediates [133, 134, 135, 25, 24], but all of them used particles or bulk film in flow-tube reactors. To the best of our knowledge, such a study of an organic monolayer at the air–water interface is still missing, probably ture and RH inside the reaction chamber and in the surrounding environment; and (ii) to measure the single component monolayer during the same beam time as the mixture monolayer.

Two days of beam time on INTER (June 2014) and four days of beam time on FIGARO (September 2014) have been awarded in order to allow the acquisition of the missing conclusive data in order for the work from this chapter to be written up for publication.

Conclusions & Outlook

The overall goal of this thesis was to increase the scientific understanding of the fate of atmospheric aerosol with respect to the oxidation of insoluble surface films. This was achieved through the investigation of spread organic monolayers at the planar air–water interface exposed to O_3 and NO_3. The real-time monitoring of the surface excess of the surfactant during oxidation was performed by NR and ellipsometry. In order to study the oxidation reactions in an optimal way, four main areas of development were addressed.

1. NR is a very powerful technique to study interfaces, in particular deuterated monolayers at the air–ACMW interface. The use of FIGARO [63] for the kinetic experiments allowed the acquisition of data typically with a time resolution of 5 s but occasionally with scans as short as 1 s, which was crucial to reconstruct the surface excess decay as a function of time. Apart from the shape of the surface excess decay, it was important to determine whether the reaction left surface active products at the air–ACMW interface or not. This demand was met by my development of a background treatment method which enabled the distinction of a bare ACMW surface from 1% of a deuterated monolayer, i.e. $\sim 2 \times 10^{16}$ molecule m^{-2} (Section 4.2). This is a significant advance since NR was used to date to investigate the surface excess of deuterated monolayers at the air–ACMW interface and the interfacial composition of mixtures with an expected precision and sensitivity of $5-10\%$ [62, 94, 95]. The newly developed background treatment was fundamental to determine the presence of surface active products and to quantify them. This information was necessary to estimate the surface

ered as substitute for the investigation of single component and isotropic monolayers. NR requires the use of deuterated compounds, which could behave differently from the natural form and could introduce artifacts due to the presence of deuterated impurities, especially for the custom-made ones. However, ellipsometry could investigate both forms of compounds and assess if the reaction has been affected by deuteration or not. The isotherms of both forms were recorded and no difference was found, confirming that no isotope effect needs to be considered for the chemicals used. The two techniques have different footprints: $\sim$ cm^2 for NR and $\sim$ mm^2 for ellipsometry. Ellipsometry may be sensitive to formation of domains, their motion and their degree of optical anisotropy, while NR provides just an average information. In order to gain the most from these two technique and to reduce any experimental errors arising from the sample environment, I designed a dedicated sample chamber (Chapter 5). The MIMIK (Multi-Instruments Miniaturised Kinetics) chamber is suitable for both NR and ellipsometry measurements and it has a gas delivery system optimised for homogeneous diffusion. While the gas flow in the chamber could induce vibrations at the air–water interface and hence affect the monolayer stability, simulations of the gas flow inside the chamber demonstrated the very low pressure gradients experienced by the water surface [110]. NR measurements of air–D_2O interface further confirmed the results of the simulations. In order to reduce the volume of the chamber there is no control of the surface pressure, i.e. movable barriers, and hence the initial surface excess and pressure are determined by the amount of molecules spread. Spreading different amounts of molecules and then exposing the monolayers to the same oxidant condition, the influence of the initial surface excess and pressure has been investigated and the surface excess decay resulted to be unaffected.

3. A quantitative study of the kinetics of the heterogeneous reactions requires knowledge of the oxidant concentrations used, which led me to model and calibrate carefully all relevant gas-phase species (Section 6.3). In the case of O_3, UV-Vis spectra were recorded and the concentration was determined from the absorption

concentrations [14]. The uncertainties in these values ranged from 30 % to 50 %, which are similar to the uncertainties on similar studies (e.g. Gross et al. [47] 40%).

4. The analysis of the kinetic experiments required the development of a model to describe the reaction, which I carried out (Section 4.3). The ozonolysis of MO was modelled as a second order reaction [33], and the differential equation was integrated analytically leading to a function that was used to fit the data. The NO_3 oxidation required the development of a more sophisticated model, which considered, in addition to the reactions, several other mechanisms, such as gas-phase species accommodation, desorption, competition for absorption sites and transport. The newly developed model was built on the formalisms of the PRA framework [96]. It is a combination of KM-SUB and K2-SURF [97, 98], and it has been adapted for planar geometry. The system of differential equations was solved numerically in Matlab [101] and the solutions, i.e. the surface excess values of the organic compound, were used as fitting function. The kinetic parameters and related uncertainties were obtained through χ^2 minimisation.

The study of the heterogeneous reaction at the air–water interface could thus be optimised by the refinement of the NR data analysis method, a substantial improvement in the sample environment, the careful calibrations and modelling of the oxidant concentrations and the development of a detailed kinetic model to interpret the data.

The kinetic experiments on single component monolayers investigated using NR and ellipsometry (Chapter 7) had two main goals: (1) to determine the kinetic parameters of the heterogeneous reaction and (2) to assess the reliability of ellipsometry as a substitute for NR. Key findings are summarised below.

1. The organic compounds chosen as proxies for insoluble films at the aerosol surface were: methyl oleate, oleic acid, stearic acid, palmitoleic acid and arachidonic acid. The oxidation of MO by O_3 and NO_3 was studied, and the other compounds were exposed just to NO_3. This selection allowed me to compare the effect of

of a thick film instead of a monolayer on a solid substrate.

The rate coefficients were not affected by a modest change in chain lengths (OA vs POA) and different headgroups (MO vs OA) to within the precision of the measurements, even though practical difficulties were experienced during the experiment on the oxidation of OA by NO_3, which would benefit from additional experiments in the future. Nevertheless, the presence of surface-active products at the end of the reaction was found to be positively correlated with the presence of a COOH headgroup (OA, POA, AA). For the ozonolysis of MO the rate coefficient was found to be higher than that for the parent fatty acid [53]. This difference can be attributed to the lower degree of order in the MO chain and the larger area occupied by the headgroup which could make the reactive site more accessible to attack by ozone.

The most substantial difference in the fate of the monolayers upon oxidative attack was made by the absence of unsaturation in the aliphatic chain. In fact, SA was not lost from the interface during the NO_3 exposure. The NR data allowed the estimation of an upper limit for the rate coefficient of 2×10^{-12} cm^2 molecule^{-1} s^{-1}, which is four orders of magnitude lower than the rate coefficient of the unsaturated molecules. This is consistent with the different and slow reaction mechanism of H abstraction compared to addition to a $C=C$ double bond. The study of the oxidation of MO upon exposure to O_3 and NO_3 shows clearly a higher uptake coefficient of NO_3 compared to O_3 by a factor of 10^2. Even if the concentration of NO_3 in the atmosphere is low compared to that of O_3 ($5-50$ ppt vs $10-100$ ppb), these results suggest that night-time oxidation will be dominated by NO_3 rather than O_3 reactions. This finding suggests that further investigation of the oxidation driven by NO_3 are needed to fully understand the fate of aerosol droplets.

2. I showed that ellipsometry is a good substitute for NR for the study of the ozonolysis of MO, while it provided complementary information on the reactions of all the organic monolayers with NO_3. Specifically, the kinetic parameters determined using NR and ellipsometry agree for MO exposed to O, while they differ

The uptake coefficients obtained for the unsaturated molecules suggest a shorter lifetime compared to the values found by field studies [133, 134, 135, 25], while they agree with other laboratory studies on related systems [132]. These observations could perhaps be rationalised if the unsaturated organics have longer lifetimes in the presence of other molecules in the mixtures. The examination of this hypothesis provided the key motivation for the investigation of the oxidation of binary mixtures, which represent closer models to real aerosol droplets.

The kinetic experiments on binary mixtures investigated using NR only (Chapter 8), these studies had the goal to determine the relative rate coefficients of the individual components by monitoring the reduction in the surface excess of a deuterated component mixed with a hydrogenated component during the oxidation reactions. I studied two systems: (1) OA-MO and (2) OA-SA. This combination allowed the investigation of two unsaturated compounds as well as an unsaturated compound mixed with a saturated compound.

1. OA-MO was studied both as dOA-hMO (sensitive primarily to the loss of OA) and dMO+hOA (sensitive primarily to the loss of MO).

   The NO_3 uptake coefficient for the pure dMO monolayer is $\sim 10^{-3}$, while the NO_3 uptake coefficient for dMO mixed with hOA is $\sim 2 \times 10^{-4}$. The mixing resulted in a decrease in the uptake coefficient of about a factor of five. Similarly to dMO-hOA, the uptake coefficient for the mixture dOA-hMO is $\sim 3.7 \times 10^{-4}$, which was about 4 times smaller than the NO_3 uptake on pure dOA (1.6×10^{-3}). The lower NO_3 uptake coefficient leads to a longer lifetime of MO and OA when mixed with another reactive molecule. This result may therefore help to explain the discrepancy often found between laboratory study and field measurements [133, 134, 135, 25].

   The interpretation of these data on binary mixtures would benefit from experimental data on the binary mixtures: dOA-hOA and dMO-hMO. Those data would help in distinguishing between the effect of the mixing of deuterated and hydrogenated forms of the same molecule from the effect due to mixing of different surfactants.

presence of hMO does not affect the reaction products of dOA exposed to NO_3, the presence of hSA modifies the product yields.

In this work, the reaction products of hSA and NO_3 and eventual intermediate products of dOA were not considered. The different behaviour of the two mixtures may be explained further in the future by investigating these intermediates. Several studies, using different oxidants and organics, aimed to describe these intermediats [133, 134, 135, 25, 24], but all of them used particles or bulk film in flow-tube reactors. To the best of our knowledge, such a study of an organic monolayer at the air–water interface is still missing, probably because of the experimental challenges to be solved, e.g. the detection of a rather small number of organic molecules in a surface film. Nevertheless, following the development presented in this thesis, the undertaking of such a project has become a real possibility.

Future perspectives

The work presented in this thesis uses a flat air–water surfaces of more than $4\,\mathrm{cm}^2$ as proxies for aerosol particles. This choice is rationalised as the aerosol surface is effectively experienced as flat on the molecular level by the gas-phase oxidants chosen. Nevertheless, it would still be interesting to reproduce an organic-coated aqueous aerosol and then study the same reaction using appropriate spectroscopic techniques.

The kinetic experiments on monolayers of both single components and binary mixtures were performed at room temperature ($25 \pm 2\,^{\circ}\mathrm{C}$). In the future, the study of the these reactions at lower temperatures, $10 - 20\,^{\circ}\mathrm{C}$, representative of the lower troposphere (altitude below $3\,\mathrm{km}$), would also be interesting. Furthermore, to assess the effect of relative humidity on the heterogeneous reactions, further work is required to obtain a reliable measurement of the NO_3 concentrations in presence of water vapour.

The investigation of binary mixtures consisting of saturated and unsaturated surfactants with different chain lengths would be interesting. Similarly, the study of mixtures at different mixing ratios, i.e. OA-SA in ratio 1:9 mol, would help to determine the dependence of the resulting uptake coefficient on the mixing ratio, if any.

Appendix A

Oleic acid exposed to NO_3: fit of the $\Gamma(t)$

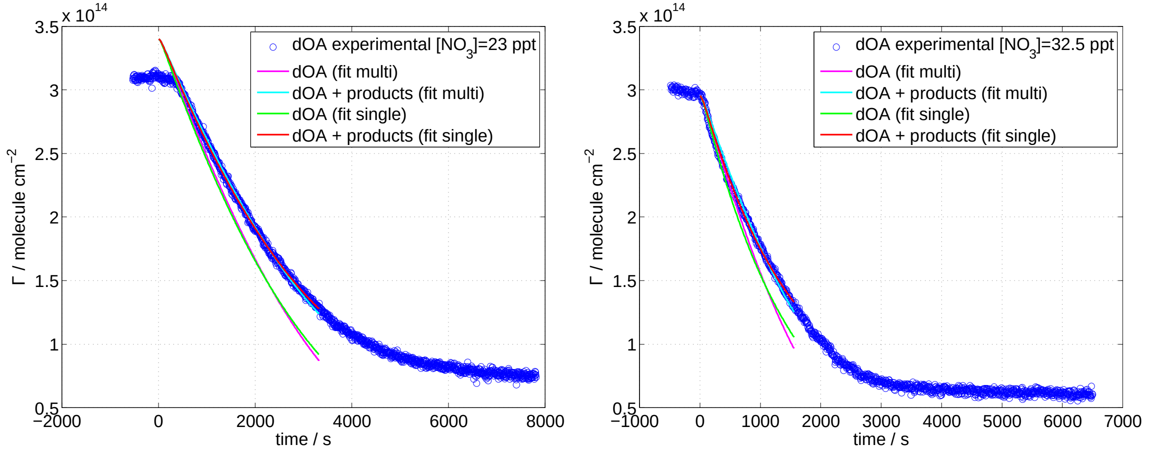

Figure A.1: Experimental surface excess of dOA monolayers exposed to NO_3 fitted with the kinetic model. Comparison of the two fitting approaches (single and multi) is displayed. The calculated decays of dOA are shown as comparison with the calculated decays of dOA and products. (left) $[NO_3] = 23\,ppt$. (right) $[NO_3] = 32.5\,ppt$

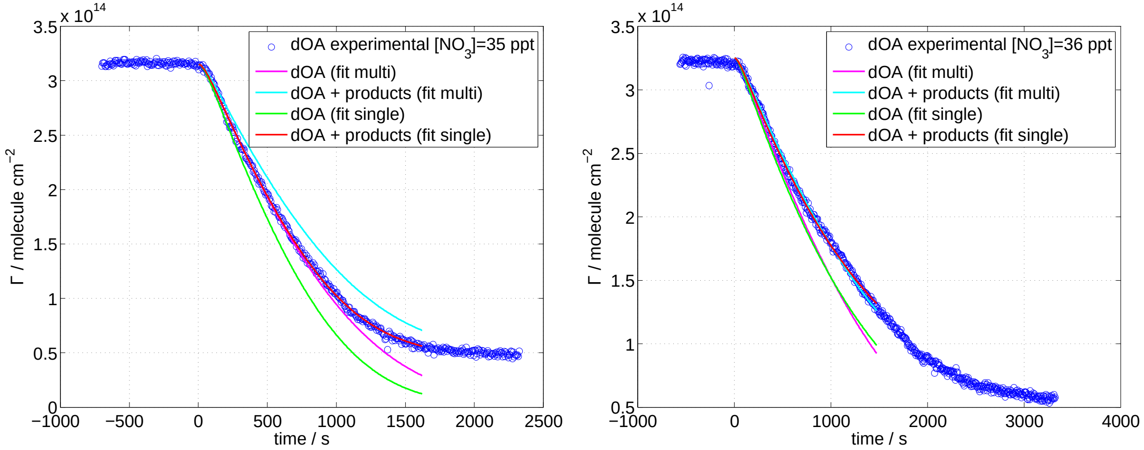

Figure A.2: Experimental surface excess of dOA monolayers exposed to NO_3 fitted with the kinetic model. Comparison of the two fitting approaches (single and multi) is displayed. The calculated decays of dOA are shown as comparison with the calculated decays of dOA and products. (left) $[NO_3] = 35$ ppt. (right) $[NO_3] = 36$ ppt

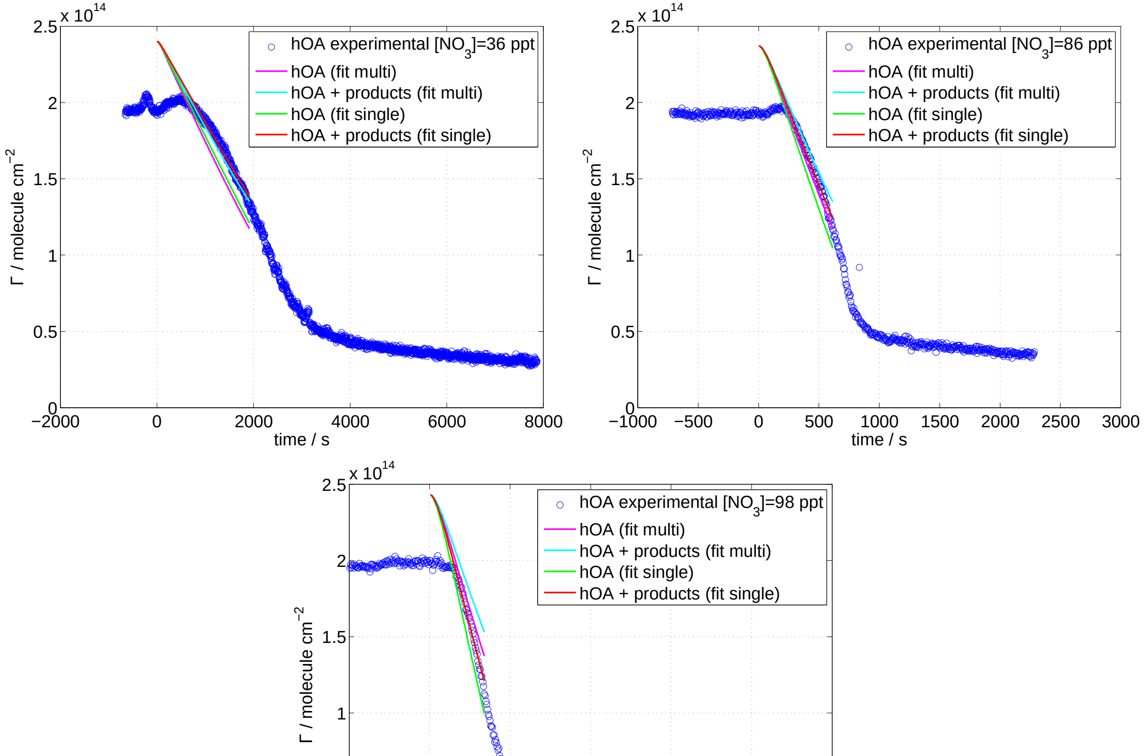

Appendix B

Palmitoleic acid exposed to NO_3: fit of the $\Gamma(t)$

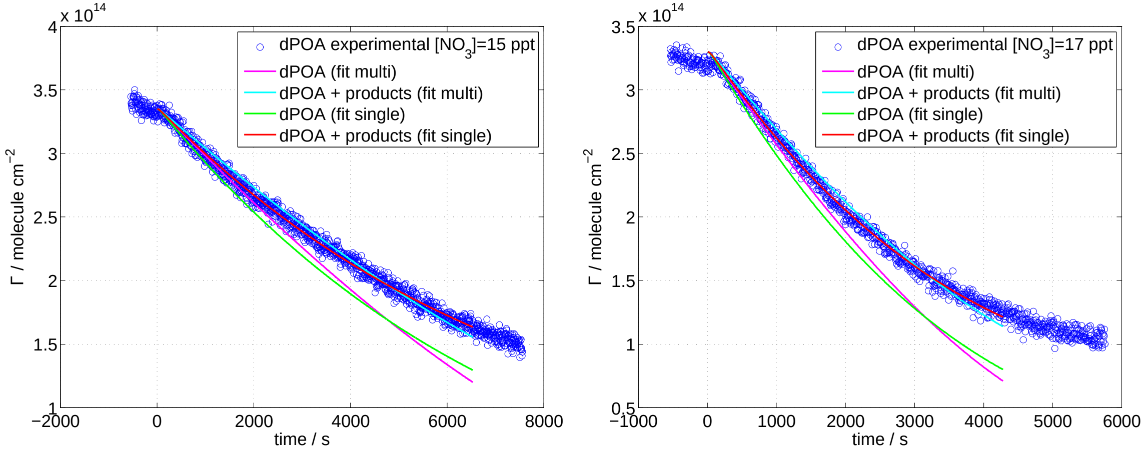

Figure B.1: Experimental surface excess of dPOA monolayers exposed to NO_3 fitted with the kinetic model. Comparison of the two fitting approaches (single and multi) is displayed. The calculated decays of dPOA are shown as comparison with the calculated decays of dPOA and products. (left) $[NO_3] = 15$ ppt. (right) $[NO_3] = 17$ ppt

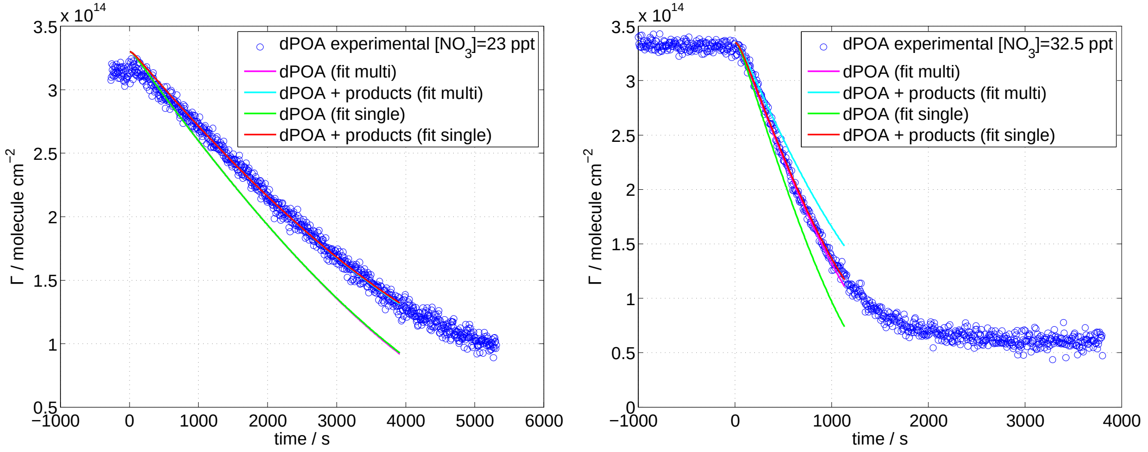

Figure B.2: Experimental surface excess of dPOA monolayers exposed to NO_3 fitted with the kinetic model. Comparison of the two fitting approaches (single and multi) is displayed. The calculated decays of dPOA are shown as comparison with the calculated decays of dPOA and products. (left) $[NO_3] = 23$ ppt. (right) $[NO_3] = 32.5$ ppt

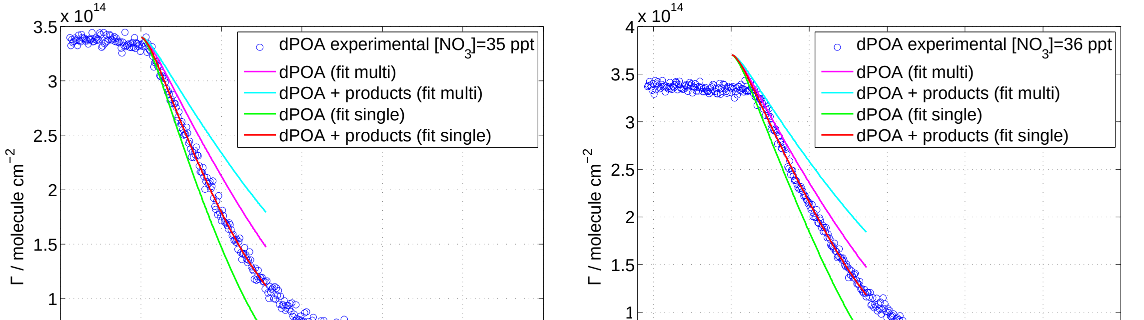

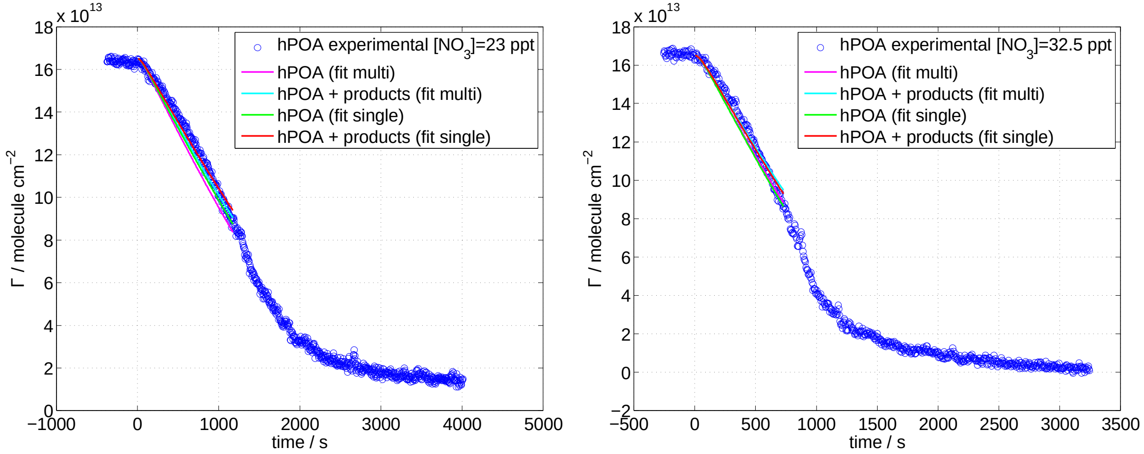

Figure B.4: Experimental surface excess of hPOA monolayers exposed to NO_3 fitted with the kinetic model. Comparison of the two fitting approaches (single and multi) is displayed. The calculated decays of hPOA are shown as comparison with the calculated decays of hPOA and products. (left) $[NO_3] =$ 23 ppt. (right) $[NO_3] =$ 32.5 ppt

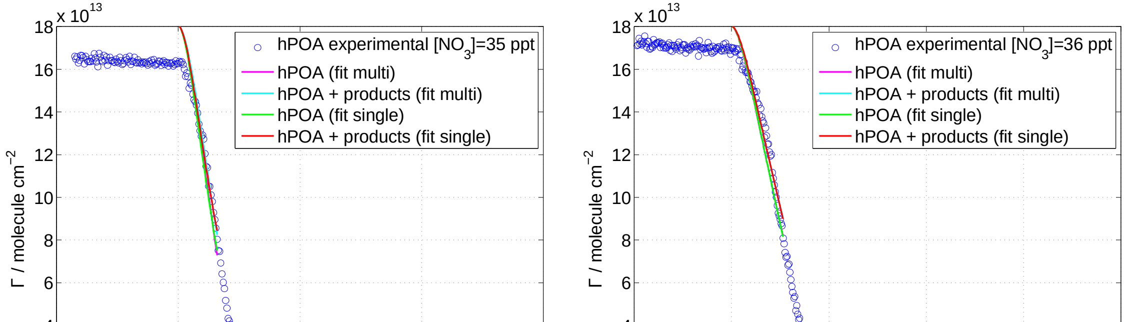

Appendix C

Methyl oleate exposed to NO_3: fit of the $\Gamma(t)$

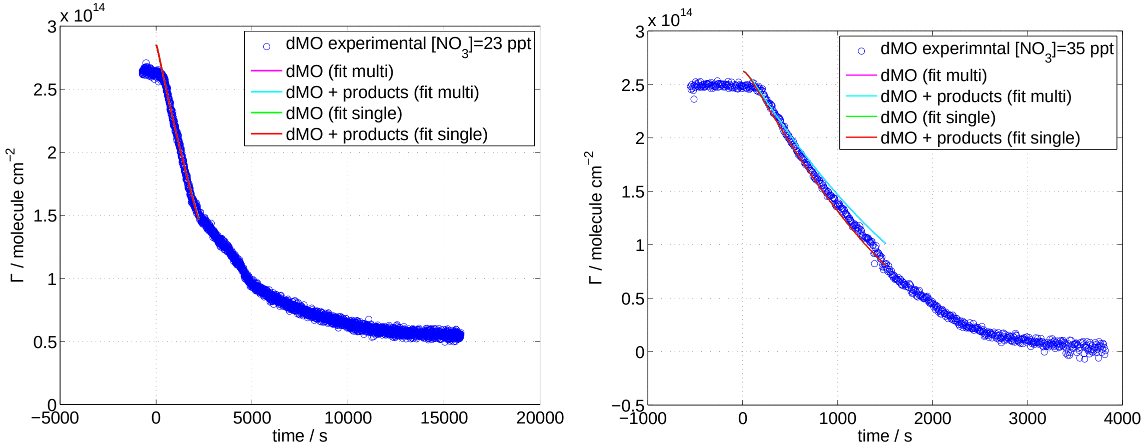

Figure C.1: Experimental surface excess of dMO monolayers exposed to NO_3 fitted with the kinetic model. Comparison of the two fitting approaches (single and multi) is displayed. The calculated decays of dMO are shown as comparison with the calculated decays of dMO and products. (left) $[NO_3] = 23$ ppt. (right) $[NO_3] = 35$ ppt

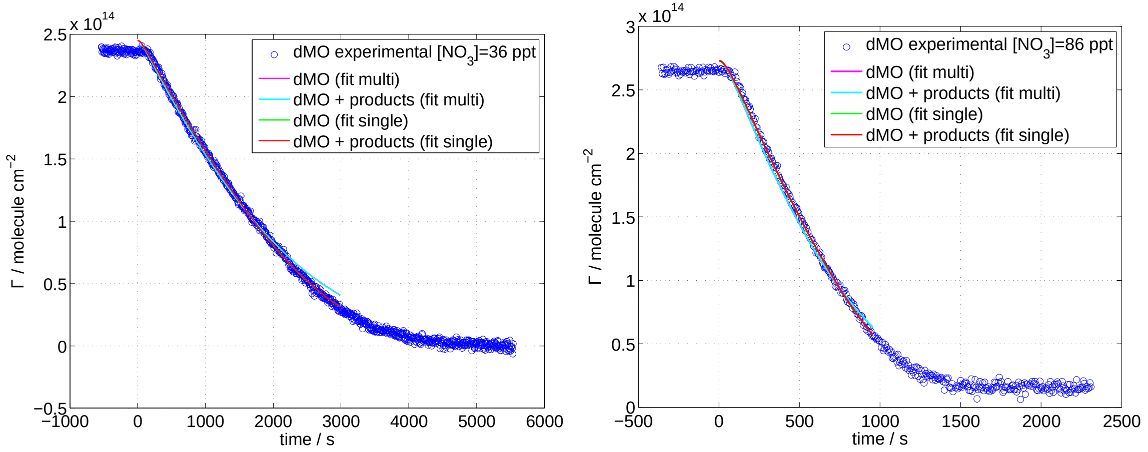

Figure C.2: Experimental surface excess of dMO monolayers exposed to NO_3 fitted with the kinetic model. Comparison of the two fitting approaches (single and multi) is displayed. The calculated decays of dMO are shown as comparison with the calculated decays of dMO and products. (left) $[NO_3] = 36$ ppt. (right) $[NO_3] = 86$ ppt

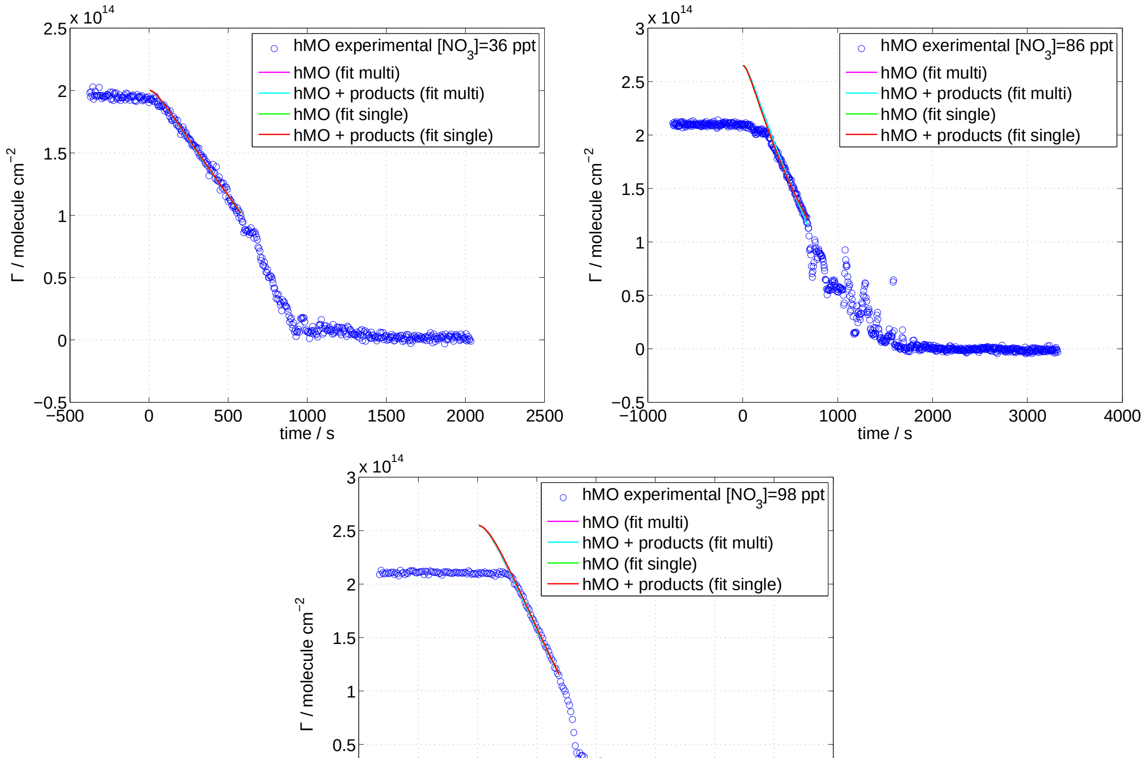

Appendix D

Arachidonic acid exposed to NO_3: fit of the $\Gamma(t)$

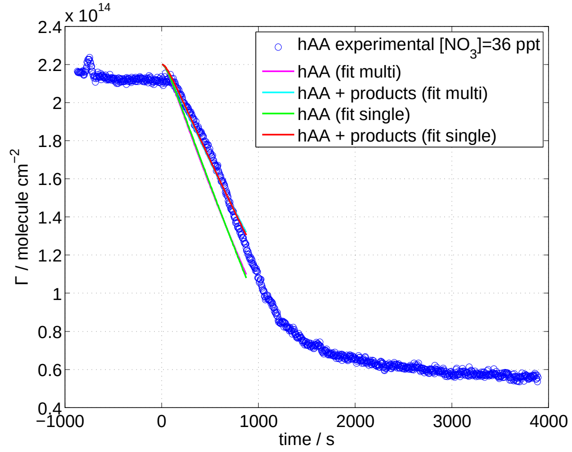

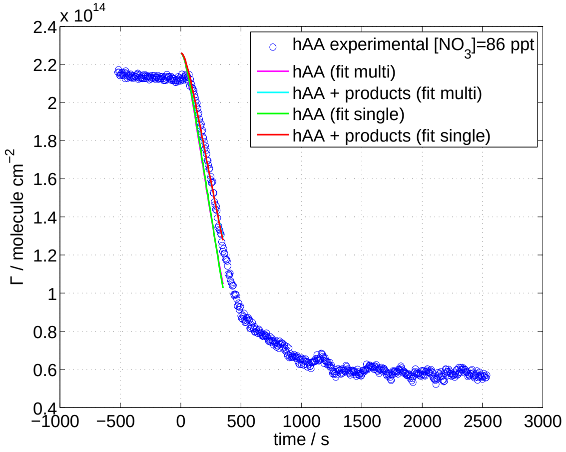

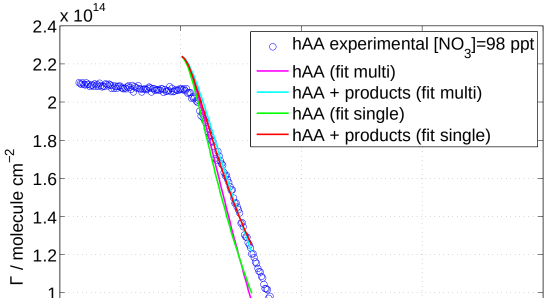

Appendix E

Binary mixture of OA and MO exposed to NO_3

Comparison with single component

dMO-hOA

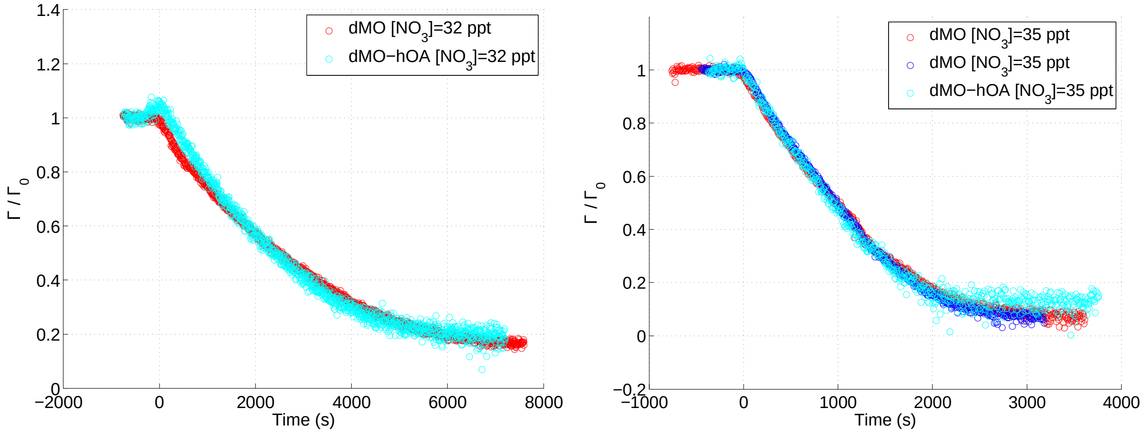

Figure E.1: Surface excess decay of dMO-hOA monolayers compared with pure dMO. Γ was normalized to its initial value to allow a clearer comparison. (left) $[NO_3] = 32\,\text{ppt}$. (right) $[NO_3] = 35\,\text{ppt}$.

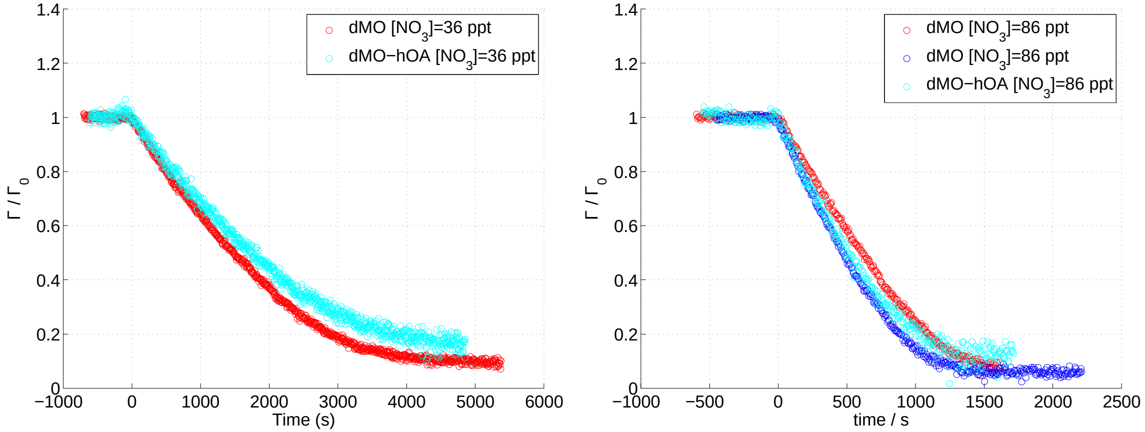

Figure E.2: Surface excess decay of dMO-hOA monolayers compared with pure dMO. Γ was normalized to its initial value to allow a clearer comparison. (left) $[NO_3] = 36$ ppt. (right) $[NO_3] = 86$ ppt.

dOA-hMO

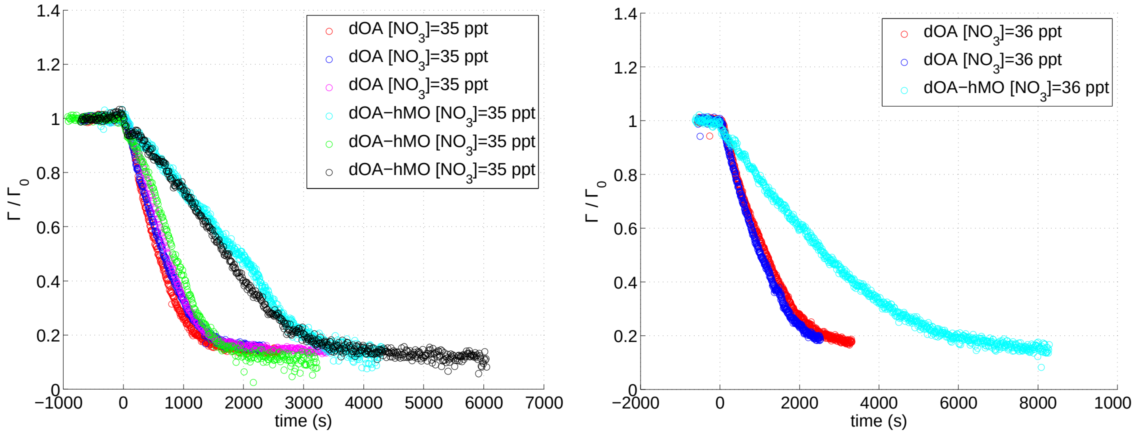

Figure E.3: Surface excess decay of dOA-hMO monolayers compared with pure dOA. Γ was normalized to its initial value to allow a clearer comparison. (left) $[NO_3] = 35$ ppt. (right) $[NO_3] = 36$ ppt.

Fit of the Γ(t)

dMO-hOA

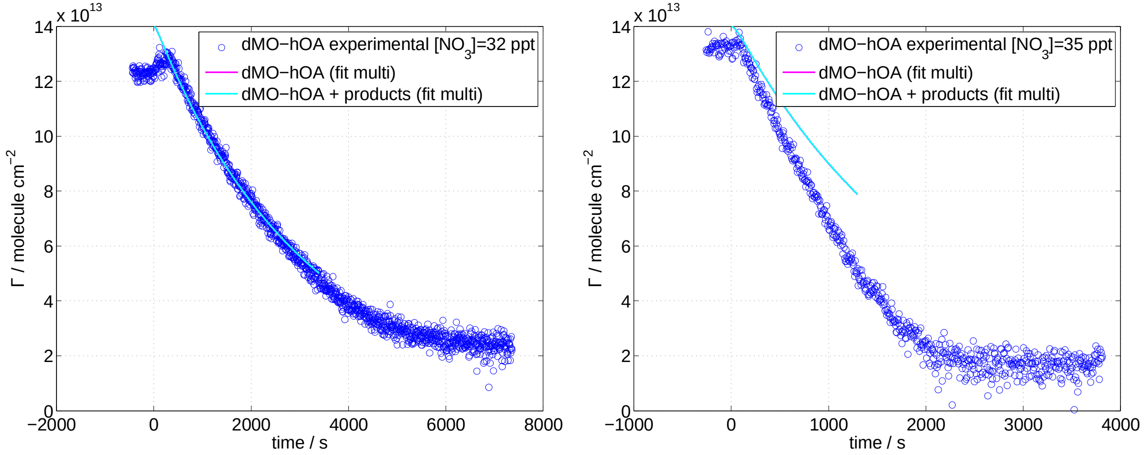

Figure E.4: Experimental surface excess of dMO-hOA monolayers exposed to NO_3 fitted with the kinetic model. The calculated decays of dMO-hOA are shown for comparison with the calculated decays of dMO-hOA and its reaction products. (left) $[NO_3] = 32$ ppt. (right) $[NO_3] = 35$ ppt.

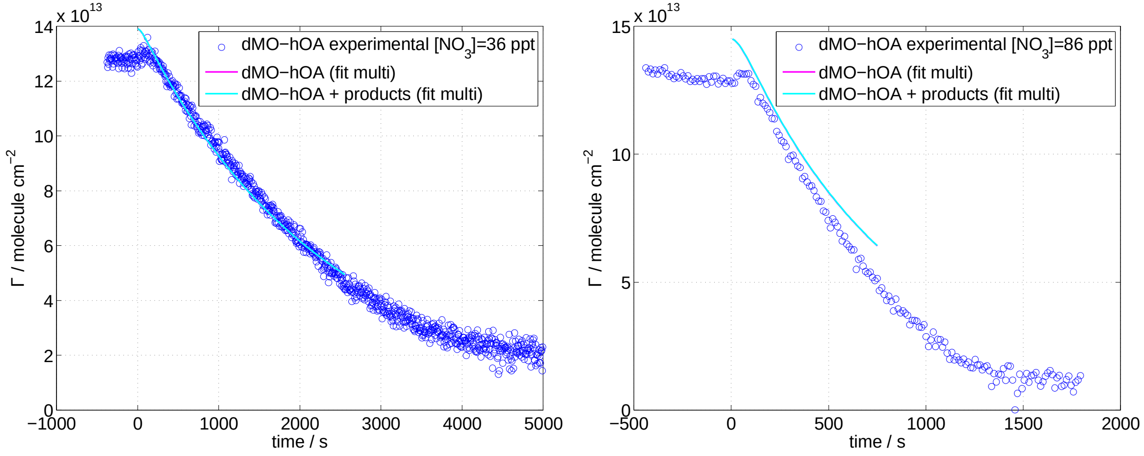

Figure E.5: Experimental surface excess of dMO-hOA monolayers exposed to NO_3

dOA-hMO

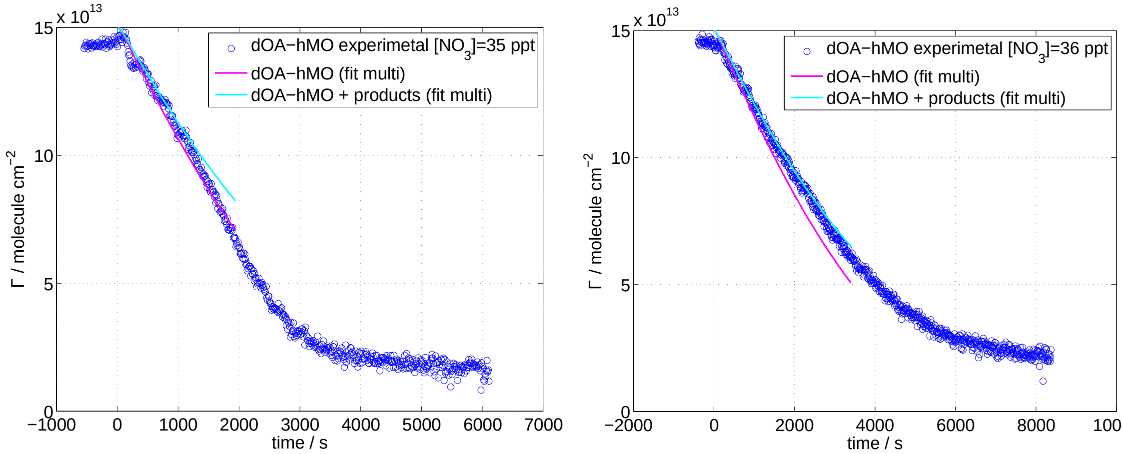

Figure E.6: Experimental surface excess of dOA-hMO monolayers exposed to NO_3 fitted with the kinetic model. The calculated decays of dOA-hMO are shown for comparison with the calculated decays of dOA-hMO and its reaction products. (left) $[NO_3] =$ 35 ppt. (right) $[NO_3] =$ 36 ppt.

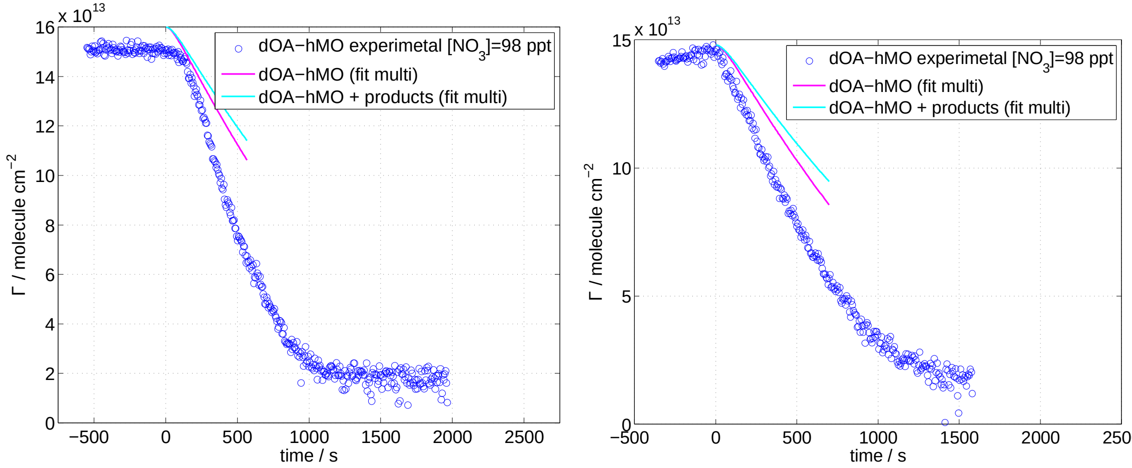

Figure E.7: Experimental surface excess of dOA-hMO monolayers exposed to NO_3 fitted with the kinetic model. The calculated decays of dOA-hMO are shown for comparison with the calculated decays of dOA-hMO and its reaction products. (left)

Appendix F

Binary mixture of OA and SA exposed to NO_3

Comparison with single component

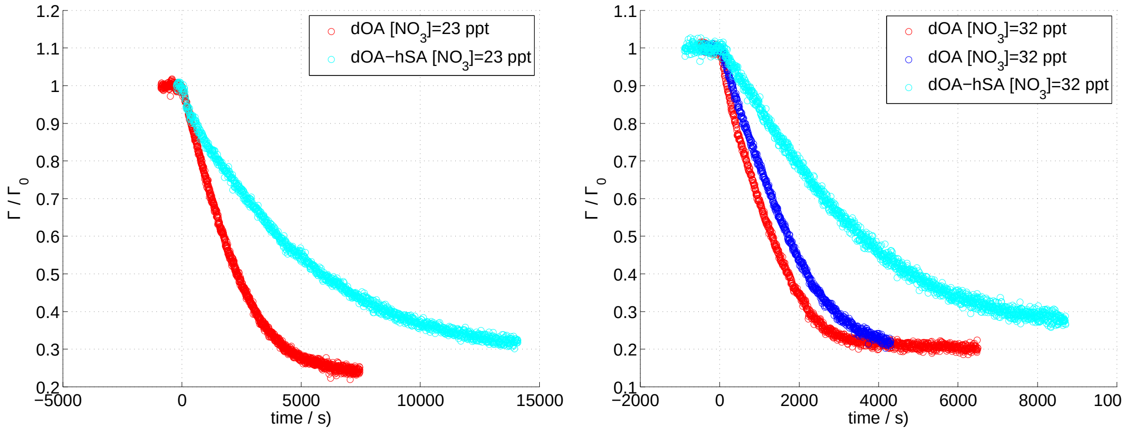

Figure F.1: Surface excess decay of dOA-hSA monolayers compared with pure dOA. Γ was normalized to its initial value to allow a clearer comparison. (left) $[NO_3] = 23$ ppt. (right) $[NO_3] = 32$ ppt.

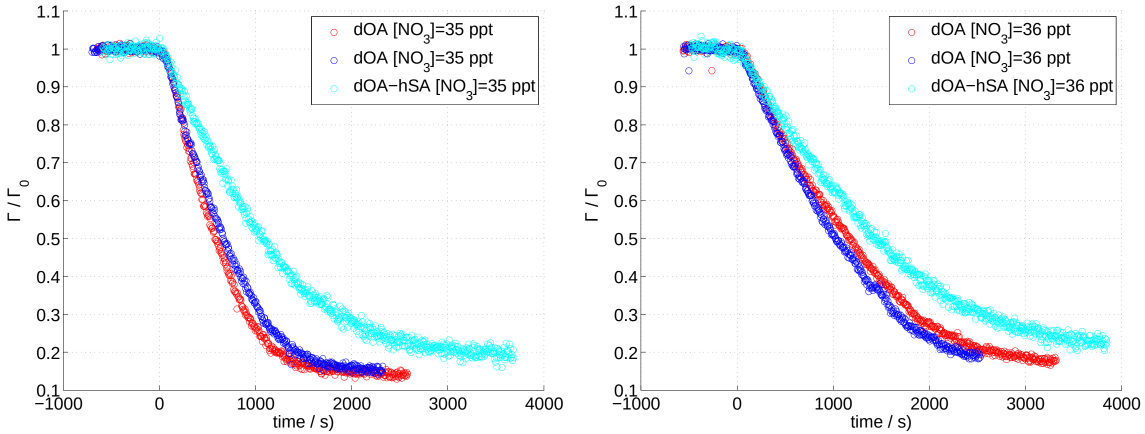

Figure F.2: Surface excess decay of dOA-hSA monolayers compared with pure dOA. Γ was normalized to its initial value to allow a clearer comparison. (left) $[NO_3] = 35\,ppt$. (right) $[NO_3] = 36\,ppt$.

Fit of the Γ(t)

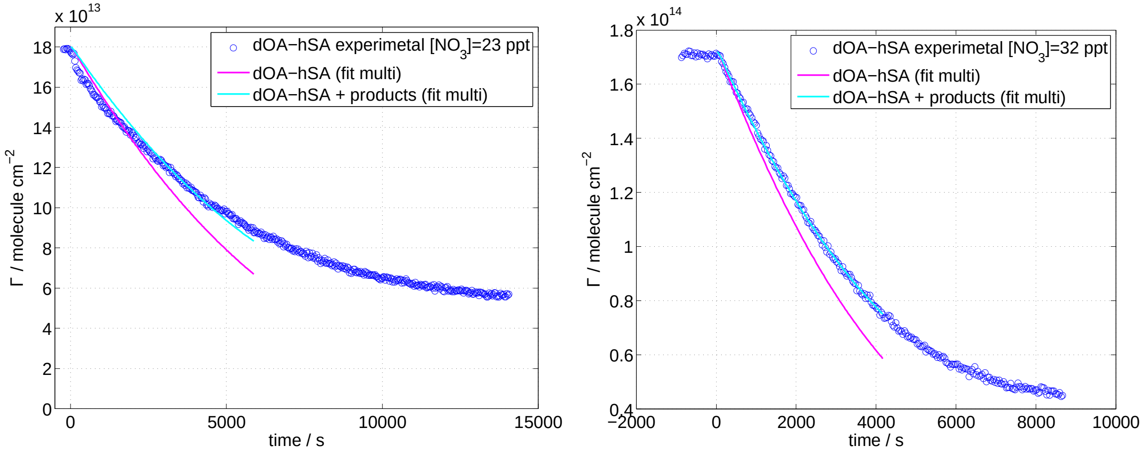

Figure F.3: Experimental surface excess of dOA-hSA monolayers exposed to NO_3 fitted with the kinetic model. The calculated decays of dOA-hSA are shown for comparison with the calculated decays of dOA-hSA and its reaction products. (left) $[NO_3] = 23\,ppt$. (right) $[NO_3] = 32\,ppt$.

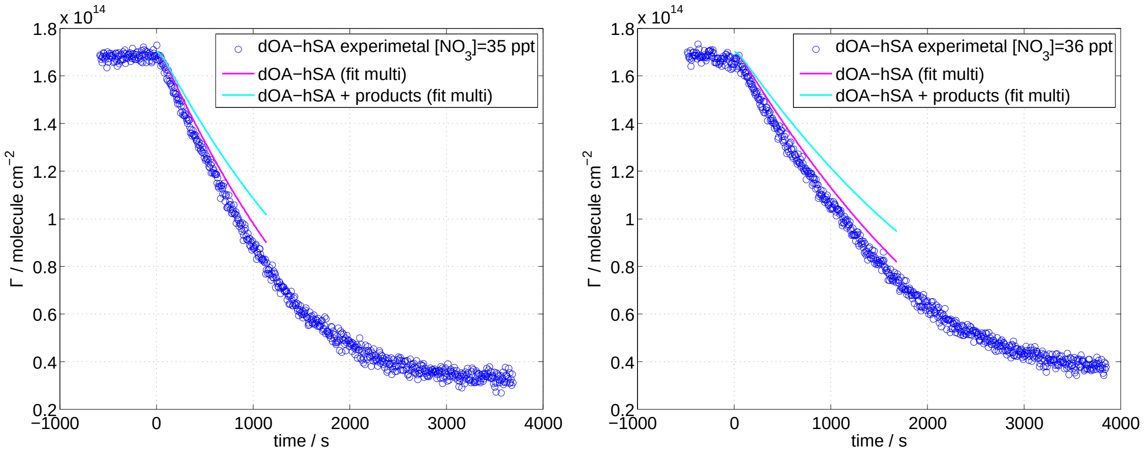

Figure F.4: Experimental surface excess of dOA-hSA monolayers exposed to NO_3 fitted with the kinetic model. The calculated decays of dOA-hSA are shown for comparison with the calculated decays of dOA-hSA and its reaction products. (left) $[NO_3] = 35\,ppt$. (right) $[NO_3] = 36\,ppt$.

Bibliography

[1] Shindell, D. T. et al., Science 326 (2009) 716.

[2] Stevens, B. and Feingold, G., Nature 461 (2009) 607.

[3] Solomon, S. et al., Contribution of working group i to the fourth assessment report of the intergovernmental panel on climate change, in Climate Change 2007 - The Physical Science Basis, Cambridge University Press, 2007.

[4] Fuzzi, S. et al., Atmospheric Chemistry and Physics 6 (2006) 2017.

[5] Robinson, A. L., Donahue, N. M., and Rogge, W. F., Journal of Geophysical Research: Atmospheres 111 (2006) n/a.

[6] Wayne, R. et al., Atmospheric Environment. Part A. General Topics 25 (1991) 1 , The nitrate radical: Physics, Chemistry, and the Atmosphere.

[7] Mora-Diez, N. and Boyd, R. J., The Journal of Physical Chemistry A 106 (2002) 384.

[8] Gross, S., Iannone, R., Xiao, S., and Bertram, A. K., Phys. Chem. Chem. Phys. 11 (2009) 7792.

[9] King, M. D., Thompson, K. C., and Ward, A. D., Journal of the American Chemical Society 126 (2004) 16710.

[10] Vesna, O. et al., Atmospheric Chemistry and Physics 8 (2008) 4683.

[15] Tsigaridis, K. et al., Atmospheric Chemistry and Physics Discussions 14 (2014) 6027.

[16] Harrison, R. M., Jones, A. M., and Lawrence, R. G., Atmospheric Environment 38 (2004) 4531 .

[17] Rogge, W. F., Mazurek, M. A., Hildemann, L. M., Cass, G. R., and Simoneit, B. R., Atmospheric Environment. Part A. General Topics 27 (1993) 1309 .

[18] Krivácsy, Z. et al., Atmospheric Environment 35 (2001) 6231 .

[19] Gross, S., Heterogeneous reactions of NO_3 and other oxidants with organic films and substrates of atmospheric relevance, Phd thesis, Faculty of Graduate Studies (Chemistry), University of British Columbia (Vancouver), 2009.

[20] Tervahattu, H., Juhanoja, J., and Kupiainen, K., Journal of Geophysical Research: Atmospheres 107 (2002) ACH 18.

[21] Tervahattu, H. et al., Journal of Geophysical Research: Atmospheres 107 (2002) AAC 1.

[22] Ellison, G. B., Tuck, A. F., and Vaida, V., Journal of Geophysical Research: Atmospheres 104 (1999) 11633.

[23] Hearn, J. D., Lovett, A. J., and Smith, G. D., Phys. Chem. Chem. Phys. 7 (2005) 501.

[24] Xiao, S. and Bertram, A. K., Phys. Chem. Chem. Phys. 13 (2011) 6628.

[25] Zahardis, J. and Petrucci, G. A., Atmospheric Chemistry and Physics 7 (2007) 1237.

[26] Schauer, J. J., Kleeman, M. J., Cass, G. R., and Simoneit, B. R. T., Environmental Science & Technology 36 (2002) 567.

[27] Allan, J. D. et al., Atmospheric Chemistry and Physics 10 (2010) 647.

[31] Shastri, L. V. and Huie, R. E., International Journal of Chemical Kinetics 22 (1990) 505.

[32] Atkinson, R., Gas-Phase Tropospheric Chemistry of Organic Compounds, American Intstitute of Physics, 1994.

[33] Pfrang, C. et al., Phys. Chem. Chem. Phys. 16 (2014) 13220.

[34] Pilling, J. and Seakins, P., Reaction Kinetics, Oxford University Press, 1996.

[35] Davidovits, P., Kolb, C. E., Williams, L. R., Jayne, J. T., and Worsnop, D. R., Chemical Reviews 106 (2006) 1323.

[36] Davidovits, P., Kolb, C. E., Williams, L. R., Jayne, J. T., and Worsnop, D. R., Chemical Reviews 111 (2011) null.

[37] Sander, S. P. et al., JPL Publication 10-6 (2011).

[38] Atkinson, R. et al., Atmospheric Chemistry and Physics 4 (2004) 1461.

[39] Danckwerts, P. V., Trans. Faraday Soc. 47 (1951) 1014.

[40] Worsnop, D. R. et al., The Journal of Physical Chemistry 93 (1989) 1159.

[41] Swartz, E. et al., Environmental Science & Technology 31 (1997) 2634.

[42] Knopf, D., Cosman, L., Mousavi, P., Mokamati, S., and Bertram, A. K., The Journal Physical Chemistry A 111 (2007) 11021.

[43] Lovejoy, E. R. and Hanson, D. R., The Journal of Physical Chemistry 99 (1995) 2080.

[44] Welter, E. and Neidhart, B., Fresenius' Journal of Analytical Chemistry 357 (1997) 345.

[45] Dennis-Smither, B. J., Hanford, K. L., Kwamena, N.-O. A., Miles, R. E. H., and

[49] Cosman, L. M. and Bertram, A. K., The Journal of Physical Chemistry A 112 (2008) 4625.

[50] Wadia, Y., Tobias, D. J., Stafford, R., and Finlayson-Pitts, B. J., Langmuir 16 (2000) 9321.

[51] Thompson, K. C. et al., Langmuir 26 (2010) 17295.

[52] King, M. D., Rennie, A. R., Pfrang, C., Hughes, A. V., and Thompson, K. C., Atmospheric Environment 44 (2010) 1822 .

[53] King, M. D. et al., Phys. Chem. Chem. Phys. 11 (2009) 7699.

[54] Fermi, E. and Zinn, W., Reflection of neutrons on mirrors, Manhattan District, 1946.

[55] Cubitt, R. and Fragneto, G., Scattering, chapter 2.8.3 - Neutron reflection: principles and examples of applications, pages 1198–1208, Academic Press London, 2002.

[56] Scherm, R., Annals of Physics 7 (1972) 349.

[57] Squires, G., Introduction to the theory of thermal neutron scattering, Cambridge University Press, 1978.

[58] Born, M. and Wolf, E., Principles of optics, Pergamon press, 6th edition, 1980.

[59] Debye, P., Annalen der Physik 348 (1913) 49.

[60] Waller, I., Zeitschrift fur Physik 17 (1923) 398.

[61] Heavens, O., Optical properties of thin solid films, Butterworths Scientific Publications, 1955.

[62] Lu, J., Thomas, R., and Penfold, J., Advances in Colloid and Interface Science 84 (2000) 143 .

[67] Barnes, G. and Gentle, I., Interfacial science: an introduction, Oxford University Press, 2nd edition, 2010.

[68] Tonigold, K., Varga, I., Nylander, T., and Campbell, R. A., Langmuir 25 (2009) 4036.

[69] Manning-Benson, S., Bain, C. D., and Darton, R. C., Journal of Colloid and Interface Science 189 (1997) 109 .

[70] Meunier, J., Light scattering by liquid surfaces and complementary techniques, Marcel Dekker, 1992.

[71] Atkins, P. W., Physical Chemistry, OUP: Oxford, 6th edition, 1997.

[72] Casson, B. D. and Bain, C. D., Langmuir 13 (1997) 5465.

[73] Manning-Benson, S., Parker, S. R. W., Bain, C. D., and Penfold, J., Langmuir 14 (1998) 990.

[74] Casson, B. D., Braun, R., and Bain, C. D., Faraday Discuss. 104 (1996) 209.

[75] Beaglehole instruments, Picometer Ellipsometer Manual, 2008.

[76] Beaglehole, D., Physica B+C 100 (1980) 163 .

[77] Benjamins, J.-W., Thuresson, K., and Nylander, T., Langmuir 21 (2005) 149 .

[78] Angus-Smyth, A., Bain, C. D., Varga, I., and Campbell, R. A., Soft Matter 9 (2013) 6103.

[79] Hénon, S. and Meunier, J., Review of Scientific Instruments 62 (1991) 936.

[80] Hönig, D. and Möbius, D., The Journal of Physical Chemistry 95 (1991) 4590.

[81] P.Drude, Ann. Phys. Chem. (Leipzeig) 43 (1891) 126.

[82] Azzam, R. and Bashara, N., Ellipsometry and Polarized light, Noth-Holland

[86] Platt, U. and Perner, D., Measurements of atmospheric trace gases by long path differential UV/Visible absorption spectroscopy, in Optical and Laser Remote Sensing, edited by Killinger, D. K. and Mooradian, A., volume 39 of Springer Series in Optical Sciences, pages 97–105, Springer Berlin Heidelberg, 1983.

[87] Hanst, P. L., Spiller, L. L., Watts, D. M., Spence, J. W., and Miller, M. F., Journal of the Air Pollution Control Association 25 (1975) 1220.

[88] Frankenberg, C., Platt, U., and Wagner, T., Atmospheric Chemistry and Physics 5 (2005) 9.

[89] Reusch, W., Visible and ultraviolet spectroscopy.

[90] Sherman Hsu, C. P., Infrared spectroscopy, in Handbook of instrumental techniques for analytical chemistry, edited by Settle, F., pages 247–283, Prentice Hall, 1983.

[91] COSMOS, NR data treatment program, http://www.ill.eu/instruments-support/instruments-groups/instruments/d17/more/documentation/d17-lamp-book/cosmos/.

[92] LAMP, the Large Array Manipulation Program, http://www.ill.eu/data_treat/lamp/the-lamp-book/.

[93] Nelson, A., Journal of Applied Crystallography 39 (2006) 273.

[94] Penfold, J. and Thomas, R. K., Journal of Physics: Condensed Matter 2 (1990) 1369.

[95] Li, P. X. et al., Langmuir 29 (2013) 9324.

[96] Pöschl, U., Rudich, Y., and Ammann, M., Atmospheric Chemistry and Physics 7 (2007) 5989.

[97] Shiraiwa, M., Garland, R. M., and Pöschl, U., Atmospheric Chemistry and

[101] MATLAB, version 7.12.0 (R2011a), The MathWorks Inc., Natick, Massachusetts, 2011.

[102] Allodi, G., FMINUIT - a binding to minuit for matlab, octave & scilab, http://www.fis.unipr.it/~giuseppe.allodi/Fminuit/Fminuit_intro.html.

[103] Angus-Smyth, A., Campbell, R. A., and Bain, C. D., Langmuir 28 (2012) 12479.

[104] de Aguiar, H. B., Strader, M. L., de Beer, A. G. F., and Roke, S., The Journal of Physical Chemistry B 115 (2011) 2970.

[105] Chevallier, E. et al., Soft Matter 7 (2011) 7866.

[106] Jordens, S., Isa, L., Usov, I., and Mezzenga, R., Nature Communications 4 (2013).

[107] Kanakidou, M. et al., Atmospheric Chemistry and Physics 5 (2005) 1053.

[108] Rudich, Y., Donahue, N. M., and Mentel, T. F., Annual Review of Physical Chemistry 58 (2007) 321, PMID: 17090227.

[109] Donaldson, D. J. and Vaida, V., Chemical Reviews 106 (2006) 1445, PMID: 16608186.

[110] Thomas, F., Fluid dynamics simulation on mimik chamber, Private communication, 2013.

[111] Systèmes, D., SolidWorks version 5000 (2012), SolidWorks corporation, Waltham, Massachusetts, 2012.

[112] Zhou, S. et al., Atmospheric Chemistry and Physics 14 (2014) 1371.

[113] McClurkin, J. D., Maier, D. E., and Ileleji, K. E., Journal of Stored Products Research 55 (2013) 41 .

[114] Seoane, R. et al., The Journal of Physical Chemistry B 104 (2000) 7735.

[119] Sander, R., Compilation of henry's law constants for inorganic and organic species of potential importance in environmental chemistry, Air Chemistry Department Max-Planck Institute of Chemistry PO Box 3060 55020 Mainz Germany, 1999.

[120] Smith, G. D., Woods, E., DeForest, C. L., Baer, T., and Miller, R. E., The Journal of Physical Chemistry A 106 (2002) 8085.

[121] Troe, J., Journal of Chemical Physics 79 (1983) 6017.

[122] Guttman, A., Journal of Quantitative Spectroscopy & Radiative Transfer 2 (1961) 1.

[123] Cantrell, C. A., Davidson, J. A., McDaniel, A. H., Shetter, R. E., and Calvert, J. G., Chemical Physics Letters 148 (1988) 358 .

[124] Hjorth, J., Ottobrini, G., Cappellani, F., and Restelli, G., The Journal of Physical Chemistry 91 (1987) 1565.

[125] Chackerian, C., Sharpe, S. W., and Blake, T. A., Journal of Quantitative Spectroscopy and Radiative Transfer 82 (2003) 429 .

[126] Ammann, M. et al., Atmospheric Chemistry and Physics 13 (2013) 8045.

[127] Brown, S. S. and Stutz, J., Chem. Soc. Rev. 41 (2012) 6405.

[128] Shiraiwa, M., Pöschl, U., and Knopf, D. A., Environmental Science & Technology 46 (2012) 6630.

[129] Knopf, D. A., Mak, J., Gross, S., and Bertram, A. K., Geophysical Research Letters 33 (2006).

[130] Gilman, J., Eliason, T., Fast, A., and Vaida, V., Journal of Colloid and Interface Science 280 (2004) 234.

[131] Craig, B. M., Canadian Journal of Chemistry 31 (1953) 499.

[137] Shiraiwa, M., Ammann, M., Koop, T., and Pöschl, U., Proceedings of the National Academy of Sciences 108 (2011) 11003.

[138] Shiraiwa, M., Zuend, A., Bertram, A. K., and Seinfeld, J. H., Phys. Chem. Chem. Phys. 15 (2013) 11441.

[139] Knopf, D. A., Forrester, S. M., and Slade, J. H., Phys. Chem. Chem. Phys. 13 (2011) 21050.

[140] Rogge, W. F., Hildemann, L. M., Mazurek, M. A., Cass, G. R., and Simoneit, B. R. T., Environmental Science & Technology 25 (1991) 1112.

[141] Hildemann, L., Markowski, G., and Cass, G., Environ. Sci. Technol. 25 (1991) 744.

[142] Schauer, J. J., Kleeman, M. J., Cass, G. R., and Simoneit, B. R. T., Environmental Science & Technology 36 (2002) 1169.

[143] Zhao, Y., Hu, M., Slanina, S., and Zhang, Y., Environmental Science & Technology 41 (2007) 99.

[144] Schütze, M. and Herrmann, H., Journal of Atmospheric Chemistry 52 (2005) 1.